Semiclassical Transition State Theory for Chemical Reactions: Theory, Development and Applications



Timothy Burd

Brasenose College

University of Oxford

A thesis submitted for the degree of

Doctor of Philosophy

Trinity 2020

Abstract

Semiclassical Transition State Theory (SCTST) is an efficient rate theory, which aims to calculate the rate constants of chemical reactions, including quantum tunnelling effects, without requiring a global potential energy surface. It has applications in understanding chemical reactions involving medium sized molecules where more computationally expensive methods are not possible. The work in this thesis aims to increase our understanding of the theory, apply the method to interesting problems in chemistry, and develop the method for the study of a broader range of systems and problems.

The **Theory** section of this thesis begins with a review of the theoretical basis of SCTST. We then illustrate how the theory can be adapted for treating complex systems with internal rotational degrees of freedom, and higher orders of perturbation theory. We then show that the SCTST method implicitly accounts for key multidimensional effects, such as corner-cutting and variational effects, and identify the limitations of this approach.

In the **Applications** section, we apply SCTST to the study of a range of chemical problems. We show that SCTST in full and reduced dimensions can be used to help understand the decay of Criegee intermediates in the atmosphere, and identify a water-catalysed route that contributes significantly to the decay process. By studying enol-formation from a phenyl pyruvic acid derivative, we provide evidence for an alternative reaction mechanism, consistent with recently performed experiments.

In the **Development** section, efforts to adapt the method to increase its range of applicability are then described. A reduced dimensional form of SCTST is discussed and shown to be particularly efficient, where the required number of electronic structure calculations is reduced to an absolute minimum. We also show how the SCTST rate equations can be recast to calculate tunnelling splittings in chemical systems in a reliable and cost efficient way.

Finally, we present a user friendly code base for SCTST calculations, made freely available for download, called *pySCTST*.

Acknowledgements

It has been a pleasure to work under the supervision of Professor Sir David Clary, who has shown continued guidance, support and enthusiasm over the course of my degree and to whom I am very thankful. I would also like to thank Dr Xiao Shan, who has been a constant source of helpful discussions on every topic in this thesis. Professor Dr. Jeremy Richardson generously let me visit his group in Zürich, where I learnt a huge amount, and Professor Bill Miller has provided many detailed and helpful discussions.

I feel privileged to have had the opportunity to produce this thesis and am hugely indebted to the continued support of my family over the course of my education. I would also like to thank everyone who has made my time studying in Oxford an absolute joy - Becca, Rob, Jamie, Quentin, Kyaw, David, Laszlo, Chloe, Matt, Max and Hannah.

This work has been funded by the EPSRC Centre for Doctoral Training in Theory and Modelling in Chemical Sciences (Project Grant No. EP/L015722/1), to whom I am also grateful.

Contents

List of Reactions **vii**

List of Abbreviations **viii**

Publications **ix**

1 Introduction **1**
1.1 Transition State Theory 1
1.2 Exact methods 3
1.3 Reduced dimensionality methods 5
1.4 Semiclassical methods 6
1.5 Semiclassical Transition State Theory 9
1.6 Tunnelling splittings 11
1.7 Thesis outline 12

2 Semiclassical Transition State Theory **14**
2.1 The WKB method for tunnelling 15
2.2 The SCTST result 19
2.3 Developments for polyatomic reactions 25
2.4 One-dimensional SCTST 28
2.5 Computational methods 30
2.6 pySCTST 32

3 SCTST in one-dimension **33**
3.1 Introduction 34
3.2 Internal rotations in SCTST 35
3.3 Comparison of 1D-SCTST to other one-dimensional methods . . . 46
3.4 The effect of deep tunnelling 48
3.5 Fourth order vibrational perturbation theory 50
3.6 Conclusions 53

4 Corner-cutting and variational effects in SCTST **55**
4.1 Introduction . . . 56
4.2 Corner-cutting in SCTST . . . 57
4.3 Variational effects . . . 64
4.4 Conclusions . . . 76

5 The decay of Criegee intermediates in the atmosphere **78**
5.1 Introduction . . . 79
5.2 Computational methods . . . 82
5.3 Results and discussion . . . 83
5.4 Microcanonical rates . . . 98
5.5 Corner-cutting paths . . . 99
5.6 Conclusions . . . 102

6 Tunnelling control in the rearrangements of carbenes **103**
6.1 Introduction . . . 104
6.2 Methylhydroxycarbene decay . . . 104
6.3 “Hydrogen Tunnelling Avoided"? . . . 105
6.4 Conclusions . . . 110

7 SCTST in reduced dimensions **113**
7.1 Introduction . . . 114
7.2 The inefficiency of SCTST in full dimensions . . . 115
7.3 The RD-SCTST framework . . . 115
7.4 Selecting active modes . . . 117
7.5 Consistent anharmonic treatment . . . 122
7.6 Application to Criegee chemistry . . . 124
7.7 Application to a carbene rearrangement . . . 126
7.8 Weighted mode selection . . . 131
7.9 Conclusions . . . 136

8 Approximate SCTST in full dimensions **139**
8.1 Introduction . . . 140
8.2 Theory . . . 141
8.3 Results . . . 142
8.4 Conclusions . . . 142

9 Semiclassical Perturbation Theory for tunnelling splittings 146
9.1 Introduction . . . 147
9.2 Breakdown of the Lifshitz-Herring formula . . . 148
9.3 An 'exact' WKB tunnel splitting . . . 150
9.4 Semiclassical Perturbation Theory of tunnelling splittings . . . 156
9.5 Application to malonaldehyde . . . 157
9.6 Application to tropolone . . . 161
9.7 Conclusions . . . 163

10 Conclusions 165

References 169

Appendices

A The pySCTST software 192
A.1 Requirements . . . 192
A.2 The repository . . . 193

B WKB tunnelling in a parabolic barrier 194

C SCTST-θ 195
C.1 Derivation . . . 195
C.2 Deep tunnelling in SCTST-θ . . . 196
C.3 1D-SCTST-θ . . . 196

D Periodic orbit splittings 198
D.1 Quantum mechanical Green's function . . . 199
D.2 Semiclassical Green's function . . . 199
D.3 Origin of the discrepancy with the Lifshitz-Herring formula . . . 203
D.4 Application to the SPT method . . . 203

List of Reactions

R1 . . . . . $CH_3 + CH_4 \rightarrow CH_4 + CH_3$

R2 . . . . . $CH_3 + CDH_3 \rightarrow CDH_3 + CH_3$

R3 . . . . . $CD_3 + CD_4 \rightarrow CD_4 + CD_3$

R4 . . . . . $CH_3 + H_2 \rightarrow CH_4 + H$

R5 . . . . . $CH_4 + O \rightarrow CH_3 + OH$

R6 . . . . . $CH_4 + OH \rightarrow CH_3 + H_2O$

R7 . . . . . $^{37}Cl + H^{35}Cl \rightarrow {}^{37}ClH + {}^{35}Cl$

R8 . . . . . $D + H\mu \rightarrow D\mu + H$

R9 . . . . . $CH_3CROO \rightarrow CH_2CROOH$

R10 . . . . . $CH_3CHOO + H_2O \rightarrow CH_2CHOOH + H_2O$

R11 . . . . . The isomerisation of cyclobutylidene

List of Abbreviations

AFD-SCTST . . Approximate full-dimensional SCTST

B3LYP . . . . . Becke, 3-parameter, Lee–Yang–Parr Exchange-correlation functional

cc-pVXZ . . . . Dunning's correlation consistent basis sets. X = D,T,Q,5...

aug-cc-pVXZ . . Augmented versions of the preceding basis sets with added diffuse functions

CCSD(T) . . . . Coupled cluster, with singles, doubles and perturbative triples

CI . . . . . Criegee intermediate

CRP . . . . . Cumulative reaction probability

DoF . . . . . Degree of freedom

DFT . . . . . Density functional theory

DT . . . . . Deep tunnelling

FD/RD/1D . . . Full-dimensional/Reduced-dimensional/One-dimensional

HR . . . . . Hindered rotation

KIE . . . . . Kinetic isotope effect

MEP . . . . . Minimum energy path

MP2 . . . . . Second order Møller-Plesset perturbation theory

PES . . . . . Potential energy surface

SCTST . . . . . Semiclassical Transition State Theory

SPT . . . . . Semiclassical perturbation theory for tunnelling splittings

TST . . . . . Transition State Theory

TS . . . . . Transition state

VPT2 . . . . . Second order vibrational perturbation theory

VTST . . . . . Variational Transition State Theory

WKB . . . . . The Wentzel-Kramers-Brillouin approximation

ZPE . . . . . Zero point energy

Publications

The work in this thesis is partially based on the following publications:

1. Burd, T. A. H., Shan, X. & Clary, D. C. Tunnelling and the kinetic isotope effect in $CH_3 + CH_4 \rightarrow CH_4 + CH_3$: An application of semiclassical transition state theory. *Chem. Phys. Lett.* **693,** 88–94 (2018).
2. Burd, T. A. H., Shan, X. & Clary, D. C. Catalysis and Tunnelling in the Unimolecular Decay of Criegee Intermediates. *Phys. Chem. Chem. Phys.* **20,** 25224–25234 (2018).
3. Shan, X., Burd, T. A. H. & Clary, D. C. New Developments in Semiclassical Transition-State Theory. *J. Phys. Chem. A* **123,** 4639–4657 (2019).
4. Burd, T. A. H., Shan, X. & Clary, D. C. Tunnelling in Cyclocarbenes: An Application of Semiclassical Transition State Theory in Reduced Dimensions. *Chem. Phys. Lett.* **735,** 136783 (2019).
5. Burd, T. A. H., Shan, X. & Clary, D. C. Hydrogen Tunnelling in the Rearrangements of Carbenes: The Role of Dynamical Calculations. *Phys. Chem. Chem. Phys.* **22,** 962–965 (2020).
6. Burd, T. A. H. & Clary, D. C. An Analytic Route to Tunnelling Splittings Using Semiclassical Perturbation Theory. *J. Chem. Theory Comput.* **16,** 3486–3493 (2020).

pySCTST

All the SCTST results presented in this thesis were generated using in-house software *pySCTST*, written between 2016 and 2020 by Timothy Burd, with some additions from Tom Young and Karl-Michael Zeims. This software, along with tutorials, example calculations, and a reproduction of many of the results in this thesis is publicly available at `bitbucket.org/timothyburd/sctst_3`.

Chapter 1

Introduction

This work is concerned with understanding the role of nuclear quantum effects in determining the rates of polyatomic chemical reactions, and developing computationally efficient methods of studying these.

Determining the rate constants of chemical reactions has widespread application in atmospheric science, biological science, catalysis design, and industrial process design. The most direct way to determine a chemical rate constant is through experiment, however these are often difficult to perform, can contain large sources of error and may be time consuming, costly or dangerous. Moreover, experiments are often difficult to interpret, particularly if the results are surprising. It is therefore useful to try to understand rate constants theoretically, without relying on experimental data - this is the *ab initio* approach.

In this chapter we discuss the state of the art methods for calculating rate constants theoretically, then we introduce the subject matter of this thesis: Semiclassical Transition State Theory.

1.1 Transition State Theory

The modern theory of reaction rates was first developed in the late 19^{th} Century. In 1888, Arrhenius[7] found empirically a simple relationship between the rate constant of a reaction, k, and its temperature:

$$k = A \exp\left(-\frac{E_a}{RT}\right), \tag{1.1}$$

where E_a is the activation energy, R is the gas constant, T is the temperature and A is a prefactor. These data form a straight line when the reciprocal temperature is plotted against Log[k] (an *Arrhenius plot*). This observation was later explained theoretically by a group of scientists including Eyring who, in 1935, wrote down the equations that formed the foundation of Transition State Theory (TST)[8]. In TST, the dynamics are considered classical and the reaction path is considered as separable from the other (bound) degrees of freedom. The TST rate is given by:

$$k_{\mathrm{TST}} = \frac{kT}{h}\frac{Q^{\ddagger}}{Q^{\mathrm{R}}}\exp\left(-\frac{\Delta V_f^{\circ}}{kT}\right), \tag{1.2}$$

where ΔV_f° is the adiabatic barrier height in the forward direction and $Q^{\ddagger}$ and Q^{R} are the partition functions of the transition state and reactant respectively. In the computation of these two partition functions, the vibrational motions are often treated using a harmonic oscillator model. The only required *ab initio* quantities, therefore, are the barrier height and the vibrational frequencies of the reactant and transition state. TST provides a simple and efficient rate theory that can give results in good agreement with experiment. Often a recrossing term, $\Gamma < 1$, is included in the prefactor to account for recrossing trajectories, a result of the reaction path not being perfectly separable from other degrees of freedom[9].

The failings of TST, however, became clear with the development of quantum theory and the possibility of reactions *tunnelling* through a barrier, an effect ignored by the classical theory. Quantum tunnelling allows for a reaction to proceed through a reaction barrier even without sufficient energy to classically overcome it. Upward curvature on an Arrhenius plot is a strong indicator that tunnelling is taking place. This effect is particularly significant for hydrogen transfer reactions, where the barriers (in reduced mass coordinates) are narrow, and can speed up a reaction by many orders of magnitude. It is thus clear that, despite the simplicity and cost-effectiveness of TST, a more sophisticated theory is required.

1.2 Exact methods

Within the Born-Oppenheimer approximation, exact-in-principle methods for a given PES, such as Quantum Reactive Scattering (QRS), can be used to determine accurate rates, but they are often too expensive to be practical. As such, these methods have been limited to reactions with six atoms or fewer[10]. The main two expenses, discussed in this section, are in producing an accurate global potential energy surface (PES), and in solving the nuclear Schrödinger equation on this surface.

1.2.1 High quality potential energy surfaces

Born-Oppenheimer potential energy surfaces are a pre-requisite for determining rates by solving the nuclear Schrödinger equation, however these typically require tens of thousands of *ab initio* calculations[11], and some procedure to fit them to a continuous PES[12–16].

Since rates depend exponentially on barrier heights (as is clear from Eq. 1.2), high quality electronic structure calculations are required to obtain quantitative results. This can be demonstrated using the symmetric reaction :

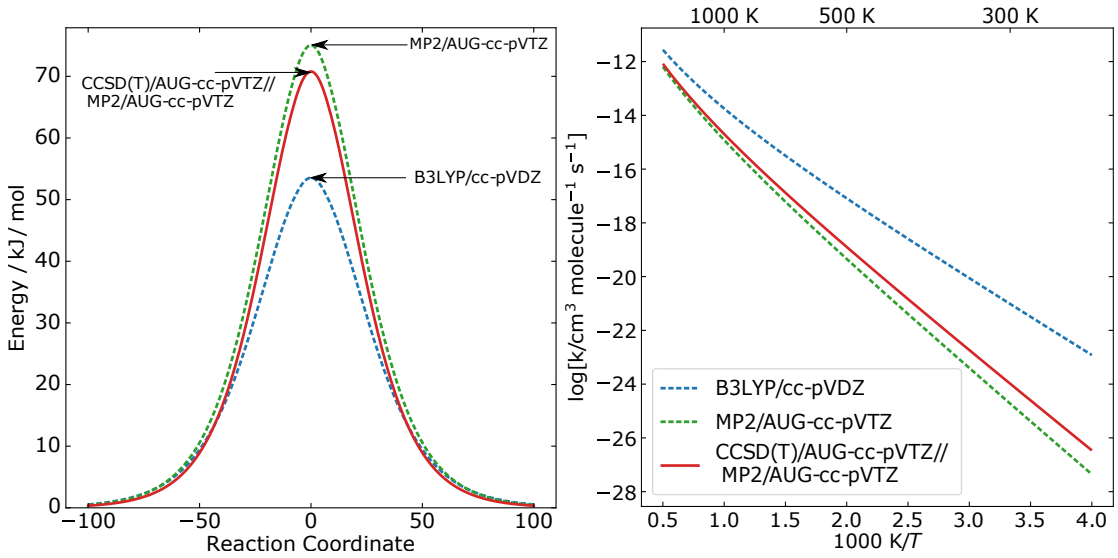
$$CH_3 + CH_4 \rightarrow CH_4 + CH_3.$$

Fig. 1.1 shows TST rates for this reaction, calculated using three levels of electronic structure theory of increasing computational expense[1]:

1. B3LYP/cc-pVDZ,
2. MP2 / Aug-cc-pVTZ,
3. CCSD(T) / Aug-cc-pVTZ // MP2/ Aug-cc-pVTZ.

The (CCSD(T)/ Aug-cc-pVTZ // MP2/ Aug-cc-pVTZ) calculations are expected to be the most accurate, and are significantly more expensive than the other two methods. Using a cheap method, for example the B3LYP functional with a

[1]Electronic structure theory acronyms are defined in the List of Abbreviations on page viii



(a) Barrier Heights. **(b)** TST rates.

Figure 1.1 Using cheaper electronic structure calculations can lead to significant errors in calculated rates, here illustrated for the reaction $CH_3 + CH_4 \rightarrow CH_4 + CH_3$, using Transition State Theory.

medium sized basis set, here gives errors in the barrier height of the order 10 kJ/mol. This causes discrepancies in the calculated rate constants of about a factor of 1000 at 200 K. This illustrates why the main factor limiting accuracy in many rate calculations is the quality of the electronic structure calculations, rather than the approximations within the dynamical method themselves, and motivates the development of rate theories that keep the number of *ab initio* calculations to an absolute minimum, allowing the highest quality calculations to be performed.

1.2.2 Solving the nuclear dynamics

Once a potential surface has been constructed, rates can be determined through quantum reactive scattering calculations, solving for the time-dependent[17] or time-independent[18] nuclear wavefunctions directly. This, in principle, can determine all possible observables of the reaction, and has been applied to many atom-diatom reactions[19–22]. Recent years have seen very accurate calculations performed for reactions with four[23], five[24, 25] six[26–30] and even seven[31, 32] atoms, although calculations on six and seven atom reactions are generally

performed in reduced-dimensions.

Ring-polymer Molecular Dynamics (RPMD) [33, 34] has greatly simplified nuclear dynamics calculations. The method makes use of a classical isomorphism, whereby the statistics of a quantum system can be approximated by those of a classical system of N-replicas, connected by harmonic springs[35]. Dynamical properties, such as rates, can thus be estimated by classical molecular dynamics simulations in the extended ring-polymer phase space. This is significantly cheaper than quantum scattering methods, and can give impressive agreement with exact quantum mechanical rate constants[36]. A full PES is still normally required, however, and so RPMD cannot yet be applied to reactions of large polyatomics without a significant expense.

1.3 Reduced dimensionality methods

Reduced dimensionality (RD) methods are able to make rate calculations more cost-effective by both reducing the number of *ab initio* calculations required to build a PES, and simplifying the dynamical calculations [37–44]. Only a subset of the degrees of freedom of the system are treated explicitly ('active' modes), while the effect of the other degrees of freedom ('spectator' modes) are generally considered only by adding their zero-point energies to the PES. The surface therefore contains the correct thermodynamics of the reaction, for example adiabatic barrier heights[45, 46]. Since some degrees of freedom are only weakly coupled to the reaction process, this can often be a very good approximation.

These methods have been shown to be very powerful at reducing the overall expense of rate calculations, provided a good choice of active degrees of freedom is made. For a two-dimensional model, for example, the key degrees of freedom are often taken to be the bond-forming and bond-breaking bond lengths, illustrated in Fig. 1.2. A two-dimensional PES can then be constructed by fixing these two bond lengths on a grid and performing a constrained optimisation and vibrational analysis at each point.

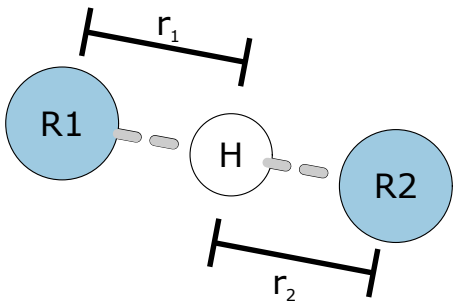


Figure 1.2 Two-dimensional quantum dynamical calculations often use the bond-breaking and bond-forming distances as active degrees of freedom.

Even with the savings offered by RD methods, these calculations are still computationally expensive for large systems, and large numbers of *ab initio* data are still required. Moreover, for more complex reactions (and unimolecular reactions, in particular) it is not obvious *a priori* which degrees of freedom can be neglected, and which must be included to obtain quantitative rates. One focus of this thesis is to develop these reduced-dimensionality methods, particularly by determining which degrees of freedom are significant for a given reaction.

1.4 Semiclassical methods

The dynamical equations themselves can also be simplified to allow for treatment of complex reactions. The 'semiclassical' approximation is a group of useful approximations to quantum mechanics, which become exact as $\hbar \to 0$. Semiclassical rate theories are able to simplify the calculation of rate constants for multidimensional reactions by defining distinct classical tunnelling pathways through which the reactive flux is calculated. Accurately determining the location of these paths on a potential energy surface is often the most complex step to determining the rate. The two most commonly used semiclassical methods are Variational Transition State Theory with semiclassical tunnelling, and the ring-polymer instanton method.

1.4.1 Variational Transition State Theory

Variational Transition State Theory (VTST) with semiclassical tunnelling, as developed by Truhlar and co-workers,[9, 47–52] uses a WKB tunnelling factor to correct TST rate constants, whilst accounting for multidimensional effects. The WKB approximation is a well established semiclassical approximation[53–55], which can be used to estimate energy levels in bound potentials, and tunnelling in scattering potentials, by constructing an approximate wavefunction. This wavefunction satisfies the one-dimensional Schrödinger equation in the limit $\hbar \to 0$, and its form is discussed in more detail in Chapter 2. This can be used as an *ad hoc* tunnelling correction to TST, provided an accurate description of the barrier is available. In VTST, the tunnelling barrier can be described in a number of ways to account for varying levels of multidimensional effects. In the zero-curvature tunnelling (ZCT) method[56, 57], the minimum energy path (MEP) is used as the tunnelling potential. It is well known, however, that tunnelling though the MEP underestimates reaction probabilities due to neglecting corner-cutting effects[58]. For reactions whose MEP exhibits large curvature, the reaction may dominantly proceed through a path with a higher, but narrower, barrier, 'cutting the corner' of the MEP. Thus the ZCT approximation is too poor to give quantitative estimates of rates at low temperatures[59, 60].

In the small-curvature tunnelling (SCT) approximation, corner-cutting is accounted for by including a negative-centrifugal effect, causing the reaction path to be shifted to the 'inside' of the MEP curve. This effectively shortens the path length. In practice, this is done by using the same MEP potential, but reducing the effective mass of the reaction coordinate[9, 61]. The new effective mass is determined from the reaction path curvature, calculated at every point along the MEP. In the large-curvature tunnelling (LCT) approximation [48, 58, 62, 63] qualitatively different tunnelling paths are included. Straight lines that connect the reactant and product sides at various positions along the path, which may also connect configurations in different vibrational states. This accounts for trajectories deep within the reaction swath, and far from the MEP. More

advanced VTST methods use a combination of all three treatments to achieve the most accurate result[48, 64].

The VTST method has been tested successfully on a wide range of reactions, but comes with a relatively large computational cost as the MEP and path-curvature calculations require a large amount of the PES. Moreover, the way in which corner-cutting effects are accounted for (particularly in the small curvature approximation) is an *ad hoc* procedure, so the limits of these approximations are not clear.

1.4.2 Semiclassical instanton rate theory

An alternative approach to semiclassical mechanics is from studying the path-integral description of quantum mechanics. Here, the quantum amplitude for a particle moving from positions x_a to x_b in a time t can be expressed as a sum over all possible trajectories between these points. As $\hbar \to 0$, 'classical' paths (i.e. those that extremise the action, according to Hamilton's principle) dominate the contribution to the propagator. Formally, this corresponds to a steepest-descent approximation to the quantum propagator, which is exact in the semiclassical limit.

Starting from the definition of the exact rate constant[65] in a path-integral representation[66] and taking a number of steepest-descent approximations, instanton rate theory can be derived [67–70]. By describing the instanton as a ring-polymer, and in combination with multidimensional optimisation techniques, instanton rate theory has been applied to a range of complex systems [71–74].

There are several limitations with this approach, however. Instanton calculations must be performed individually for each temperature at which the rate is required, and become increasingly more expensive as the temperature decreases as the instanton becomes spread out on the PES. Whilst this typically requires knowledge of a substantial part of the PES, recent advances, using Gaussian Process Regression, have reduced the number of *ab initio* calculations substantially[75]. The theory is also known to overestimate rate constants around the crossover temperature, which indicates the onset of the deep-tunnelling

regime[76]. The method cannot be used above this temperature, as the instanton collapses to the top of the barrier. Generally, a parabolic barrier tunnelling approximation can be used accurately in the regime instead. Alternatively, development of a microcanonical instanton approach may be able to avoid this limitation[69, 77].

1.5 Semiclassical Transition State Theory

Semiclassical Transition State Theory (SCTST), as developed by Miller and co-workers[78–80], aims to overcome many of the disadvantages of the above methods. It is a WKB based theory, but accounts for multidimensional effects using vibrational perturbation theory, in an analytic, physically meaningful and cost-efficient fashion. The method has the distinct advantage that a global potential energy surface in all degrees of freedom from reactants to products is not needed. Instead all that is required is an expansion of the force-field around the transition state. In doing this, SCTST removes the need to find distinct tunnelling paths by directly calculating the tunnelling probabilities from analytical formulae in terms of the “good" (*i.e.* adiabatically invariant) action variables [79, 81] of the transition state. Miller showed that these action variables can be calculated using a perturbation theory analysis of the transition state, allowing for direct computation of rates from *ab initio* calculations[80]. Implicit in this approach is the ergodicity assumption, whereby energy is exchanged between vibrational modes on a timescale much shorter that with which the reaction proceeds.

Since then, various developments have been made by other researchers to improve the method’s accuracy and scalability. Wang and co-workers have developed efficient methods to perform the required anharmonic density of states calculation using a Monte Carlo method[82–86] and Wagner improved the behaviour of the method in the deep tunnelling regime[87]. Stanton has shown that the use of higher order vibrational perturbation theory can improve the description of tunnelling at low energies, although this comes with significant additional computational cost[88, 89].

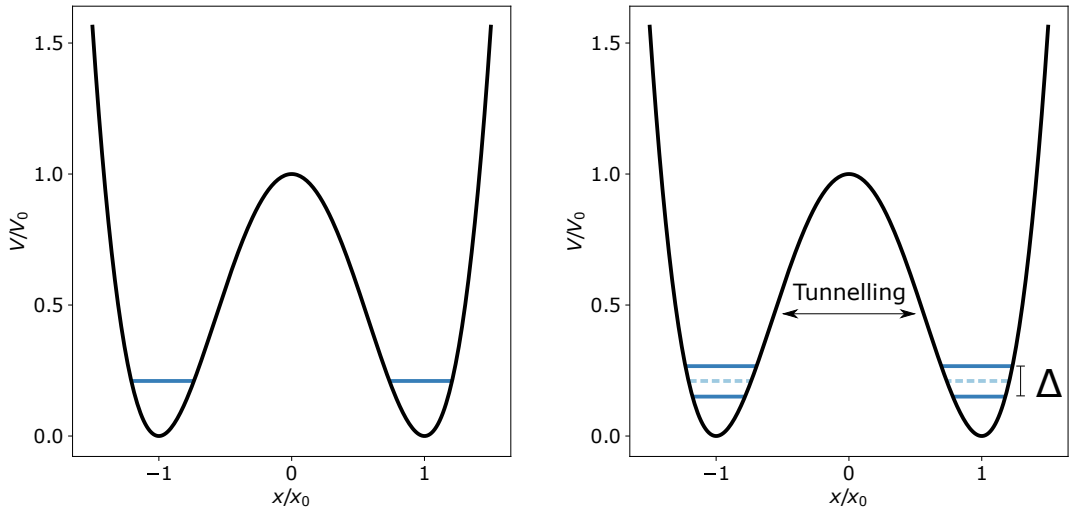
As such it has become clear in recent years, by comparison with QRS calculations and experimental measurements, that this theory can give reliable results for rate constants for small reactive systems such as $HO + H_2$[90], $HO + NH_3$[91], $H + CH_4$[92], $NO_2 + O$[93], $H + C_2H_6$[94] and others[95–104].

A SCTST calculation requires a total of $(2 + 2F)$ Hessian calculations, where F is the number of degrees of freedom of the system. For small molecules, this is likely to be significantly cheaper than both VTST/SCT (which requires a large number of Hessians) and instanton approaches (which typically require a whole PES). For larger systems, SCTST scales less well than VTST, so the cost is likely similar for medium sized molecules.

SCTST also has the distinct advantage that it is possible to calculate barrier heights, vibrational frequencies and anharmonic constants each at different levels of theory; this allows for efficient use of computer time by calculating only the most sensitive parameters at the highest level of theory, allowing for practical and accurate application to relatively large molecules.

Greene *et al.* introduced a one-dimensional form of SCTST[92], which assumes the separability of the reaction coordinate but requires far less computation than a full dimensional treatment. This has been shown to give good agreement with experiment in some cases[105–107]. They have also tested the method's performance on reduced-dimensional surfaces [94, 108] with promising results.

SCTST has therefore emerged as a powerful and direct approach for computing rate constants. Its widespread usage has, however, been limited due to a lack of detailed testing on large and complex systems, the expense of the full dimensional SCTST method and the absence of a user-friendly codebase to perform these calculations. The aim of this thesis is therefore to develop our understanding of SCTST by studying its theory, testing the method (and its variants) on real reactions and developing the method to allow for more efficient treatment of large systems.



(a) No Tunnelling. **(b)** With Tunnelling.

Figure 1.3 How tunnelling influences the energy levels of a double well potential.

1.6 Tunnelling splittings

A phenomenon closely related to reaction rates is that of tunnelling splittings. These are spectroscopically observable properties of chemical systems where tunnelling between multiple degenerate minima is possible. They can be thought of as a result of quantum interactions between two potential wells connected by a tunnelling path, where the overlap of two localised vibrational wavefunctions (one in each potential well) leads to symmetric and anti-symmetric eigenstates. These states are separated by an energy Δ, as shown schematically in Fig. 1.3.

In molecular systems, isomerisation between two degenerate molecular configurations can produce a splitting which can be measured experimentally[109–115], and can provide insight into system dynamics, for example in the rearrangement of water clusters[116, 117]. The size of the splitting is determined by the extent of overlap of the wavefunctions, and therefore on the ability to tunnel through the potential barrier separating the two wells.

Analogously to reaction rate theories, tunnelling splittings can be calculated using quantum calculations on a full PES[11, 118–126], within a reduced dimensionality framework[127], or through a semiclassical approach[72, 117, 128–132].

These existing methods are limited in the same way as their analogous rate theories, and so the development of a simple, efficient and analytical route to calculating tunnelling splittings would be useful.

1.7 Thesis outline

This thesis is comprised of three parts: Theory, Application and Development.

Theory

First, we aim to better understand theoretical aspects of the SCTST method. In Chapter 2 we derive the key theoretical result and discuss its modifications for complex systems. In Chapter 3 we then discuss the details of one dimensional SCTST calculations, including the treatment of internal rotational degrees of freedom, the use of higher order perturbation theory and a quantitative comparison to other rate theories of a similar expense. In Chapter 4 we study in detail the extent to which SCTST in full dimensions accounts for key multidimensional effects such as corner-cutting and variational effects in practice.

Application

We then use the SCTST method to make predictions about real chemical systems and to aid the interpretation of experimental data. Chapter 5 describes the application of SCTST to an important atmospheric process - the unimolecular decay of Criegee intermediates - shedding light on the applicability of SCTST to complex reactions and the impact of water catalysis on this system. In Chapter 6 we apply 1D-SCTST to rationalise the surprising results of recent experiments on tunnelling controlled carbene rearrangements. To perform these calculations, we have developed the *pySCTST* software package, which is described in detail in Appendix A.

Development

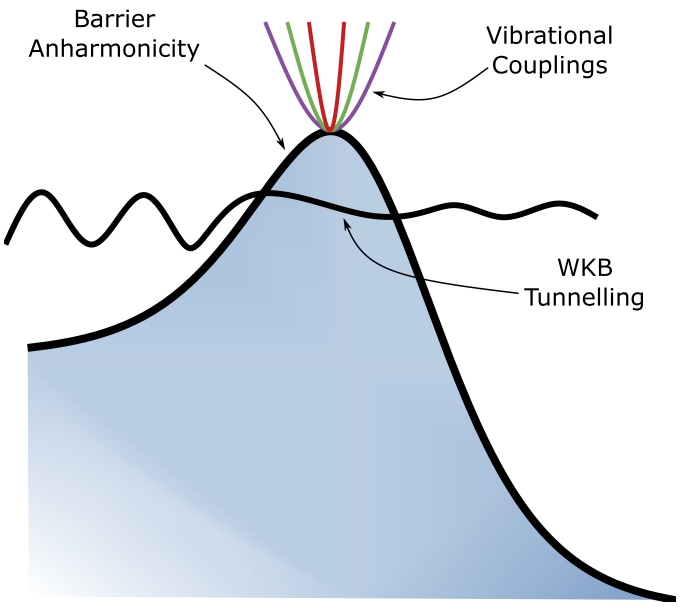
Finally, we aim to increase the efficiency and applicability of SCTST for a range of problems. We develop the SCTST method in Chapter 7 by investigating efficient and automated ways to reduce the dimensionality of the system within the SCTST framework, and show this can lead to very accurate results for a fraction of the cost of a full dimensional calculation. In Chapter 8, we derive and test an alternative, full dimensional approximation to SCTST. Finally, in Chapter 9 we show that the SCTST equations can be recast to estimate tunnelling splittings in multidimensional systems, and test this new analytic method on some key systems.

Finally, Chapter 10 summarises the key conclusions of this work.

Chapter 2

Semiclassical Transition State Theory

In this chapter, the main Semiclassical Transition State Theory result is derived. We begin by studying a simple one-dimensional model of tunnelling, then describe its generalisation, using vibrational perturbation theory, to multidimensional systems, to reach the SCTST result. We then discuss two key modifications to the basic theory to make the method computationally tractable for large systems, and quantitatively accurate at all temperatures. The one-dimensional form of SCTST, and the computational methods used throughout this thesis, are also described.



Abstract 2 The SCTST picture of chemical reactions

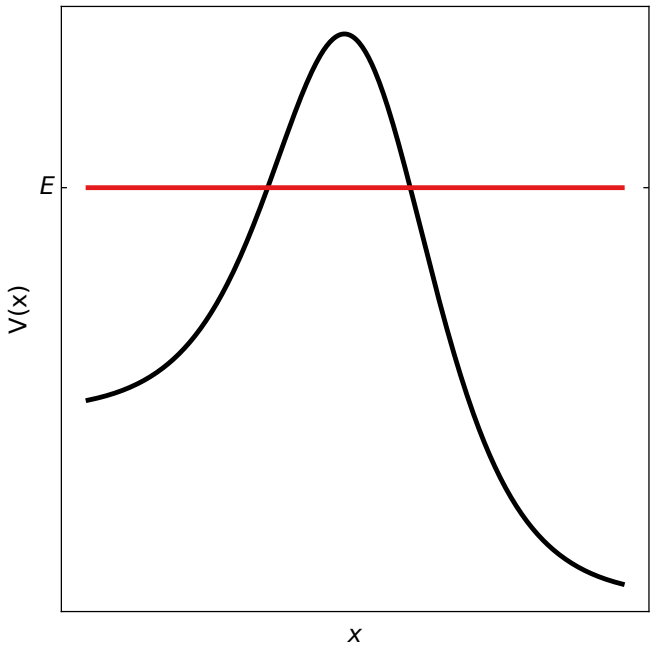


Figure 2.1 A one-dimensional reaction barrier.

2.1 The WKB method for tunnelling

The simplest model of tunnelling is that of a one-dimensional square barrier. In this case, it is simple to determine the analytical transmission probability by exact solution of the one-dimensional time-independent Schrödinger equation:

$$-\frac{\hbar^2}{2m}\frac{\partial^2}{\partial x^2}\psi(x)+V(x)\psi(x)=E\psi(x), \tag{2.1}$$

in all three regions of the potential, then 'matched' at the boundaries. The transmission probability is then found from the square of the ratio of transmitted intensity and incident amplitudes. Despite its simplicity, the square barrier is still used as a model for reaction barriers in some applications, for example astrochemical calculations[133–135], however it is not generally appropriate for calculating quantitative rate constants.

A more realistic barrier (for the purposes of studying chemical reactions), however, is not so simply treated. Such a barrier is illustrated in Fig. 2.1. In this case, there is no analytical, *exact* solution to the Schrödinger equation

along the potential. There is, however, a simple *approximate* wavefunction, the Wentzel–Kramers–Brillouin (WKB) wavefunction[53–55], given by:

$$\psi_{\mathrm{WKB}}(x) = \exp\left[\frac{i}{\hbar}\int^{x} dy\sqrt{2m(E-V(y))}\right] \tag{2.2}$$

where m is the reduced mass of the system and $V(y)$ is the barrier potential at coordinate y. The lower limit of the integral acts as a phase reference level[136]. This wavefunction can be derived in several ways[136, 137], however it is simplest to verify the solution by comparison with Eq. 2.1. From Eq. 2.2, it is simple to show that:

$$-\frac{\hbar^2}{2m}\frac{\partial^2}{\partial x^2}\psi_{\mathrm{WKB}}(x)+V(x)\psi_{\mathrm{WKB}}(x) = E\psi_{\mathrm{WKB}}(x)+\psi_{\mathrm{WKB}}(x)\left(\frac{\hbar i}{2}\sqrt{\frac{1}{2m(E-V(x))}}\frac{dV}{dx}\right). \tag{2.3}$$

It is clear, therefore, that $\psi_{\mathrm{WKB}}(x)$ satisfies the Schrödinger equation except for the addition of the final term. ψ_{WKB} is thus a solution to the Schrödinger equation in the limit that $\hbar \to 0$ (the 'classical limit', and so this is known as a 'semiclassical' approximation[1]). It also requires that the solution is far from a classical turning point, and that the potential is slowly changing. As expected, in the classically allowed region, the wavefunction is oscillatory, whilst in the classically forbidden region the solution is growing or decaying.

Behaviour near the classical turning points requires an alternative solution to Eq. 2.1. Near the classical turning points, a linear potential approximation can be used, as illustrated in Fig. 2.2. In this case, the 1D Schrödinger equation reduces to the Airy equation, with known solutions, the Airy functions[137].

To obtain the global wavefunction, $\psi(x)$ must be matched at either side of the classical turning points. The WKB wavefunctions away from the turning point are matched to the asymptotic limits of the Airy functions[2]. A full description

[1] Since $\hbar$ is not unitless, we need to specify compared to what it must be small. $\hbar$ has the units of action, and therefore the characteristic mass, length and velocity of a trajectory must be such that its action is large compared to $\hbar$.

[2] Note that an alternative derivation of the semiclassical tunnelling in a one-dimensional barrier is given by use of the stationary phase approximation. In this case, only the classically forbidden region of space need be considered. At the classical turning points, the WKB wavefunction appears invalid since $E = V(x)$. This is not the case, however, in the momentum representation

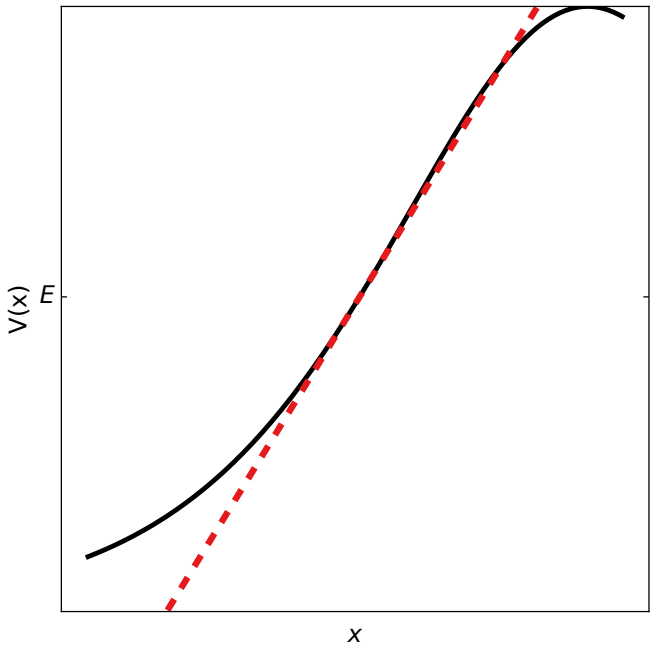


Figure 2.2 At the classical turning points, a linear potential approximation can be made.

of this process can be found in ref. [137]. Using this combined wavefunction, the transmission probability is then given by:

$$\begin{aligned} P_1(E) &= \exp\left[-2\int_{x_1}^{x_2}\sqrt{\frac{2m}{\hbar^2}(V(x)-E)}dx\right] \\ &= \exp\left[-2\theta(E)\right] \end{aligned} \tag{2.4}$$

where $\theta(E)$ is the penetration integral:

$$\theta(E) \equiv \frac{1}{\hbar}\int_{x_1}^{x_2} dx\sqrt{2m\left(V(x)-E\right)} \tag{2.5}$$

and (x_1, x_2) are the classical turning points at energy E. This gives the *exact* quantum tunnelling probability in the limit of a high and wide barrier [69]. This form, however, gives qualitatively incorrect results when $\theta(E)$ becomes small *i.e.* for tunnelling near the barrier top. Here the action is not sufficiently small that

of the wavefunction. Thus a Fourier transform can convert the wavefunction from the position representation to the momentum representation, and back again, either side of the classical turning points. Since these transformations cannot be done exactly analytically, the stationary phase approximation is used to evaluate them to first order in $\hbar$.[138]

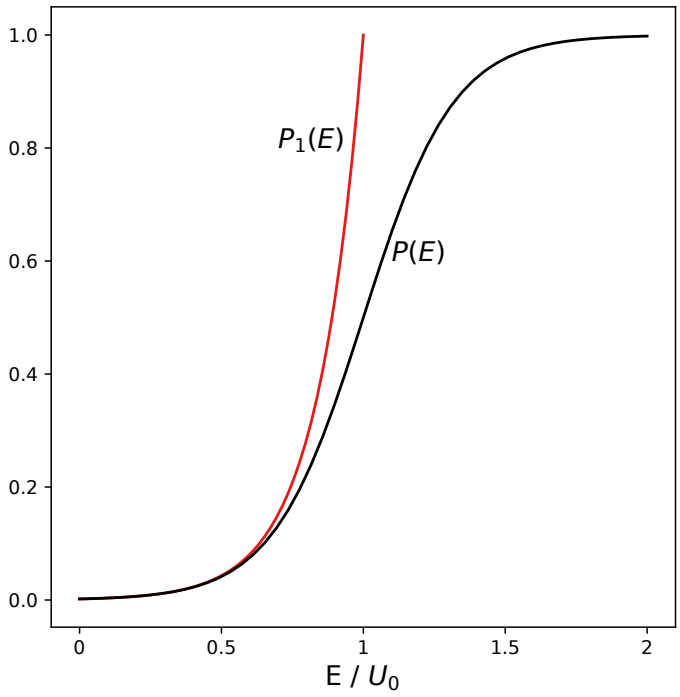


Figure 2.3 The tunnelling probability for a parabolic barrier using Eqs. 2.4 and 2.8. $P_1(E)$ gives qualitatively incorrect tunnelling near the barrier top, which can be improved with the uniformly valid $P(E)$ expression.

the WKB approximation is valid. This is clear from the behaviour of $P_1(E)$ at the barrier top, where the exact probability is $\frac{1}{2}$, rather than 1 as predicted by Eq. 2.4.

Eq. 2.4 can be improved by considering the WKB tunnelling probability for a parabolic barrier, for which the integral in Eq. 2.5 can be calculated analytically (as shown explicitly in Appendix B). This gives:

$$P_1^{\text{parabola}}(E) = \exp\left[-2i\pi\frac{U_0 - E}{\omega}\right], \tag{2.6}$$

which can be compared to the exact expression for tunnelling in a parabolic barrier:

$$P_{\text{exact}}^{\text{parabola}}(E) = \frac{1}{1+\exp\left[2i\pi\frac{U_0-E}{\omega}\right]}. \tag{2.7}$$

The two tunnelling expressions are compared in Fig. 2.3, which clearly agree in the limit that $\frac{U_0-E}{|\omega|} \gg 1$ *i.e.* for deep tunnelling trajectories, or for wide barriers. They diverge, however, near the barrier top where the action is small.

This comparison suggests an improved semiclassical tunnelling result[139]:

$$P(E) = \frac{1}{1+\exp\left[2\theta(E)\right]}. \tag{2.8}$$

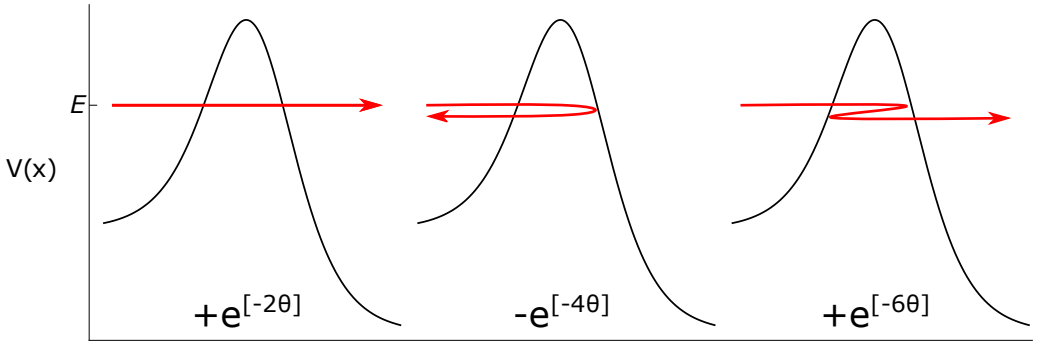


Figure 2.4 Each term in the Taylor expansion of Eq. 2.8 corresponds to a reactive or unreactive trajectory with differing actions.

This gives the correct parabolic result near the barrier top, and returns to the WKB result for deep tunnelling trajectories. The relationship between the two tunnelling expressions is clear; $P_1(E)$ represents just the first term in the Taylor expansion of $P(E)$:

$$\begin{aligned} P(E) &= \left[1+e^{2\theta(E)}\right]^{-1} \\ &= e^{-2\theta(E)} - e^{-4\theta(E)} + e^{-6\theta(E)} - \ldots \\ &\approx P_1(E) \qquad\qquad (\theta(E) \gg 1) \end{aligned} \tag{2.9}$$

The Taylor expansion of $P(E)$ also gives a clear link to periodic orbit theory, where each term in Eq. 2.9 can also be interpreted as the contribution of trajectories with differing number of 'bounces' in the classically forbidden region[79], illustrated in Fig. 2.4. Since it gives the exact semiclassical tunnelling in both the limits of a high and wide barrier, and a parabolic barrier, we expect this form to be accurate over the whole range of tunnelling energies[3].

2.2 The SCTST result

Equation 2.8 can be used directly if the one-dimensional tunnelling potential is known, as done, for example, in VTST calculations[9]. In this case the integral

[3]Neglection of these higher order terms is exactly the reason the semiclassical instanton rate is inaccurate close to the cross over temperature. By neglecting these higher order terms, a final steepest-descent approximation to the Boltzmann integral can be made, leading to the instanton result.

in Eq. 2.8 is evaluated numerically at each energy. Whilst Eq. 2.8 gives the desired tunnelling probability, it requires the tunnelling potential, and thus the optimal tunnelling path, to be known. For a multidimensional PES, however, this is not known *a priori*.

To reach the final SCTST result, Bohr-Sommerfeld theory, in conjunction with vibrational perturbation theory, is used to determine $\theta(E)$ as an analytic function of *ab initio* parameters. The tunnelling path, therefore, need not be determined explicitly.

The SCTST result is found by noting that the integral $\theta(E)$ corresponds to the "good" action variable of the one-dimensional system as given by Bohr-Sommerfeld theory[79],

$$\begin{aligned} I = \hbar\left(n+\frac{1}{2}\right) &= \frac{1}{2\pi}\oint p\mathrm{d}q \\ &= \frac{1}{2\pi}\oint \sqrt{2m(E-V(q))}\mathrm{d}q \\ &= \frac{i\hbar}{\pi}\theta(E) \end{aligned} \tag{2.10}$$

An analytical expression for $\theta(E)$ can therefore be found by writing the total energy as a function of its action variables, and inverting this expression for $\theta(E)$.

This can be done by comparison to the analogous bound potential problem. Here, the energy levels of a potential well can be written as an expansion in terms of the systems action variables with harmonic and anharmonic constants[4]:

$$E = U_0 + \hbar\omega\left(n+\frac{1}{2}\right) + X\left(n+\frac{1}{2}\right)^2 + \ldots \tag{2.11}$$

where $'\ldots'$ may contain higher order, anharmonic terms. Miller noted that these action variables also exist at a transition state[79], where ω is pure-imaginary and its corresponding action variable becomes continuous. As such, the term $(n+\frac{1}{2})$ can be eliminated by comparison with Eq. 2.10, giving an analytical relation for $E(\theta)$:

[4]Note that the existence of good action variables (corresponding to quantum numbers) in the vicinity of the stationary point is assumed here. Cases for which the system is non-integrable (and so has no good action variables) are beyond the scope of our consideration.

$$E = V_0 + i\omega\left(\frac{\theta(E)}{\pi}\right) - X\left(\frac{\theta(E)}{\pi}\right)^2 + \ldots \tag{2.12}$$

$\theta(E)$ can then be found by inverting this relation. If Eq. 2.11 is truncated after the $\left(n+\frac{1}{2}\right)^2$ term, this is simply an inversion of a quadratic expression for $\theta(E)$. Eq. 2.12 thus presents an analytical relation between the energy of an incoming wave packet, and its penetration integral, as a function of its harmonic and anharmonic constants. This can then be used in combination with Eq. 2.8 to determine analytic tunnelling probabilities of various one-dimensional barriers.

By altering the energy expression in Eq. 2.11, tunnelling expressions for different systems can be found. In the following sections this process is first illustrated for a one-dimensional parabolic barrier and then generalised to multidimensional, anharmonic barriers.

2.2.1 Parabolic SCTST

To illustrate the method outlined above, we can recover the exact quantum tunnelling probability for a parabolic barrier. In this case all anharmonic terms are exactly zero and so Eq. 2.12 becomes:

$$E = U_0 + i\omega\left(\frac{\theta(E)}{\pi}\right) \tag{2.13}$$

rearranging to give:

$$\theta(E) = i\pi\frac{U_0 - E}{\omega}. \tag{2.14}$$

The transmission probability, Eq. 2.8, becomes:

$$P(E) = \frac{1}{1+\exp\left[2i\pi\frac{U_0-E}{\omega}\right]} \tag{2.15}$$

which is the correct expression for tunnelling in a parabolic barrier.

2.2.2 VPT2-SCTST

In order to account for multidimensional effects, the energy expression in Eq. 2.11 must incorporate anharmonic contributions from multiple degrees of freedom coupled to the reaction coordinate. The desired expression can be found using vibrational perturbation theory.

We begin with the harmonic Hamiltonian at a stationary point:

$$\hat{H}^{(0)} = \Delta V_f + \sum_i^F \left(-\frac{\hbar^2}{2}\frac{\partial^2}{\partial q_i^2} + \frac{1}{2}\omega_i^2 q_i^2 \right), \tag{2.16}$$

where q_i represent distances along one of the F normal modes, in mass-weighted coordinates, with units of $[\text{Mass}]^{\frac{1}{2}}[\text{Length}]$, and ΔV_f is the energy of the stationary point. The energy in terms of the harmonic system's action variables is known exactly:

$$E_{\{n\}}^{(0)} = \Delta V_f + \sum_i^F \hbar\omega_i \left(n_i + \frac{1}{2} \right), \tag{2.17}$$

where ω_i are the harmonic frequencies of the F internal degrees of freedom, and $\{n\}$ represents the vector of the F vibrational quantum numbers. We then include, as a perturbation, up to fourth-order derivatives of the PES:

$$\hat{H}^{(1)} = \frac{1}{3!}\sum_i^F\sum_j^F\sum_k^F f_{ijk} q_i q_j q_k + \frac{1}{4!}\sum_i^F\sum_j^F\sum_k^F\sum_l^F f_{ijkl} q_i q_j q_k q_l \tag{2.18}$$

where:

$$f_{ijk} \equiv \frac{\partial^3 V(\mathbf{q})}{\partial q_i \partial q_j \partial q_k}, \qquad f_{ijkl} \equiv \frac{\partial^4 V(\mathbf{q})}{\partial q_i \partial q_j \partial q_k \partial q_l} \tag{2.19}$$

which are evaluated at the stationary point of the potential. Note that, in principle, additional rotational coupling terms can be included. In practice these were found to have a negligible impact on the reactions in this work (this is true for large and medium sized molecules in general), so are not discussed further here. In second order vibrational perturbation theory (VPT2), the system's energy is expressed as a sum of zeroth, first and second order terms:

$$E_{\{n\}} = E_{\{n\}}^{(0)} + E_{\{n\}}^{(1)} + E_{\{n\}}^{(2)}. \tag{2.20}$$

A detailed work through of the perturbation theory problem described here is given in ref. [140]. The result is the energy expression:

$$E_{\{n\}} = \Delta V_f + \sum_i^F \hbar\omega_i(n_i+\frac{1}{2}) + \sum_{i,j}^F x_{ij}(n_i+\frac{1}{2})(n_j+\frac{1}{2}) + G_0, \tag{2.21}$$

where the anharmonic terms are given by[80]:

$$x_{ik} = \frac{1}{4\omega_i\omega_k}\left(f_{iikk} - \sum_{j=1}^F \frac{f_{iij}f_{jkk}}{\omega_j^2} + \sum_{j=1}^F \frac{2f_{ijk}^2\left(\omega_i^2+\omega_k^2-\omega_j^2\right)}{\left[(\omega_i+\omega_k)^2-\omega_j^2\right]\left[(\omega_i-\omega_k)^2-\omega_j^2\right]}\right), i\neq k \tag{2.22}$$

$$x_{ii} = \frac{1}{16\omega_i^2}\left(f_{iiii} - \sum_{j=1}^F \frac{f_{iij}^2}{\omega_j^2}\frac{8\omega_i^2-3\omega_j^2}{4\omega_i^2-\omega_j^2}\right), \tag{2.23}$$

and:

$$\begin{aligned} G_0 = &\frac{1}{64}\sum_{i=1}^F \frac{f_{iiii}}{\omega_i^2} - \frac{7\hbar^2}{576}\sum_{i=1}^F \frac{f_{iii}}{\omega_i^4} + \frac{3\hbar^2}{64}\sum_{i\neq k}^F \frac{f_{iik}^2}{\left(4\omega_i^2-\omega_k^2\right)\omega_i^2} \\ &-\frac{\hbar^2}{4}\sum_{i<j<k}^F \frac{f_{ijk}^2}{\left[(\omega_i+\omega_k)^2-\omega_j^2\right]\left[(\omega_i-\omega_k)^2-\omega_j^2\right]}. \end{aligned} \tag{2.24}$$

Note that special care must be taken to eliminate terms with Fermi resonances[141]. We can expect this perturbation theory picture to be accurate if the terms of the anharmonic matrix, x_{ij}, are much smaller than the harmonic frequencies, indicating fast convergence of the perturbation series.

At a transition state, exactly one frequency, ω_F, is imaginary. As before, Eq. 2.10 is used to eliminate the $\left(n_F+\frac{1}{2}\right)$ terms in Eq. 2.21:

$$\begin{aligned} E_{\{n\}} = &\Delta V_f + \sum_i^{F-1}\hbar\omega_i(n_i+\frac{1}{2}) + \sum_{i,j}^{F-1} x_{ij}(n_i+\frac{1}{2})(n_j+\frac{1}{2}) + G_0 \\ &+\hbar\omega_F\left(\frac{i\theta(E)}{\pi}\right) + \left(\frac{i\theta(E)}{\pi}\right)\sum_i^{F-1} x_{iF}(n_i+\frac{1}{2}) + x_{FF}\left(\frac{i\theta(E)}{\pi}\right)^2. \end{aligned} \tag{2.25}$$

This is then solved for $\theta(E)$, by inverting the quadratic equation, arriving at an expression that is a function of not just the energy, but also of the quantum numbers of the $(F-1)$ bound vibrations of the transition state, $\{n\}'$:

$$\theta_{\{n\}'}(E_v) = \pi\frac{-\Omega_{\{n\}'} \pm \left[\Omega_{\{n\}'}^2 + 4x_{FF}\left(\Delta V_f + G_0 + E_{\{n\}'} - E_v\right)\right]^{1/2}}{2x_{FF}} \tag{2.26}$$

where

$$\Omega_{\{n\}'} = \frac{\omega_F}{i} + \sum_{i=1}^{F-1} \frac{x_{iF}}{i}(n_i + 0.5), \tag{2.27}$$

and

$$E_{\{n\}'} = \sum_{i}^{F-1} \omega_i(n_i + \frac{1}{2}) + \sum_{i,j}^{F-1} x_{ij}(n_i + \frac{1}{2})(n_j + \frac{1}{2}), \tag{2.28}$$

and $\{n\}'$ represents the vector of the $F-1$ bound vibrational quantum numbers. The correct choice of $\pm$ in Eq. 2.26 is found by requiring the boundary condition:

$$\theta_{\{n\}'}(E_v) = 0 \quad \text{when} \quad E_v = \Delta V_f + G_0 + E_{\{n\}'} \tag{2.29}$$

as this gives the correct tunnelling probability at the barrier top, requiring the '+' sign. The main VPT2-SCTST result is therefore:

$$\theta_{\{n\}'}(E_v) = \pi \frac{-\Omega_{\{n\}'} + \left[\Omega^2_{\{n\}'} + 4x_{FF}\left(\Delta V_f + G_0 + E_{\{n\}'} - E_v\right)\right]^{1/2}}{2x_{FF}}. \tag{2.30}$$

Note that in general VPT2-SCTST is referred to simply as SCTST, as this is by far the most common form used in practice. This method can, however, be extended to higher orders of perturbation theory, as discussed in Chapter 3.

The state-dependent reaction probability is given by analogy with Eq. 2.8 as:

$$P_{\{n\}'}(E_v) = \frac{1}{1 + \exp\left[2\theta_{\{n\}'}(E_v)\right]}, \tag{2.31}$$

and the cumulative reaction probability (CRP) is given by the sum over all state-dependant reaction probabilities:

$$N(E_v) = \sum_{\{n\}'} P_{\{n\}'}(E_v). \tag{2.32}$$

Microcanonical rate constants are given by:

$$k(E_v) = \frac{N(E_v)}{2\pi\hbar\rho(E_v)} \tag{2.33}$$

where $\rho(E_v)$ is the density of states in the reactant, whilst thermal rate constants are given by the Boltzmann-weighted average of the CRP[142]:

$$k(T) = \frac{1}{h} \frac{Q^\dagger_{\text{trans}}(T) Q^\dagger_{\text{rot}}(T) Q^\dagger_{\text{elec}}(T)}{Q_{\text{r}}(T)} \int_0^\infty N(E_v) \exp\left(\frac{-E_v}{kT}\right) dE_v \tag{2.34}$$

where Q and $Q^\dagger$ represent partition functions of the reactant and transition states, respectively.

2.3 Developments for polyatomic reactions

In recent years, several adaptations of this method have been developed, to allow for an accurate and efficient treatment of larger systems.

2.3.1 Summing over vibrational states

The sum in Eq. 2.32 is over every vibrational configuration of the transition state. Whilst for small systems it is feasible to iterate over all sets of quantum numbers, this becomes prohibitively expensive for large molecules with many degrees of freedom, since the number of such states scales exponentially with the system size. The Wang-Landau algorithm [82, 83, 143] and its implementation for parallel architectures [86, 144] has been developed to tackle this. The key advantage of the Wang-Landau method over other methods of calculating densities of states (such as the Beyer-Swineheart method[145] and the Stein-Rabinovitch method[146]) is that it allows for application to coupled, anharmonic systems (in fact it allows for the treatment of any vibrational energy expression written as a function of the vibrational quantum numbers).

The simulation is a random walk algorithm, in energy space, with the aim of calculating accurately the density of states, $G(E)$. The method is based on the principle that if vibrational states are sampled with probability $1/G(E)$, then energy space is sampled uniformly.

The simulation is run with energy space discretised into a set of energy bins of width δE. An initial trial density of states is assumed to be uniform, $G(E) = 1$. Beginning with a random vibrational configuration, a random walk through state-space is performed. Each state can be assigned an energy bin using Eq. 2.21. Unbound states should not be counted, and are identified by calculating the derivative of Eq. 2.21 with respect to each of the quantum numbers, which is negative for an unbound state. At each step of the simulation, a new vibrational configuration (with energy E_{new}) is generated by shifting one or more quantum

numbers ± 1. The step is accepted with probability:

$$P_{\text{accept}} = \text{Min}\left[\frac{G(E_{\text{old}})}{G(E_{\text{new}})}, 1\right]. \tag{2.35}$$

This allows for sampling states with probability $1/G(E)$. Each time an energy bin is sampled, the histogram of total visits, $H(E)$, is updated, and that bin's trial density of states is adjusted:

$$H(E) \to H(E)+1 \qquad G(E) \to G(E)f \tag{2.36}$$

where $f > 1$, and is initially set, for example, at e^1. The walk continues until the accumulated histogram of visits to each bin, $H(E)$, is flat, indicating $G(E)$ has converged. This process is illustrated in Fig. 2.5. The simulation is then restarted, using $G(E)$ as the new trial density of states, and f is decreased, for example, $f \to \sqrt{f}$. The error in the density of states is proportional to $\log f$, so this process is repeated until f is sufficiently small to reach the desired accuracy. Note that detailed balance is only satisfied asymptotically as $G(E)$ approaches the true density of states.

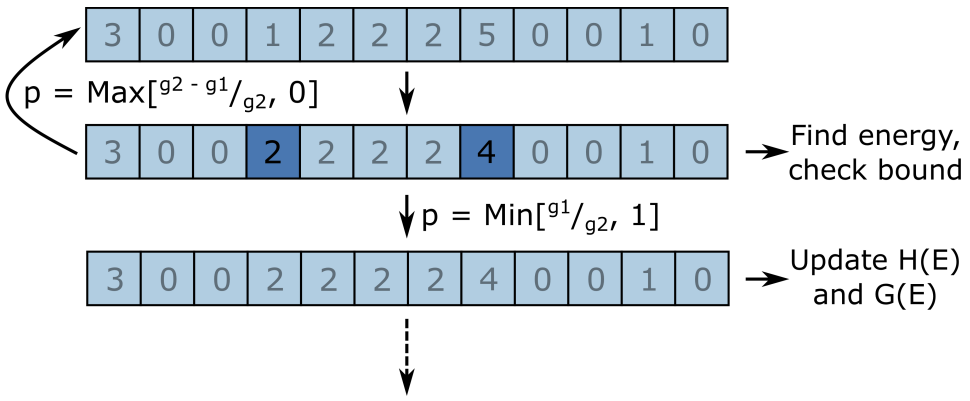
For SCTST calculations, the state dependent term $\Omega_{\{n\}'}$ is also required for each bin. In this case, the coupling of each bin, is calculated as the *average* of the couplings of the vibrational states found within it, $\langle\Omega(E_i)\rangle$. $\langle\theta(E_i)\rangle$ can then be found from Eq. 2.30. The CRP is then given by:

$$N(E) = \sum_{i}^{E/\delta E} \frac{G(E_i)}{1+\exp\left[2\langle\theta(E_i)\rangle\right]}\delta E. \tag{2.37}$$

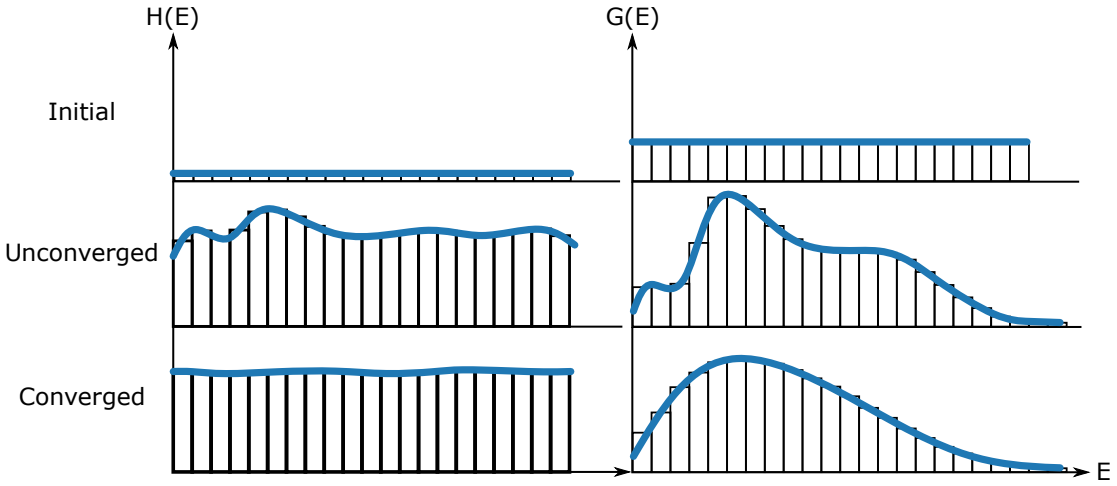
2.3.2 Deep tunnelling corrections

The VPT2-SCTST result can be improved in the deep tunnelling regime. It is clear from Eq. 2.30 that there is no (real) value of $\theta(E)$ when the discriminant of the equation is negative. There is therefore a 'threshold' energy, E_T, given by:

$$E_T = \Delta V_f + G_0 + E_{\{n\}'} + \frac{\Omega^2_{\{n\}'}}{4x_{FF}}, \tag{2.38}$$



(a) The random walk algorithm.



(b) Convergence of the histogram $H(E)$, and the density of states, $G(E)$ over the course of a simulation.

Figure 2.5 Illustration of the Wang-Landau method for computing density of states.

below which $\theta(E)$ becomes complex, and no tunnelling is possible. The physical interpretation of this is clear; there is no tunnelling allowed below the reactant asymptote of the potential energy surface. This method, however, whilst qualitatively giving the correct behaviour, generally gives an incorrect energy for the reactant asymptote. This is not surprising given the VPT2 result is based entirely on a Taylor expansion of the surface at the TS, and so the energetics of the PES well away from the TS are unlikely to be treated accurately. This can lead to significant errors in the rate, especially at low temperatures when tunnelling from low energy trajectories play a significant role.

This effect, and its solution from Wagner[87], are best illustrated by comparison to a Morse potential. The VPT2-SCTST result in one-dimension gives the exact semiclassical tunnelling probability for an inverted Morse potential of the form:

$$V_{\text{Morse}}(q) = V_0 - D_e\left(1 + \left[2e^{\alpha q} - e^{2\alpha q}\right]\right) \tag{2.39}$$

with:

$$V_0 = \Delta V_f + G_0 + E_{\{n\}'}, \qquad D = -\frac{\Omega^2_{\{n\}'}}{4x_{FF}}, \qquad \alpha = \sqrt{\frac{-8x_{FF}}{\hbar^2}} \tag{2.40}$$

and where the energy zero is taken as the reactant energy. This barrier has an asymptote energy as $q \to -\infty$ at:

$$V_{\text{Morse}}(q \to -\infty) = \Delta V_f + G_0 + E_{\{n\}'} - D_e \tag{2.41}$$

which coincides with the threshold energy in Eq. 2.38, but does not necessarily coincide with the 'true' reactant asymptote energy of zero.

Wagner suggested a simple and efficient deep tunnelling correction for SCTST[87]. Since the true barrier height is known already, an improved barrier can be constructed using a three-piece potential of three Eckart barrier segments. The central segment is fit to reproduce the frequency and anharmonic constant at the transition state, and the reactant and product segments ensure the correct forward and reverse barriers are used. The pieces are matched to give a smooth potential with analytical tunnelling probabilities. Fig. 2.6 illustrates this for a hypothetical reaction barrier.

This method maintains the accurate treatment of VPT2 near the barrier top, whilst giving the correct low-energy behaviour. The only additional *ab initio* cost of including this correction is that of knowing the reverse reaction barrier height.

2.4 One-dimensional SCTST

The computational expense of the *ab initio* calculations in SCTST in full dimensions ('FD-SCTST') scales poorly with system size, as the number of third and fourth order derivatives of the PES increase rapidly with the number of degrees of

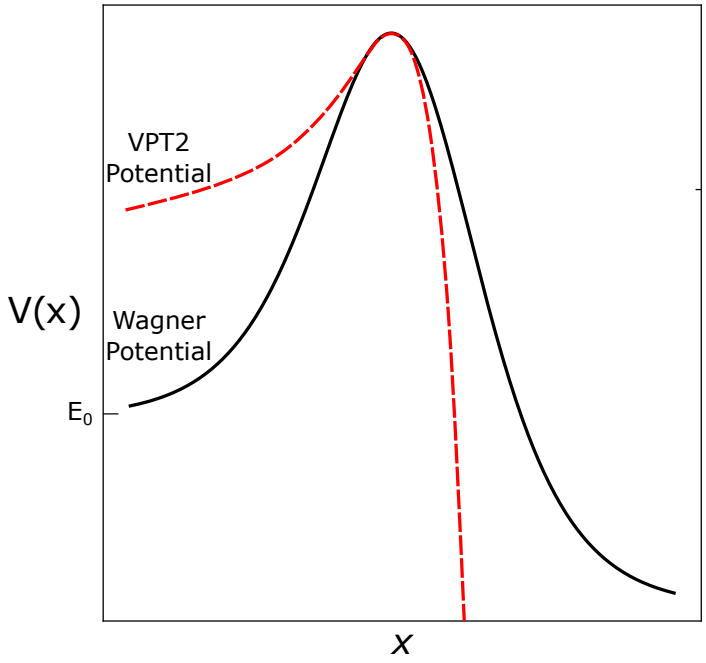


Figure 2.6 Comparison of pure VPT2, and Wagner improved barriers for a one-dimensional reaction. The reactant energy is at E_0.

freedom ($\mathscr{O}(n^3)$). An alternative approach is to use SCTST within a reduced dimensionality (RD) framework[1–3, 92, 94, 107, 108]. In the simplest model, one-dimensional SCTST ('1D-SCTST'), only the reaction mode is treated as anharmonic, while the remaining 'spectator' vibrational modes are treated using a simple harmonic oscillator model. Thus:

$$f_{ijk} = f_{iijj} = 0 \text{ unless } i = j = k = F, \tag{2.42}$$

and so the number of required *ab initio* derivatives, on top of those needed for a TST calculation, is reduced to simply finding f_{FFF} and f_{FFFF} . The anharmonic matrix is greatly simplified:

$$\begin{aligned} \mathbf{x} &= \begin{bmatrix} x_{11} & x_{12} & x_{13} & \dots & x_{1F} \\ x_{21} & x_{22} & x_{23} & \dots & x_{2F} \\ \vdots & \vdots & \vdots & \ddots & \vdots \\ x_{F1} & x_{F2} & x_{F3} & \dots & x_{FF} \end{bmatrix} \\ \rightarrow \mathbf{x}_{1\mathrm{D}} &= \begin{bmatrix} 0 & 0 & 0 & \dots & 0 \\ 0 & 0 & 0 & \dots & 0 \\ \vdots & \vdots & \vdots & \ddots & \vdots \\ 0 & 0 & 0 & \dots & x_{FF}^{1\mathrm{D}} \end{bmatrix} \end{aligned} \tag{2.43}$$

and the one-dimensional value of x_{FF} is given by:

$$x_{FF}^{1D} = \frac{\hbar^2}{16\omega_F^2}\left(f_{FFFF} - \frac{5f_{FFF}^2}{3\omega_F^2}\right), \tag{2.44}$$

which serves as an approximation to the FD expression given by Eq. 2.23.

In addition to lowering the *ab initio* cost, the full set of harmonic bound vibrational states can be enumerated analytically so there is no need for the Wang-Landau sampling method described in Section 2.3.1. This method has shown promising results when applied to simple hydrogen abstraction reactions[92, 94, 108], and one focus of this thesis is to determine its applicability to larger, more complex systems.

2.5 Computational methods

This section outlines the key computational details used in calculations throughout this thesis.

2.5.1 Wang-Landau Sampling

For full-dimensional SCTST calculations, the densities of states were calculated using the Wang-Landau method, as described in Section 2.3.1. The $G(E)$ adjustment parameter, f, was given for each iteration by:

$$f_0 = e \qquad f_{i+1} = \sqrt{f_i} \qquad i_{\max} = 21. \tag{2.45}$$

Energies in the range $[0 \rightarrow 800$ kJ/mol$]$ were divided into 6000 energy bins of width $\delta E = 11$ cm^{-1}.

2.5.2 Electronic structure calculations

All electronic structure calculations in this thesis have been carried out in Gaussian09[147]. Molecular geometries and harmonic frequencies have been optimised using a *tight* convergence criteria.

For FD-SCTST calculations, the anharmonic **x** matrix was found using the *freq=anharmonic* keyword in Gaussian[147]. This finds the required derivatives

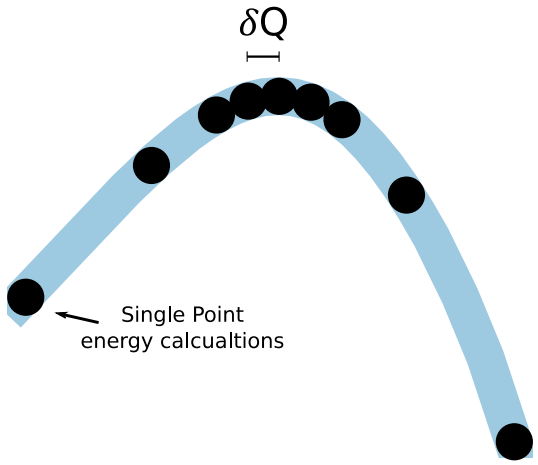


Figure 2.7 Richardson extrapolation, used for 1D-SCTST, requires eight single point energy calculations along the reaction mode, in addition to the energy of the transition state itself.

by numerical differentiation of Hessian matrices displaced along each degree of freedom[141]:

$$f_{iikk} = \frac{1}{2}\left(\frac{H_{kk}(\delta Q_i) + H_{kk}(-\delta Q_i) - 2H_{kk}(0)}{\delta Q_i^2} + \frac{H_{ii}(\delta Q_k) + H_{ii}(-\delta Q_k) - 2H_{ii}(0)}{\delta Q_k^2}\right) \tag{2.46}$$

and

$$f_{ijk} = \frac{1}{3}\left(\frac{H_{jk}(\delta Q_i) - H_{jk}(-\delta Q_i)}{2\delta Q_i} + \frac{H_{ki}(\delta Q_j) - H_{ki}(-\delta Q_j)}{2\delta Q_j} + \frac{H_{ij}(\delta Q_k) - H_{ij}(-\delta Q_k)}{2\delta Q_k}\right) \tag{2.47}$$

where $H_{ij}(\delta Q_k)$ is element (i, j) of the Hessian matrix calculated at a geometry displaced from the transition state by a distance δQ_k along mode k. For these calculations, a step size of 0.025 Å was used.

2.5.3 Richardson extrapolation

For 1D-SCTST calculations, the anharmonic derivatives along the reaction coordinate, f_{FFF} and f_{FFFF}, were calculated using second order Richardson extrapolation[148] based on single-point energy calculations at nine geometries along the reaction coordinate, close to the transition state. This is illustrated in Fig. 2.7, and described in detail by Greene *et al.*[92]. The method is an efficient way to

determine low-order derivatives of a function numerically, whilst removing the effect of higher order terms. Previous studies[92, 107] have suggested this order of extrapolation is sufficient to give converged derivatives for a typical barrier. These single point calculations were carried out at the same level of theory as the optimisation and frequency calculations.

The 1D-SCTST calculations thus require just eight additional single-point calculations over that which is required for a TST calculation.

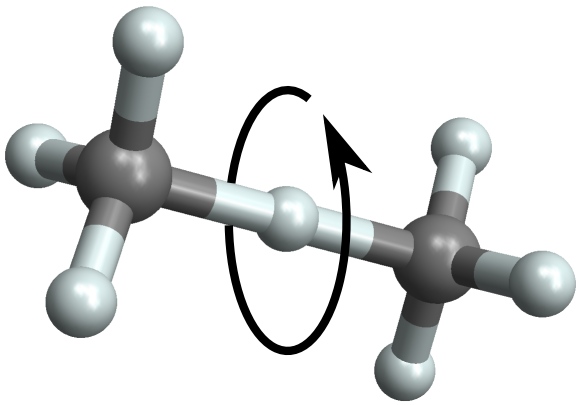
2.6 pySCTST

All the calculations in this thesis were performed using the *pySCTST* software package, which was written specifically for this project. The software is freely available at `bitbucket.org/timothyburd/pysctst` and contains tutorials and example scripts that reproduce many of the results in this thesis. Appendix A describes the codebase, and outlines the requirements to perform SCTST calculations with it, and to reproduce many of the key results from this thesis.

Chapter 3

SCTST in one-dimension

Semiclassical Transition State Theory in one-dimension (1D-SCTST) is an efficient route to the SCTST rate, in which the reaction mode is considered separable from the other bound degrees of freedom, which in turn are treated harmonically. In this chapter, we first investigate the method's accuracy using a symmetric hydrogen transfer reaction, and show how hindered internal rotations can be accounted for in these calculations. We then illustrate the advantages of 1D-SCTST over other rate theories of similar expense, assess the impact of deep-tunnelling corrections, and investigate the inclusion of higher order levels of perturbation theory.



Abstract 3 Internal rotational degrees of freedom can be accurately described within 1D-SCTST.

3.1 Introduction

In this chapter, one-dimensional Semiclassical Transition State Theory, as described in Section 2.4, is applied to study the rate constants of the symmetric hydrogen transfer reaction:

$$CH_3 + CH_4 \rightarrow CH_4 + CH_3 \tag{R1}$$

and its hydrogen-substituted isotopic analogues:

$$CH_3 + CDH_3 \rightarrow CDH_3 + CH_3 \tag{R2}$$

$$CD_3 + CD_4 \rightarrow CD_4 + CD_3. \tag{R3}$$

These form excellent models for more complex polyatomic reactions due to the hindered rotor (HR) vibration in the transition states, and the availability of high-level quantum reactive scattering data. These reactions are also used as a model for other 'heavy-light-heavy' reactions where a light atom is transferred between two heavy molecules[149]. Reaction R1 is known to be significant in combustion and decomposition processes, and so accurate rate constant values are of importance. As such, it has been studied extensively both experimentally[150–152] and theoretically[45, 153–158]. Comparison of R1 to R2 will exhibit primary kinetic isotope effects, whilst comparison of R2 and R3 will show secondary isotope effects.

These reactions each have a hindered rotor vibration at their transition states, as shown in Fig. 3.1, which requires careful treatment. In Section 3.2, we outline how these vibrations can be included in a 1D-SCTST treatment and compare these results to those calculated through reduced dimensional quantum reactive scattering calculations performed by Remmert *et al.*[45]. In Section 3.3 we then use the same reaction to compare 1D-SCTST to results from parabolic and Eckart tunnelling models, and in Section 3.4 we illustrate the effect of deep tunnelling. Finally, in Section 3.5 we show how fourth order perturbation theory can be

incorporated into the 1D-SCTST framework, and evaluate its performance.

3.2 Internal rotations in SCTST

Implicit in SCTST (both in full and reduced dimensions) is the assumption that vibrational degrees of freedom (DoFs) are well approximated by a Taylor expansion about the stationary point. Whilst this is a good approximation for bond stretching modes, and, to a lesser extent, bending modes, internal rotational (or hindered rotational, HR) degrees of freedom must be treated very carefully. These modes behave as harmonic oscillators at low temperature, but as free rotors in the high temperature limit - yet there is no simple analytical expression for their partition function. Moreover, internal rotations can lead to anomalous coupling terms if included in a VPT2 treatment, a result of their motion being poorly described by Cartesian (as opposed to internal, curvilinear) coordinates.

Their careful treatment is especially important for reactions in which an internal rotation is present in only one of the reactant or transition states; in this case, there can be no cancellation of errors when the ratio of the partition function is taken in order to calculate the rate constant. This is true of reaction R1, which will be the focus of this chapter.

Several approximate treatments for internal rotational DoFs have been suggested[159–162]. Here, we focus on simple one-dimensional treatments. For larger molecules with many HR modes, all possible conformers of the molecule must be taken into account, and summed over, in order to determine an accurate partition function[106, 107].

Since the HR vibrational mode of reactions R1 - R3 is only found in the TS and not in the reactants, these reactions provide an opportunity to study the effect of different treatments to the HR partition function. In this work, we use two methods of treatment of the HR; an analytic approximation suggested by Truhlar *et al.*[163] to move smoothly between the harmonic and free rotor behaviours, and eigenvalue summation of the 1D rotor. These are compared to a simple

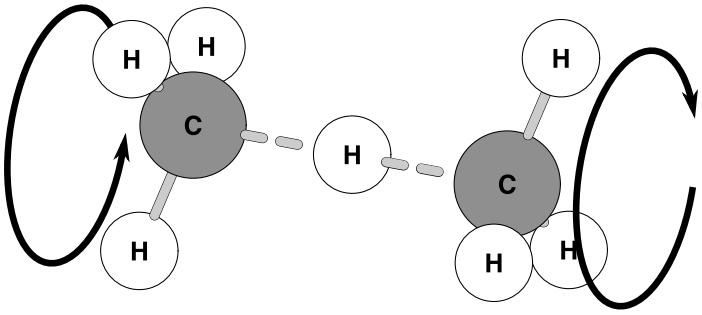


Figure 3.1 The hindered rotational mode for reaction R1.

harmonic approximation.

3.2.1 Theory

An initial approximation is that the HR is separable from the other degrees of freedom. This can be assessed by determining the change in normal mode frequencies when the internal rotor is projected out of the Hessian matrix. This is often found to be valid, owing to the significantly lower frequency internal rotors typically have. The separability of some vibrational degrees of freedom is also implicit in reduced-dimensionality approaches to SCTST. This separation allows for the HR to be treated with a simple 1D partition function treatment. Note that this strategy of separating the HR mode from the vibrational modes is equally applicable to FD treatments. Thus the partition function can be written as the product of a vibrational part and a rotor part, and the problem is reduced to one-dimension.

Truhlar *et al.*[163] have suggested an approximate 1D partition function that moves smoothly from the harmonic (low temperature) limit, to the free rotor (high temperature) limit, given by:

$$Q = Q^{\mathrm{HO}} \tanh\left(\frac{Q^{\mathrm{FR}}}{Q^{\mathrm{I}}}\right) \tag{3.1}$$

where

$$Q^{\mathrm{HO}} = \frac{e^{-\hbar\omega/2kT}}{1-e^{\hbar\omega/kT}} \tag{3.2}$$

is the partition function for the harmonic oscillator approximation,

$$Q^{\mathrm{FR}} = \frac{(2\pi I_m kT)^{1/2}}{\hbar\sigma} \tag{3.3}$$

is the partition function for a free rotor, and

$$Q^{\mathrm{I}} = \frac{kT}{\hbar\omega} \tag{3.4}$$

is the high temperature limit of the harmonic oscillator partition function. Here a value of $\sigma = 3$ was used, due to the three-fold symmetry of the rotor. The reduced moment of inertia, I_m, can be calculated in rectilinear coordinates:

$$I_m = \frac{I_1 I_2}{I_1 + I_2}, \tag{3.5}$$

where I_1 and I_2 are the moments of inertia of the two tops rotating relative to one another about the axis of rotation. Eq. 3.1 will be referred to in this work as the 'tanh' approximation for the hindered rotor. No additional *ab initio* calculations are required in this treatment.

The partition function can also be found numerically by solving the rotational Schrödinger equation for the system with the Hamiltonian[164]:

$$\hat{H} = -\frac{\partial}{\partial\theta} B(\theta) \frac{\partial}{\partial\theta} + V(\theta) \tag{3.6}$$

where θ is the angle of the rotation, and $B(\theta)$ is the effective rotational constant[165]. For a spherical top, $B(\theta)$ is independent of θ, simplifying the equation. The barrier height can be determined from a torsional scan. The rotor potential for reactions R1-R3 was found to be accurately approximated by:

$$V(\theta) = W\cos(3\theta) \tag{3.7}$$

where W is the rotational barrier height, as shown in Fig. 3.2. Eq. 3.6 can then be solved numerically to find a spectrum of eigenvalues, which determine the partition function. Calculating the partition function from the eigenvalues of Eq. 3.6 is referred to in the following as the 'numerical solution' to the hindered rotor, and is assumed to be the most accurate treatment presented here.

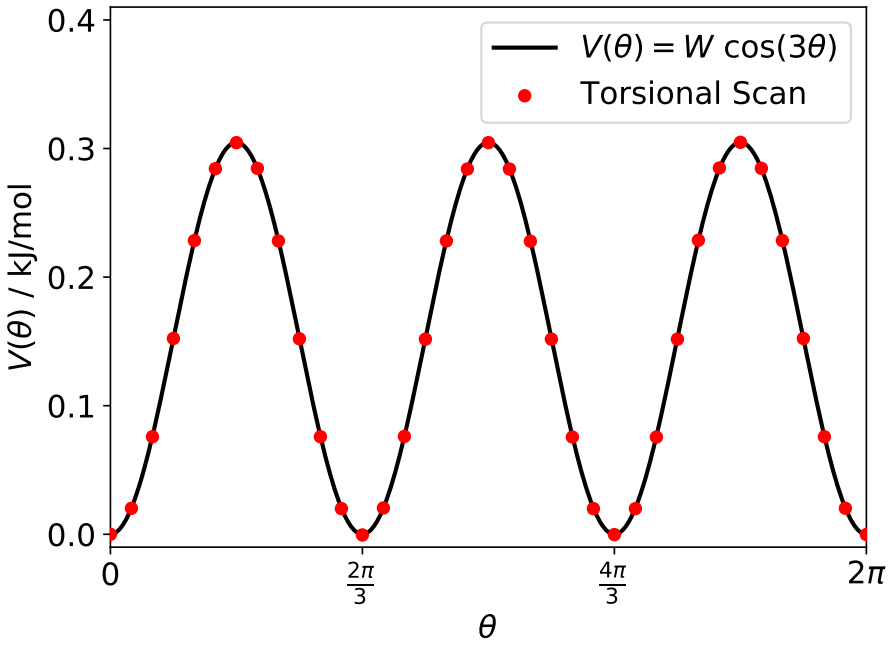


Figure 3.2 The rotational potential surface for $CH_3{-}H{-}CH_3$.

Note that whilst the 1D solution to hindered rotor treatments is straightforward, their treatment in a FD-SCTST calculation is less simple, as they cannot be treated as separable from other degrees of freedom. A treatment by rectilinear (Cartesian) normal modes can lead to unphysically large couplings between it and other modes[166, 167], but a more sophisticated method, utilising VPT2 in curvilinear coordinates, is not currently routine. It is likely that more error is introduced by including a hindered rotor in a VPT2 calculation, than by projecting it out of the Hessian matrix and treating it in one dimension. This leaves an $(F-1)$ dimensional SCTST calculation.

3.2.2 Computational methods

1D-SCTST calculations for reactions R1, R2 and R3 were carried out using the *pySCTST* software package[168]. Structure optimisations and vibrational frequencies were calculated at the MP2/cc-pVTZ level of theory, and single point energy calculations were performed at the CCSD(T)/cc-pVTZ // MP2/cc-pVTZ[169] level of theory. Energy calculations using cc-pVQZ and cc-pV5Z

basis sets were also performed, allowing extrapolation to the complete basis set (CBS)[170]. For the Richardson extrapolation calculations, a step size of $\Delta Q = 0.02$ $\mathrm{Da}^{0.5}$ a_0 was used, and Wagner's DT corrections were included, as described in Section 2.3.2.

3.2.3 Results and discussion

Stationary point analysis

The geometry of the transition state is shown in Fig. 3.3 and the harmonic frequencies of each of the stationary points before and after projecting out the HR degree of freedom are shown in Table 3.1. Compared to the transition state of R1, the transition states of R2 and R3 have lower imaginary frequencies due to the increased mass of the central atom. The hindered rotor frequency is significantly lower in R3, where the rotating atoms have increased in mass. After projecting out the hindered rotor degree of freedom, the vibrational frequencies change very little indicating the separability assumption is good. The classical reaction barrier is shown in Table 3.2 at different levels of theory. Increasing the size of the basis set leads to a decrease in barrier height of approximately 0.6 kJ/mol. The barrier used is about 1 kJ/mol smaller than that of Ramazani *et al.* and 1 kJ/mol larger than that calculated by Temelso *et al.*[155]. Other transition state data are shown in Table 3.3.

Effect of the harmonic approximation

The extent of the error introduced by the harmonic approximation for the hindered rotor can be seen from Fig. 3.4, which shows the relative partition functions of the harmonic oscillator, the free rotor and the hindered rotor. The harmonic approximation breaks down above just 25 K. Above 200 K, the rotor behaves as a free rotor.

Species	Frequencies / cm^{-1}			
CH_3	3372 (E)	3201 (A_1')	1450 (E)	501 (A_2')
CD_3	2513 (E)	2264 (A_1')	1067 (E)	389 (A_2')
CH_4	3216 (T_2)	3093 (A_1)	1600 (E)	1358 (T_2)
CDH_3	3215 (E)	3129 (A_1)	2328(A_1)	1535 (E)
	1353 (A_1)	1201 (E)		
CD_4	2381(T_2)	2188 (A_1)	1132 (E)	1027 (T_2)
TS (R1)	1931 **i** (A_{2u})	3263 (E_u)	3262 (E_g)	3127 (A_{1g})
	3125 (A_{2u})	1506 (E_u)	1474 (E_g)	1394 (E_u)
	1211 (A_{2u})	1170 (A_{1g})	715(E_g)	544 (A_{1g})
	331 (E_u)	**56** (A_{1u})		
TS (R1)	1931 **i** (A_{2u})	3263 (E_u)	3262 (E_g)	3127 (A_{1g})
Post projection	3125 (A_{2u})	1506 (E_u)	1474(E_g)	1392 (E_u)
	1211 (A_{2u})	1170 (A_{1g})	715 (E_g)	544 (A_{1g})
	331 (E_u)			
TS (R2)	1442 **i** (A_{2u})	3262 (E_u)	3262 (E_g)	3127 (A_{1g})
	3125 (A_{2u})	1474 (E_u)	1474 (E_g)	1170 (E_u)
	1165 (A_{2u})	1114 (A_{1g})	715 (E_g)	544 (A_{1g})
	304 (E_u)	**56** (A_{1u})		
TS (R2)	1442 **i** (A_{2u})	3262 (E_u)	3262 (E_g)	3127 (A_{1g})
Post projection	3126 (A_{2u})	1474(E_u)	1474 (E_g)	1170(E_u)
	1165 (A_{2u})	1114 (A_{1g})	715(E_g)	544 (A_{1g})
	304 (E_u)			
TS (R3)	1421 **i** (A_{2u})	2423 (E_u)	2423 (E_g)	2228 (A_{1g})
	2224 (A_{2u})	1075 (E_u)	1073(E_g)	1029 (E_u)
	931(A_{2u})	906 (A_{1g})	535 (E_g)	480 (A_{1g})
	234 (E_u)	**40** (A_{1u})		
TS (R3)	1422 **i** (A_{2u})	2423 (E_u)	2423 (E_g)	2228 (A_{1g})
Post projection	2224 (A_{2u})	1075(E_u)	1073 (E_g)	1029 (E_u)
	931 (A_{2u})	906(A_{1g})	535 (E_g)	480 (A_{1g})
	234 (E_u)			

Table 3.1 Harmonic frequencies at the stationary points in reactions R1-R3 pre- and post- projection of the hindered rotor degree of freedom. Hindered rotor frequencies are in bold. Symmetry labels are given in parenthesis and degenerate frequencies are not repeated.

3.2.4 SCTST results

The results of the SCTST calculation using the *tanh* method are compared to 2D-QRS calculations by Remmert *et al.*[45] and experimental results[150, 151] in Fig. 3.5a , showing good agreement. 1D-SCTST can be seen to underestimate the

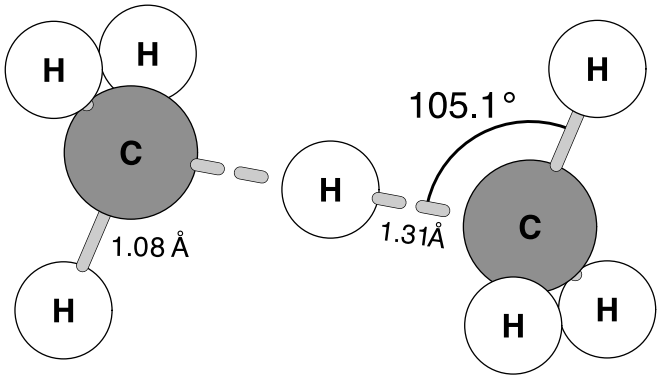


Figure 3.3 Transition state for reaction (R1). Within the Born-Oppenheimer approximation, the geometry is unchanged under isotopic substitution.

MP2	CCSD(T)			
cc-pvtz	cc-pvtz	cc-pvqz	cc-pv5z	CBS
78.5	76.1	75.4	75.3	75.3

Table 3.2 Classical barrier heights for the series of reactions R1-R3 calculated at different levels of theory with increasingly large basis sets. CBS is the complete basis set extrapolation[170]. Energies in kJ mol^{-1}.

Reaction	x_{FF} (cm^{-1})	G_0 (kJ/mol)	W (kJ/mol)	$I_m/10^{-47}$ (kg m^2)
R1	-315	-0.94	0.305	2.73
R2	-565	-1.69	0.305	2.73
R3	-582	-1.74	0.305	5.45

Table 3.3 Transition state data for reactions R1-R3.

experimental rates and the results of 2D-QRS calculations. 1D-SCTST gives a rate about three times lower than the 2D-QRS result at 500 K; moreover the results do not converge exactly at high temperature, where tunnelling effects are negligible.

Note that our 1D-SCTST barrier height was calculated in the complete basis set limit, whereas the 2D-QRS calculations were performed at the cc-pVTZ level of theory. The difference in barrier height between the two calculations, however, is just 1% (75.3 kJ/mol for 1D-SCTST and 76.1 kJ/mol for 2D-QRS) and so should have only a small effect on the estimated rate constants.

In the 2D-QRS study, the internal rotation was treated as a harmonic oscillator.

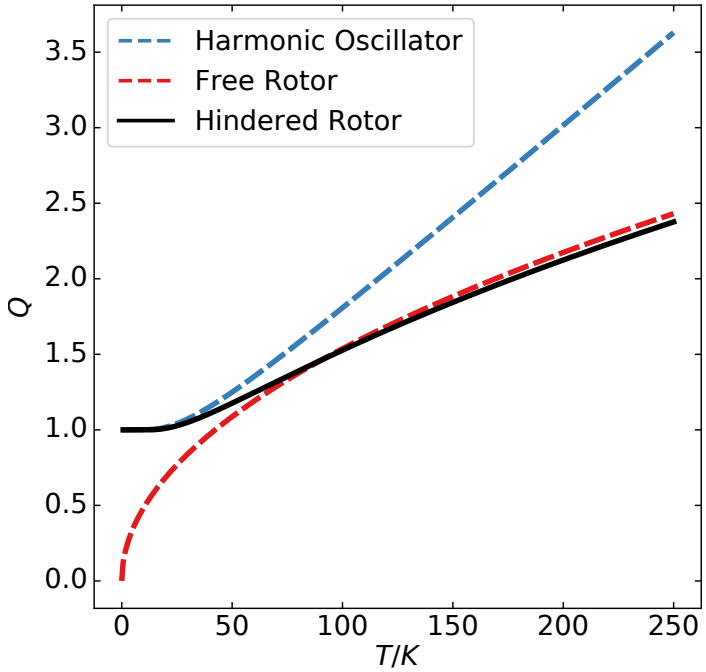
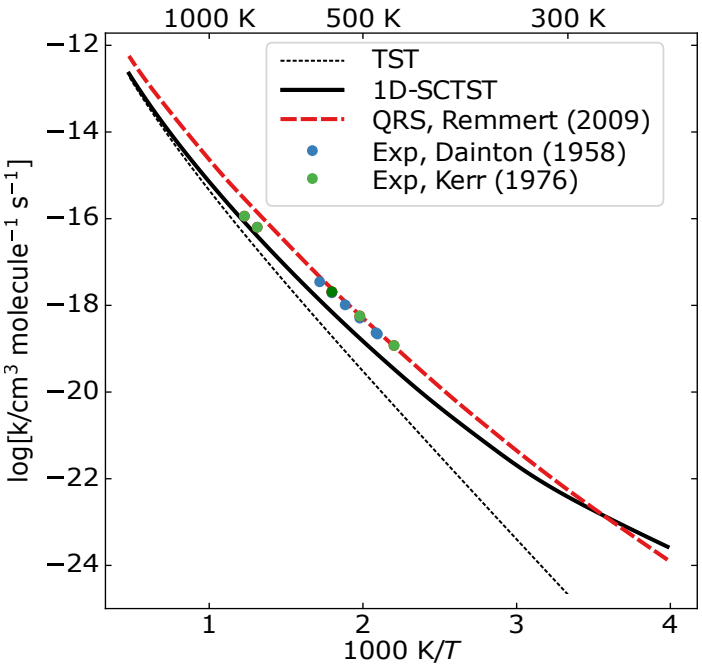


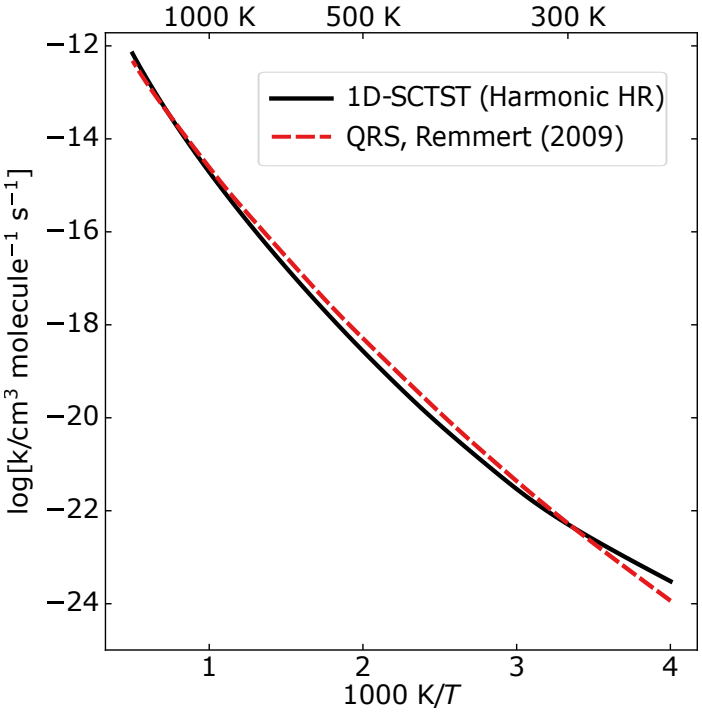
Figure 3.4 Partition functions for a free rotor and a harmonic oscillator compared to the *tanh* approximation for the hindered rotor in the transition of reaction R1. It is clear the harmonic approximation is very poor above 100 K.

To investigate the effect of this, we calculated the 1D-SCTST rate constant using a simple harmonic oscillator partition function for the hindered rotor mode and compared it to the 2D-QRS results in Fig. 3.5b. It can be seen that the two curves now have excellent agreement over the entire temperature range. This shows the discrepancies found between 1D-SCTST and 2D-QRS are largely due to the application of the hindered rotor partition function. In Fig. 3.5a, we also compare the 1D-SCTST rate constant to experimental results reported in refs. [150, 151]. We can see that the 1D-SCTST results have better agreement to the experimental data than the 2D-QRS at higher temperature; however, there is a small underestimation at lower temperature. This is likely due to the neglection of multidimensional tunnelling effects, such as corner-cutting [58].

The results of using three different treatments of the hindered rotor are compared in Fig. 3.6. The harmonic oscillator overestimates the rotor partition function, giving a value about two times too large at 500 K, but converges to that of the numerical solution at low temperature (when the barrier to rotation



(a) SCTST calculations using the numerical solution to the hindered rotor partition function compared to experiment[150, 151] and 2D-QRS calculations[45].



(b) 1D-SCTST and 2D-QRS[45] compared directly with the same treatment of the hindered rotor degree of freedom.

Figure 3.5 Arrhenius plots for the reaction $CH_3 + CH_4 \longrightarrow CH_4 + CH_3$.

T(K)	$4k_{R2}/k_{R1}$	k_{R3}/k_{R1}
300	0.0167 (0.056)	0.020 (0.020)
350	0.0523 (0.085)	0.059 (0.040)
400	0.102 (0.120)	0.111 (0.066)
450	0.157 (0.160)	0.165 (0.097)
500	0.210 (0.202)	0.216 (0.130)
550	0.258 (0.245)	0.263 (0.164)
600	0.303 (0.286)	0.305 (0.198)
800	0.439 (0.438)	0.435 (0.326)
1000	0.528 (0.564)	0.519 (0.433)
1500	0.642 (0.772)	0.631 (0.610)
2000	0.690 (0.870)	0.679 (0.698)

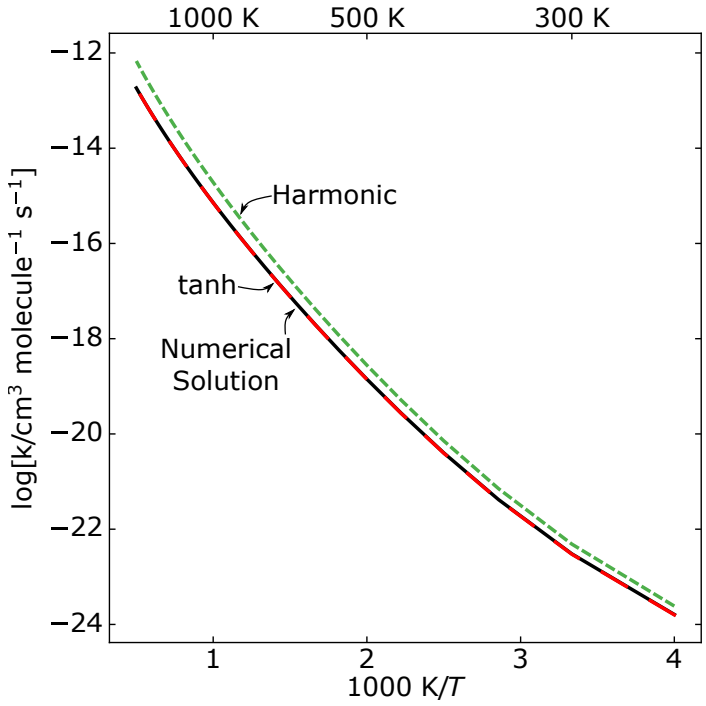
Table 3.4 Kinetic isotope effects in reactions R2 and R3. Values in brackets are those calculated from quantum reactive scattering calculations[45].

is much larger than the thermal energy in this degree of freedom). The *tanh* approximation, gives excellent agreement over the whole temperature range, differing at most by 0.7 % from the numerical solution, and thus can provide an excellent approximation for this and similar systems.

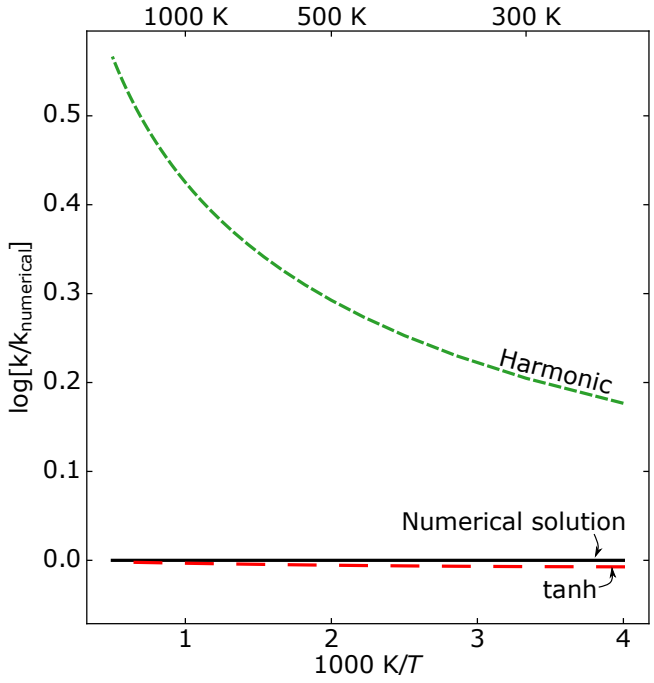
Kinetic isotope effects

Both primary and secondary isotope effects can be seen by comparing reactions R1, R2, and R3, whose rates are compared in Fig. 3.7, where the hindered-rotor partition function was calculated numerically. The rate for R2 has been multiplied by four to account for the differences in symmetry numbers between the three reactions, allowing the rates to be compared directly. Differences in rate between R1 and R2 are due to the primary isotope effect (a result of altering the tunnelling atom). This is seen to significantly decrease the rate as a result of the heavier tunnelling atom. The decreased imaginary frequency at the transition state of R2 (compared to that of R1) indicates a flatter and thus wider barrier, thus the rate is decreased. The decreased contribution of tunnelling can be seen in the smaller curvature in the Arrhenius plot.

Comparing R2 and R3 illustrates the secondary isotope effect caused by replacing the non-reactive hydrogen atoms with deuterium atoms. The secondary



(a) Arrhenius Plot.



(b) Relative rates.

Figure 3.6 Rate constant comparisons for reaction R1 using three treatments of the hindered rotor.

effect is much smaller, and in our calculations can increase or decrease the rate depending on temperature. These results are in good agreement with those of

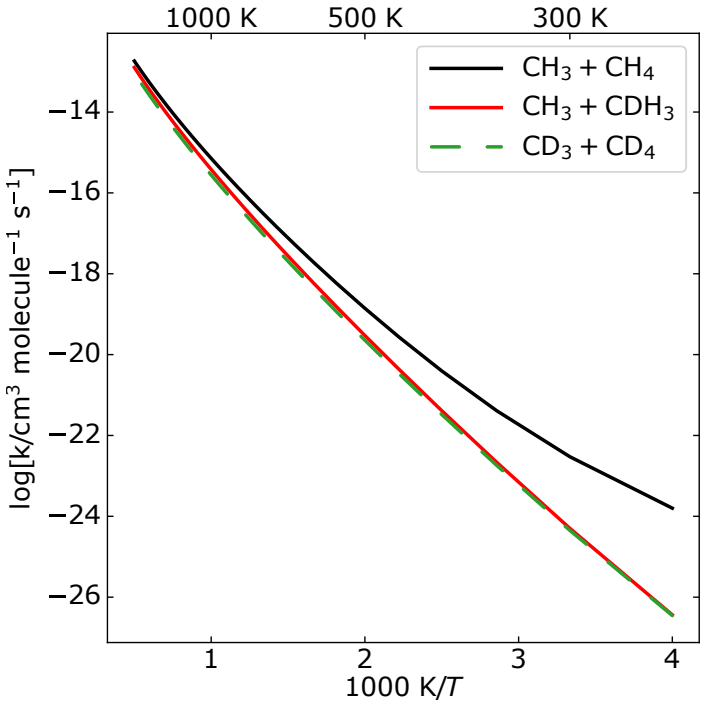


Figure 3.7 Rate constant comparison for reactions R1, R2 and R3.

Remmert *et al.*[45] as shown in Table 3.4. The agreement with previous work is excellent for the primary effect ($4k_2/k1$) over the whole temperature range. For the secondary effect, the agreement is worse for mid-range temperatures, between 400-600 K. This is likely a result of the improved treatment of the hindered rotor in this study; as R1 and R2 have the same HR frequency, their HR contributions will exactly cancel in the ratio $4k_2/k_1$ and thus this ratio is insensitive to the hindered rotor treatment. R1 and R3, however, have differing hindered rotor frequencies, and so the ratio k_3/k_1 is dependent on the HR treatment.

3.3 Comparison of 1D-SCTST to other one-dimensional methods

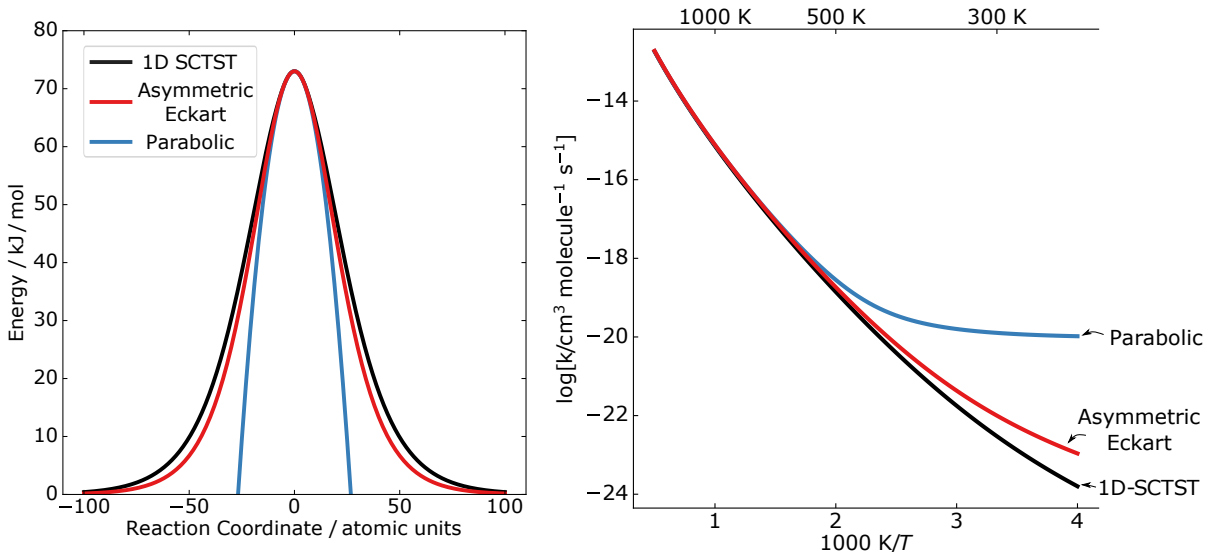
We have shown 1D-SCTST can give good agreement with experimental rate constants and rate constants from QRS calculations[92, 94, 108], however the method's performance has not been directly compared in the literature to other one-dimensional tunnelling models of similar expense. The key advantage of 1D-SCTST over similar methods is an improved description of reaction barrier

width. The rate of a reaction depends exponentially on the reaction barrier width, as well as height. This suggests that in general, the width of the barrier should be treated as carefully as the barrier height is, to obtain quantitative results. 1D-SCTST remains slightly more expensive than other commonly used 1D tunnelling methods such as parabolic tunnelling[171, 172] and asymmetric Eckart tunnelling[57, 173–175], as it gives a more detailed description of the barrier width by including third and fourth order derivatives along the reaction mode. In this section we explore the impact of this improved description, by demonstrating how the resultant rate constants depend critically on the choice of 1D model, and that an accurate description of barrier width is often required to give quantitative results. Note that VTST with zero-curvature tunnelling also falls into this category of 1D methods[56, 57]. Its implementation, however, requires a full minimum energy path, and so many more *ab initio* calculations than the other methods discussed here.

The transmission probability for a parabolic barrier, in general, overestimates the thermal tunnelling rates significantly. Whilst this is in general too poor an approximation to be used at low temperatures, it is often used to study reactions where multidimensional methods are too expensive[176–181], or to calculate tunnelling in instanton calculations above the critical temperature, where the instanton is collapsed [71] (since this only represents tunnelling at the very top of the barrier, the approximation is not so severe).

A much better approach is calculating tunnelling through an asymmetric Eckart barrier[182–195], whose exact quantum transmission coefficient was determined by Johnston and Heicklen[196]. Just the forward and reverse barrier heights, and the imaginary frequency are required.

The effect of these different treatments was assessed for reaction R1. Fig. 3.8 shows that including additional information about the barrier width has a significant effect on the resulting rate of reaction, lowering the overall rate by nearly a factor of seven at 250 K. Significantly better agreement with QRS calculations can be found for the 1D-SCTST case, justifying the minor additional expense of the



(a) Reaction Barriers.

(b) Arrhenius Plot.

Figure 3.8 Comparison of 1D treatments for reaction R1.

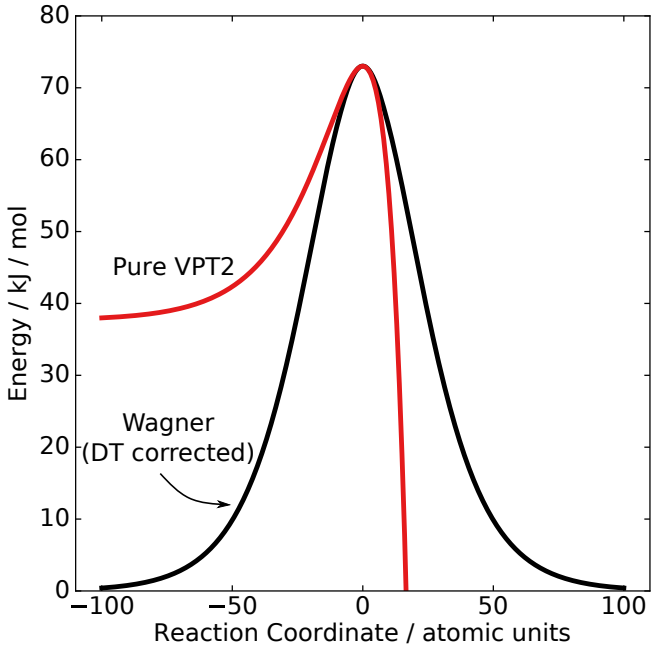
method.

3.4 The effect of deep tunnelling

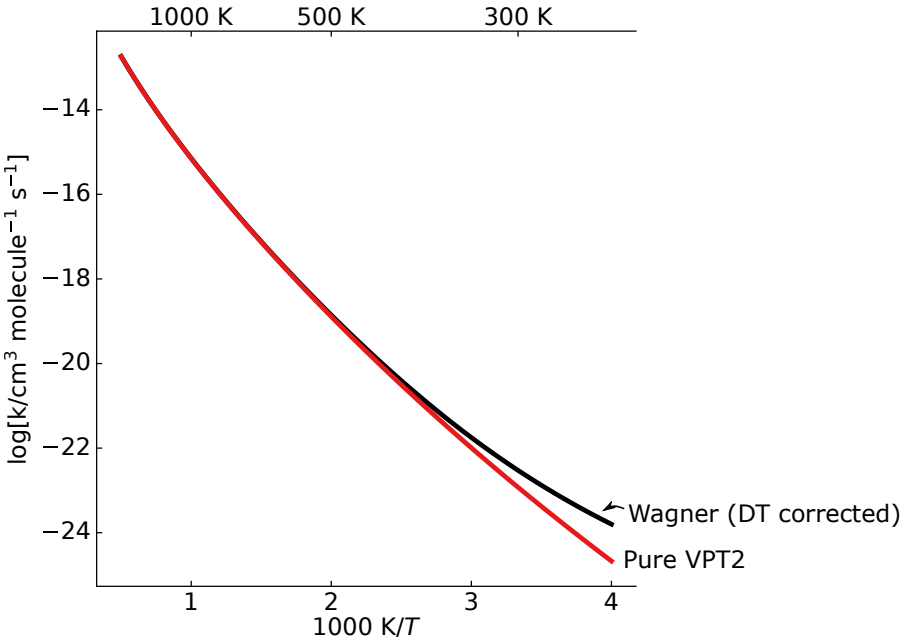
In this section we show that the deep-tunnelling correction of Wagner[87], discussed in Section 2.3.2, is particularly crucial for 1D-SCTST, and determine its impact on reaction R1. The influence of this correction on real reactions has not been discussed in detail in the literature, and many SCTST calculations are done without it[93, 97–100, 103, 197].

Fig. 3.9 shows the importance of this correction for reaction R1. The effective VPT2 tunnelling barrier height is about half the true barrier height, thus the rate is significantly reduced, by a factor of more than seven at 250 K.

The reason for the significant impact of Wagner's method on 1D-SCTST is clear. In VPT2-SCTST, the effective tunnelling barrier height is a function of all the anharmonic couplings of the bound modes of the TS. When the number of active dimensions is reduced, information of these couplings is lost and so the effective barrier height is underestimated. This is illustrated in Fig. 3.10. As such, 1D-SCTST without deep tunnelling corrections tends to underestimate the rate



(a) Reaction Barriers.



(b) Arrhenius Plot.

Figure 3.9 Effect of deep tunnelling corrections on 1D treatments of reaction R1.

significantly. This effect is also present in SCTST in full-dimensions, although inclusion of couplings allows for a more realistic effective barrier height.

3.5 Fourth order vibrational perturbation theory

Recently Stanton and coworkers have written down the equations to perform vibrational perturbation theory to fourth, rather than second, order - VPT4[88, 89]. In principle this should improve the description of the barrier, particularly in the deep tunnelling regime, although this has only been tested on one-dimensional model potentials to date. To determine the SCTST formulae at VPT4 level, Eq. 2.11 becomes a cubic polynomial in θ (here written for one-dimension, for clarity):

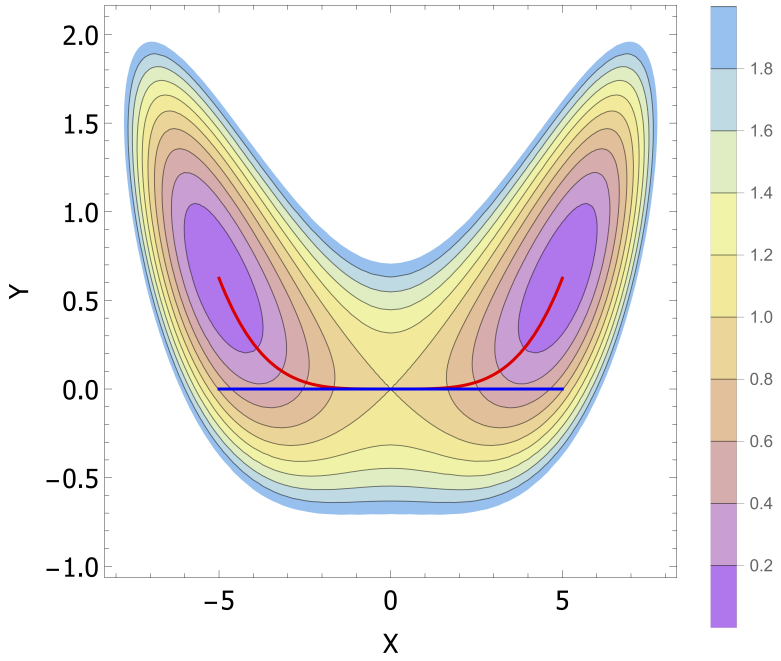
$$E = V_0 + G + W\left(n+\frac{1}{2}\right) + X\left(n+\frac{1}{2}\right)^2 + Y\left(n+\frac{1}{2}\right)^3 \tag{3.8}$$

where V_0 is the potential barrier height, G is the anharmonic correction to the potential, and W, X, and Y are given by unwieldy, but analytical functions of up to sixth order derivatives of the PES at the transition state[88]. $\theta(E)$ is thus found by inverting a cubic equation:

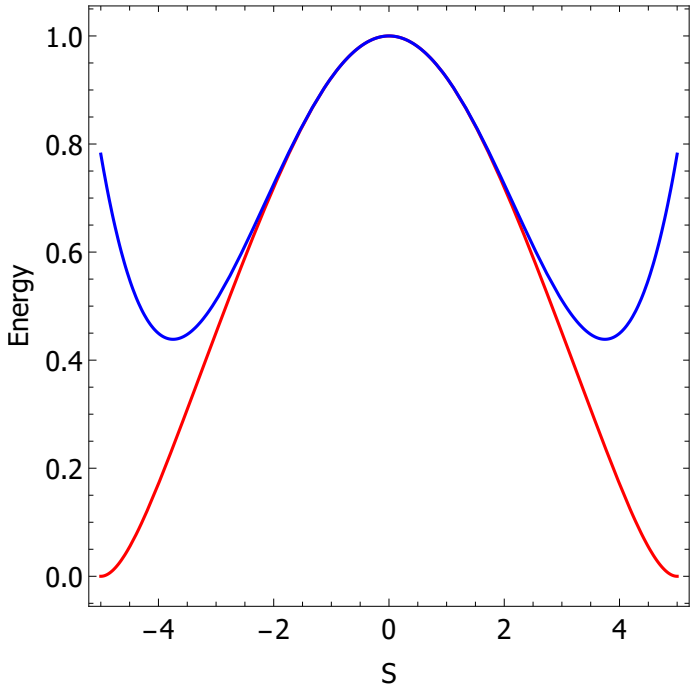
$$E(\theta) = V_0 + G + W\left(\frac{\theta}{\pi}\right) + X\left(\frac{\theta}{\pi}\right)^2 + Y\left(\frac{\theta}{\pi}\right)^3. \tag{3.9}$$

When inverting the cubic equation, unlike in the quadratic case, it is not clear, analytically, which root gives the correct behaviour. Thus there is no analytical way to solve for $\theta(E)$ correctly. In order to maintain the analyticity of SCTST, it is necessary in this case to use a different formulation of SCTST, termed SCTST-θ, as first discussed by Hernandez and Miller [198]. It is formally equivalent to SCTST as derived in Chapter 2 but does not require inversion of Eq. 3.9, and is derived in Appendix C.

It is clear the VPT4 approach requires significantly more *ab initio* calculations, in order to determine the fifth and sixth order derivatives of the potential. Within the one-dimensional approximation this becomes a tractable expense.



(a) Reaction surface with two pathways.



(b) Energy along the paths in (a).

Figure 3.10 Comparison of treating a PES in full dimensions (following the red path) and taking a one-dimensional slice (blue path). The one-dimensional slice can significantly underestimate the barrier height.

	Polynomial Fit	Richardson Extrapolation	Difference
G	−81.6	−78.8	4%
X	−326.6	−315.4	4%
Y	−55.6	–	–

Table 3.5 VPT2 and VPT4 constants calculated using a fit to a sixth order polynomial, and as calculated previously using Richardson extrapolation. Values in cm^{-1}.

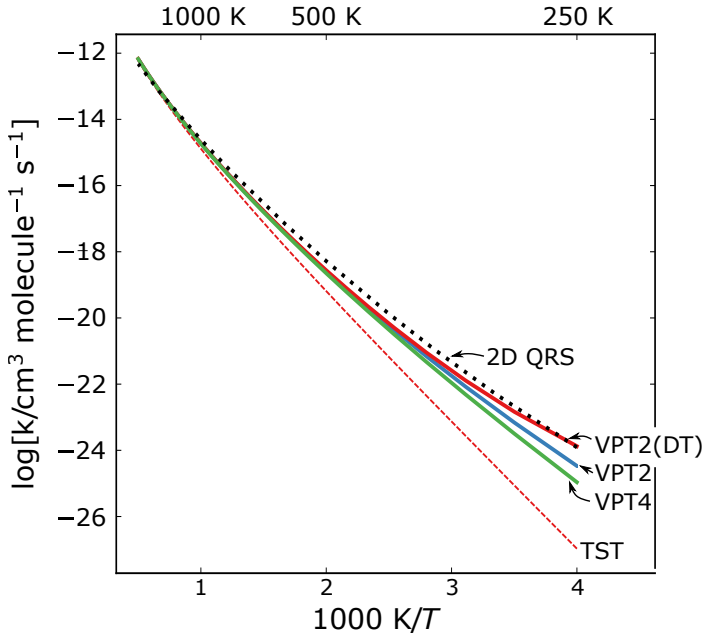


Figure 3.11 1D-SCTST results using VPT4, VPT2 and VPT2 with deep tunnelling corrections for reaction R1, compared to a 2D QRS result[46].

To investigate the effect of higher order perturbations on real reactions, we compared the various methods to reaction R1 in one-dimension. The VPT4 coefficients were determined from derivatives obtained from a sixth order polynomial function fitted to a total of 21 single point energies at the TS and the displaced geometries along the reaction coordinate. This method was able to reproduce VPT2 coefficients calculated using Richardson extrapolation to good accuracy, as shown in Table 3.5.

The 1D-SCTST rate constants calculated using VPT4, VPT2 and VPT2 with deep tunnelling corrections are shown in Fig. 3.11. By comparison to results obtained from 2D QRS calculations[46], we can see that the DT corrected VPT2 rate constant has the best agreement to the QRS for the entire temperature range. Both

VPT2 and VPT4 underestimate the reaction rate, especially at temperatures below 300K, where deep tunnelling has a more significant contribution to the reaction.

In previous studies[88, 89], VPT4 has been shown to improve behaviour in the deep tunnelling regime, in contrast to what we observe here. In these studies, only one-dimensional potentials were studied. VPT4 in one dimension is likely to improve the description of the 1D 'slice' of the PES (see Fig. 3.10), but this slice is not, itself, representative of the reaction. Whilst previous results suggest that VPT4 will improve the description of a one-dimensional, Eckart-like potential, this may not be true of a multidimensional, complex potential seen in real chemical systems, as any one-dimensional description of the surface at the TS will not correctly estimate the barrier height, no matter the level of expansion.

Even a full-dimensional VPT4 expansion is unlikely to be sufficient to substantially improve behaviour in the deep tunnelling regime. Accurately determining the threshold energy from derivatives at the TS requires substantial knowledge about the inter-mode couplings, since these couplings have a severe impact on the reaction path away from the TS. Therefore we expect only a very high order of multidimensional perturbation theory could correctly describe the deep tunnelling regime. The Wagner deep tunnelling correction, however, introduces this information directly and exactly. It is thus clear that the method of Wagner is a more efficient way to ensure the behaviour is correct, without requiring detailed knowledge of these couplings.

Wagner's corrections can similarly be combined with the VPT4 calculation, in which case terms of the fourth and fifth power of θ can be added to Eq. 3.9 to correct E_{min} such that $E_{\text{min}} = 0$. This may lead to slightly more accurate results.

3.6 Conclusions

One-dimensional semiclassical transition state theory (1D-SCTST) presents a computationally cheap way to include quantum tunnelling effects in the calculation of chemical reaction rate constants. It requires only two Hessian calculations, significantly less than SCTST in full-dimensions, and other popular methods such

as VTST/SCT and instanton rate theory. This is an inexpensive method that has scope to be used on much larger systems than SCTST in full dimensions. Using a simple hydrogen transfer reaction and its isotopologues, we have shown that this method is capable of producing rate constants and kinetic isotope effects in good agreement with both experiment and quantum scattering calculations.

A careful treatment of hindered internal rotational degrees of freedom is important and achievable within the 1D-SCTST formalism. We have shown that the choice of treatment of the hindered rotor degree of freedom can significantly influence the results of an SCTST calculation. Using a harmonic oscillator partition function for reaction R1 overestimates the rate by a factor of two at 500 K and by more than a factor of three at 1500 K. The accuracy of the analytical *tanh* approximate hindered rotor partition function [163] has been tested by comparing its results to that of numerically solving the Schrödinger equation on an approximate torsional potential. We found that for this set of reactions, the *tanh* approximation is in excellent agreement to the numerical results.

1D-SCTST has comparable cost to the commonly used Eckart barrier model. We have found that the effect of SCTST's improved description of barrier width is substantial, giving significantly better agreement with higher level calculations. We also showed that Wagner's deep tunnelling corrections are essential for quantitative results in bimolecular reactions.

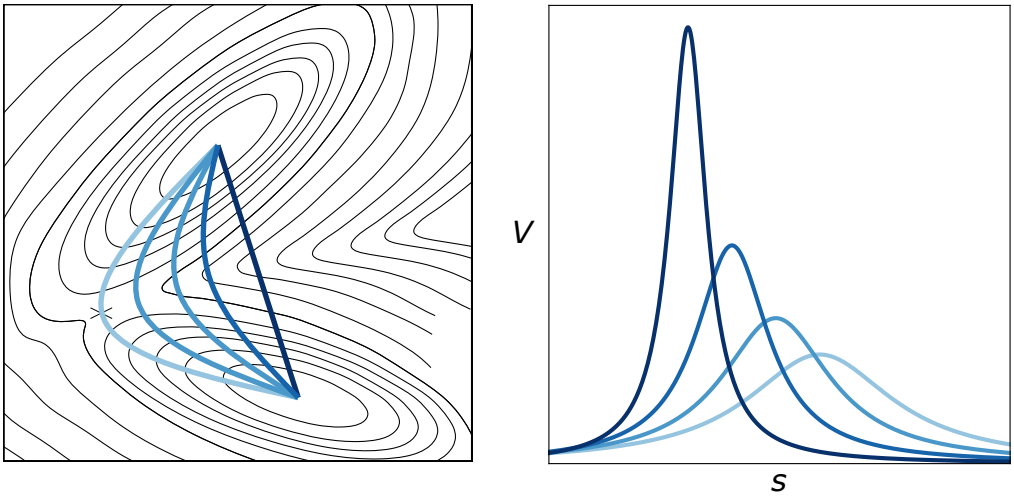
Extending the SCTST method to fourth order perturbation theory is computationally feasible in one dimension, and gives an improved description of the barrier top. We find, however, that VPT4 offers no benefit over VPT2 in the 1D-SCTST framework. This is because the main inaccuracies of 1D-SCTST are caused by inaccuracies in the reactant asymptote, and multidimensional coupling, rather than an inadequate description of the barrier top.

Used appropriately, it is clear 1D-SCTST with internal rotation and deep-tunnelling corrections is a powerful rate theory that offers an improved model to Eckart tunnelling without significant additional expense.

Chapter 4

Corner-cutting and variational effects in SCTST

Corner-cutting and variational effects arise in multidimensional reaction dynamics, and are explicitly accounted for in semiclassical rate theories such as the instanton method or VTST. SCTST in full dimensions, however, does not account *explicitly* for these effects and thus the approximations and limitations of the method are not clear. In this chapter, we show that SCTST accounts *implicitly* for corner-cutting trajectories and variational effects. By isolating these trajectories, we can investigate the significance of corner-cutting in real reactions, and determine the applicability of SCTST to treat these effects accurately.

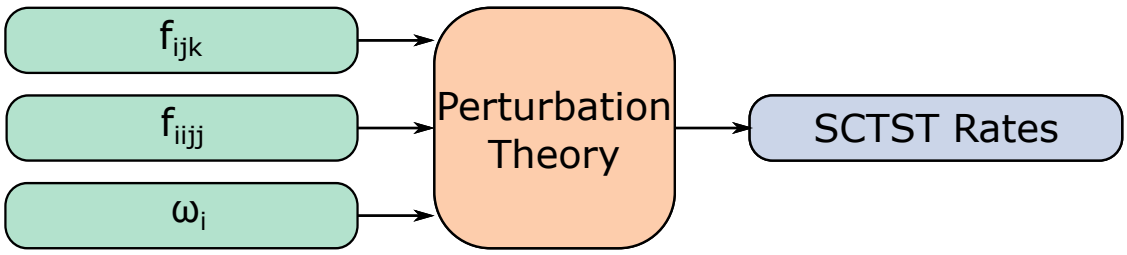


Abstract 4 Illustration of possible corner-cutting trajectories on a potential energy surface.

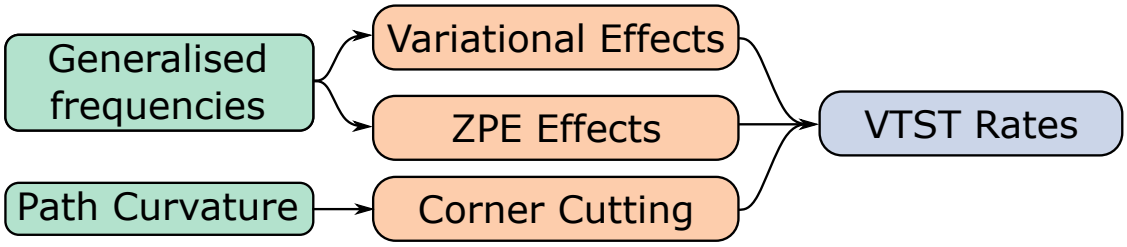
4.1 Introduction

SCTST in full-dimensions improves upon the one-dimensional tunnelling model through the use of multidimensional vibrational perturbation theory (typically to second order). This allows for an improved description of the barrier shape, and the incorporation of multidimensional tunnelling effects, without requiring an explicit tunnelling path.

A disadvantage of the perturbation theory approach is that physical intuition of the problem is lost, and it is not clear what effects are accounted for, which approximations have been made, and which effects are dominant in a particular reaction. This limits the confidence with which SCTST can be applied to unusual problems, for example chemical reactions known to have strong variational effects[199]. It is also hard to extract physical information about the reaction, such as the impact of corner-cutting on the rate. This is because the calculated anharmonic constants represent an amalgamation of variational effects, anharmonic ZPE effects and corner-cutting effects, in a way that are not easily uncoupled. In other words, the input data to the SCTST method is the set of third and fourth order derivatives of the PES at the transition state, which do not have obvious physical interpretations:



This is in contrast to, for example, VTST/SCT where generalised vibrational frequencies, and reaction path curvature, along the reaction path are explicitly found, and incorporated into the theory as distinct correction factors to the rate:



It would therefore be useful to understand how, and to what extent, SCTST accounts for these effects, and give a physical picture of the significance of each effect on a particular reaction. We will first investigate the SCTST treatment of corner-cutting, then discuss its treatment of variational effects.

4.2 Corner-cutting in SCTST

The key semiclassical approximation in chemical physics is the steepest-descent approximation to the path integral description of tunnelling. This turns a sum over all possible trajectories to one just over classical paths *i.e.* those that extremise the action. Corner-cutting is the quantum dynamical effect whereby these trajectories take paths with a higher overall barrier than the minimum energy path, but are narrower, and therefore easier to tunnel through. This effect is known to be most significant for 'heavy-light-heavy' reactions, in which a light atom is transferred between two heavy centres, as these reactions have significant reaction path curvature. The effects of corner-cutting on the dynamics of chemical reactions have been studied extensively [58, 62, 63, 200–206], where a key challenge is determining the location on the PES of the important pathways. This must be done accurately as the height and width of the pathways very sensitively determine the tunnelling probability.

A simple choice of pathway is the minimum energy path (MEP) from the reactant to product configurations, as illustrated in Fig. 4.1a, which is easily found by following the path of steepest descent on the Born-Oppenheimer surface from the TS. It is well known that tunnelling through the MEP often underestimates

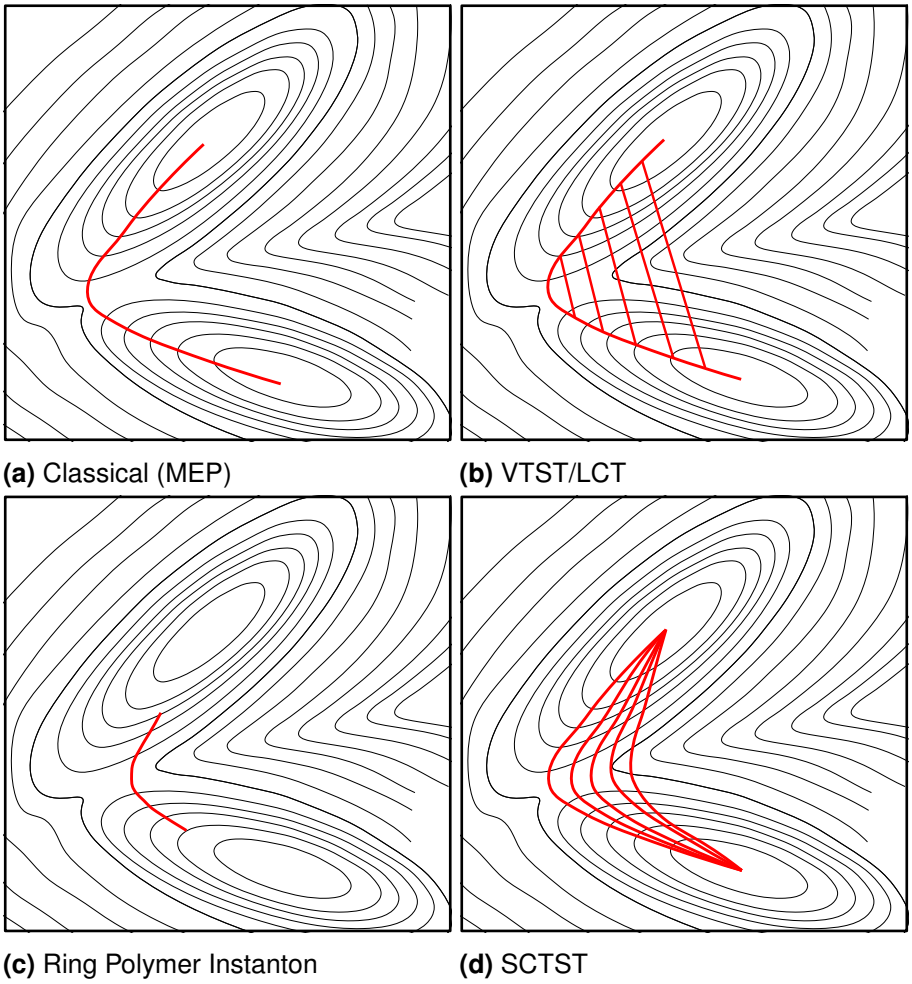


Figure 4.1 Illustration of how corner-cutting effects are accounted for in three semi-classical methods.

reaction probabilities due to neglecting corner-cutting effects[58], for reactions whose MEP exhibits large curvature.

Truhlar and coworkers have developed *ad hoc* methods to incorporate multidimensional tunnelling effects in Variational Transition State Theory (VTST), accounting for corner-cutting effects. In the small-curvature tunnelling approximation (SCT), corner-cutting is accounted for by reducing the effective mass of the reaction coordinate, equivalent to shortening the tunnelling path[9, 207, 208]. The new effective mass is determined from the reaction-path curvature as calculated along the MEP. The large-curvature tunnelling (LCT) approximation [48, 58, 62, 63, 209] includes tunnelling paths that are straight lines that connect the reactant and product wells, as illustrated in Fig. 4.1b. These paths can

also connect configurations in different vibrational states. In microcanonically optimised tunnelling VTST (μOMT), the tunnelling is calculated as the maximum of the SCT and LCT probabilities. Finally, the least-action tunnelling model (LAT)[64, 210] considers a large number of paths between the limits of the MEP and LCT paths. An advantage of this is that it is clear which effects are (and are not) being accounted for, and the contribution of each effect can be investigated individually, and the validity of the approximations involved is easily determined. This does, however, lose the analyticity and cost-effectiveness that makes SCTST such a powerful method.

Ring-polymer instanton rate theory[69, 71] determines a single dominant tunnelling pathway by finding the path that represents a saddle point in the ring-polymer action, shown in Fig. 4.1c. The instanton is therefore expected to accurately capture the corner-cutting effects of the potential energy surface.

In order to confidently apply SCTST to new problems, where these effects may be significant, we will now discuss how SCTST accounts for these effects both in theory and in practice.

4.2.1 SCTST as a sum of corner-cutting trajectories

In this section we show that the SCTST rate can be interpreted as a sum of 1D-SCTST rate constants, each corresponding to a different effective barrier height and width. These barriers can be interpreted as distinct corner-cutting trajectories, as illustrated in Fig. 4.1d. This interpretation gives a novel physical picture of how corner-cutting paths are incorporated into SCTST, and can allow us to determine the impact of corner-cutting in a particular reaction.

The connection between FD-SCTST, and individual 1D-SCTST paths is clear from comparing the key formulae for the rate. For a one-dimensional system, the action variable of the F^{th} degree of freedom is given by:

$$\theta_{\text{1D}}(E_v, \Delta V_f, \omega_F) = \pi \frac{i\omega_F + \left[-\omega_F^2 + 4x_{FF}\left(\Delta V_f + G_0 - E_v\right)\right]^{1/2}}{2x_{FF}}. \tag{4.1}$$

In the case where the barrier height is replaced by an effective barrier,

$$V^{\text{eff}}_{\{n\}'} = \Delta V_f + E_{\{n\}'} \tag{4.2}$$

with

$$E_{\{n\}'} = \sum_{i=1}^{F-1} \hbar\omega_i \left(n_i + 0.5\right) + \sum_{i<j}^{F-1} x_{ij} \left(n_i + 0.5\right)\left(n_j + 0.5\right), \tag{4.3}$$

and the frequency replaced with an effective frequency,:

$$\omega^{\text{eff}}_{\{n\}'} = \omega_F + \sum_{i=1}^{F-1} x_{iF}(n_i + 0.5), \tag{4.4}$$

the FD expression for the action, Eq. 2.30, is returned:

$$\begin{aligned}\theta_{\text{1D}}(E_v, V^{\text{eff}}_{\{n\}'}, \omega^{\text{eff}}_{\{n\}'}) &= \pi \frac{-\Omega_{\{n\}'} + \left[\Omega^2_{\{n\}'} + 4x_{FF}\left(\Delta V_f + G_0 + E_{\{n\}'} - E_v\right)\right]^{1/2}}{2x_{FF}} \\ &= \theta_{FD}(E_v, \{n\}').\end{aligned} \tag{4.5}$$

The state-dependent reaction probability is then given by:

$$P_{\{n\}'}(E_v) = \left(1 + \exp\left[2\theta_{\text{1D}}(E_v, V^{\text{eff}}_{\{n\}'}, \omega^{\text{eff}}_{\{n\}'}\right]\right)^{-1} \tag{4.6}$$

and the cumulative reaction probability is given by the sum over all state-dependant reaction probabilities at the energy E_v:

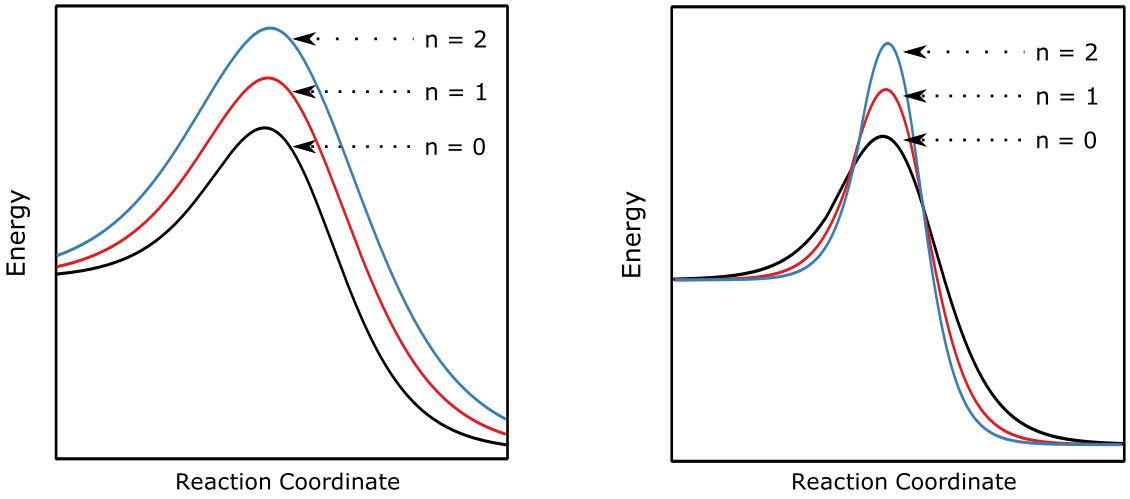
$$N(E_v) = \sum_{\{n\}'} P_{\{n\}'}(E_v). \tag{4.7}$$

This can thus be interpreted as a sum over one-dimensional barriers, with an effective barrier height and frequency given by Eqs. 4.2 and 4.4. The FD rate is given by a sum over one-dimensional rates constants:

$$k_{\text{FD}} = \sum_{\{n\}'} k_{\text{1D}}(V^{\text{eff}}_{\{n\}'}, \omega^{\text{eff}}_{\{n\}'}) \tag{4.8}$$

where Eq. 4.8 is equally applicable to thermal and microcanonical rate constants.

The interpretation of the sum over vibrational configurations of the TS, therefore, is that of a sum over one-dimensional reaction trajectories with barrier height and reaction mode frequency given by Eqs. 4.2 and 4.4. As a mode's quantum number, n_i, increases, the effective barrier height increases. If $x_{iF} > 0$,



(a) Harmonic case. **(b)** Significant coupling.

Figure 4.2 Illustrative barriers for different bound mode quantum numbers.

the corresponding effective frequency will also increase, representing a narrower barrier. These distinct barriers may therefore be interpreted as corner-cutting paths, as illustrated in Fig. 4.2, where barriers for a harmonic system are compared to a strongly anharmonic system. This picture mirrors previous work, in which reactions can be approximated as proceeding via vibrational adiabats[211]. In the harmonic case, $x_{iF} = 0$, multiple paths are still summed over, and each subsequent barrier is higher than the last, but no barrier narrowing is seen. Note that in the harmonic case, the sum-over-barriers can be performed analytically as the harmonic vibrational partition function of the TS.

It is interesting to ask whether these distinct pathways can be located on a given potential energy surface, in order to give insight about how the reaction proceeds. This is not, in general, possible, since VPT2 is not exact for a multidimensional PES. The only simple potential for which VPT2 is exact is uncoupled harmonic oscillators or Morse functions. For coupled potentials, these paths do not exist on the 'real' PES, but rather on a 'pseudo-surface' for which VPT2 is exact, and whose third and semi-diagonal fourth order derivatives match those of the 'real' surface. The VPT2 treatment generates the parameters for these paths, but (unfortunately) no spatial information.

4.2.2 Determining corner-cutting effects in real reactions

We have shown that the FD-SCTST rate constant can be written as a sum of one-dimensional rate constants, each with an adjusted effective barrier and frequency, corresponding to different pathways over the potential energy surface. These higher order paths are similar in nature to the straight line 'Large Curvature Tunnelling' trajectories of Truhlar and coworkers. As noted by Truhlar *et al.*, for some reactions these significantly corner-cutting paths are not required, and a small-curvature approximation can be used instead.

In this section we show that within SCTST, it is possible to make a similar small curvature tunnelling (SCT) approximation, in which only tunnelling through the lowest energy path is explicitly considered (and the other paths contribute through only their partition function). This assumes that tunnelling is dominant though the lowest order pathway, and that extreme corner-cutting trajectories are not significant. By comparing this to the FD-SCTST rate, we can deduce the impact of these extreme paths on any particular reaction.

We begin with the exact expression for the FD-SCTST rate as a sum of rates of through 1D barriers from Eq. 4.8. It is possible to show, using the SCTST-θ formalism introduced by Hernandez and Miller[198], that each 1D rate can be written as the product of a classical (TST) rate, and a tunnelling correction factor, κ, which depends on the height and width of the barrier. This is shown explicitly in Appendix C. This gives:

$$k_{\mathrm{FD}} = \sum_{\{n\}'} \kappa(V^{\mathrm{eff}}_{\{n\}'}, \omega^{\mathrm{eff}}_{\{n\}'}) k^{\mathrm{TST}}(V^{\mathrm{eff}}_{\{n\}'}). \tag{4.9}$$

Using the Eyring equation for the TST rate,

$$\begin{aligned} k_{\mathrm{FD}} &= \sum_{\{n\}'} \kappa(V^{\mathrm{eff}}_{\{n\}'}, \omega^{\mathrm{eff}}_{\{n\}'}) \frac{kT}{hQ^{\mathrm{R}}} \exp\left(\frac{-V^{\mathrm{eff}}_{\{n\}'}}{kT}\right) \\ &= \sum_{\{n\}'} \kappa(V^{\mathrm{eff}}_{\{n\}'}, \omega^{\mathrm{eff}}_{\{n\}'}) \frac{kT}{hQ^{\mathrm{R}}} \exp\left(\frac{-(V^{\mathrm{eff}}_{\{n\}'} - V^{\mathrm{eff}}_{0})}{kT}\right) \exp\left(\frac{-V^{\mathrm{eff}}_{0}}{kT}\right) \end{aligned} \tag{4.10}$$

We now make the approximation that each barrier contributes to the SCTST rate in the *same proportion* as it contributes to the total TST rate. This is equivalent to saying $\kappa(V^{\mathrm{eff}}_{\{n\}'}, \omega^{\mathrm{eff}}_{\{n\}'}) = \kappa(V^{\mathrm{eff}}_0, \omega^{\mathrm{eff}}_0)$ and is the same for all barriers. Since corner-cutting paths will have larger values of κ than the lowest energy path, we expect that reactions where corner-cutting is significant to be underestimated by this approximation. The small curvature SCTST rate, $k^{\mathrm{SCT}}_{\mathrm{FD}}$, is then given by:

$$\begin{aligned} k^{\mathrm{SCT}}_{\mathrm{FD}} &= \sum_{\{n\}'} \kappa(V^{\mathrm{eff}}_0, \omega^{\mathrm{eff}}_0) \frac{kT}{hQ^{\mathrm{R}}} \exp\left(\frac{-(V^{\mathrm{eff}}_{\{n\}'} - V^{\mathrm{eff}}_0)}{kT}\right) \exp\left(\frac{-V^{\mathrm{eff}}_0}{kT}\right) \\ &= \left[\sum_{\{n\}'} \exp\left(\frac{-(V^{\mathrm{eff}}_{\{n\}'} - V^{\mathrm{eff}}_0)}{kT}\right)\right] \kappa(V^{\mathrm{eff}}_0, \omega^{\mathrm{eff}}_0) k^{\mathrm{TST}}_0(V^{\mathrm{eff}}_0, \omega^{\mathrm{eff}}_0) \\ &= Q^{\mathrm{TS}}_{\mathrm{vib}} \kappa(V^{\mathrm{eff}}_0, \omega^{\mathrm{eff}}_0) k^{\mathrm{TST}}_0(V^{\mathrm{eff}}_0, \omega^{\mathrm{eff}}_0) \end{aligned} \tag{4.11}$$

Therefore the SCT rate can be written as:

$$k^{\mathrm{SCT}}_{\mathrm{FD}} = Q^{\mathrm{TS}}_{\mathrm{vib}} k_{1\mathrm{D}}(V^{\mathrm{eff}}_0, \omega^{\mathrm{eff}}_0). \tag{4.12}$$

The result is an approximate expression for the FD-SCTST rate, written in the form of a 1D-SCTST rate multiplied by a vibrational partition function. This approximation is analogous to the commonly used 'J-shifting' approximation[212–215] in which the $J = 0$ rotational energy level is assumed to dominate the dynamics.

Note that the small-curvature rate has the same computational expense as FD-SCTST, but can be used to elucidate the importance of corner-cutting, once a full dimensional SCTST calculation has been performed. A comparison of the SCTST rate to the small-curvature rate and the one-dimensional rate will indicate the significance of small-curvature and large-curvature corner-cutting effects in a reaction. This is applied in Chapter 5 to two atmospheric reactions.

Note that the small-curvature approximation to SCTST, combined with a harmonic vibrational mode approximation, gives an approximate form of SCTST that only requires anharmonic constants of the form x_{iF}. This could be a potentially

efficient route to rates for reactions with only small reaction path curvature. This idea is explored in detail in Chapter 8.

4.3 Variational effects

It is well known that the saddle point of the electronic energy of a molecule may not correspond exactly to the saddle point of free energy of that species. This is caused by the generalised frequencies of vibrational modes perpendicular to the reaction path changing along the reaction trajectory. As a result, classical trajectories moving on the vibrationally adiabatic PES may pass through the transition state dividing surface, but recross at a later time, and thus not contribute to the rate - as such the TST rate is overestimated. By optimising the location of the dividing surface, the 'generalised' transition state can be found, which minimises the TST rate, and thus minimises the effect of recrossings. A reaction's 'variational effect' is the ratio of the rate as calculated through the electronic and generalised transition state dividing surfaces. Work using VTST has identified generalised transition states for a range of reactions which may lie up to 1 a_0 away from the classical TS [48, 199, 216–221] and variational effects of over two orders of magnitude have been reported[48].

In this section we investigate how well SCTST accounts for variational and other adiabatic effects. Here we take adiabatic effects to mean the difference between moving on the reaction path over the PES, and moving on the vibrationally adiabatic potential. This can cause barrier broadening/narrowing effects as well as variational effects, in which the generalised transition state is displaced along the path from the saddle point of the PES, and is higher in free energy than at the classical saddle point. The method's ability to capture these and other adiabatic effects has not been discussed explicitly in the literature. Here we show how these effects are accounted for accurately in the adiabatic limit (*i.e.* in the limit that motion along the reaction coordinate is slow compared to other degrees of freedom). We then discuss the applicability of these approximations to a range of real reactions, whose variational effects have been previously studied in detail

using VTST.

4.3.1 A model two-dimensional potential

We can investigate explicitly how SCTST accounts for adiabatic effects by using a two-dimensional model potential for the transition state region. In VPT2-SCTST, terms beyond quartic order are not accounted for, so we limit our model potential to a quartic function of the reaction coordinates. We start with an anharmonic barrier with a harmonic spectator mode, and no coupling between them, as shown in Fig. 4.3a. Its two-dimensional potential function is given by:

$$V_0(Q_F, Q_0) = \frac{1}{2}\omega_F^2 Q_F^2 + \frac{1}{2}\omega_0^2 Q_0^2 + \frac{1}{6}f_{FFF}Q_F^3 + \frac{1}{24}f_{FFFF}Q_F^4. \tag{4.13}$$

The minimum energy path is a straight line along $Q_0 = 0$. The generalised ZPE along the path can be defined from the frequency of the motion perpendicular to the reaction path. The ground-state vibrationally adiabatic potential energy can then be constructed from the sum of the MEP energy, and the ZPE. The energy profiles of the MEP and the adiabatic potential are shown in Fig. 4.3b. Here, the adiabatic potential has the same shape as the MEP, and the barrier height is modulated by the ZPE at the TS.

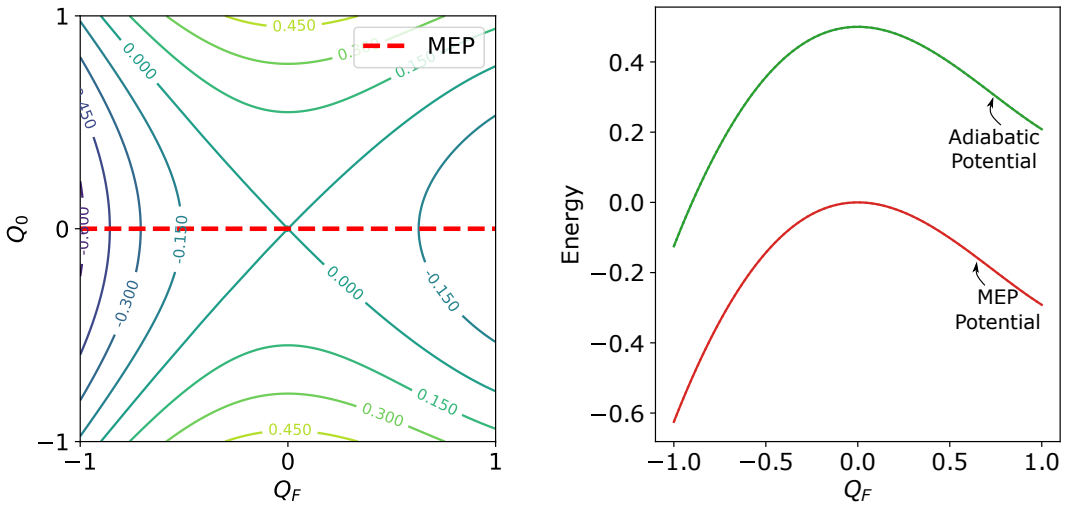
The VPT2 parameters for this surface are:

$$\begin{aligned} x_{0F} &= 0, \\ x_{00} &= 0, \\ x_{FF} &= \frac{1}{16\omega_F^2}\left(f_{FFFF} - \frac{5}{3}f_{FFF}\right). \end{aligned} \tag{4.14}$$

The SCTST effective barrier height and imaginary frequency of the ground state trajectory are given by Eqs. 4.2 and 4.4:

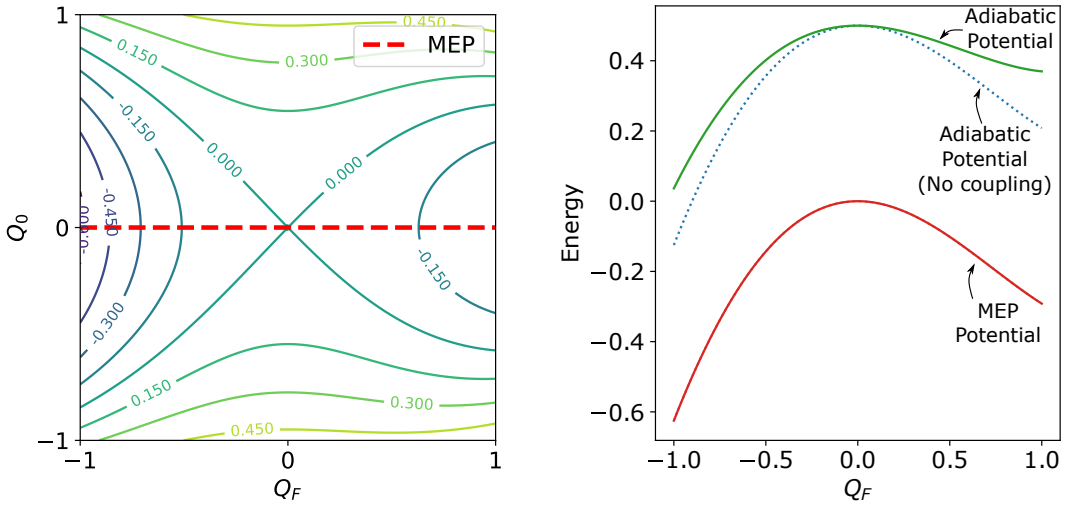
$$\begin{aligned} \omega^{\mathrm{SCTST}} &= \omega_F \\ V^{\mathrm{SCTST}} &= \frac{1}{2}\omega_0 \end{aligned} \tag{4.15}$$

which, of course, are correct descriptions of the adiabatic barrier in Fig. 4.3b. We will now add coupling terms to produce adiabatic effects, and compare the SCTST



(a) Potential energy surface **(b)** Potential barriers.

Figure 4.3 An uncoupled potential, Eq. 4.13. The potential is given by Eq. 4.13 with $\omega_F^2 = -\omega_0^2 = -1$, $f_{FFF} = f_{FFFF} = 1$.



(a) Potential energy surface. **(b)** Potential barriers.

Figure 4.4 The squeezed potential, Eq. 4.16. Quartic coupling modulates the width of the adiabatic barrier. Here $f_{00FF} = 1.5$.

barriers to the 'true' adiabatic barriers.

A 'squeezed' potential

By adding a quartic coupling term, f_{FF00}, the width of the adiabatic barrier can be adjusted. The 'squeezed' potential is given by:

$$V(Q_F, Q_0) = V_0(Q_F, Q_0) + \frac{1}{4} f_{FF00} Q_F^2 Q_0^2 \tag{4.16}$$

and is shown in Fig. 4.4. Within an SCTST treatment of this system, only the x_{0F} term is changed:

$$x_{0F} = \frac{f_{FF00}}{4\omega_0 \omega_F}. \tag{4.17}$$

The effect on the SCTST rate is thus to modulate the effective frequency of the lowest energy path:

$$\begin{aligned} \omega^{\text{SCTST}} &= \omega_F + \frac{1}{2} x_{0F} \\ &= \omega_F + \frac{f_{FF00}}{8\omega_0 \omega_F} \end{aligned} \tag{4.18}$$

The effective barrier height remains unchanged from the uncoupled case. We can also calculate explicitly the imaginary frequency of the adiabatic potential. The generalised ZPE along the MEP is given by:

$$V^{ZPE}(Q_F) = \frac{1}{2} \sqrt{\frac{\partial^2 V}{\partial Q_0^2}|_{Q_0=0}}. \tag{4.19}$$

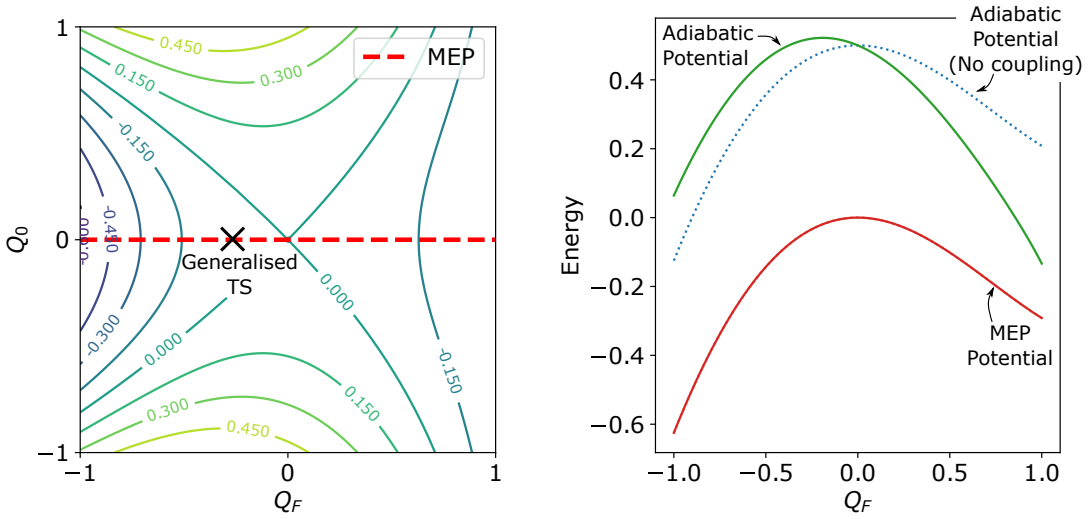
The effective potential along the adiabat, $V^\circ(Q_F)$, is given by:

$$\begin{aligned} V^\circ(Q_F) &= V(Q_F, 0) + V^{ZPE}(Q_F) \\ &= \frac{1}{2}\omega_F^2 Q_F^2 + \frac{1}{6} f_{FFF} Q_F^3 + \frac{1}{24} f_{FFFF} Q_F^4 + \frac{1}{2}\sqrt{\omega_0^2 + \frac{1}{2} f_{FF00} Q_F^2}. \end{aligned} \tag{4.20}$$

The imaginary frequency of the adiabat, ω°, is therefore given by:

$$\begin{aligned} (\omega^\circ)^2 &= \frac{\partial^2 V^\circ}{\partial Q_F^2}|_{Q_F=0} \\ &= \omega_F^2 + \frac{f_{FF00}}{4\omega_0} \\ \omega^\circ &\approx \omega_F + \frac{f_{FF00}}{8\omega_0 \omega_F} \qquad \left(\frac{f_{FF00}}{\omega_0 \omega_F^2} << 1\right) \\ &= \omega^{\text{SCTST}} \end{aligned} \tag{4.21}$$

For the squeezed potential, Eq. 4.16, the barrier frequencies therefore agree when the perturbation is sufficiently small.



(a) Potential Energy Surface. **(b)** Potential Barriers.

Figure 4.5 A variational surface, Eq. 4.22, with $f_{00F} = -0.9$.

A variational potential

We now consider a surface with a generalised TS that is not located at the classical saddle point, causing a variational effect. This can be introduced into the model potential with a cubic coupling term:

$$V(Q_F, Q_0) = V_0(Q_F, Q_0) + \frac{1}{2} f_{00F} Q_F Q_0^2 \tag{4.22}$$

This PES is plotted in Fig. 4.5, where it is clear the generalised TS is displaced from the saddle point of the PES, and the effective barrier height and width are changed from the uncoupled case.

The VPT2 parameters are now given by:

$$\begin{aligned} x_{00} &= -\frac{f_{00F}^2}{16\omega_0^2\omega_F^2}\frac{8\omega_0^2 - 3\omega_F^2}{4\omega_0^2 - \omega_F^2}, \\ x_{0F} &= -\frac{f_{00F} f_{FFF}}{4\omega_0\omega_F^3} + \frac{f_{00F}^2}{2\omega_F\omega_0(4\omega_0^2 - \omega_F^2)}, \\ G_0 &= \frac{3}{64}\frac{f_{00F}^2}{(4\omega_0^2 - \omega_F^2)\omega_0^2}. \end{aligned} \tag{4.23}$$

The ground state SCTST barrier height and effective imaginary frequency are

thus given by:

$$\begin{aligned} V^{\mathrm{SCTST}} &= \frac{\omega_0}{2} + \frac{1}{4}x_{00} + G_0 \\ &= \frac{\omega_0}{2} - \frac{f_{00F}^2}{32\omega_0^2\omega_F^2}\left(\frac{4\omega_0^2 - 3\omega_F^2}{4\omega_0^2 - \omega_F^2}\right) \end{aligned} \tag{4.24}$$

$$\begin{aligned} \omega^{\mathrm{SCTST}} &= \omega_F + \frac{1}{2}x_{0F} \\ &= \omega_F - \frac{f_{00F}f_{FFF}}{8\omega_0\omega_F^3} + \frac{f_{00F}^2}{4\omega_F\omega_0(4\omega_0^2 - \omega_F^2)} \end{aligned} \tag{4.25}$$

We can now explicitly find the correct barrier and imaginary frequency on the adiabatic potential. The adiabatic potential is now:

$$\begin{aligned} V^{\circ}(Q_F) &= V_2(Q_F, 0) + V^{ZPE}(Q_F) \\ &= \frac{1}{2}\omega_F^2 Q_F^2 + \frac{1}{6}f_{FFF}Q_F^3 + \frac{1}{24}f_{FFFF}Q_F^4 + \frac{1}{2}\sqrt{\omega_0^2 + f_{00F}Q_F}. \end{aligned} \tag{4.26}$$

The generalised TS can then be found from the stationary point on this path, and, since the perturbation is small, with the assumption that the generalised TS is close to the classical TS:

$$Q_{TS} = -\frac{f_{00F}}{4\omega_F^2\omega_0}. \tag{4.27}$$

We can now find the imaginary frequency at this point:

$$\begin{aligned} (\omega^{\circ})^2 &= \frac{\partial^2 V^{\circ}}{\partial Q_F^2}|_{Q_F = Q_{TS}} \\ &\approx \omega_F^2\left(1 - \frac{f_{FFF}f_{00F}}{4\omega_F^4\omega_0} - \frac{f_{00F}^2}{8\omega_0^3\omega_F^2}\right) \\ \omega^{\circ} &\approx \omega_F\left(1 - \frac{f_{FFF}f_{00F}}{8\omega_F^4\omega_0} - \frac{f_{00F}^2}{16\omega_0^3\omega_F^2}\right) \\ &\approx \omega^{\mathrm{SCTST}} \qquad (\text{Eq. 4.25, for } \omega_0 >> |\omega_F|) \end{aligned} \tag{4.28}$$

Thus SCTST correctly reproduces the barrier width in the adiabatic limit. Similarly, for the barrier height:

$$\begin{aligned} V^{\circ}(Q_{TS}) &\approx \frac{\omega_0}{2} - \frac{f_{00F}^2}{32\omega_0^2\omega_F^2} \\ &\approx V^{\mathrm{SCTST}} \qquad (\text{Eq. 4.24, for } \omega_0 >> |\omega_F|) \end{aligned} \tag{4.29}$$

This is the correct SCTST barrier height given in equation from Eq. 4.24, in the adiabatic limit. The SCTST barrier therefore accurately accounts for variational effects, as long as the perturbation is sufficiently small, in the adiabatic limit. Note that this implies that adiabatic effects caused by coupling to low frequency modes will be treated least accurately, as expected, since the assumption of quantisation along these modes is poor.

4.3.2 Variational effects in real reactions

We have discussed above how well SCTST reproduces adiabatic effects on a quartic surface. We will now investigate to what extent SCTST will handle these effects *in practice*, by studying the profiles of generalised normal mode frequencies along reaction paths of real reactions. SCTST cannot be accurate if the quartic expansion of the PES is insufficient to describe these changes in frequency between the classical and generalised transition states.

For a quartic PES, generalised frequencies of modes perpendicular to the reaction mode are treated up to quadratic order along the reaction path. For example, for a MEP with no curvature, the generalised frequency of the i^{th} normal mode is approximately:

$$\begin{aligned} \omega_i^2(s) &= \frac{\partial^2 V(\mathbf{Q})}{\partial Q_i^2}|_{Q_i=0} \\ &= \left(\omega_i^{s=0}\right)^2 + f_{iiF}s + \frac{1}{2}f_{iiFF}s^2 \\ \omega_i(s) &\approx \omega_i^{s=0} + \frac{f_{iiF}}{2\omega_i^{s=0}}s + \frac{f_{iiFF}}{4\omega_i^{s=0}}s^2 \end{aligned} \tag{4.30}$$

where $\omega_i^{s=0}$ is the frequency at the classical transition state. If the generalised TS lies close enough to the classical TS such that the frequency profiles are approximately quadratic, it is likely these variational effects are well treated.

In practice, variational effects in hydrogen transfer reactions are often the result of a single, rapidly changing generalised frequency across the reaction path, called the 'reactive mode', which is strongly coupled to the reaction mode. This effect is particually strong for heavy-light-heavy reactions, as illustrated in Fig. 4.6.

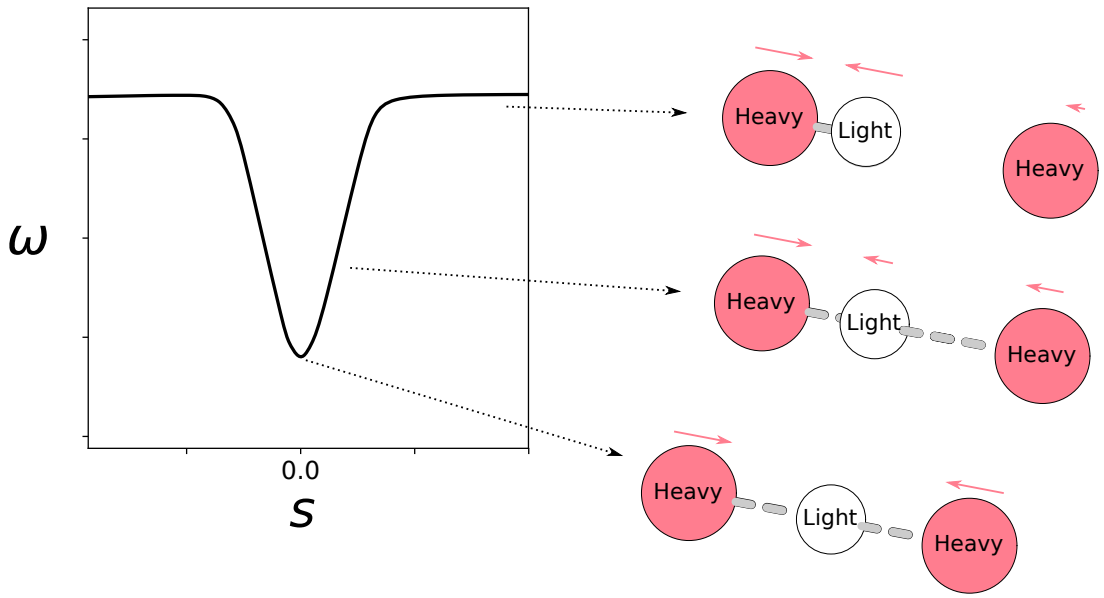


Figure 4.6 Heavy-light-heavy (HLH) reactions have large variational effects. The 'reactive mode' corresponds to a heavy-light vibration in the reactant/product region, but a heavy-heavy vibration in the saddle point region. As a result of the differing reduced masses, this causes a large increase in frequency away from the classical TS.

These reactions have a small skew angle at the transition state, and a low frequency bound reactive mode, corresponding to the motion of the two heavy outer groups. As the system moves away from the TS, this frequency increases rapidly as the bonds form. The result is an increase in the adiabatic barrier away from the TS.

In the subsequent sections, we investigate reactions with modest, strong and extreme variational effects.

Simple Hydrogen Abstraction reactions

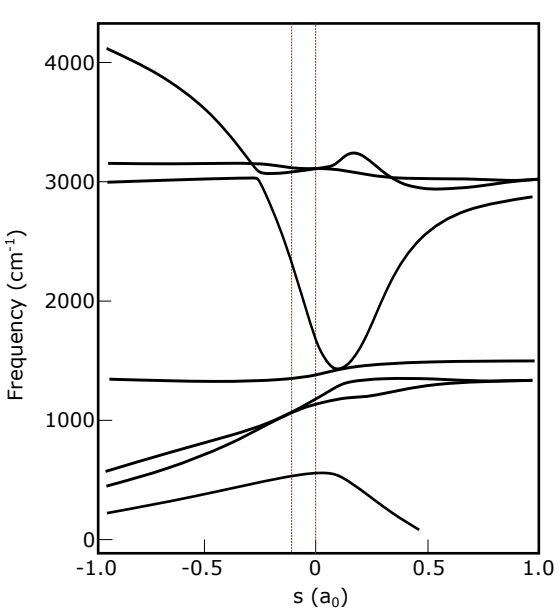
An example of a reaction with modest variational effects is the abstraction reaction:

$$CH_3 + H_2 \rightarrow CH_4 + H, \tag{R4}$$

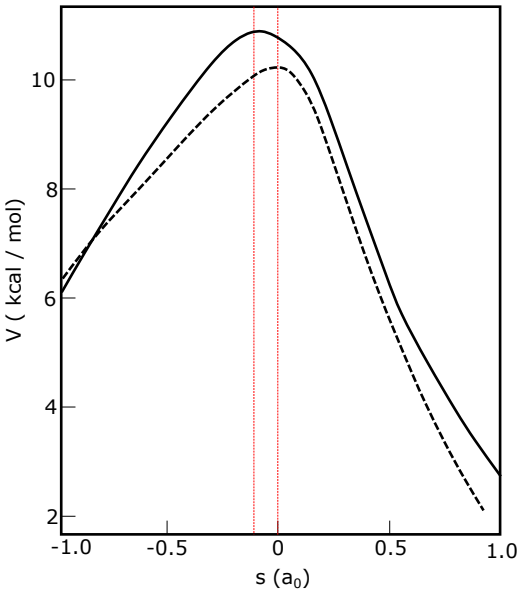
which was studied in detail using VTST by Truhlar and coworkers[216, 222].

Using a semi-empirical PES, fitted to *ab initio* electronic structure data and experimental thermochemical quantities, they calculated the generalised normal modes and their frequencies along the minimum energy path. These are repro-

duced in Fig. 4.7a. The resultant adiabatic potential is compared to the MEP in Fig. 4.7b. Very similar profiles are found across four different potential energy surfaces in their study, and in other studies [216, 223]. Here, the generalised transition state was shifted about 0.1 a_0 from the classical TS, due to the increase in frequency of the reactive mode.



(a) Generalised vibrational frequencies.



(b) MEP (dashed) and adiabatic (solid) barriers.

Figure 4.7 MEP analysis adapted from ref.[222], studying the $H_2 + CH_3$ potential energy surface. Vertical lines correspond to classical and generalised transition state coordinates, at $s = 0$ and $s = -0.11$, respectively.

The frequency profile seen here is typical of many hydrogen abstraction reactions[219, 220, 224, 225]. Modes only weakly involved in the reaction have a near constant frequency across the path. 'Transitional' modes (which correspond to relative translations and rotations in the reactants and products, and low frequency bends in the transition state), can be seen to increase then decrease in frequency across the path. The normal mode most involved in the reaction, the 'reactive' mode, is clearly identifiable, as it drops in frequency rapidly near the saddle point. It is an accurate treatment of this reactive mode which is critical.

In this case, it is clear that the reactive mode is sufficiently 'well-behaved' in the transition state region. It changes smoothly and slowly across the path, and

the generalised TS lies within a region well described by a quadratic fit. This is consistent with the excellent performance of SCTST in application to this and similar reactions[90, 91, 225].

A heavy-light-heavy reaction

Studying the generalised normal mode frequencies for heavy-light-heavy reactions can help deduce the applicability of SCTST to these reactions. The HLH reactions:

$$CH_4 + O \rightarrow CH_3 + OH \tag{R5}$$

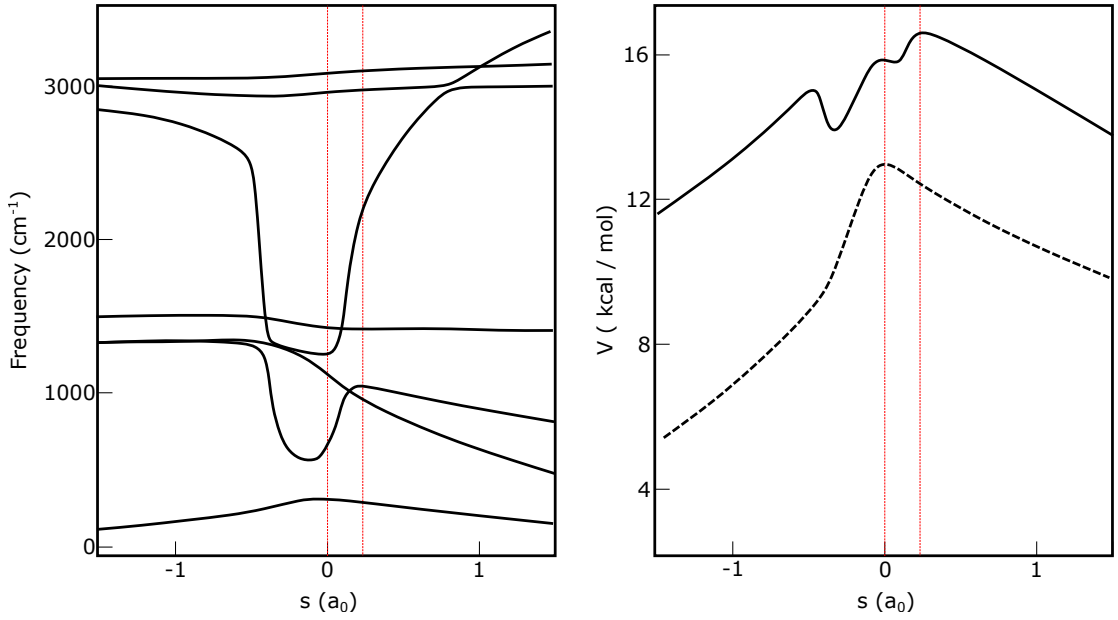
and

$$CH_4 + OH \rightarrow CH_3 + H_2O \tag{R6}$$

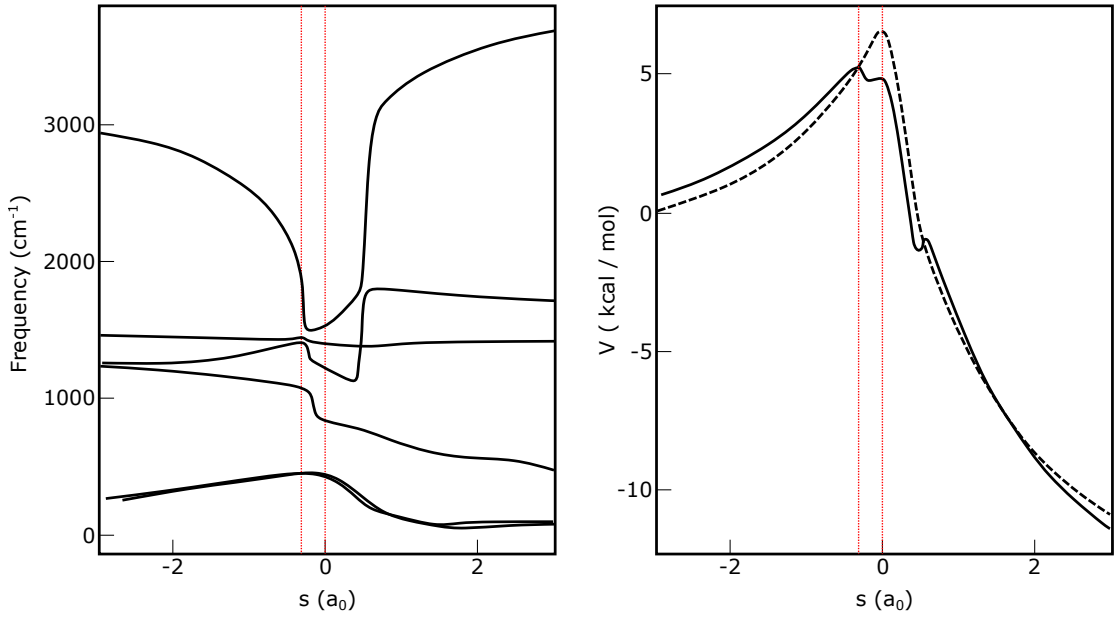
have been studied in detail using VTST by Espinosa-Garcia and co-workers[219, 220] using an analytical potential calibrated with experimental quantities such as barrier heights, and vibrational frequencies and geometries at stationary points. They found variational effects of about a factor of seven for reaction R5 at 200 K.

Fig. 4.8 shows their determined generalised normal mode frequencies along the MEPs, and their ground-state vibrationally adiabatic potential energy curves. The reactive modes are clearly visible from the steep drop in the vicinity of the TS. In contrast to reaction R4, both reactions show sudden changes in the frequency of the reactive mode. These sharp features, make these effects unlikely to be accurately treated by SCTST. Note that even higher order (e.g. VPT4) treatments[88] are unlikely to give a better result, due to the dramatic profile of the reactive mode making any Taylor expansion method poor.

The methods used to determine the PES, however, were based on simple analytical potentials. As such, it is unclear to what extent these effects are artefacts of the PES, and more detailed studies would be useful to determine how realistic and common these features are.

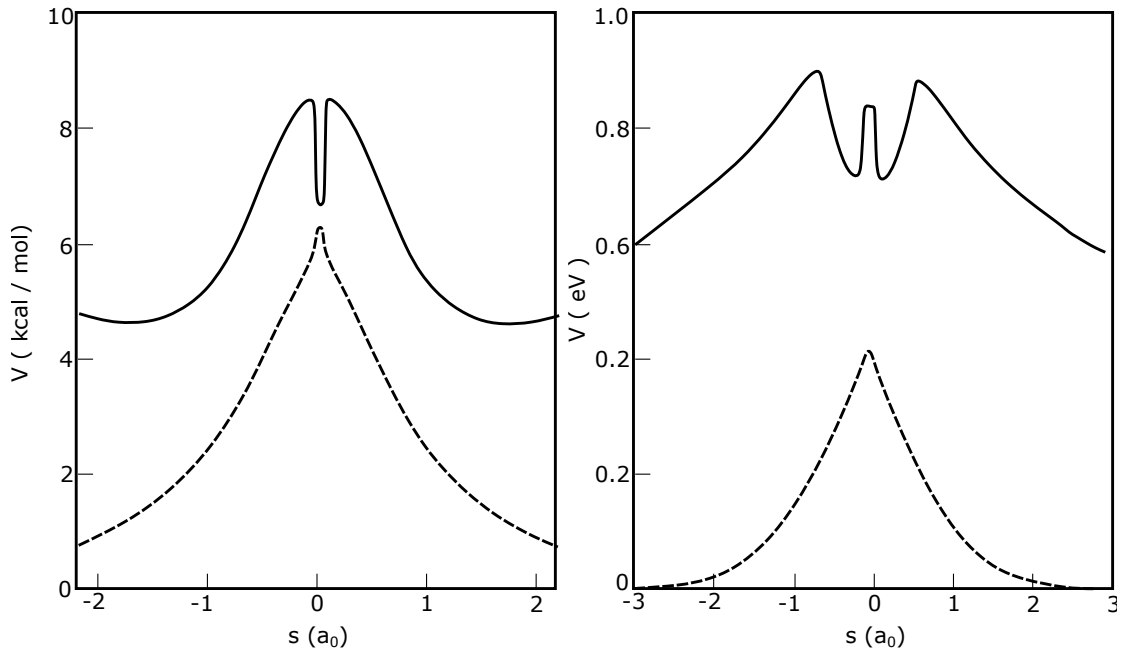


(a) Generalised frequencies (reaction R5) . **(b)** Barriers (reaction R5).



(c) Generalised frequencies (reaction R6) . **(d)** Barriers (reaction R6) .

Figure 4.8 Generalised frequency profiles and barriers for two heavy-light-heavy reactions, adapted from refs. [220] and [219]. MEPs are shown as dashed lines, and adiabats with solid lines. Vertical lines correspond to classical and generalised transition state coordinates.



(a) Reaction R7. **(b)** Reaction R8.

Figure 4.9 MEP (dashed line) and adiabatic (solid line) barriers for two reactions with extreme variational effects, adapted from refs. [48] and [226].

Extreme variational effects

Some reactions have qualitatively different adiabatic potentials to those studied above. Garrett *et al.* studied in detail the colinear reaction[48] :

$$^{37}\mathrm{Cl} + \mathrm{H}^{35}\mathrm{Cl} \rightarrow {}^{37}\mathrm{ClH} + {}^{35}\mathrm{Cl} \qquad \text{(R7)}$$

which represents the extreme limit of commonly studied heavy-light-heavy reactions. They observed a variational effect of a factor of 110 at 200 K (this factor reduces to 21 for the deuterium substituted reaction). The energy profile is reproduced in Fig. 4.9a. Note that the generalised TS is less than 0.1 a_0 away from the classical TS in this case, however the frequency of the reactive mode changes from 337 cm^{-1}at the classical TS to 1682 cm^{-1}at the generalised TS. The adiabatic potential has two maxima.

A similarly extreme profile is seen for the reaction:

$$D + H\mu \rightarrow D\mu + H \qquad \text{(R8)}$$

	$[\mathrm{H-H-H}]^{\ddagger}$	$[\mathrm{D}-\mu-\mathrm{H}]^{\ddagger}$
ω_F / $i\mathrm{cm}^{-1}$	1968	4877
x_{FF} / cm^{-1}	-217	+172

Table 4.1 SCTST parameters for reaction R8 and its isotopologue at the MP2/cc-pVTZ level of theory.

where μ is a muonium atom, made up of an antimuon and an electron, with total mass 0.114 u. This was studied by Pérez De Tudela *et al.* using a range of rate theories[226]. The adiabatic potential, based on the H_3 BKMP2 potential energy surface by Boothroyd *et al.*[227] is reproduced in Fig. 4.9b. Due to the lightness of the transferring atom, the PES has an extreme skew angle, thus this reaction was described as a *stress test* for rate theories by the authors. This adiabat, similarly, is qualitatively different to that which is approximated by SCTST, and the generalised TS lies more than 0.7 a_0 from the classical TS.

It is obvious that perturbation theory will not give an accurate variational treatment for either of these two surfaces. SCTST parameters for reaction R8 are shown in Table 4.1, along with the parameters for the isotopologue reaction $\mathrm{H}+\mathrm{H}_2 \rightarrow \mathrm{H}_2+\mathrm{H}$. For reaction R8, x_{FF} is calculated to be *positive*; this leads to qualitatively incorrect behaviour, for example $\theta(E)$ becomes complex for high energies, as the effective tunnelling barrier is inverted. Thus in this case SCTST is not just inaccurate but unusable.

Whilst the quantitative accuracy of the features in Fig. 4.9 are unclear, the features seen here are qualitatively and significantly beyond what SCTST can accurately describe. It is thus clear SCTST cannot handle these effects in extreme heavy-light-heavy reactions.

4.4 Conclusions

In this chapter we have investigated how SCTST accounts for two key multidimensional effects: corner cutting and variational effects, which are accounted for explicitly in other semiclassical rate theories. We showed that both these effects are accounted for implicitly by the method. We showed how the impact of corner

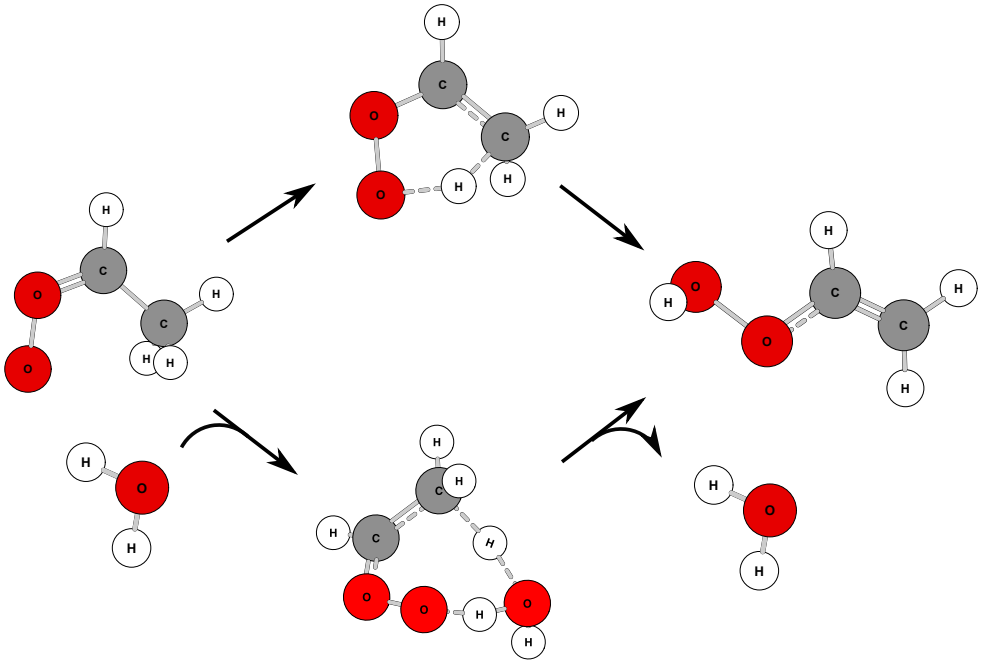
cutting paths can be elucidated using a small-curvature approximation to SCTST.

We showed variational effects are accounted for, in the adiabatic limit, as long as the perturbations are sufficiently small, and that the quartic expansion of the surface is sufficient to describe the key characteristics of the reaction. An investigation of reaction frequency profiles from other studies suggests the local effect assumption is valid for reactions with modest variational effects, but is unlikely to be accurate for extreme cases, or reactions with unusual PES features.

Chapter 5

The decay of Criegee intermediates in the atmosphere

We now use the SCTST method to perform calculations on complex chemical systems. The unimolecular decay of Criegee intermediates is the major producer of OH radicals in the atmosphere. In this chapter, SCTST in full and one dimension is used to determine rate constants for their unimolecular decay, as well as their decay catalysed by a single water molecule, and thus predict the relative significance of these pathways in the atmosphere.



Abstract 5 Criegee intermediates can decay either unimolecularly, or with water as a catalyst.

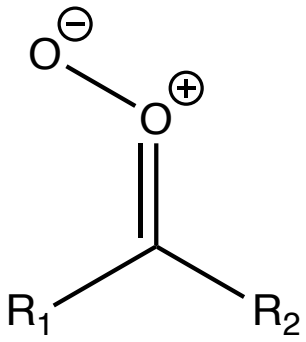
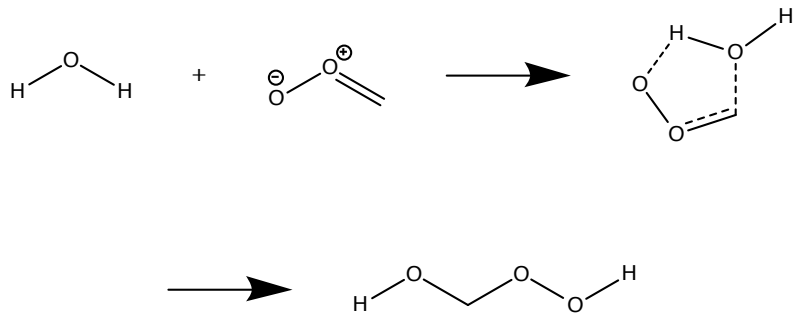


Figure 5.1 Representation of a Criegee intermediate.

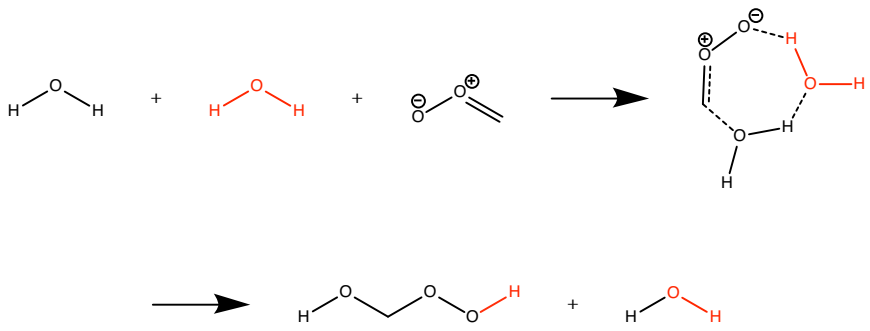
5.1 Introduction

Criegee intermediates (CIs), whose general structure is shown in Fig. 5.1, are formed by the ozonolysis of alkenes in the atmosphere and are intermediates in a number of critical atmospheric reaction pathways[228, 229]. The branching between these various reaction paths is key in determining the overall effects of CIs on the atmosphere; for example it is thought the majority of atmospheric OH radical production is a result of CI decomposition[230]. As a result, the reactivity of these species has been the subject of extensive experimental and theoretical studies in recent years[175, 231–239].

After the CIs are formed, they can react bimolecularly with other atmospheric molecules, the 'Criegee scavengers', (H_2O[236, 240–242], NO_2[240, 243], SO_2[240, 243, 244]) or with another CI[245, 246]. One scavenger of particular interest is atmospheric water. Water has been shown to be capable of catalysing several gas-phase reactions[247–251] and various reactions of CIs have also been found to be catalysed by atmospheric water[234, 252, 253]. The reaction of CIs with water as a scavenger (an example of which is shown in Fig. 5.2) has been shown to have a quadratic rate dependence on the concentration of water, suggesting two water molecules are involved in the reaction[236, 237, 241, 254]. This has been backed up by theoretical studies[253, 255–258] which have shown the extra molecule completely removes the reaction barrier. This is likely the major atmospheric sink of H_2COO[241].



(a) Reaction with a single water molecule.



(b) Reaction with two water molecules (Catalytic).

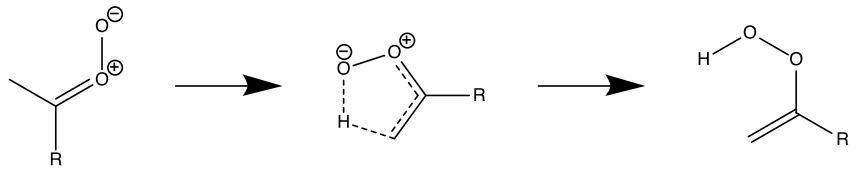
Figure 5.2 'Scavenger' reaction of a CI with water.

CIs are also susceptible to unimolecular decay, either via three membered ring transition states[259] or, if there is a syn-alkyl hydrogen, via a 1,4 hydrogen transfer reaction, as studied experimentally and theoretically by Fang *et al.*[260] and shown in Fig. 5.3a:

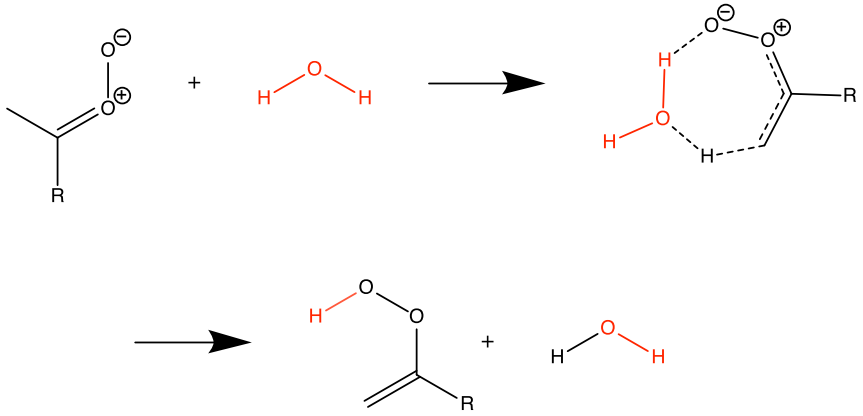
$$CH_3CROO \rightarrow CH_2CROOH \tag{R9}$$

Here R = H (the 'unmethylated' reaction) or R = Me (the 'methylated' reaction). As *anti*- CIs are not susceptible to this decay pathway, they are not considered further in this work. This reaction has the potential to be catalysed by water, as shown in Fig. 5.3b:

$$CH_3CHOO + H_2O \rightarrow CH_2CHOOH + H_2O \tag{R10}$$



(a) 1,4 hydrogen transfer reaction (R9).



(b) One Water (Catalytic) (R10) - Same reaction as in (a), but with a single water molecule in the transition state, shown in red .

Figure 5.3 Unimolecular decay pathways of the Criegee intermediate.

These catalysed reactions have also been studied theoretically by Anglada *et al.* [255] and Long *et al.* [261] using Variational Transition State Theory with tunnelling corrections.

The unimolecular decay of CIs provide interesting challenges to rate constant calculations. The reactant molecule contains an internal rotational degree of freedom (the reactive methyl group) that becomes constrained in the TS. Methods to treat such degrees of freedom are discussed in Chapter 3. In addition, in the large cyclic TS of the water catalysed reaction, several low frequency, and hence large amplitude, vibrational modes exist. A normal harmonic treatment to their vibrational partition functions may be inaccurate. Since these modes only appear in the transition state (i.e. they are not present in the reactant state), the effect of these modes on the reaction may be significant. Finally, the catalysed reaction involves the transfer of two hydrogen atoms, rather than one, a form of reaction on which SCTST has not previously been tested.

In this chapter, 1D and FD-SCTST results are compared to experiment in order to evaluate the accuracy of SCTST and the importance of treating anharmonicity in these reactions. In addition, we also assess treating anharmonicity at various levels of electronic structure theory. The findings suggest a procedure for applying SCTST to complex reactions with reasonable computational expense.

This chapter is organised as follows: Section 5.2 describes the computational details used in the calculations, and section 5.3 details the results and key findings of this work. Section 5.4 also presents microcanonical rate constants and compares them to recent experimental results. Section 5.6 discusses the key conclusions of this chapter.

5.2 Computational methods

5.2.1 *ab initio* Calculations

Molecular geometries and harmonic frequencies were optimised at the MP2/aug-cc-pVTZ[169] level of theory in Gaussian 09[147] using the *tight* convergence criteria. Single point energies at these geometries were then calculated at the CCSD(T) level of theory, with the same basis set.

For the FD calculations, the *freq=anharmonic* keyword was used, at the same level of theory, to determine the **x** matrix, as described in detail by Barone[141]. The use of Density Functional Theory (DFT) to determine the anharmonic **x** matrix was also tested, using the B3LYP functional[262] with the aug-cc-pVTZ basis set, and a geometry optimised at this level of theory.

Previous studies[263, 264]have suggested single-reference electronic structure calculations are sufficient to accurately reproduce the experimentally measured geometry of Criegee intermediates, and so no multi-reference methods were used in this study.

For the 1D calculation, x_{FF} was determined from 9 MP2 single point energies along the reaction coordinate, in the vicinity of the transition state, and using second order Richardson extrapolation as described by Greene *et al.*[92]. A step size of $\Delta Q = 0.05$ $\mathrm{Da}^{0.5}$ a_0 was used.

For the water catalysed reaction, which has two, nearly degenerate transition states, only one transition state, was analysed with full dimensional VPT2 at MP2 level, due to the large cost of this calculation. For the 1D rate, the contribution from each TS was nearly identical, so it was assumed the FD contribution from each TS was approximately equal, and the total rate can be calculated as twice the rate through one transition state.

5.2.2 Treatment of hindered rotational degrees of freedom

Internal rotational degrees of freedom present a challenge for rate theories and are discussed in detail in Chapter 3.

The methylated reactant and transition states include three dihedral angles, shown in Fig. 5.4, which can, in principle, be treated as internal rotors. The first - (a) - is a rotation about the central C-O bond, with significant double bond character - this has a very high barrier to rotation (120 kJ / mol [228]), and so can be accurately considered as a harmonic vibrator rather than a rotor. The second - (b) - is the rotation of the reactive methyl group. Since this rotation is constrained in the transition state, its treatment is expected to be critical. The third - (c) - is the non-reactive methyl group in the methylated CI species. For rotors (b) and (c), rates using the harmonic oscillator approximation were compared to those using the 'tanh' approximation discussed in Chapter 3, to evaluate the importance of anharmonicity in these modes.

5.3 Results and discussion

5.3.1 Triplet state species

Since CIs are a biradical species, it may be important to consider the contribution of the electronic triplet state to the dynamics. The geometry was optimised for the triplet state configuration, and its energy was found to be 182 kJ/mol larger than the singlet state. As shown in Fig. 5.5, this means less than 0.1 % of the reactant molecule are in the exited state even at 2000 K, and so this state can be safely

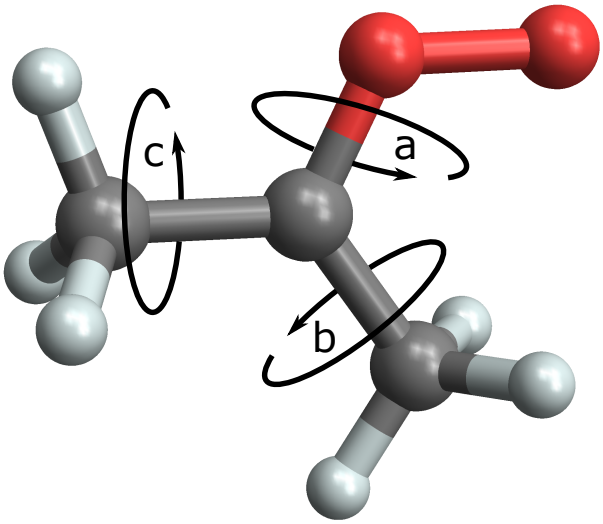


Figure 5.4 The three internal rotational degrees of freedom in the methylated Criegee species.

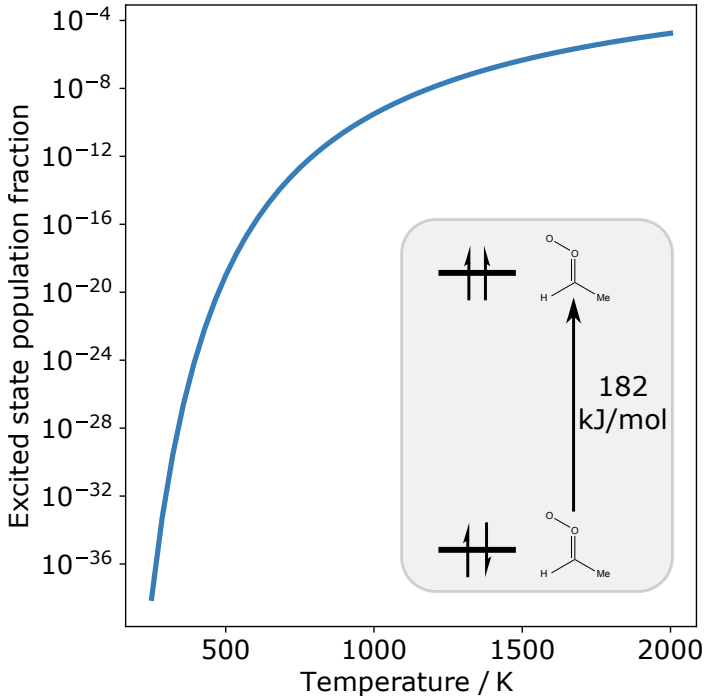


Figure 5.5 The triplet state need not be considered for these calculations.

neglected in our calculations.

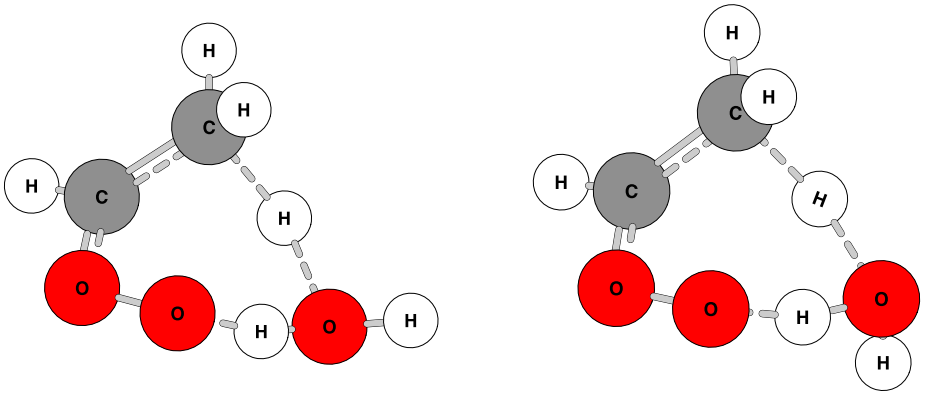


Figure 5.6 Two transition state structures of the water catalysed reaction.

5.3.2 Stationary point analysis

Two nearly degenerate transition state structures were found for the water catalysed reaction, corresponding to the external water hydrogens pointing 'up' or 'down' in the seven-membered ring, as shown in Fig. 5.6. The total reaction rate can be found as the sum of the rates through each of these transition states. All the transition states identified are chiral, and so correspond to two degenerate reaction pathways passing through each. Harmonic frequencies at the stationary points are listed in Table 5.1 and values of x_{FF} and G_0 are compared in full and one dimension in Table 5.2. The barrier height for the uncatalysed, unmethylated reaction lies within 1 kcal/mol of other recent studies[265–267], and is changed by less than 1% when a complete basis set extrapolation is applied[170], using double, triple and quadruple-zeta basis sets.

5.3.3 Hindered rotor

The unmethylated reaction has a single hindered rotor degree of freedom in the reactant state, corresponding to rotation of the reactive methyl group. 1D-SCTST rates were calculated using harmonic and 'tanh' treatments of this mode. Surprisingly, the difference between the harmonic model, and a hindered rotor treatment is very small, differing at most by 10% at the highest temperatures studied in this work, and by less than 0.1% at 298 K. This is owing to the relatively high frequency of the rotation mode (224 cm^{-1}) a result of the interaction

Reactant, R = H								
3253	3207	3102	3048	1515	1474	1457	1398	1296
1131	1031	996	940	745	699	481	304	224
Reactant, R =Me								
3202	3192	3142	3116	3069	3055	1560	1498	1489
1476	1454	1417	1398	1325	1094	1069	991	947
931	830	624	490	352	318	290	209	170
Transition State, R =H								
1523 i								
3252	3237	3117	1875	1558	1505	1360	1282	1224
1037	1010	970	858	771	746	533	518	
Transition State, R =Me								
1501 i								
3240	3188	3161	3119	3078	1891	1566	1530	1491
1480	1417	1377	1352	1093	1057	1006	990	955
872	758	674	549	515	358	290	136	
Transition State + H_2O, R =H								
1587 i								
3831	3271	3195	3142	1745	1650	1632	1573	1448
1368	1325	1264	1203	1037	1022	932	886	766
677	654	598	508	434	415	312	192	

Table 5.1 Harmonic frequencies calculated at the MP2/aug-cc-pVTZ level for key stationary point (cm^{-1}). Imaginary frequencies are in bold.

TS	$\omega_{reaction}$	x_{FF}(1D)	G_0 (1D)	x_{FF}(FD)	G_0 (FD)
Uncatalysed					
R=H	1523	-95.67	-19.49	-82.30	-24.86
R=Me	1501	-100.8	-20.80	-90.64	-15.53
Water Catalysed					
R=H	1587	-193.1	-34.01	-115.0	-13.12

Table 5.2 Transition State data. All values in cm^{-1}.

between the methyl group and the oxygen atoms, hindering rotation at all but the highest temperatures.

In the methylated reaction, treating the external methyl group - rotor (c) in Fig. 5.4 - also has a negligible effect. Here the effect is small because the differences in partition functions largely cancel out between the reactant and transition state. The rates differ by less than 2% at 298 K.

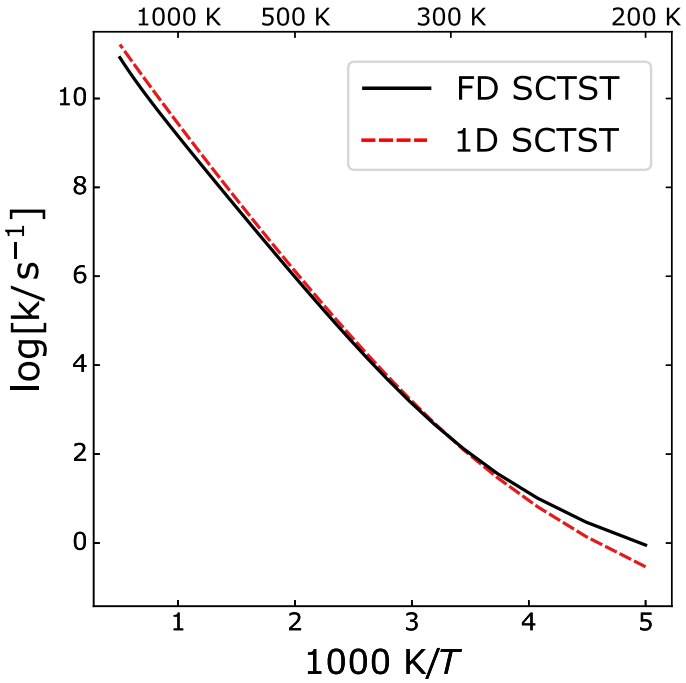


Figure 5.7 Unimolecular Criegee intermediate decay rates in full and one dimension, for the unmethylated reaction.

5.3.4 Effect of mode-mode couplings

The effect of mode-mode couplings can be assessed by comparing 1D- and FD-SCTST rates, as the 1D method neglects anharmonicity in all but the reactive mode. The thermal rate constants are compared in Fig. 5.7 for the unmethylated reaction, as well as in Fig. 5.8 for the methylated reaction. It can be seen that for both reactions, 1D-SCTST slightly underestimates tunnelling at temperatures below 300 K, but gives very accurate rate constants in the range 300-2000 K. At 298 K, the 1D and FD results differ by just 38% and 15% for the methylated and unmethylated reactions respectively.

The FD rates are also in good agreement with other work, and our result at 298 K lies within the range of values calculated by other theoretical studies[265–268].

For a large system, the calculation of the anharmonic constant matrix, $\mathbf{x}$, is the most expensive part of the FD-SCTST calculation, but in general the calculated rate has a weaker dependence on these values than the energy barrier (here calculated

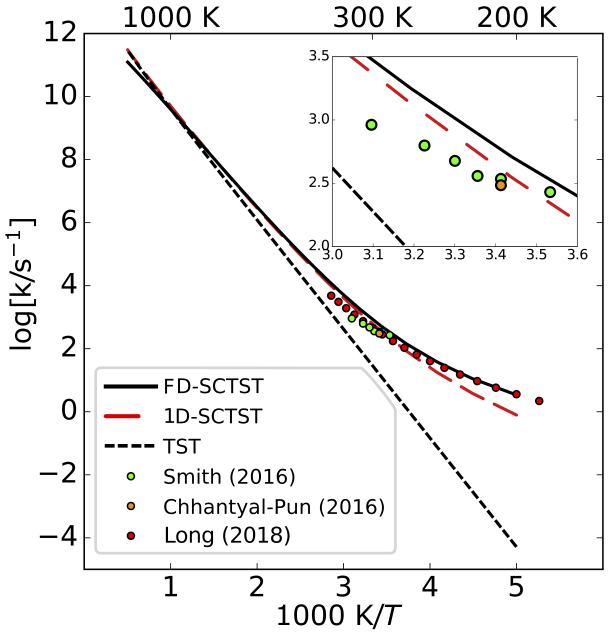


Figure 5.8 Unimolecular rate constants for the methylated, uncatalysed decomposition reaction. Comparison of experimental measurements (Chhantyal-Pun[269] and Smith[270]) and other theoretical results (Long [261]) with TST and SCTST in full and one dimensions (this work). The inset shows more clearly the comparison of this work to experiment.

at CCSD(T) level of theory) and the harmonic frequencies (here calculated at MP2 level of theory). We investigated using cheaper methods of electronic structure theory to calculate the **x** matrix. Fig. 5.9 shows a comparison of MP2 and DFT methods to calculate the **x** matrix. The DFT calculation, despite taking less than one tenth of the computer time, gives excellent agreement with MP2, even at low temperatures where the 1D rate was less accurate. At 298 K, the DFT method underestimated the rate by just 15%. This suggests DFT could be reliable in calculating the **x** matrix for other SCTST calculations.

5.3.5 Comparison to Experiment

Chhantyal-Pun *et al.* [269] directly measured the rate of the thermal unimolecular decay of $(CH_3)_2COO$ at 293 K using cavity ring-down experiments. The same reaction was studied by Smith *et al.*[270] between 283 K and 303 K using time resolved UV absorption. Their measured rate constants are compared to SCTST

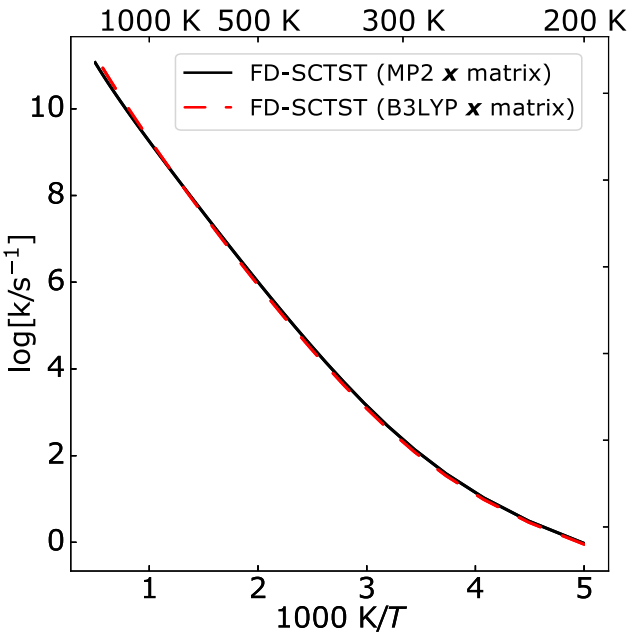


Figure 5.9 Two methods of calculating $\mathbf{x}$ matrix contributions to the VPT2 energy for the unmethylated, uncatalysed reaction reaction.

in full and one dimension in Fig. 5.8. Also presented are the VTST with small curvature tunnelling corrections results of Long *et al.*[261]. It is clear that 1D- and FD-SCTST give good agreement both with one another and with the available experimental data, especially for these relatively cheap calculations. A contributor to the discrepancy between these theoretical and experimental results is the assumption of fast collisional relaxation of the Criegee species, upon formation. In reality, these species may be formed in a vibrationally excited state, and react before they are fully thermalised. Quantum tunnelling dominates the rate at low temperatures, as seen by the difference between the TST and SCTST results. The 1D approximation here performs accurately, despite a dramatic cost reduction compared to FD-SCTST. SCTST can also be seen to perform well compared to VTST[261] at low temperatures, where deep tunnelling is significant.

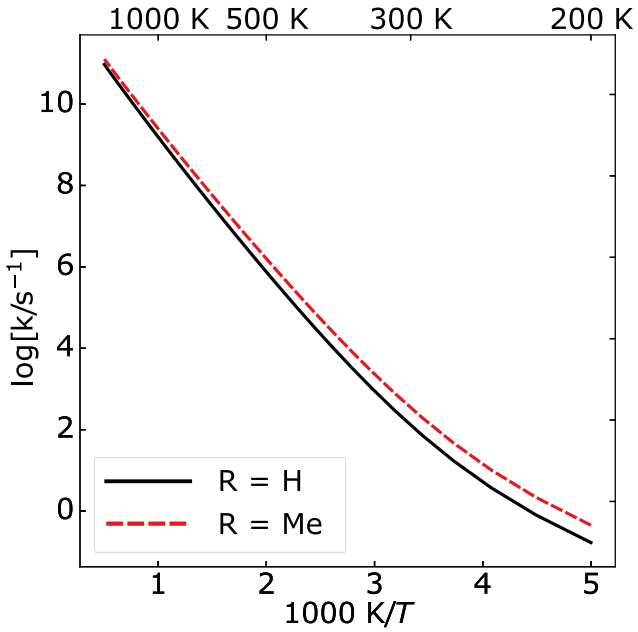


Figure 5.10 Effects of methylation on the rate of unimolecular decay on the uncatalysed reaction, calculated using 1D-SCTST.

5.3.6 Effect of substituent groups

By comparing the rates of the methylated and unmethylated reactions, the effects of changing the spectator *R* group on the reaction can be established. These are compared in Fig. 5.10. The addition of the methyl group slightly increases the rate of reaction. This effect can be attributed to two factors - first, the lowering of the reaction barrier with the methyl group, from 68 kJ/mol to 65 kJ/mol, and second, the harmonic frequency of the methyl group rotor is lower in the transition state than the reactant state, increasing the entropy of the transition state, reducing the entropic barrier. When the transition state forms, the ring formation pulls adjacent groups away from the methyl group, reducing steric interactions, and lowering the species relative energy, as well as the rotor frequency. The presence of the methyl group effectively catalyses the reaction.

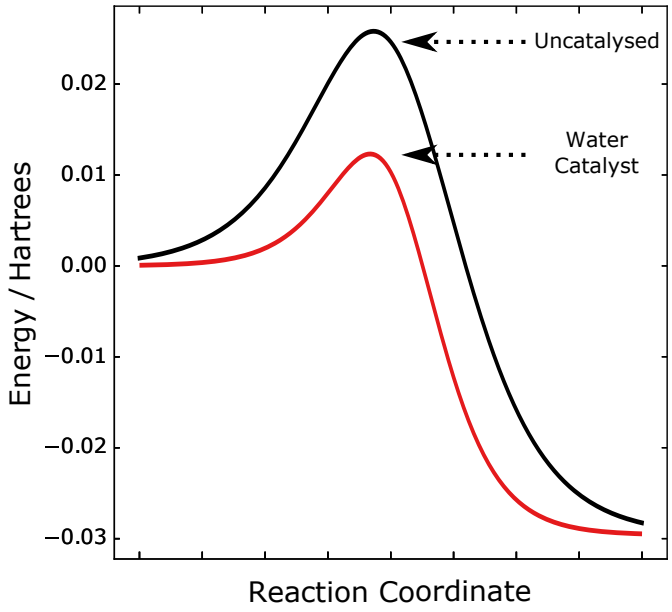


Figure 5.11 1D-SCTST effective barrier shapes for the uncatalysed and catalysed unmethylated reactions. Since the two transition states in the catalysed reaction are nearly degenerate, only one barrier is shown.

5.3.7 Water catalysis

The addition of a water molecule to the transition state can be seen to dramatically reduce the energy barrier to reaction from 68 kJ/mol to 33 kJ/mol, as well as reducing the width of the barrier, as shown in Fig. 5.11. Since the imaginary frequencies of the transition states are very similar, the change in width of the barrier can be attributed to the large change in the anharmonic constant, x_{FF}.

The rates calculated by 1D-SCTST and FD-SCTST calculations are shown in Fig. 5.12. In contrast to the uncatalysed reaction, 1D-SCTST fails to accurately predict the rate at low temperatures, particularly lower than 350 K. At 298 K, 1D-SCTST underestimates the rate by about a factor of three. Using DFT to calculate the **x** matrix dramatically reduces the computational cost (by about a factor of ten in this example), yet gives a very good estimate of the rate over the whole temperature range.

The origin of the large discrepancy between the 1D and FD methods for the water catalysed reaction can be attributed to three possible causes:

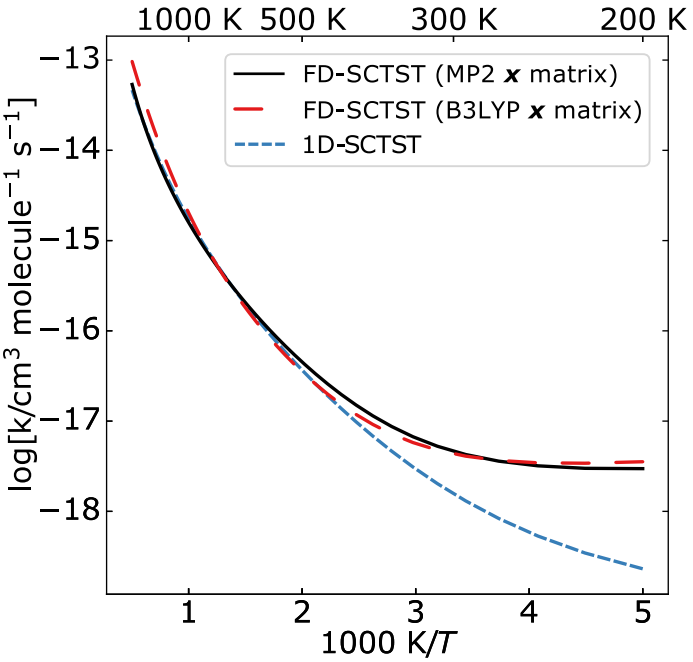


Figure 5.12 Comparison of 1D-SCTST and FD-SCTST for the unmethylated catalysed reaction.

1. The coupling between the non-reactive modes (x_{ij} with $i, j \neq F$) is non-negligible.

2. The coupling between the reactive and non-reactive modes (x_{iF} with $i \neq F$) is non-negligible.

3. The 1D estimate of x_{FF} is poor.

The first of these manifests itself in the difference in the harmonic and anharmonic vibrational partition functions of the reactant and transition state. The partition functions were found to be very similar over the whole temperature range, such that this cannot be the major source of the difference. This is shown in Fig. 5.13. It is interesting that the harmonic treatment performs so well for the transition state, given the presence of several low frequency ring bending modes.

The significance of the remaining two sources of error can be determined by performing a 1D-SCTST calculation using the FD value of x_{FF}. Here we call this the '1D+' method, and is further investigated in Chapter 7. The results are shown in Fig. 5.14. Clearly, the 1D+ method recovers a large amount of the

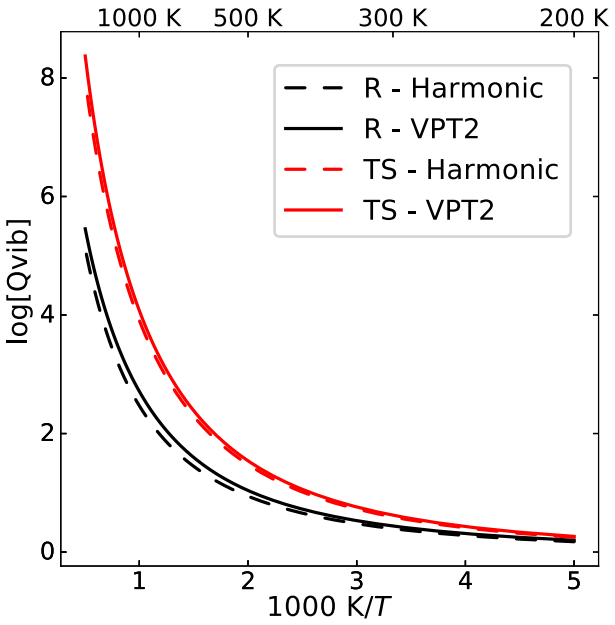


Figure 5.13 Comparison of Harmonic and VPT2 vibrational partition functions for the unmethylated reactant and transition state with a water molecule.

difference, of which the remainder can be attributed to coupling between the non-reactive modes and the reactive mode.

The reason for the discrepancy between FD and 1D values of x_{FF} can be investigated. For the 1D calculation, derivatives of the form f_{FFi}, with $i \neq F$, are neglected. Fig. 5.15 shows the values of these derivatives for both the catalysed and uncatalysed transition states, as well as their values as calculated using DFT. From inspecting Fig. 5.15, it is clear that for the uncatalysed transition state, only one non-reactive mode couples strongly to the reaction mode through the third order derivative. This mode corresponds to the movement of the reactive hydrogen perpendicular to the reaction direction, out of the plane of the ring. In contrast, for the catalysed reaction, many modes couple strongly to the reactive mode, all of which correspond to the in-ring hydrogen atoms moving out of the plane.

Finally, the error due to neglecting x_{iF} is investigated. In Fig. 5.16, we show the values of x_{iF} calculated at MP2 and B3LYP level of theories for both the catalysed and uncatalysed transition states. Once again, for the uncatalysed species, only

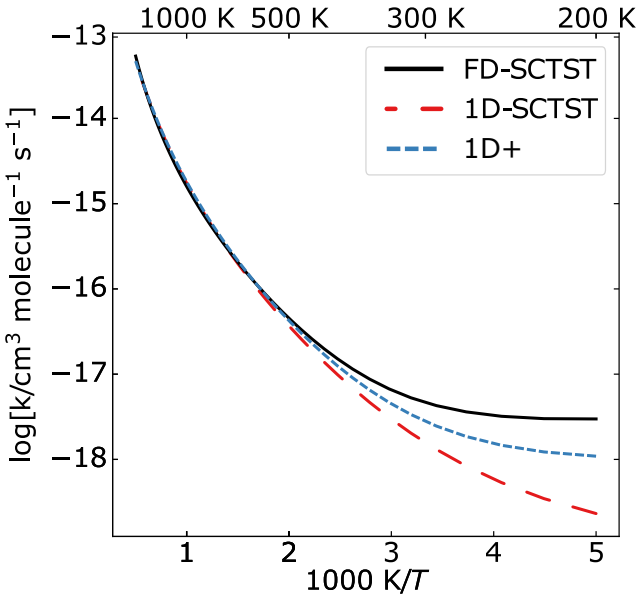


Figure 5.14 Comparison of FD-SCTST, 1D-SCTST and the 1D+ method for the unmethylated, catalysed reaction.

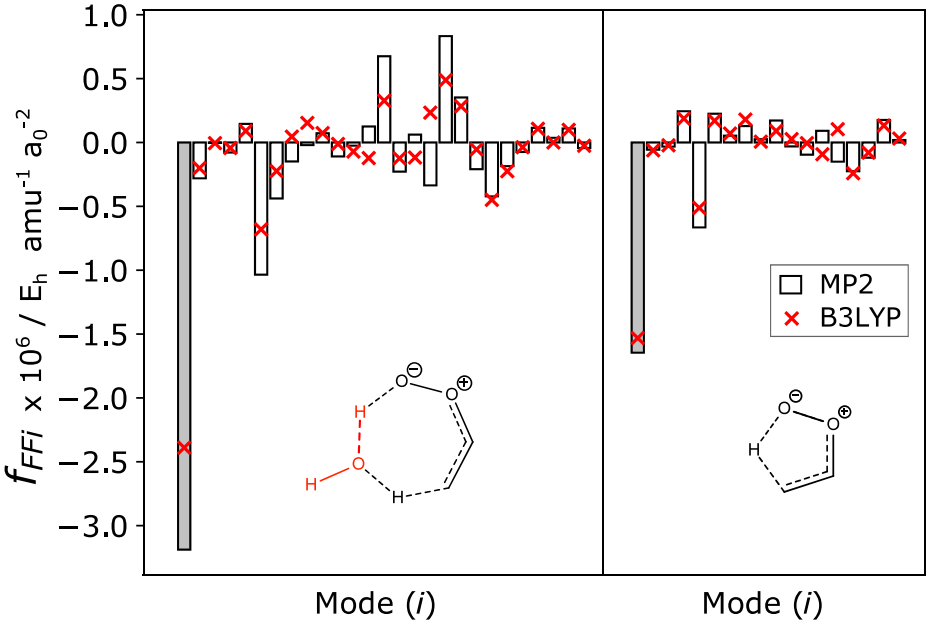


Figure 5.15 Comparison of derivatives contributing to the calculation of x_{FF}. Modes are in order of descending frequency, and the pure reaction mode derivative (f_{FFF}) is highlighted in grey.

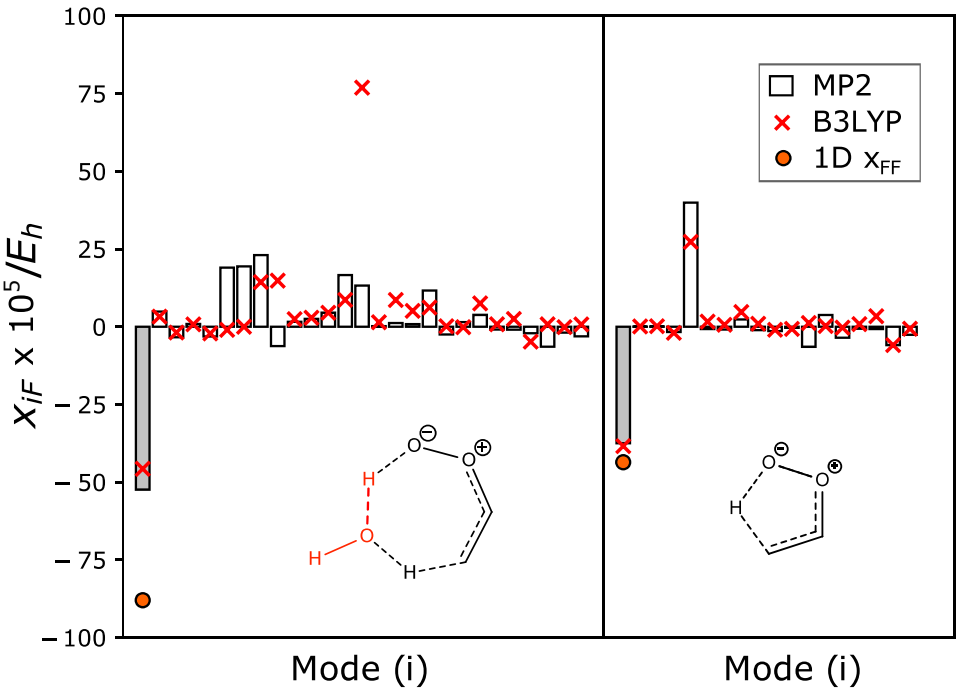


Figure 5.16 Comparison of values of x_{iF} for the catalysed and uncatalysed reaction. The reaction mode anharmonic constant (x_{FF}) is highlighted in grey, and the 1D value of x_{FF} is shown as a circle.

one x_{iF} has a significantly large value. It corresponds to the same spectator mode as we found in Fig. 5.15. On the other hand, several spectator modes are found to be strongly coupled to the reaction mode in the catalysed transition state.

Vibrational locality

One possible way of understanding these differences between the catalysed and uncatalysed reactions is by comparing the 'locality' of the reactive modes. The catalysed reaction has two atoms contributing significantly to the reaction mode, whereas the uncatalysed reaction has just one. This allows more of the non-reactive degrees of freedom to interact strongly with the reaction mode, increasing the likelihood of coupling to many modes. This suggests a simple criteria for predicting the success of 1D-SCTST; if the reaction mode is simple, and highly localised, higher order couplings are likely to be smaller, and so 1D approaches are valid. For complex, delocalised reaction modes, this may not be the case.

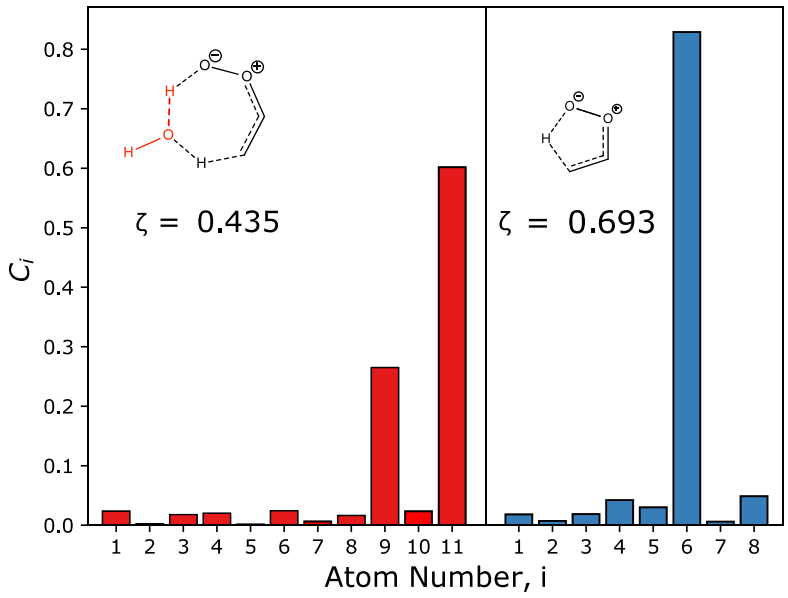


Figure 5.17 Locality of the two reactive modes. The atoms with large C_i correspond to the hydrogen atoms being transferred.

The locality of a mode, $\mathbf{Q}$, can be defined as[271]:

$$\zeta(\mathbf{Q}) = \sum_i (C_i)^2 \tag{5.1}$$

where C_i corresponds to the contribution of nucleus i to the normal mode $\mathbf{Q}$:

$$C_i = \sum_{\alpha=x,y,z} (Q_{i\alpha})^2 . \tag{5.2}$$

C_i also corresponds to the fraction of the kinetic energy of atom i in the normal mode. Thus ζ is large for modes in which only one atom contributes significantly, and low for modes in which many atoms are moving together. Its maximal value is one, when only a single atom has a contribution.

Fig. 5.17 shows the values of C_i for both reaction modes, as well as the overall value of ζ. It is clear that the catalysed reaction has a significantly less localised reactive mode, as a result of two hydrogens being transferred, rather than one.

The relation between the localisation of a vibrational mode, and its coupling to other modes has been explored in the context of optimising coordinate systems for anharmonic vibrational spectra[271–273]. It has been shown that using a

coordinate system that maximises the locality of the modes speeds up the convergence of the n-mode expansion of the energy *i.e.* localised modes have weaker inter-mode couplings at third and fourth order. This relation between locality and inter-mode coupling may indicate that it is possible to predict how strongly the reactive mode couples to other modes (and thus if the 1D approximation is valid) by calculating the locality of this mode.

5.3.8 Improving 1D-SCTST

The significant improvement of 1D-SCTST when the FD value of x_{FF} is used, demonstrated in Fig. 5.14, motivates further developments of the '1D +' method. It is, in fact, possible to obtain all the required derivatives to calculate the FD value of x_{FF} with just two additional Hessian matrices displaced along the reaction mode:

$$f_{Fij} = \frac{H_{ij}(\delta Q_F) - H_{ij}(-\delta Q_F)}{2\delta Q_F} \tag{5.3}$$

and

$$f_{FFii} = \frac{H_{ii}(\delta Q_F) + H_{ii}(-\delta Q_F) - 2H_{ii}(0)}{\delta Q_F^2} \tag{5.4}$$

where $H_{ij}(\delta Q)$ is element (i,j) of the Hessian matrix calculated at a geometry displaced from the transition state by a distance δQ. The values of x_{FF} calculated in this way, for both the catalysed and uncatalysed transition states, are within 0.5% of the values calculated in the normal full-dimensional calculation. For the uncatalysed reaction, this method also brings the 1D results closer to the FD results. This idea is further explored in Chapter 7.

5.3.9 Catalysis in the atmosphere

We can use these calculations to make a prediction as to the impact of water catalysis on the decay of CIs in the atmosphere. The effective first order rate constant for the decomposition of the Criegee intermediate in the atmosphere can be written as:

$$k^{1^{\text{st}}}_{pseudo} = k^{1^{\text{st}}}_{\text{uncatalysed}} + k^{2^{\text{nd}}}_{\text{catalysed}} [\text{H}_2\text{O}]_{\text{atmosphere}} \tag{5.5}$$

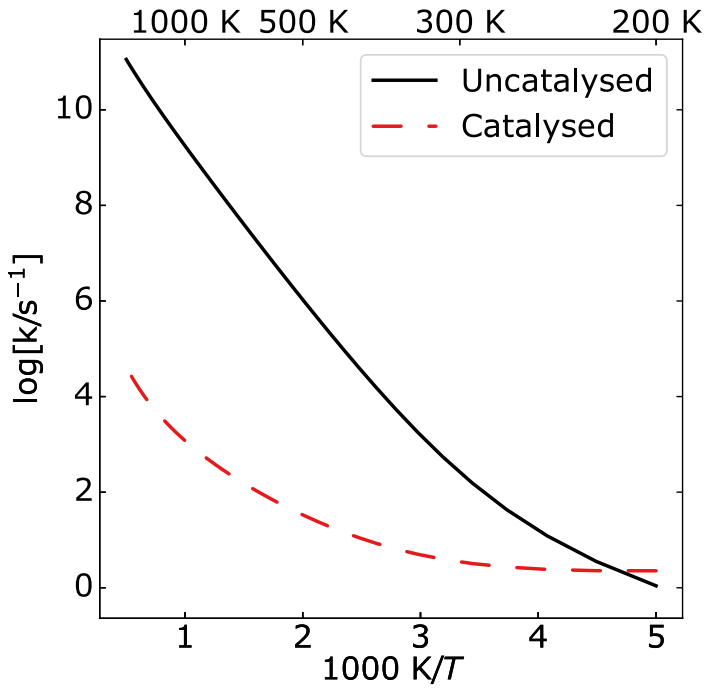


Figure 5.18 FD-SCTST rates comparing uncatalysed and catalysed unmethylated reaction at atmospheric water concentration.

where the first term corresponds to the uncatalysed contribution, and the second term corresponds to the catalysed contribution. Their respective contributions are shown in Fig. 5.18, where an atmospheric water concentration of 7.64×10^{17} cm^{-3} was used[274]. The unimolecular dissociations of CIs are generally understood to be important within the planetary boundary layer of the atmosphere, where temperatures are about 300 K[275]. The figure suggests that at atmospheric temperatures, the water catalysed reaction can have a significant contribution to the total rate, and so should not be ignored in models of these pathways.

5.4 Microcanonical rates

Experiments are also able to probe microcanonical rates, which are often more relevant in atmospheric chemistry where unstable species may react before being thermalised. It is also a more direct measure of tunnelling, since classically the microcanonical rate is zero for all energies below the barrier height, and a more direct way of evaluating the performance of SCTST, since there is no thermal

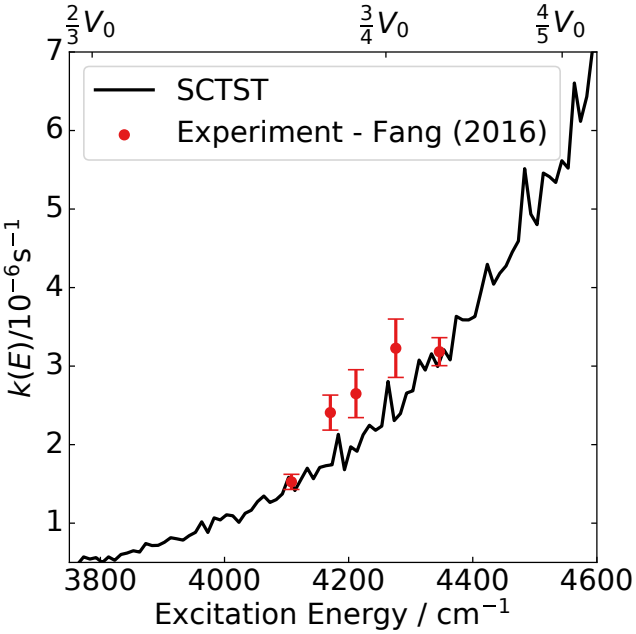


Figure 5.19 Microcanonical FD-SCTST rates for the unmethylated, uncatalysed reaction, in the tunnelling regime, compared with experimental results[268]. Here V_0 is the adiabatic barrier height.

averaging to disguise errors.

The results for the uncatalysed decay are shown in Fig. 5.19, where excellent agreement is seen. The roughness of the SCTST result is an artefact of the Wang-Landau density of states calculation, where a finite energy box size must be chosen. Here intervals of 11 cm^{-1} were used.

5.5 Corner-cutting paths

We can also investigate the significance of corner-cutting in these reactions, by comparing the effective barrier shapes in the 1D, 1D+ and FD treatments of the reactions, and by using the small curvature approximation to SCTST introduced in Chapter 4 to determine the impact of higher energy corner-cutting paths.

By plotting the effective VPT2-Morse tunnelling barriers, we can see explicitly the effect of corner-cutting on the ground state trajectory of the reactions. The effective barriers for reaction R10 are shown in Fig. 5.20. It is clear that the FD

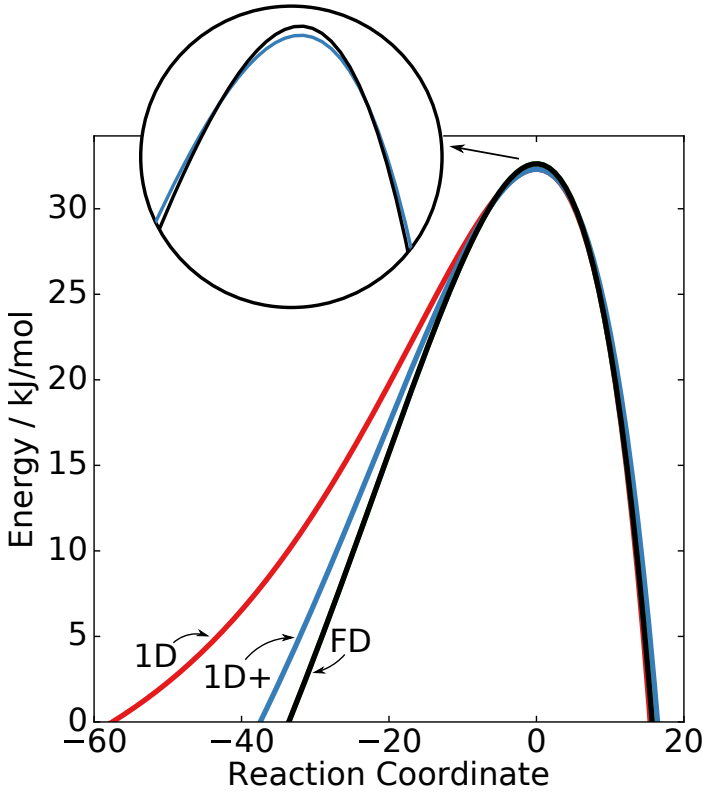
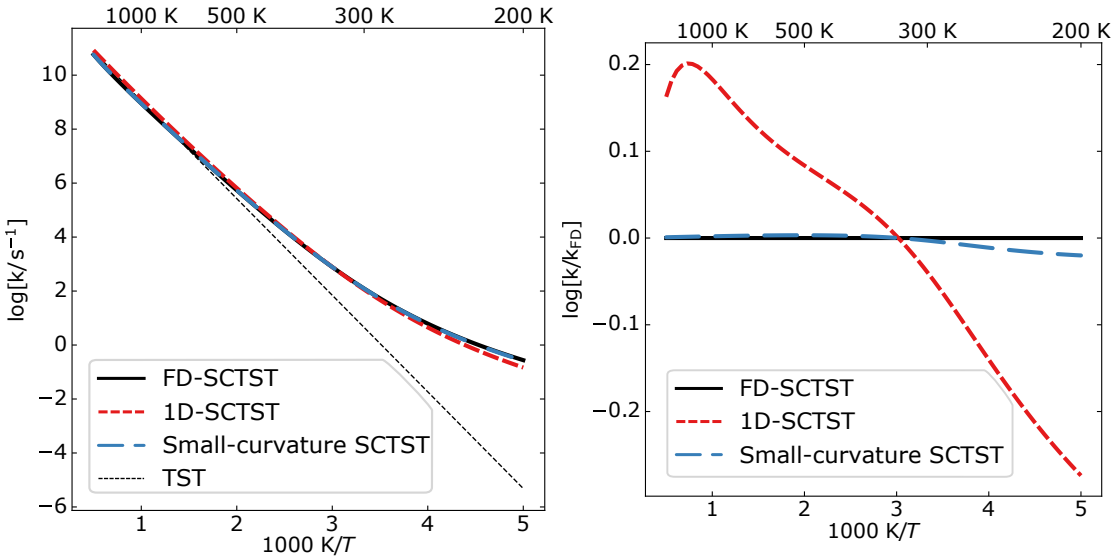


Figure 5.20 Effective barriers for the catalysed Criegee decay (R10), using FD, 1D+, and 1D-SCTST.

barrier is narrower and higher than the 1D and 1D+ barriers, corresponding to a corner-cutting trajectory. The difference between the 1D and the 1D+ barrier corresponds to more accurately describing the MEP by including some couplings along the reaction mode.

We can also see the effect of higher energy corner-cutting paths by comparing the FD-SCTST rate to the small curvature SCTST rate. Figs. 5.21 and 5.22 show the effect of neglecting corner-cutting through higher energy paths. In both cases, the rate decreases. It is clear that the uncatalysed Criegee decay is only slightly impacted by tunnelling though these higher order paths, with the small-curvature rate differing by about 5% at 200 K. This indicates the lowest order path sufficiently describes the trajectory.

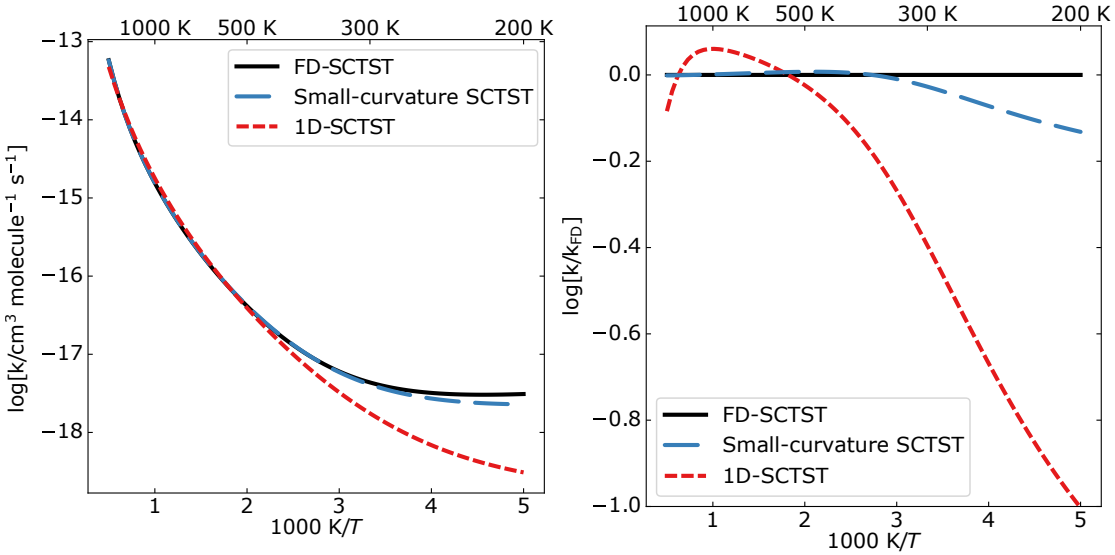
For the catalysed reaction, in contrast, the importance of higher order paths at low temperature is clear, and contribute about 30% of the rate at 200 K (that is, the rate drops by 30% when not considering explicit tunnelling through higher



(a) Arrhenius Plot.

(b) Ratios.

Figure 5.21 Comparison of 1D, FD, and small-curvature SCTST for reaction R9 (unmethylated). Note the symmetry factor of two has not been included here.



(a) Arrhenius Plot.

(b) Ratios.

Figure 5.22 Comparison of 1D, FD, and small-curvature SCTST for reaction R10.

order paths). Significant corner-cutting through high-barrier, narrow pathways is present.

5.6 Conclusions

The unimolecular decay of two simple Criegee intermediates has been investigated using Semiclassical Transition State Theory in full and one dimension, and for thermal and microcanonical rates. For the uncatalysed decay process, 1D-SCTST reproduces well the full-dimensional rate constant. Both methods also give good agreement with available experimental data, generally to within a factor of two, suggesting SCTST is a reliable predictor at a range of temperatures and for related reactions.

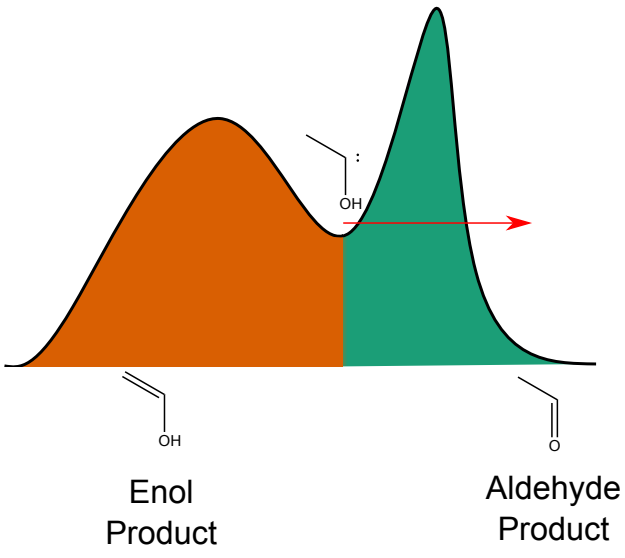
We have also shown that 1D-SCTST rate constants do not compare well with the full dimensional rates for the water catalysed decay process. This is a result of strong coupling of the reaction mode to other spectator modes, which may be understood in terms of the delocalisation of the reactive mode. We have shown that the accuracy of 1D-SCTST can be improved by using an approximate full-dimensional method (termed 1D+) where only derivatives with at least one index corresponding to the reaction mode are included, an idea which is further explored in Chapter 7.

Finally, it was shown that water catalysis has a significant impact on the overall rate of Criegee intermediate decomposition under atmospheric conditions. As well as its inherent interest, understanding how a small number of water molecules can act catalytically in gas phase reactions is also key to solution phase reaction dynamics, where explicit solvent-solute interactions can significantly alter how the reaction proceeds. Understanding these interactions will be key to developing rate theories for the condensed phase.

Chapter 6

Tunnelling control in the rearrangements of carbenes

In this chapter we use SCTST in one dimension to better understand the results of recent experiments on tunnelling controlled reactions. These are reactions which preferably proceed through pathways with high but narrow potential energy barriers, via quantum tunnelling, resulting in a product that would be disfavoured classically. These reactions are particularly sensitive to barrier width, height and temperature, so dynamical theoretical methods are required to describe these processes. Recent experimental work on charge-tagged phenyl pyruvic acid derivatives has found results differing from those of similar systems, which we rationalise using 1D-SCTST.



Abstract 6 Tunnelling control in the decay of methylhydroxycarbene

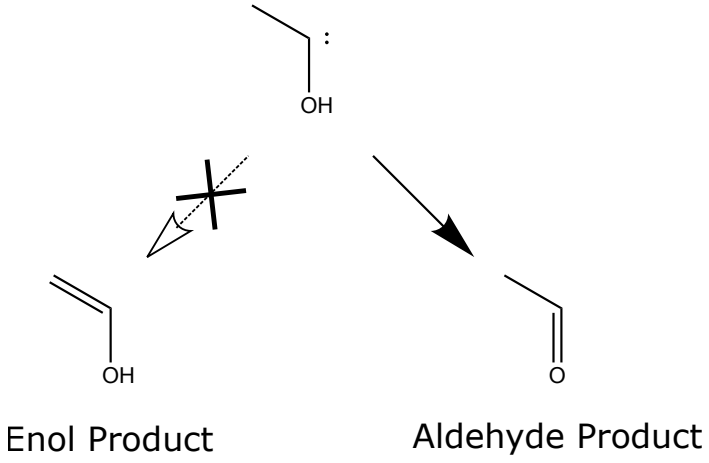
6.1 Introduction

In recent years, it has been shown that quantum tunnelling can supersede traditional kinetic control of chemical reactions, making some reaction paths with high energy barriers more favourable than alternative pathways with lower barriers[276, 277]. This effect has been coined 'tunnelling control'[278]. For theoretical studies, this highlights the importance of considering reaction path width, and dynamical tunnelling calculations, rather than relying on barrier heights alone. A well studied example of this is the family of hydroxycarbenes (R-C-OH)[276, 278–282], which form the subject of this chapter. In order to allow for a high level of theory in our *ab initio* calculations, here with up to 29 atoms, we keep the number of such calculations to a minimum by using 1D-SCTST.

6.2 Methylhydroxycarbene decay

Recent work[278, 281] has identified methylhydroxycarbene as a molecule that decays via a tunnelling controlled pathway, shown in Scheme 6.1. Experimental work on this molecule at 11 K in an argon matrix shows the only observed product of this decay is the aldehyde, despite the lower barrier required to reach the enol product. This effect has been observed at low temperatures for other substituted carbenes[283], and some theoretical rate calculations confirm these findings[284]. This mechanism has also led to spectroscopic observation of hydrogen tunnelling above room temperature[280].

Our 1D-SCTST calculations for the decay of methylhydroxycarbene, performed at the CCSD(T)/cc-pVTZ // MP2/cc-pVTZ level of theory, are consistent with these experimental findings, as shown in Fig. 6.1. These suggest the aldehyde product dominates at low temperature, with the two pathways being equally fast at 287 K. This is in good agreement with instanton calculations performed in full-dimensions, which estimate the crossing point to be 277 K[284]. Classical transition state theory, as expected, incorrectly suggests that the enol product is the dominant product at all temperatures, as it does not account for tunnelling.



Scheme 6.1 Methylhydroxycarbene decay is tunnelling controlled at 11 K. The aldehyde product is found, despite the higher energy barrier.

Scheme	Reaction	V_0(kJ/mol)	ω_F($i$cm^{-1})	x_{FF}(cm^{-1})
6.1	Aldehyde Pathway	134	1979	-78.1
	Enol Pathway	108	1469	-63.9
6.2	Aldehyde Pathway	153	2075	-97.2
	Enol Pathway	96	1342	-30.6
6.2	Enol (Deuterated)	96	1030	-18.3

Table 6.1 Barrier heights, imaginary frequencies and anharmonic constants for the five reactions studied in this work.

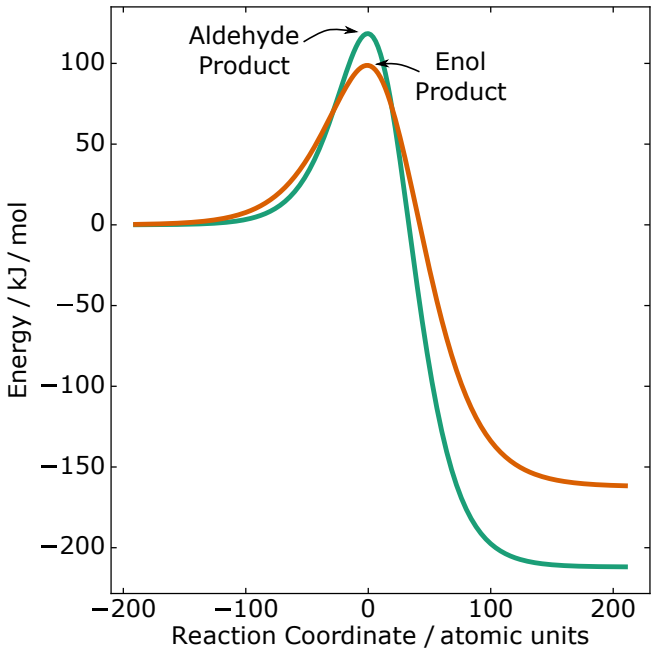
Calculated barrier heights, frequencies and anharmonic constants for all reactions in this work can be found in Table 6.1.

6.3 “Hydrogen Tunnelling Avoided"?

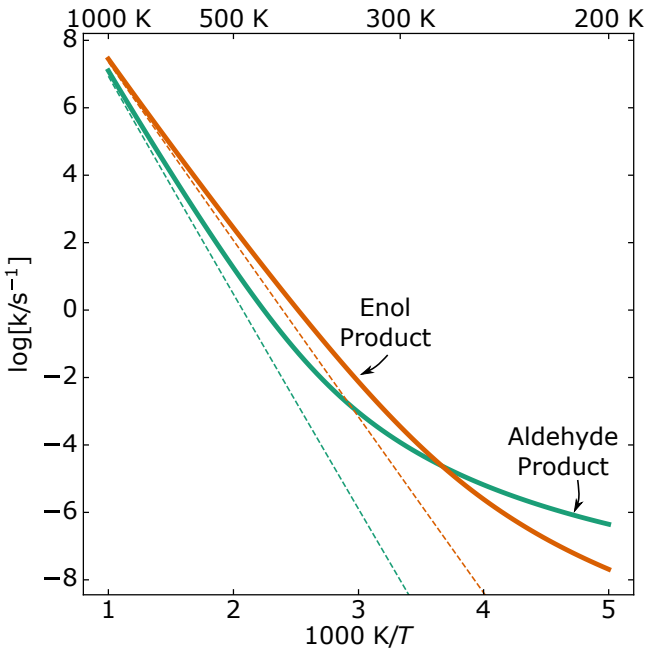
In a recent paper[282],

> Paul, M. *et al.* Hydrogen Tunneling Avoided: Enol-Formation From a Charge-Tagged Phenyl Pyruvic Acid Derivative Evidenced by Tandem-MS, IR Ion Spectroscopy and Theory. *Phys. Chem. Chem. Phys.* (2019)

a similar reaction was investigated at higher temperature both experimentally and theoretically, with results contrasting those of methylhydroxycarbene decay. In this study a charge-tagged phenyl pyruvic acid derivative (shown at the top of Scheme 6.2) was generated, which then loses CO_2 in collision induced dissociation



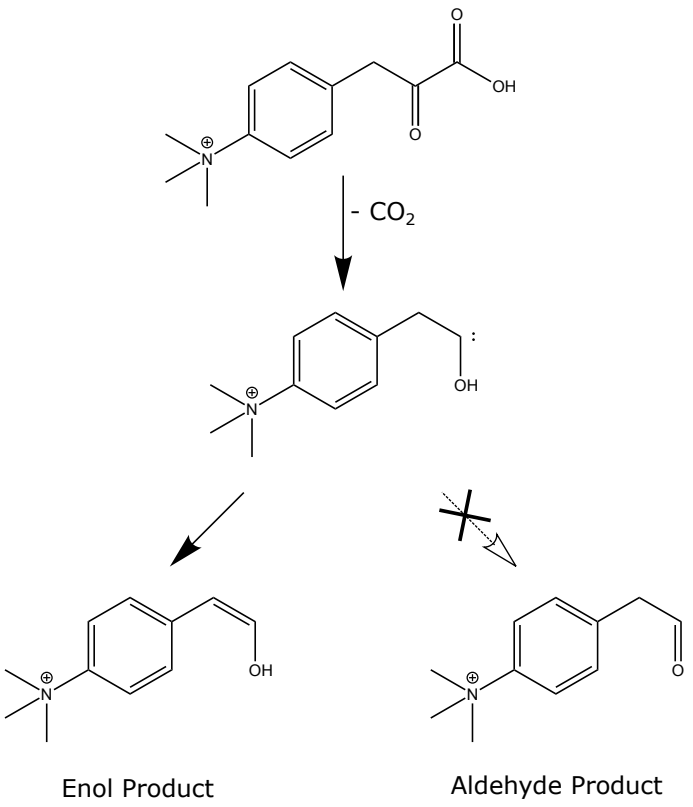
(a) Reaction Barriers.



(b) Arrhenius Plot. TST results shown as dotted lines.

Figure 6.1 Tunnelling control in the decay of methylhydroxycarbene.

experiments, forming a carbene intermediate at about 320 K. IR spectroscopy (and comparison with theoretically calculated spectra) show that an enol acid is formed, as shown at the bottom left of Scheme 6.2, and no evidence of the (tunnelling controlled) aldehyde product was detected. This is despite the calculated potential barriers being qualitatively similar to those of the methylhydroxycarbene case. The authors conclude this result implies that the reaction proceeds without tunnelling, and only 'over-the-barrier' reaction trajectories are significant, a result of the carbene being formed initially in a vibrationally excited state somewhere between the two barrier top energies, allowing for direct over-the-barrier transmission towards the enol (but not the aldehyde) product.



Scheme 6.2 The kinetic control (enol) product is found.

Here we aim to compliment these experiments with additional theoretical findings, and present an alternative conclusion, whereby the experimental findings are entirely consistent with a quantum tunnelling picture from a thermalised

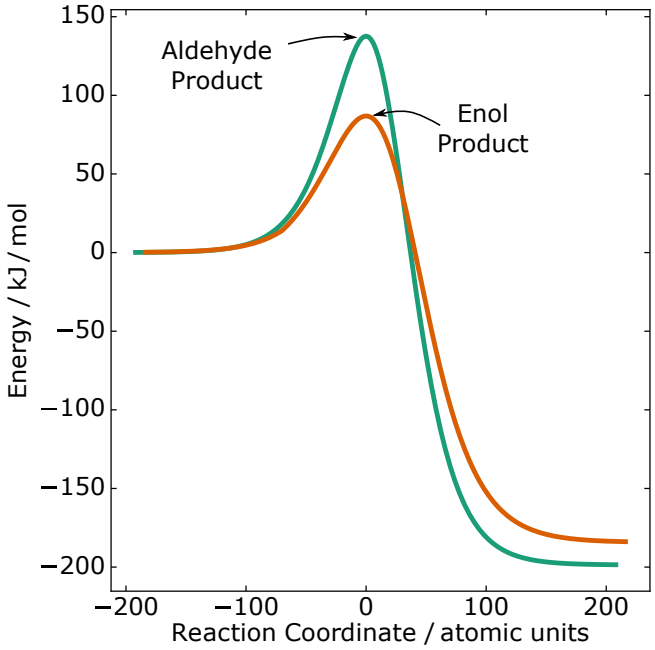
carbene. Since both pathways involve the transfer of a light hydrogen atom, it also seems very likely *a priori* that tunnelling is significant.

We performed 1D-SCTST calculations to determine the relative rates of enol and aldehyde products, from the carbene species. SCTST in full dimensions, whilst likely to be more accurate, is prohibitively expensive for this system, with 29 atoms. The results of our SCTST calculations, performed at the M06-2X/cc-pVTZ level of theory[285] are shown in Fig. 6.2. This functional has been used previously in SCTST calculations with larger molecules[106] and is known to be accurate for kinetics and main group chemistry[285]. Our calculated barrier heights for the enol and aldehyde pathways are 152 and 96 kJ/mol respectively, slightly larger than those calculated using B3LYP (131 and 88 kJ/mol, respectively) by the original authors[282].

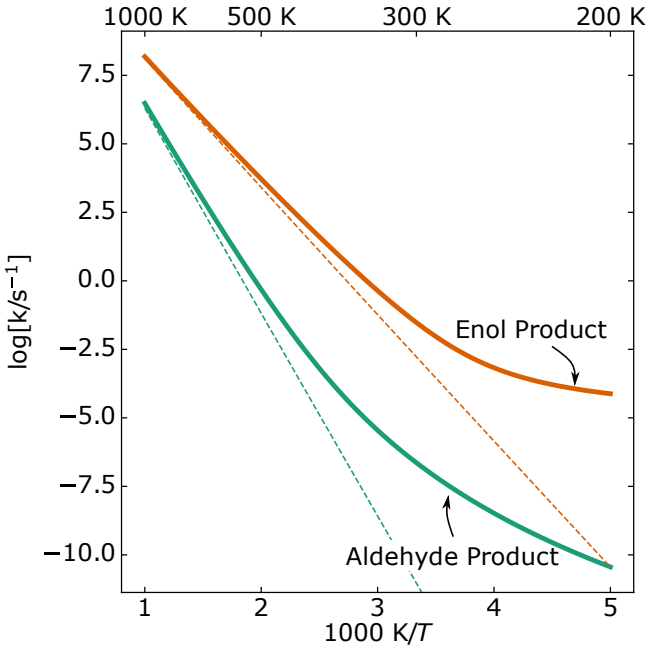
Our results suggest that, in contrast to the case of methylhydroxycarbene, the aldehyde reaction barrier is not sufficiently narrow to allow for tunnelling control, even at very low temperatures. At the temperatures at which the experiments were performed, the enol-product formation is more than 10,000 times faster than the aldehyde decay, as shown in Fig. 6.2b, so our results are consistent with the experimental results. The disparity with the methylhydroxycarbene results is the much larger difference in barrier height between the two pathways (a difference of 57 kJ/mol compared to a difference of 26 kJ/mol), and the much higher temperature at which the experiments have been performed. It is clear, however, that tunnelling *does* contribute significantly to the reaction, even through the kinetic (enol) pathway. Fig. 6.3 shows that tunnelling speeds up the reaction by a factor of 10 at 320 K for the enol-product pathway.

A key experimental indicator of tunnelling is a large kinetic isotope effect. This can be investigated by determining the rates when the hydrogen atom involved is substituted for deuterium. Fig. 6.4a shows this has a significant impact on the rate of the enol path, with a predicted kinetic isotope effect at 320 K of :

$$\mathrm{KIE} = \frac{k(\mathrm{H})}{k(\mathrm{D})} = 9.1 \tag{6.1}$$



(a) Reaction Barriers.



(b) Arrhenius Plot. TST results shown as dotted lines.

Figure 6.2 Kinetic control dominates in the decay of charge-tagged phenyl pyruvic acid derivative, but tunnelling is significant.

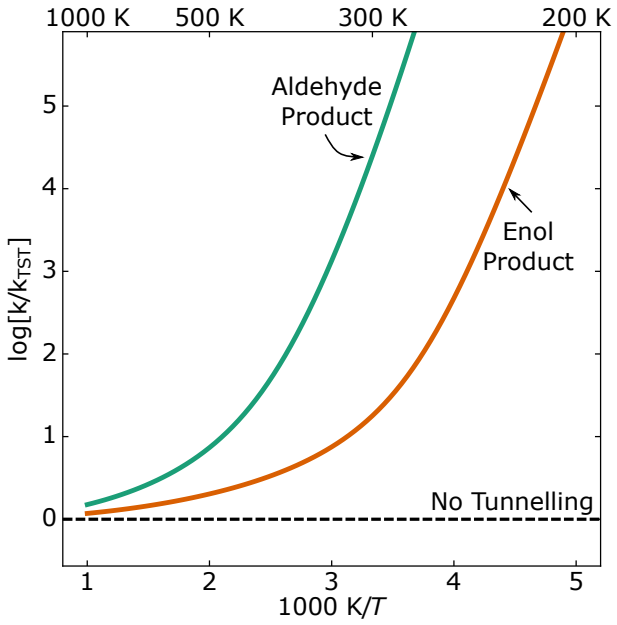
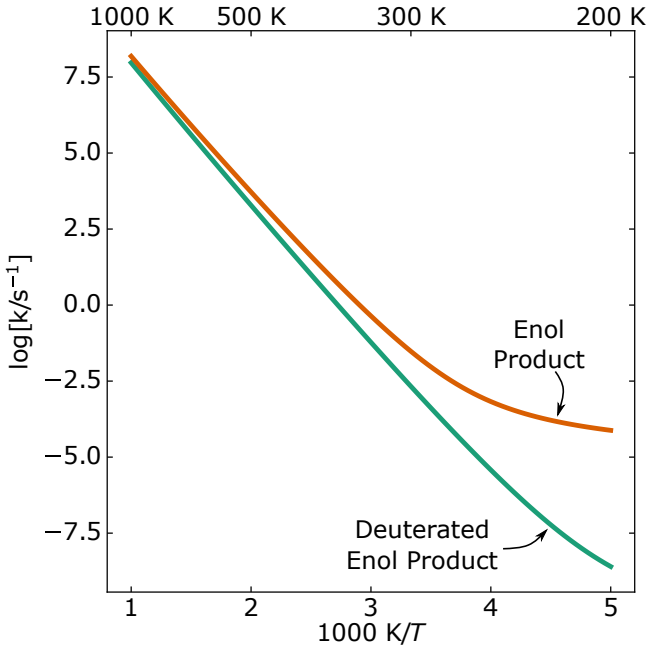


Figure 6.3 The tunnelling speed-up factor of each pathway in the decay of the charge-tagged phenyl pyruvic acid derivative (Scheme 6.2). The enol pathway has a tunnelling speed up of a factor of 11.7 at 320 K.

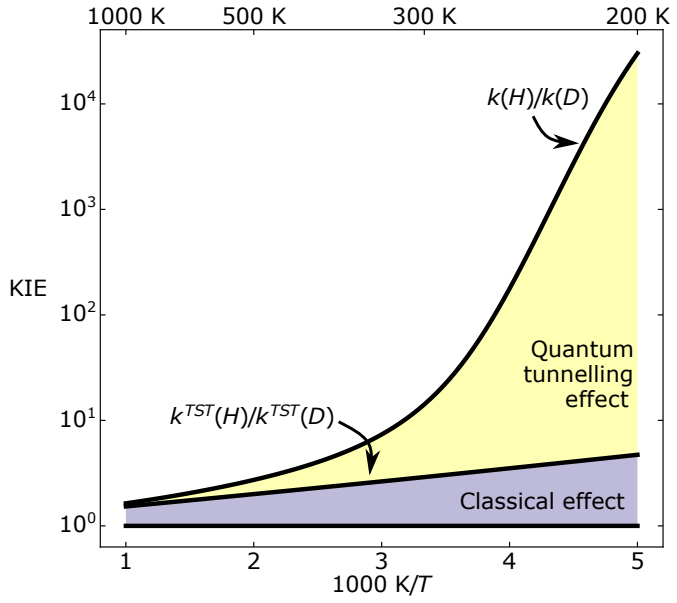
which is owing to two factors; the slight increase in barrier height due to changes in ZPEs of the reactant and transition state (a classical effect), and the increased mass of the tunnelling atom, making tunnelling much less favourable (a quantum effect). The contributions of these two effects are illustrated in Fig. 6.4b. The enol pathway remains the dominant pathway under these conditions.

6.4 Conclusions

The key conclusion of this chapter is that the absence of tunnelling control does not imply the absence of tunnelling. We have found tunnelling is a significant factor in the decay of phenyl pyruvic acid derivative carbenes, despite the wider, lower barrier being preferred. Moreover, no vibrationally excited carbenes need be invoked in order to explain the experimental results. This is in contrast to the conclusions drawn in ref. [282]. Since tunnelling control is highly sensitive to temperature and barrier height and width, it is not sufficient to look at just



(a) Arrhenius Plot.



(b) Relative Rates.

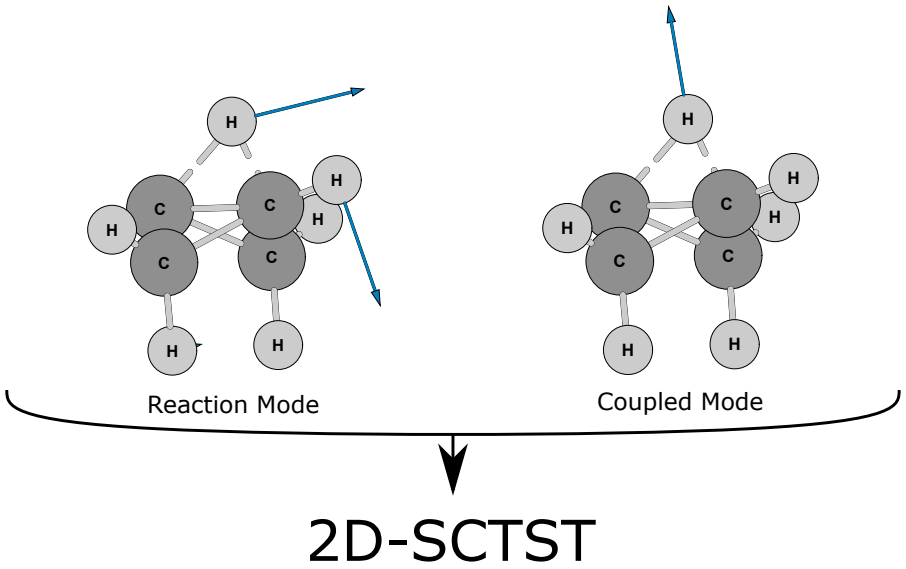
Figure 6.4 A strong kinetic isotope effect is predicted for the enol product pathway in the decay of the charge-tagged phenyl pyruvic acid derivative (Scheme 6.2).

barrier heights, nor barrier shapes, but rather dynamical calculations are needed to determine their behaviour, which may change qualitatively with temperature. SCTST is a convenient method to study this and similar systems, and may prove a powerful tool in understanding similar organic systems.

Chapter 7

SCTST in reduced dimensions

In this chapter we develop SCTST for use in reduced dimensions in which some, but not all, of the bound vibrational modes are included in the anharmonic SCTST treatment. A key challenge is determining which degrees of freedom to include explicitly, for which we suggest a simple 'signposting' method. We then apply this method to three key reactions and show it allows for the accurate and efficient calculation of rate constants.



Abstract 7 SCTST in reduced dimensions can give accurate rates with a fraction of the computational effort

7.1 Introduction

We have shown in previous chapters that FD-SCTST is capable of making accurate reaction rate predictions. For large molecules, however, this remains very expensive and more approximate methods would be beneficial. In some systems, however, a one-dimensional treatment may fail to give sufficient accuracy. An intermediate treatment is therefore useful, such as a reduced-dimensionality (RD) calculation. Here we will use the term RD- to refer to reduced dimensional methods other than in one-dimension. RD methods have previously been applied successfully in QRS reactions[212, 286–291] and reduce the number of *ab initio* calculations required to generate a PES, and enable cheaper dynamical calculations on the PES. Whilst reduced dimensionality SCTST calculations have been done before[108], these have always been performed on pre-existing reduced dimensionality surfaces. Here we aim to develop RD-SCTST for complex reactions without requiring a PES.

One choice that must be made when performing a RD calculation is which degrees of freedom (DoFs) to treat explicitly. In quantum scattering studies of bimolecular hydrogen transfer reactions, the active degrees of freedom are often chosen based on chemical intuition. Previous work in the Clary group[38, 41, 46, 292] has used potential energy surfaces in which the bond-breaking and bond-forming bond lengths are used as the two 'active' degrees of freedom, and have shown this can give excellent agreement with experiment. There are several limitations to the above approach. For unimolecular reactions, or more complex bimolecular reactions, the choice of active DoFs is less clear, as many atoms may be involved in the reaction process. Moreover, it may not be clear how to extend this to higher dimensional (for example three or four dimensional) calculations in cases where a two-dimensional treatment is insufficient. Thus, as well as developing a SCTST method in reduced dimensions, we also seek a method of predicting cheaply in advance whether RD-SCTST is required, and which and how many DoFs will be needed to achieve an accurate result.

In this chapter we first explain in more detail our motivation for developing SCTST in reduced dimensions. We then describe a methodology to systematically perform these calculations, including a novel signposting method to identify key modes, and test it on the Criegee decay reactions studied in Chapter 5, and to a carbene rearrangement for which 1D-SCTST fails significantly. We then outline and evaluate an alternative signposting method.

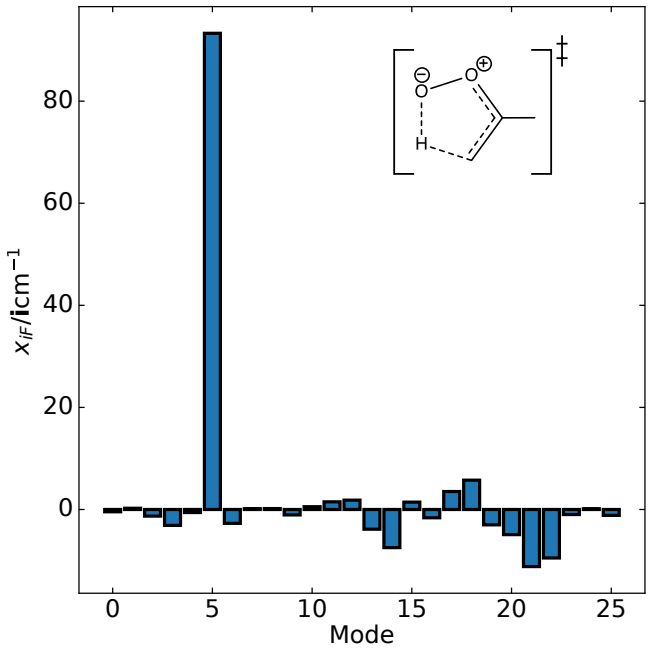
7.2 The inefficiency of SCTST in full dimensions

The contribution of each vibrational mode to the tunnelling process in a FD calculation can be investigated by studying the values of x_{iF}. These are shown for the Criegee transition states of reactions R9 and R10, studied in Chapter 5, in Fig. 7.1. These are the anharmonic coupling terms between a vibrational mode, i, and the reaction mode. It is clear that many of the spectator modes do not couple strongly to the reaction mode, and thus their inclusion in the FD model has little effect on the result. In particular, for the uncatalysed reaction, only one bound mode is seen to interact strongly with the reaction mode. This suggests that whilst a 1D model may be inadequate, the FD model is inefficient, as much computational time is spent calculating coupling constants that are close to zero.

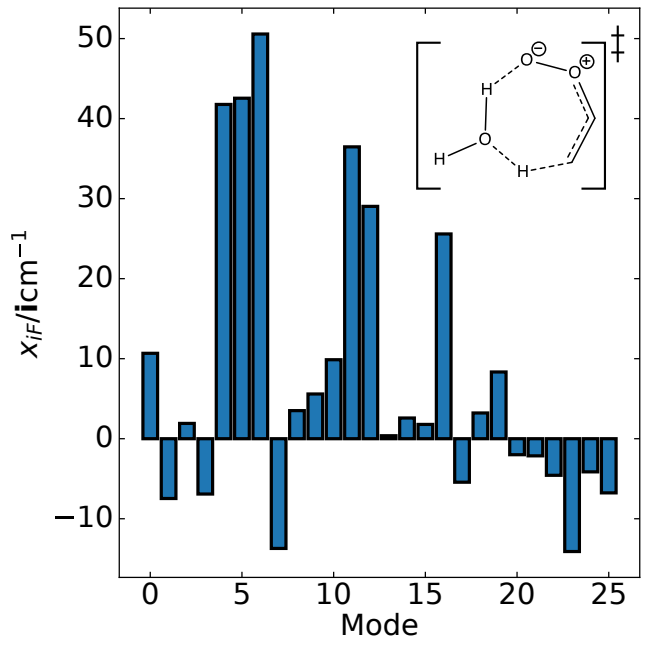
RD-SCTST seeks to bridge this gap, by treating some, but not all, of the bound modes as coupled to the reaction mode. In this way, key couplings can be included, but no time is wasted including modes that are unimportant. RD-SCTST calculations are potentially much more efficient than FD-SCTST, as long as the significant modes can be identified in advance, cheaply.

7.3 The RD-SCTST framework

In principle, RD-SCTST can use any set of degrees of freedom as a basis to form the active space; previous SCTST studies have used potential energy surfaces based on bond-breaking and bond-forming bond length bases to perform a two-dimensional calculation for simple hydrogen abstraction reactions[92, 108]. Here



(a) Uncatalysed Criegee reaction transition state (R9, methylated).



(b) Catalysed Criegee reaction transition state (R10).

Figure 7.1 Comparison of values of x_{iF} for two transition states studied in Chapter 5. Modes labelled in order of decreasing frequency.

we study reactions for which no PES is available and so we use the transition state normal modes as the basis for the active degrees of freedom. We will see this allows for straightforward identification of strongly coupled degrees of freedom, easy generalisation for higher dimensions, and can reduce the overall number of *ab initio* calculations required.

For a d-dimensional calculation, normal modes of the transition state can be divided into d active modes and F-d spectator modes:

$$\nu = \left(\begin{array}{c} \nu_1 \\ \vdots \\ \nu_{F-d} \\ \nu_{F-d+1} \\ \vdots \\ \nu_F \end{array} \right) \begin{array}{l} \left. \begin{array}{l} \\ \\ \\ \end{array} \right\} \text{Spectator modes} \\ \left. \begin{array}{l} \\ \\ \\ \end{array} \right\} \text{Active modes} \end{array}$$

The active modes are comprised of the reaction mode, and the $d-1$ 'transition' modes. Spectator modes are treated harmonically, as in 1D-SCTST, and so only contribute to the rate through their partition function and zero point energy.

RD-SCTST in this form presents two unique challenges - determining which modes are significant without calculation of the full $\mathbf{x}$ matrix, and ensuring a consistent anharmonic treatment of reactants and products. These are discussed in turn in the subsequent sections.

7.4 Selecting active modes

Unlike 1D or FD calculations, to perform an RD-SCTST calculation special care must be taken to decide which, and how many, degrees of freedom to treat as active modes. A poor choice of active modes can lead to wasted computational effort, or introduction of errors that are fortuitously cancelled in a one-dimensional calculation. Adding in a single transition mode may over compensate in one direction, and give a worse result than the one-dimensional calculation. This is illustrated in Fig. 7.2.

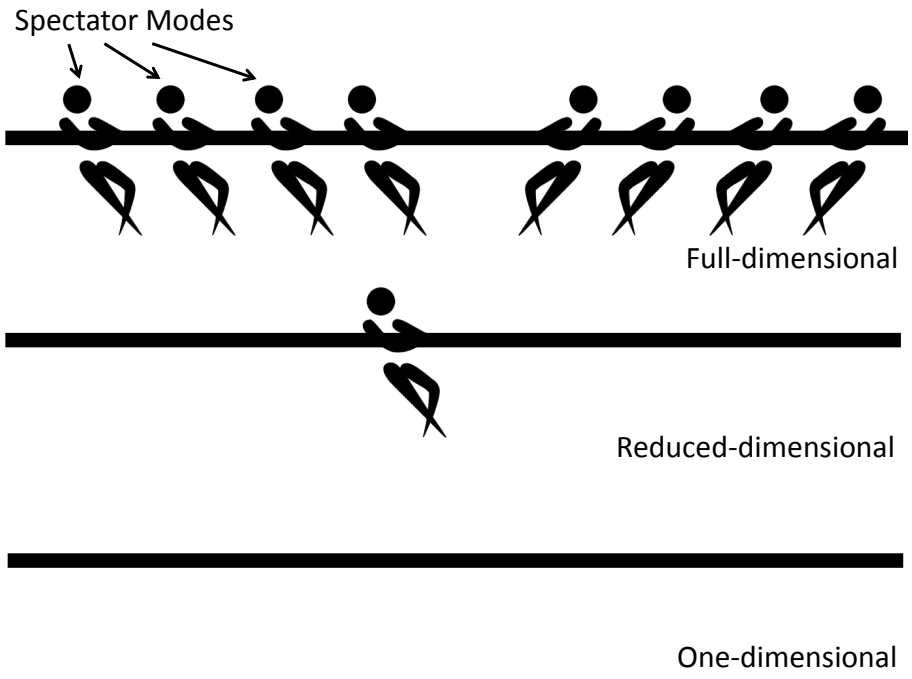


Figure 7.2 How reduced dimensionality calculations can go wrong, by comparison to modelling a tug-of-war. If the tug of war is close, the 1D model (with no players) is more accurate than the RD model (with one player pulling in one direction). In the same way, including some modes but not others in an SCTST calculation can give you the wrong answer. Here, the one-dimensional result is accurate due to a cancellation of errors in the full-dimensional calculation - this is lost in the two-dimensional calculation.

Thus we seek a cheap, automated method to estimate the coupling of each mode to the reaction mode using, for example, data available from a one-dimensional calculation. A direct way to determine the significant couplings is to study the semi-diagonal fourth order derivatives, f_{FFii}, and third order derivatives of the form f_{Fij}, which are available from just two Hessians, at geometries displaced along the reaction coordinate:

$$f_{FFii} = \frac{H_{ii}(\delta Q_F) + H_{ii}(-\delta Q_F) - 2H_{ii}(0)}{\delta Q_F^2} \tag{7.1}$$

and

$$f_{Fij} = \frac{H_{ij}(\delta Q_F) - H_{ij}(-\delta Q_F)}{2\delta Q_F} \tag{7.2}$$

where $H_{ij}(\delta Q)$ is element (i,j) of the Hessian matrix calculated at a geometry displaced from the transition state by a distance δQ. Note this calculation is significantly cheaper than calculating the $2F$ Hessians required for a FD calculation.

Using these, and the harmonic frequencies, x_{iF} can be approximated by x_{iF}^{approx}:

$$x_{iF}^{\text{approx}} = \frac{1}{4\omega_i\omega_F}\left(f_{iiFF} + \sum_{j=1}^{F} \frac{2f_{ijF}^2\left(\omega_i^2+\omega_F^2-\omega_j^2\right)}{\left[(\omega_i+\omega_F)^2-\omega_j^2\right]\left[(\omega_i-\omega_F)^2-\omega_j^2\right]}\right), \tag{7.3}$$

which serves as an approximation to the full expression:

$$x_{iF} = \frac{1}{4\omega_i\omega_F}\left(f_{iiFF} - \sum_{j=1}^{F}\frac{f_{iij}f_{jFF}}{\omega_j^2} + \sum_{j=1}^{F} \frac{2f_{ijF}^2\left(\omega_i^2+\omega_F^2-\omega_j^2\right)}{\left[(\omega_i+\omega_F)^2-\omega_j^2\right]\left[(\omega_i-\omega_F)^2-\omega_j^2\right]}\right) \tag{7.4}$$

where the term in red is not present in x_{iF}^{approx}. This is the 'Two Hessian' approximation.

From these values, 'candidate modes' can be identified as those with large approximate couplings. By then taking Hessians along the candidate modes (2 Hessians per mode), the estimates can be refined and the accurate x_{iF} term can be calculated using Eq. 7.4. This method thus yields *accurate* values of the anharmonic constants x_{ij} where i and j are active modes, which can then be included in the SCTST calculation. Following this procedure, in a case of n candidate modes, a total of $2n$ Hessian calculations are required in addition to a standard TST calculation.

A special case of the RD-SCTST method is 1D-SCTST, which can have two interpretations - either as described in Chapter 3 (in which all coupling to the reaction mode is neglected), or as an extension of the RD method (where coupling to other modes is partially accounted for by taking two Hessians displaced along the reaction mode). They differ just in whether x_{FF} is evaluated using Eq. 2.23 or 2.44. In this work (and to be consistent with previous work) we will refer to the fully-decoupled method as 1D-SCTST, and the Two Hessian version as (1D+)-SCTST. This 1D+ method has been shown in Chapter 5 to yield better results than the simple 1D-SCTST for the Criegee reactions.

First, we determine the accuracy of the Two Hessian approximation to x_{iF}. We have evaluated sets of x_{iF} and x_{iF}^{approx} at a low level of theory (B3LYP/cc-pvdz),

for eleven transition states, shown in Fig. 7.3, chosen to be representative of a wide range of hydrogen transfer reactions. Using a high level of theory is not critical here as we are comparing calculations on the *same* surface. The results are shown in Fig. 7.4.

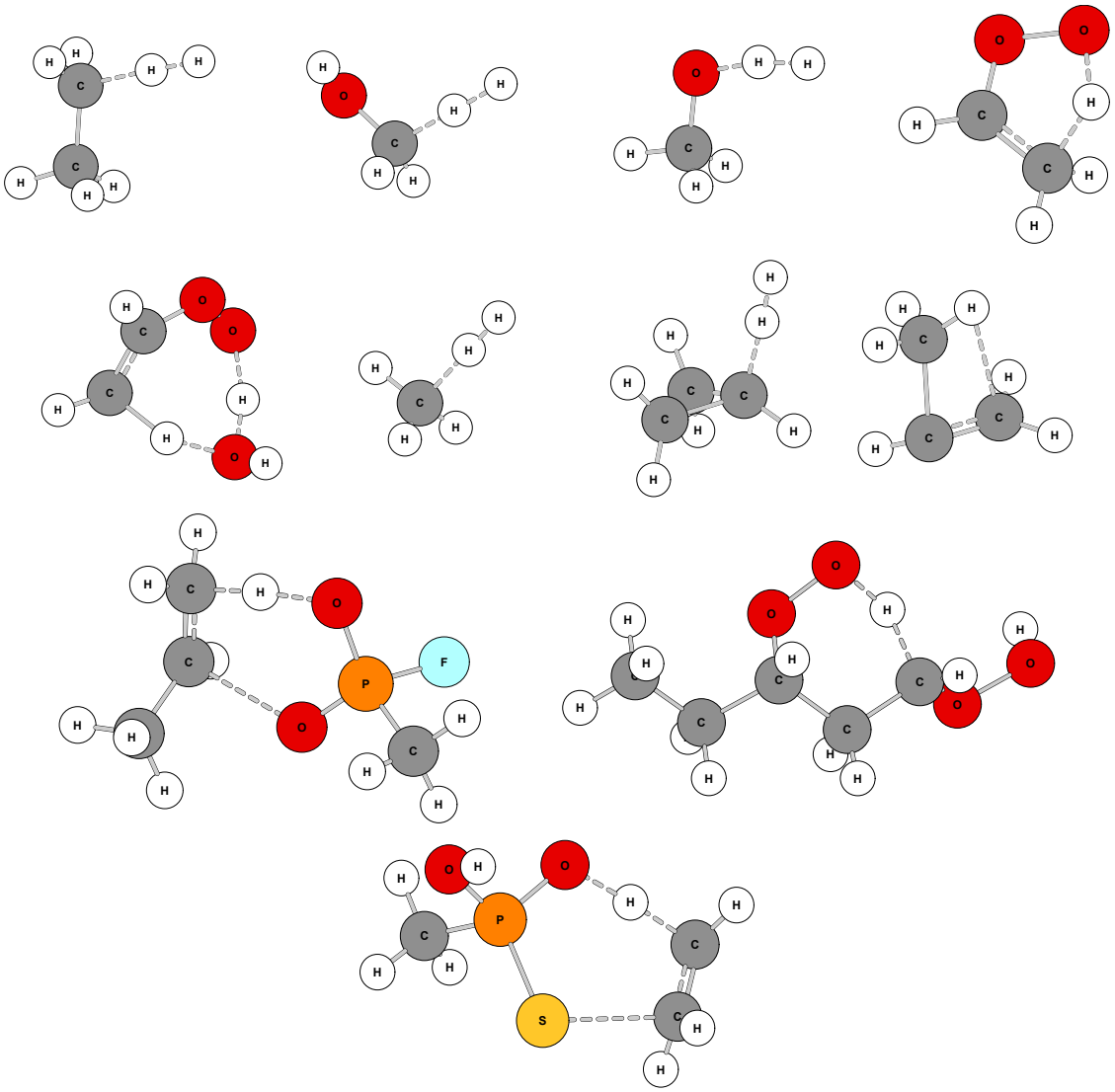
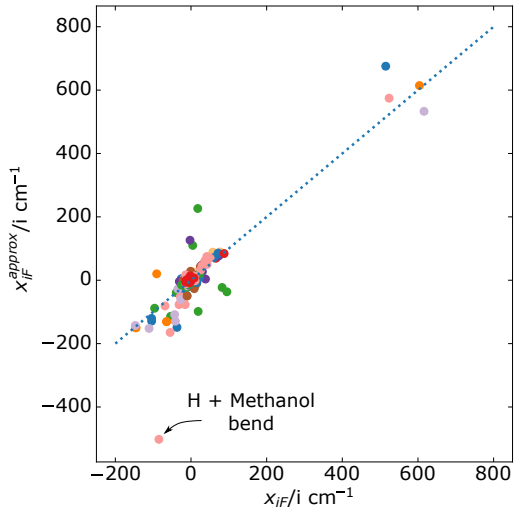
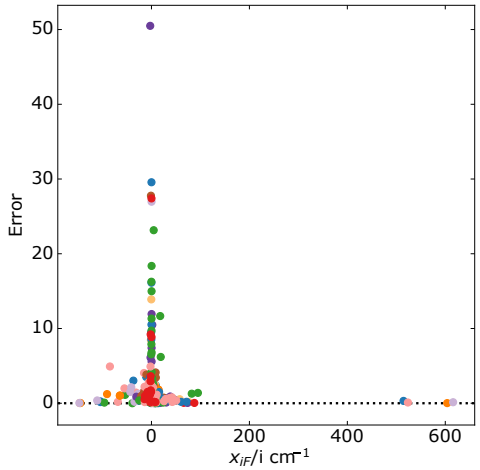


Figure 7.3 The transition states used in testing x_{iF}^{approx}.

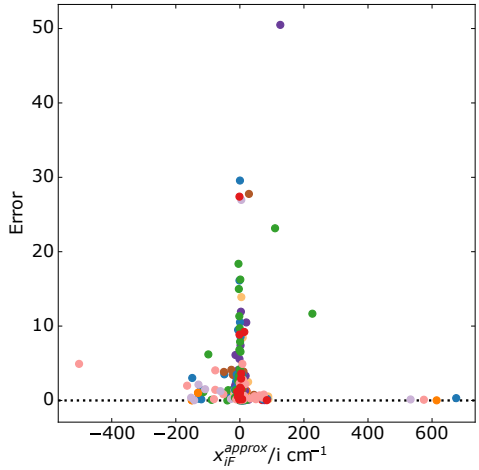
In Fig. 7.4a, a direct comparison is shown between the exact and approximate values. This indicates that the Two Hessian approximation is, in general, a good one which manages to capture the key contributions to the coupling elements. In Fig. 7.4b, the fractional absolute error is shown as a function of the exact x_{iF} value, and shows that large values of x_{iF} are estimated with high accuracy, whilst smaller



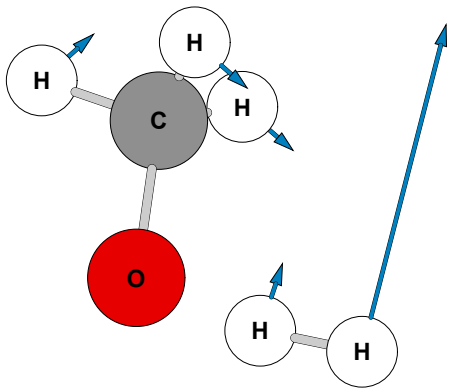
(a) Direct comparison.



(b) Error as a function of x_{iF}.



(c) Error as a function of x_{iF}^{approx}.



(d) The labelled mode in (a).

Figure 7.4 Using the Two Hessian approximation for x_{iF}. Each colour represents a different molecule in Fig. 7.3. The dotted line represents $x_{iF}^{\text{approx}} = x_{iF}$.

values are susceptible to very large fractional errors. This means significant modes are accurately identified, and we found no significant examples of 'false-negatives'.

In Fig. 7.4c the fractional absolute error is shown as a function of the x_{iF}^{approx} value. This figure shows that not all modes that are estimated as being significant are, in fact, significant. Inspection of these 'false-positives' shows no obvious way to predict in advance where errors lie. For example, the outlier mode in Fig. 7.4a, labelled *H + Methanol bend* has an x_{iF} of -84$i$cm^{-1}but an x_{iF}^{approx} of -502$i$cm^{-1}. This corresponds to a bending mode in the reaction of H with

Methanol, and is shown in Fig. 7.4d.

It is therefore clear that this method is excellent at signposting strongly coupled modes (and thus excellent for informing a RD-SCTST calculation as discussed in section 7.4). The method is also prone to false positives. This is not a problem in our RD-SCTST framework, as the Two Hessian method is simply indicating which modes may be significant. Their accurate x_{iF} values are calculated before being used in the SCTST calculation.

7.5 Consistent anharmonic treatment

Once the significant modes have been determined, the way in which their anharmonicity is included must be considered. As the rate is calculated by taking the ratio of vibrational partition functions of the transition state and reactants, anharmonicity must be treated in an equivalent way in both systems in order to ensure the associated errors cancel as much as possible.

The most rigorous way to perform an RD calculation is to isolate the $(F-d)$ spectator degrees of freedom through a curvilinear projection in the transition state, and their projection onto the reactant state. This leaves a system with d-degrees of freedom with which a d-dimensional SCTST calculation can be done in much the same way as a FD-SCTST calculation is done normally. This method does not limit RD calculations to using a normal mode basis, but could be implemented using, for example, a 'bond-breaking' and 'bond-forming' DoF basis for a 2D calculation. It should be noted that projecting out some degrees of freedom to treat them separately has been used within SCTST previously, for example, to account for internal rotational degrees of freedom, as discussed in Chapter 3.

Whilst theoretically rigorous, this method may be less convenient than others. It requires further Hessians to be calculated in the reactant state, in order to account for anharmonicity of the projected modes. Moreover, this becomes a less simple extension of 1D-SCTST, which is the desired outcome. The normal mode basis is also a convenient way to look at the reaction for when it is not clear *a priori* what degrees of freedom may be relevant. Choosing an orthogonal basis

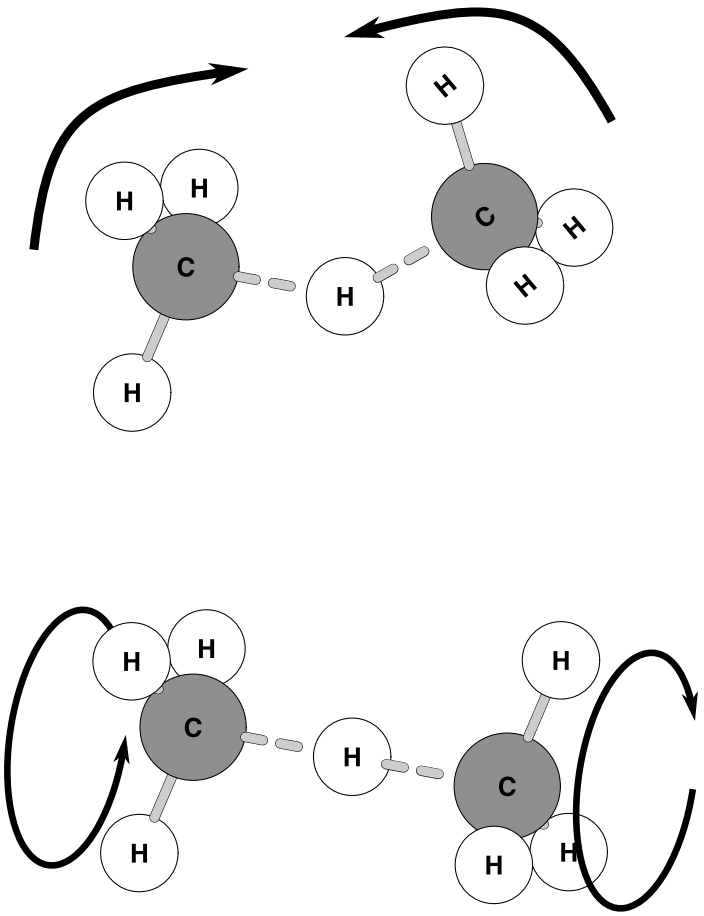


Figure 7.5 Two transition state vibrational modes that correspond to relative translational and rotational modes in the reactant state.

(unlike bond length bases) also allows for systematic inclusion of more modes, where each can build directly on the computation of the previous result.

When only a few modes are to be considered active ($d \ll F$) it is likely the error in treating these modes anharmonically in only the TS will be small. This is especially true in bimolecular reactions if the active modes partially or completely project onto degrees of freedom in the reactant state which correspond to relative translational/rotational degrees of freedom (whose contribution to the vibrational partition function is zero). In this case, ignoring the anharmonic effects of this mode in the reactant state is rigorous. Such modes are illustrated in Fig. 7.5 for the $H_3C{-}H{-}CH_3$ transition state of reaction R1 . In this work we have adopted this simplified approach.

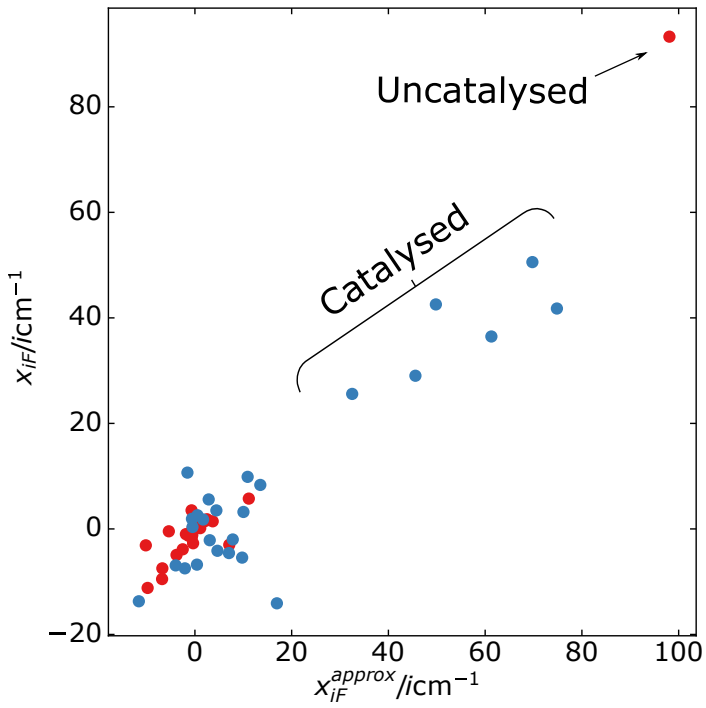
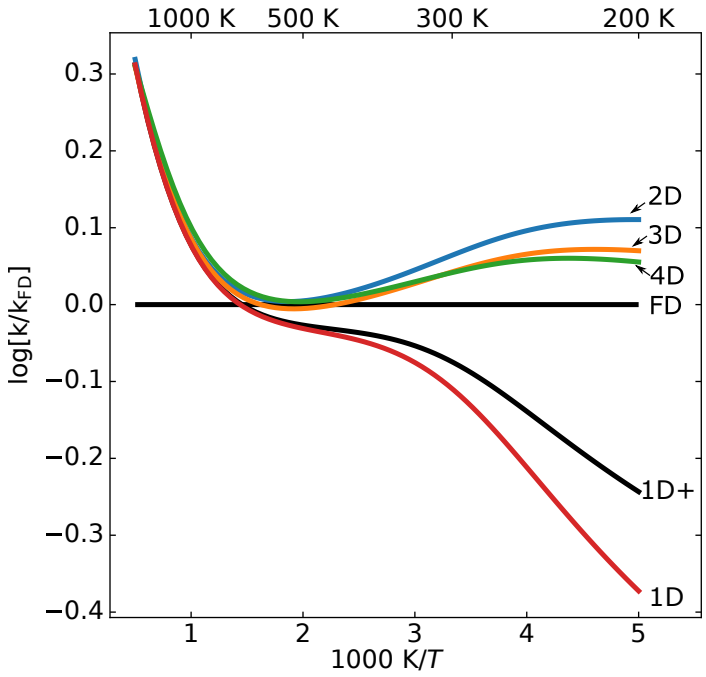


Figure 7.6 Comparison of x_{iF} and x_{iF}^{approx} calculated using a step size of 0.05 a_0 Da$^{0.5}$. This allows the significant modes to be identified. Here, modes of the uncatalysed TS are in red, and modes of the catalysed TS are in blue.

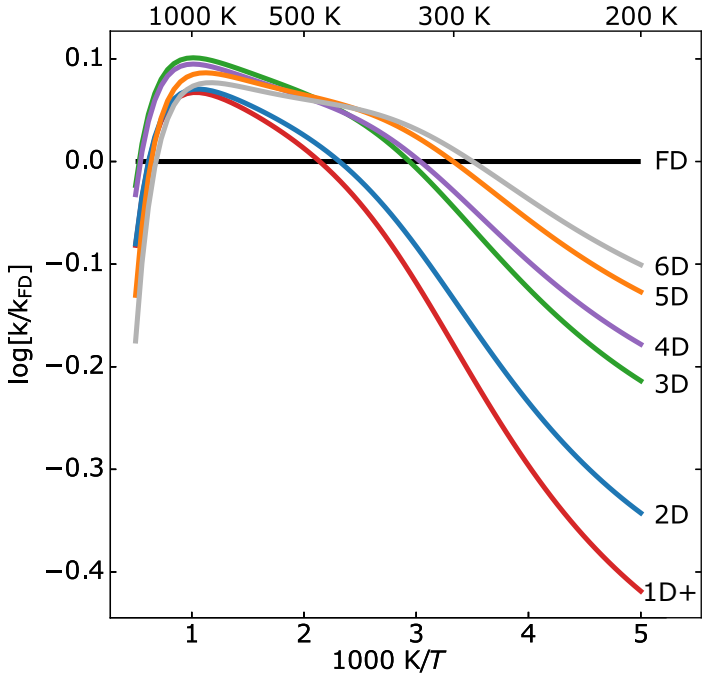
7.6 Application to Criegee chemistry

To test the accuracy of this method, we calculated RD-SCTST rates for two Criegee decay reactions studied in Chapter 5; the methylated unimolecular Criegee decay, R9, and the water catalysed process, R10. First, the Two Hessian approximation was used to identify the key modes. These approximate couplings are compared to the accurate (FD) values in Fig. 7.6. For the uncatalysed reaction, this procedure clearly identifies a single mode is significant ($\omega = 1891$ cm^{-1}). For the catalysed reaction several modes are identified as significant ($\omega = 1745, 1633, 1264, 1650, 1203, 886$ cm^{-1}).

The results of including these DoFs for the two reactions are shown in Fig. 7.7. From Fig. 7.7a it is clear that adding in just a single bound mode gives a significant improvement to the uncatalysed Criegee rate. Whereas the 1D+ method is a factor of two smaller than the FD rate at 200K, the 2D calculation differs by just 25%. As expected from our signposting analysis, adding in more modes to the



(a) Uncatalysed Criegee reaction (R9, methylated)



(b) Catalysed Criegee reaction (R10).

Figure 7.7 Effect of including additional degrees of freedom in tunnelling calculations. The modes selected are those with the largest values of x_{iF}^{approx}.

active space has only a small effect on the rate.

For the catalysed reaction, multiple modes contribute significantly to the tunnelling process, and so a number of modes are required to achieve a similar accuracy to that of the uncatalysed reaction. The six-dimensional rate lies within 30% of the FD rate at all temperatures.

7.7 Application to a carbene rearrangement

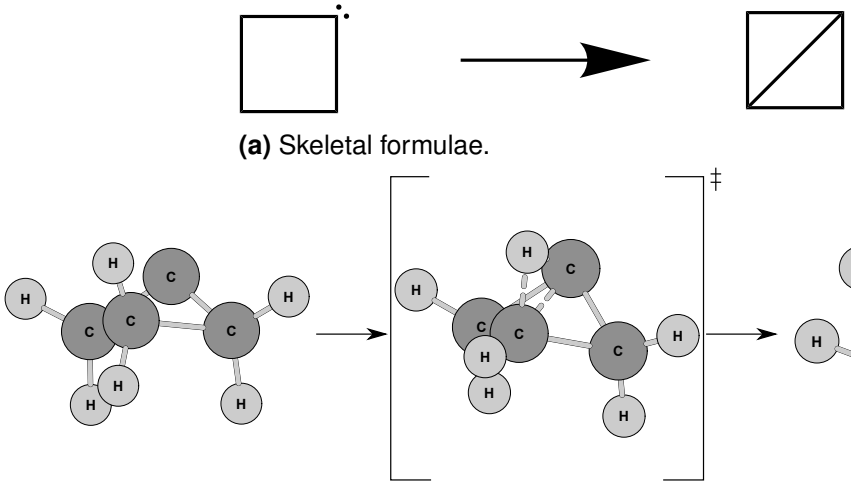
Now we will test this method on a new system for which 1D and FD-SCTST results disagree substantially at low temperature - the isomerisation of cyclobutylidene.

Tunnelling in the reactivity of carbenes has been the focus of much attention in recent years, particularly in the context of tunnelling controlled reaction pathways[276, 278, 281], and due to their importance in organic synthesis[293]. The reactions of cyclocarbenes, and the effects of their substituents have also been the subject of much theoretical scrutiny[294–298].

Here we investigate tunnelling in the unimolecular isomerisation of cyclobutylidene, reaction R11, shown in Fig. 7.8, which has previously been studied with Variational Transition State Theory (VTST) with the small curvature tunnelling (SCT) approximation[294], as well as experimentally[299]. Note that other rearrangement reactions of the reactant also occur[295]. In this section, we first verify that FD-SCTST gives good agreement with VTST results when using the same level of *ab initio* theory, even at very low temperatures (100 K). We then determine the accuracy of the reduced-dimensional approach for this system.

7.7.1 Computational methods

In order to compare with VTST/SCT calculations[294], we performed *ab initio* calculations with the M06-2X DFT functional[285] and the 6-311+G(d,p) basis set[300]. A Richardson step size of $\delta Q = 0.02\ a_0\ \mathrm{Da}^{0.5}$ was used.



(a) Skeletal formulae.

(b) 3D Structures.

Figure 7.8 The isomerisation of cyclobutylidene, reaction R11.

7.7.2 FD and 1D-SCTST

We first compare FD and 1D-SCTST to VTST/SCT calculations on reaction R11[294] at the same level of electronic structure theory. SCTST parameters for this reaction are shown in Table 7.1. The level of theory used was chosen to replicate previous calculations, but the barrier heights agree within 6% of our calculations at the much higher CCSD(T) / cc-pVTZ // MP2/cc-pVTZ level of theory. The CCSD(T) barrier height was 57.8 kJ / mol, compared to the DFT barrier of 61.1 kJ/mol. The value of x_{FF} is seen to differ greatly between its 1D and FD expression. Such extreme behaviour has not been seen in other systems studied in this work, and is likely to be a large source of error in the 1D result.

V_0 / (kJ/mol)	ω_F / $i$cm^{-1}	x_{FF}^{1D}/ cm^{-1}	x_{FF}^{FD}/ cm^{-1}
61.16	823.08	-34.47	-1.830

Table 7.1 SCTST parameters for the isomerisation of cyclobutylidene.

The results of these rate calculations are shown in Fig. 7.9, which shows that whilst 1D-SCTST fails to accurately capture the low-temperature behaviour of the system, FD-SCTST is in good agreement with the VTST/SCT results over the whole temperature range; they differ by a factor of three at 100 K, but less than 20% above 200 K. 1D-SCTST underestimates the rate by several orders of magnitude

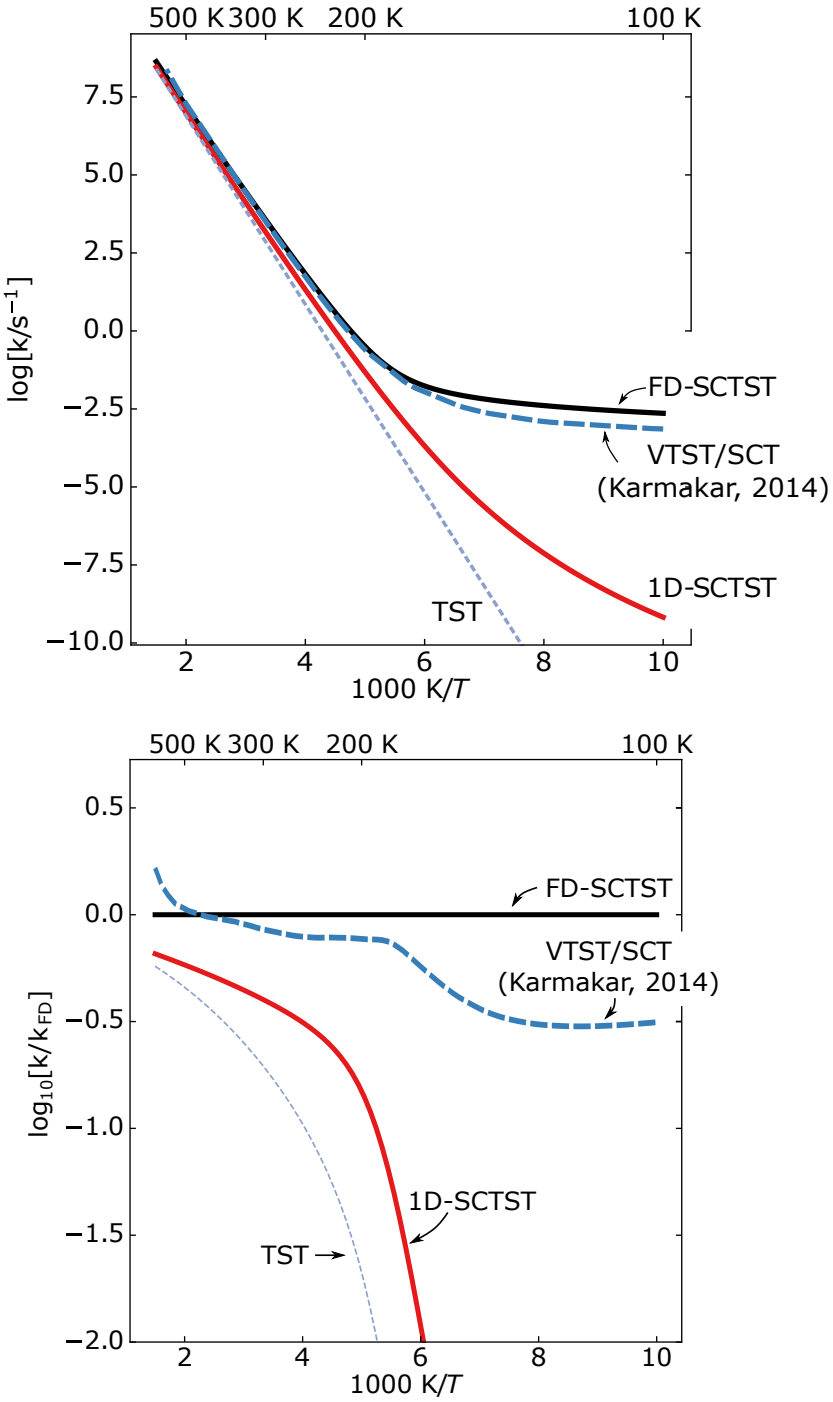


Figure 7.9 FD-SCTST has excellent agreement with VTST/SCT calculations by Karmakar *et al.* for the unimolecular isomerisation of cyclobutylidene [294].

at lower temperatures. The impressive agreement between VTST and SCTST further supports the conclusion that SCTST is able to pick up corner-cutting effects accurately[3], as discussed in Chapter 4, since VTST/SCT accounts for these explicitly. It is important to note, however, that the accuracy of VTST/SCT itself, at these temperatures, is not clear. The near temperature-independence of the rate at low temperature is commonly observed in unimolecular tunnelling systems[284, 301, 302], but is not picked up in the 1D treatment as its very negative value of x_{FF} gives a quantitatively incorrect barrier shape in the deep tunnelling regime, disallowing tunnelling from the bottom of the reactant potential energy well. The FD-SCTST calculation, however, required 49 Hessian calculations at the TS, and so a RD treatment is desirable.

7.7.3 RD-SCTST

To perform the RD calculation, the key coupled modes in the transition state must be identified. First the Two Hessian method is used to identify the key modes, then Hessians along the candidate modes are calculated, and the estimates of x_{iF}^{approx} are updated. Table 7.2 shows how the approximate x_{iF} values change as Hessians are added. This is also illustrated in Fig. 7.10, including a direct comparison of the approximate and accurate values of x_{iF} (calculated previously for the FD calculation).

In this case, the initial approximation identifies two candidate modes (modes 3 and 6), with x_{iF}^{approx} values of -64i and 164i cm^{-1}respectively (shown in the top left of Fig. 7.10). Including Hessians displaced along mode 6 (top-right) then allows for accurate calculation of x_{6F} as 101i cm^{-1}. Mode number 6 is illustrated in the bottom right of Fig. 7.10, and corresponds to movement of the transferring H atom perpendicular to the reaction path, out of the ring. Including Hessians along mode 3, however, shows a significant change in the value of x_{3F} to +11.6i cm^{-1}. This places this mode within the grouping of other (insignificant) modes, and thus was discounted from the rest of the calculation. The possibility of large shifts between approximate and accurate x_{iF} values is why the approximate x_{iF}s

		x_{iF} / $i$cm^{-1}			
		1D+	2D	3D	FD
# Hessians		3	5	7	49
i	F	-1.83	-1.83	-1.83	-1.83
	1	-5.10	-5.18	-1.85	-2.50
	2	-4.46	-4.51	-1.60	-2.15
	3	-64.08	-63.91	11.65	11.63
	4	-5.86	-6.03	-2.01	-2.34
	5	-5.96	-6.20	-2.57	-2.88
	6	164.17	101.16	101.16	101.19
	7	-1.11	-1.31	-1.89	-1.52
	8	-1.20	-1.31	-1.95	-1.35
	9	-17.29	-11.29	-12.14	-8.65
	10	-1.53	-6.91	-10.34	-21.98
	11	-3.33	-3.51	-9.52	-6.14
	12	-3.98	-4.53	-5.10	-5.06
	13	0.80	0.66	0.01	2.53
	14	-3.47	-3.77	-8.02	-7.12
	15	1.44	1.19	-0.42	1.34
	16	1.56	1.45	0.65	1.93
	17	-3.21	-2.82	-4.17	-3.14
	18	0.81	1.68	-3.85	-4.37
	19	-0.40	0.20	-8.69	-7.20
	20	-17.03	-17.07	-20.96	-17.80
	21	-9.65	-9.96	-10.76	-9.95
	22	-16.14	-13.79	-26.25	-21.61
	23	1.22	1.33	0.22	-1.82

Table 7.2 How the approximate values of x_{iF} compare to the (accurate) FD value, as more Hessians are added. Coloured cells show the 'active' modes in each calculation. These data are shown schematically in Fig. 7.10. The computational cost of a calculation is indicated as the number of Hessian matrices required.

are not, themselves, suitable for use in an SCTST calculation. Note that the accurate values of x_{iF} are shown in Fig. 7.10 to illustrate the accuracy of the RD method, but are *not* required to perform the RD analysis. The rate was then calculated in two-dimensions, as described in Section 7.3. This calculation thus required a total of 7 Hessians at the TS.

In Fig. 7.11 we compare this 2D-SCTST result to the FD-SCTST calculation above, and the (1D+)-SCTST result. It is clear that 2D-SCTST performs remarkably well, despite its modest computational cost. It overestimates the FD-rate by just a factor of two at 100 K. Note the 1D+ calculation also performs rather

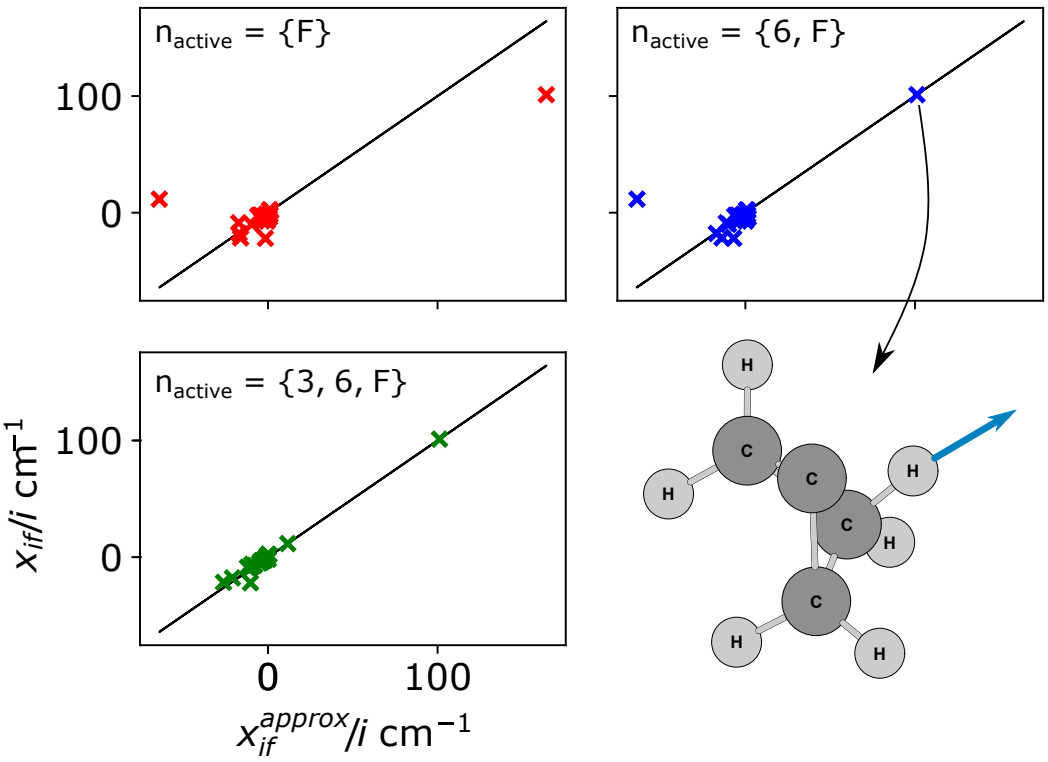


Figure 7.10 Determining the key modes in cyclobutylidene. Comparison of the approximate values of x_{iF} with their accurate values (from a full-dimensional VPT2 calculation), as more Hessians are added. Only one bound mode is found to couple significantly to the reaction mode. These data are tabulated in Table 7.2.

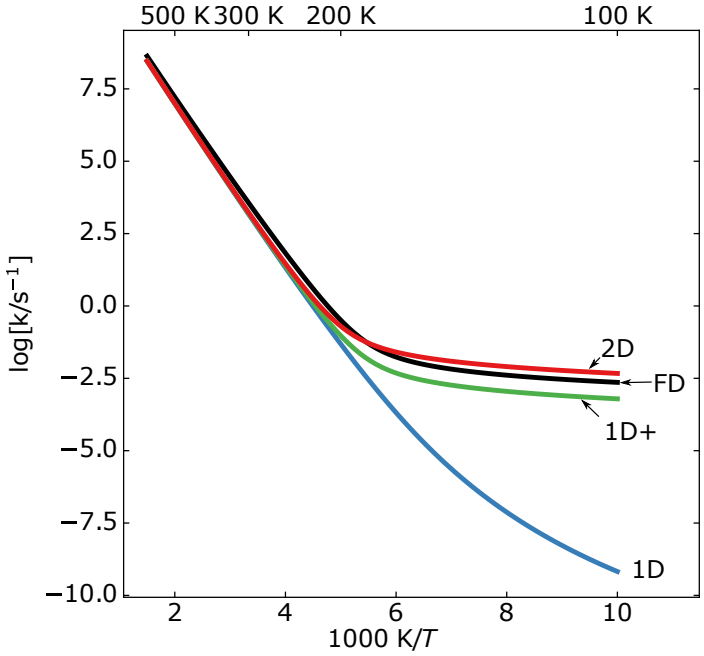
well, within a factor of four at 100 K, since the shape of the barrier is significantly corrected by the accurate x_{FF} term.

Overall, it is clear 2D-SCTST performs excellently for this system.

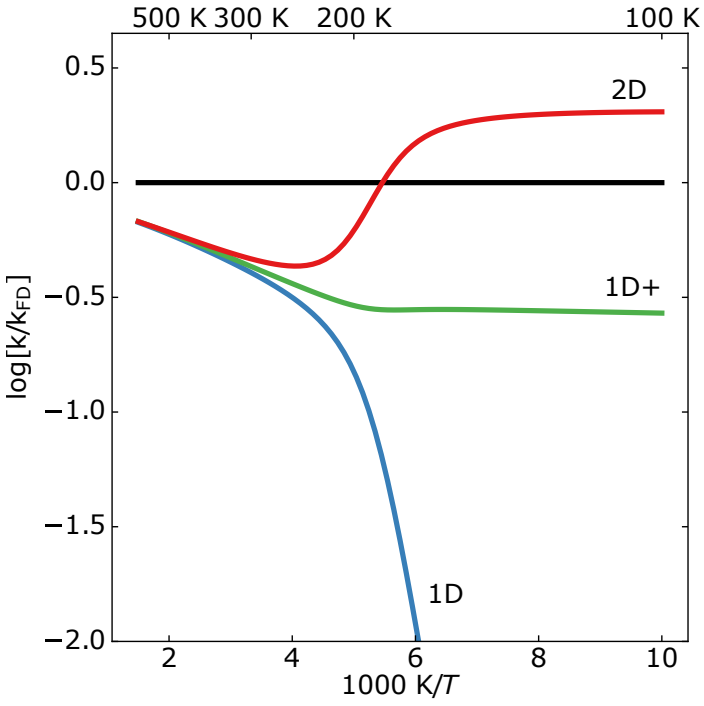
7.8 Weighted mode selection

In this section, we discuss in more detail methods to predict which modes are significant in a RD-SCTST calculation. We have shown that x_{iF} can be predicted with sufficient accuracy to indicate key modes cheaply. So far we have used the values of x_{iF}^{approx} alone to indicate key modes.

This simple approach has some limitations as it does not account for the fact that lower frequency modes are more likely to be vibrationally excited at any



(a) Arrhenius plot.



(b) Rate ratios.

Figure 7.11 2D-SCTST is an excellent approximation to the FD result in this case, whilst the 1D+ method is a significant improvement to the simple 1D-SCTST.

given temperature. Studying just the values of x_{iF} accounts for the effect of the mode on the effective frequency of the trajectory through the vibrational ground state of the transition state only:

$$i\Omega_0 = \omega_F + \sum_i^{F-1} \frac{1}{2} x_{iF}. \tag{7.5}$$

The more general, state-dependent, expression for the effective frequency is:

$$i\Omega_{\{n\}'} = \omega_F + \sum_i^{F-1} \left(n_i + \frac{1}{2} \right) x_{iF}. \tag{7.6}$$

Clearly, when a mode is vibrationally excited, it has a larger effect on the effective frequency. Rather than comparing values of x_{iF}, it is therefore more meaningful to compare the quantity:

$$\chi_i(T) = x_{iF} \left(\langle n_i \rangle_T + \frac{1}{2} \right), \tag{7.7}$$

where $\langle n_i \rangle_T$ is the expectation value of the quantum number of mode i at temperature T. This means modes with larger x_{iF} or larger n_i *on average* should be included in the RD treatment. Within a harmonic approximation, the average value of n_i is a simple function of the frequency ω_i and the temperature:

$$\begin{aligned} \langle n_i \rangle_T &= \frac{\sum_n n \exp\left[-\frac{n\omega_i}{kT}\right]}{\sum_n \exp\left[-\frac{n\omega_i}{kT}\right]} \\ &= \frac{1}{\exp\left[\frac{\omega_i}{kT}\right] - 1} \end{aligned} \tag{7.8}$$

which is plotted in Fig. 7.12, as a function of temperature for several values of ω_i. We thus have:

$$\begin{aligned} \chi_i(T) =& x_{iF} \left(\frac{1}{\exp\left[\frac{\omega_i}{kT}\right] - 1} + \frac{1}{2} \right) \\ =& \frac{x_{iF}}{2} \left[\frac{\exp\left[\frac{\omega_i}{kT}\right] + 1}{\exp\left[\frac{\omega_i}{kT}\right] - 1} \right]. \end{aligned} \tag{7.9}$$

At low temperatures this becomes proportional to x_{iF}:

$$\chi_i(T) \sim x_{iF} \qquad (\text{for } \omega_i >> kT) \tag{7.10}$$

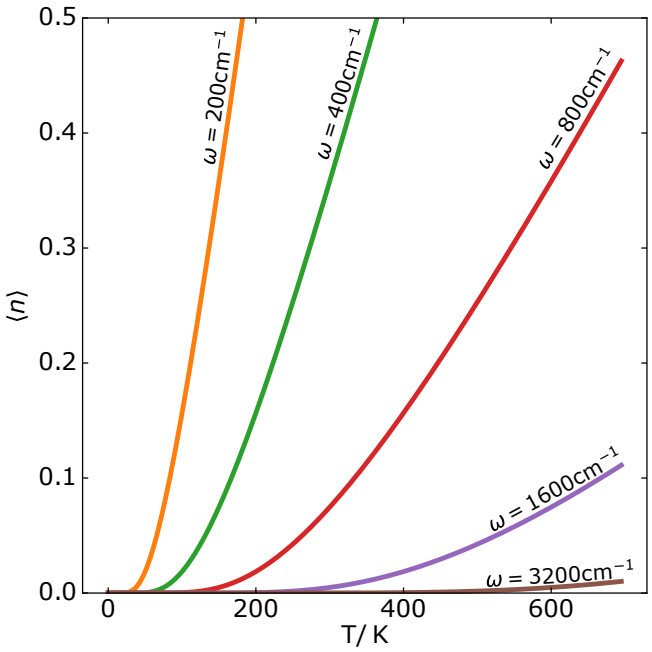


Figure 7.12 Average quantum number of a harmonic vibrational mode at different temperatures, for several frequencies.

and the procedure reduces to simply comparing values of x_{iF}, as before. At high temperatures, a simple reciprocal relation is found:

$$\chi_i(T) \sim \frac{x_{iF}}{\omega_i} \qquad (\text{for } \omega_i << kT). \tag{7.11}$$

In the high temperature limit, however, tunnelling is not generally significant and these couplings are unimportant.

The temperature dependence of this factor is inconvenient, and it would be useful to evaluate this at some meaningful temperature. A meaningful temperature to evaluate this quantity may be the cross-over temperature, T_c. This is the temperature that marks the onset of the 'deep tunnelling regime', and has a particular significance in ring-polymer instanton calculations[303]. Above this temperature, multidimensional tunnelling effects are unlikely to be significant.

The cross-over temperature, T_c, is given by a simple function of the imaginary vibrational frequency:

$$kT_c = \frac{|\omega_F|}{2\pi}. \tag{7.12}$$

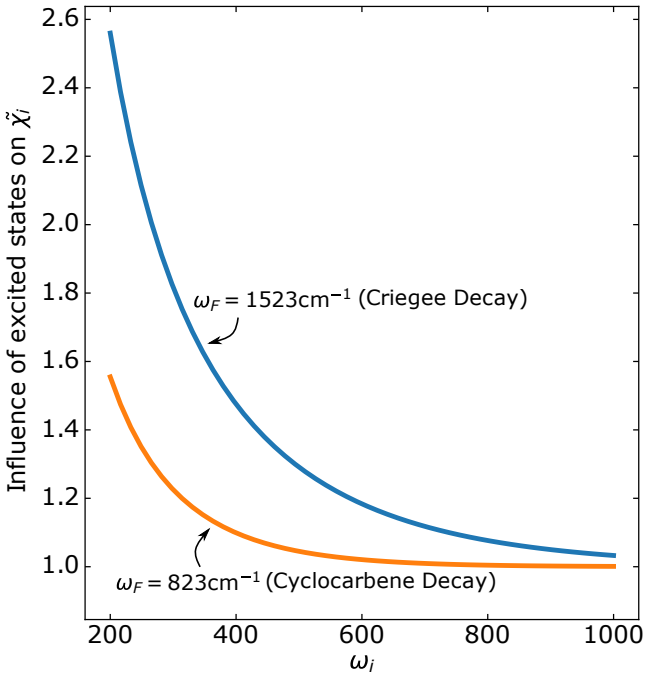


Figure 7.13 The term in square brackets in Eq. 7.13. This is the effect of considering excited vibrational states, shown here for the cyclocarbene reaction and the unimolecular Criegee decay.

Finally, we can define the real, dimensionless and temperature independent quantity $\tilde{\chi}_i$:

$$\tilde{\chi}_i = \frac{\chi_i(T_c)}{\omega_F} = \frac{x_{iF}}{2\omega_F}\left[\frac{\exp\left[\frac{2\pi\omega_i}{|\omega_F|}\right]+1}{\exp\left[\frac{2\pi\omega_i}{|\omega_F|}\right]-1}\right]. \tag{7.13}$$

This is equal to the fractional value of the second term of Eq. 7.6, compared to the first. This is a far more satisfactory measure of a bound mode's significance. The term in square brackets is the effective impact of considering higher order excitations. This term is shown in Fig. 7.13, as a function of ω_i for two transition states we have studied previously. As expected, low frequency modes coupled to high frequency reaction modes are more strongly represented using this method, although the effect is relatively small.

7.8.1 Effect on reactions R9, R10 and R11

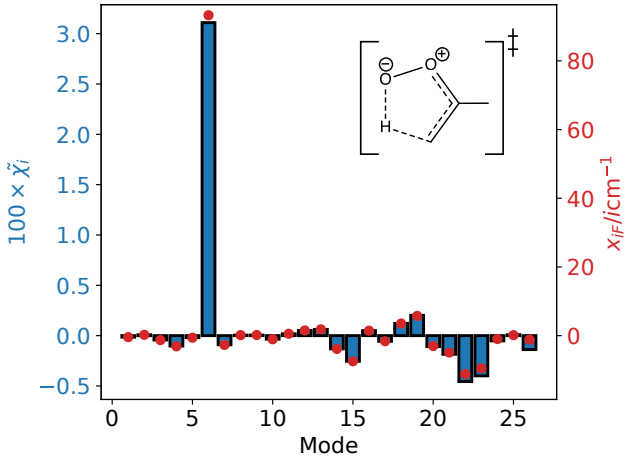
We can now evaluate the impact of this method on the choice of active modes for reactions R9, R10 and R11. Fig. 7.13 suggests the effect of considering excited modes in reaction R11 to be very small. The two Criegee decay reactions (R9 and R10) have higher imaginary frequencies and so higher cutoff temperatures. The catalysed transition state also contains low-frequency bending modes. As such, Fig. 7.13 suggests a more significant impact of considering $\tilde{\chi}_i$ rather than x_{iF} on these reactions.

Values of x_{iF} and $\tilde{\chi}_i$ are compared in Fig. 7.14 for reactions R9, R10 and R11. It can be seen that in each case the lowest frequency modes get a slight boost compared to the higher frequency modes, but not enough to impact mode selection. Implementing this more sophisticated approach thus has no effect on the choice of active modes for these reactions. Overall, it is clear that whilst comparing values of $\tilde{\chi}_i$ to perform mode selection is the most rigorous method, using values of x_{iF}^{approx} will lead to the same selection in all but the most extreme cases. It does, however, provide a dimensionless property, that can more easily be compared across reactions.

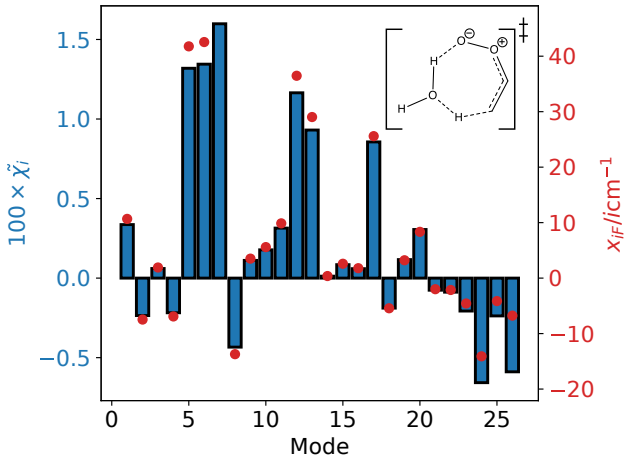
7.9 Conclusions

In this chapter, we have motivated, developed and analysed a reduced-dimensionality approach to SCTST.

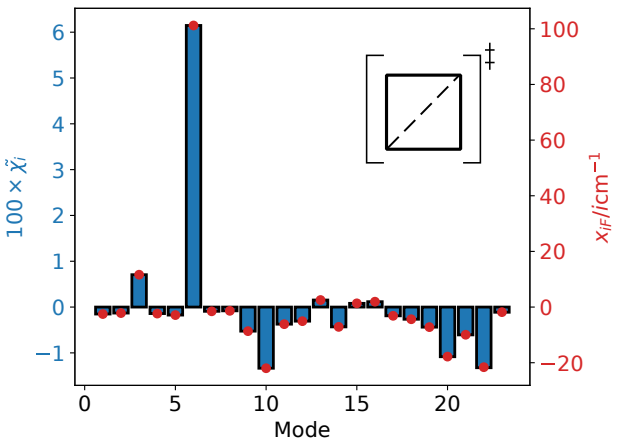
Through an approximate signposting method, we can identify the key modes to include in the calculation cheaply. This requires just two Hessian calculations on top of *ab initio* data required for TST rates. We have tested this approximation, and shown it is excellent at indicating the key coupled modes. We then outlined the framework in which RD-SCTST calculations can be performed, being careful to allow for consistent anharmonic treatment between the reactant and transition states.



(a) Reaction R9.



(b) Reaction R10.



(c) Reaction R11.

Figure 7.14 Comparison of x_{iF} (red dots) and $\tilde{\chi}_i$ (blue bars) for three transition states. Note the different scales. The same modes are identified as significant using both methods.

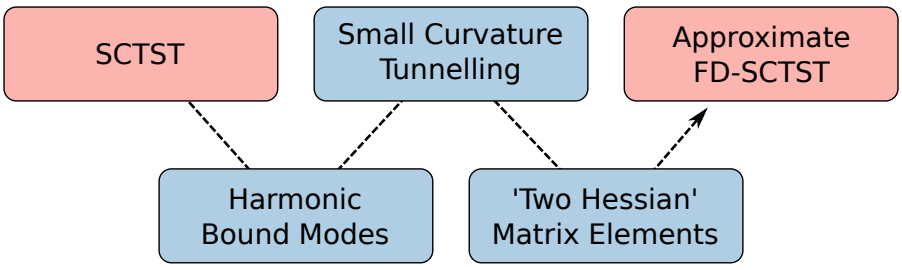
Testing this method on the Criegee decay processes discussed in Chapter 5 as well as a unimolecular carbene rearrangement shows this method can be very powerful. In some cases, FD quality results can be achieved with just a 2D-SCTST calculation. We further investigated a more rigorous signposting method, that accounts for the impact of excited states, but showed it indicates modes in agreement with those found using the simpler procedure.

Overall it is clear that RD-SCTST presents a powerful method, which may prove essential for accurate treatments of large molecules for which 1D-SCTST fails to capture the key dynamics.

Chapter 8

Approximate SCTST in full dimensions

For some systems, a reduced dimensionality treatment is insufficient to capture the key physics of a reaction, for example those reactions where many or all vibrational modes are strongly coupled to the reaction mode. These systems motivate the development of an alternative approximate treatment to that of Chapter 7, whereby rather than treating a subset of the DoFs exactly, we treat all of the DoFs approximately. In this chapter we show how such an approximation can be made, giving an approximate FD-SCTST rate (AFD-SCTST), for very little computational expense.



Abstract 8 A summary of the approximations in the AFD-SCTST method

8.1 Introduction

In Chapter 7 we showed that by identifying the most significant bound modes in a reaction, and treating just these modes explicitly, an SCTST calculation can be greatly simplified. We found, however, that some reactions require many modes to be included to reach FD quality results. An alternative approximate FD-SCTST method ('AFD-SCTST') can be developed, which allows for a full-dimensional picture of the reaction, whilst reducing the number of *ab initio* calculations significantly. This can be achieved by a combination of three approximations previously discussed separately in this thesis:

1. A small-curvature approximation, in which only the lowest energy vibrational state in the TS is treated explicitly, and so higher order states are included only approximately. This approximation was introduced in Chapter 4 and utilised in Chapter 5.

2. A harmonic approximation, in which all the bound degrees of freedom are treated as separable from one another, but coupled to the reaction mode. This approximation is well tested, for example in Transition State Theory and instanton rate theory, and benefits from a cancellation of errors when harmonic partition functions for reactant and transition states are used.

3. The Two Hessian approximation for the matrix elements, x_{iF}, requiring just two, rather than $2F$ displaced Hessian matrices, as introduced in Chapter 7.

Using these approximations, a calculation which requires just four Hessian calculations in total can be derived. It has the computational expense of a 1D+ calculation, but approximately incorporates curved reaction path effects. Note that the combination of all three approximations are required in order to make this computational saving, and removing any one of these approximations would require calculation of the full $2F$ set of Hessian matrices required for a FD calculation. In the following sections, the AFD result is first derived, then we test the method to evaluate its accuracy.

8.2 Theory

To reach the AFD result, we begin with the full-dimensional SCTST expression for the rate, written as a sum of one-dimensional rate constants, derived in Chapter 4:

$$k_{\mathrm{FD}} = \sum_{\{n\}'} k_{\mathrm{1D}}(V^{\mathrm{eff}}_{\{n\}'}, \omega^{\mathrm{eff}}_{\{n\}'}). \tag{8.1}$$

Then, as outlined in Chapter 4, using the small-curvature approximation gives:

$$k^{\mathrm{SCT}}_{\mathrm{FD}} = Q^{\mathrm{TS}}_{\mathrm{vib}} k_{\mathrm{1D}}(V^{\mathrm{eff}}_0, \omega^{\mathrm{eff}}_0) \tag{8.2}$$

We then apply the harmonic approximation such that the vibrational partition function becomes an analytical function of the harmonic frequencies:

$$k^{\mathrm{SCT}}_{\text{harm - FD}} = Q^{\mathrm{TS}}_{\text{harm-vib}} k_{\mathrm{1D}}(V^{\mathrm{eff}}_0, \omega^{\mathrm{eff}}_0) \tag{8.3}$$

with

$$V^{\mathrm{eff}}_0 = \Delta V_f + \frac{\hbar}{2} \sum_{i=1}^{F-1} \omega_i \tag{8.4}$$

and:

$$\omega^{\mathrm{eff}}_0 = \omega_F + \frac{1}{2} \sum_{i=1}^{F-1} x_{iF}. \tag{8.5}$$

The harmonic small-curvature rate is therefore given by a 1D-SCTST rate constant with the harmonic adiabatic reaction barrier height and an adjusted effective frequency:

$$\omega_F \rightarrow \omega_F + \sum_{i=1}^{F-1} \frac{1}{2} x_{iF}. \tag{8.6}$$

In general, 2F Hessians are required to determine the full set of derivatives needed to calculate all the x_{iF}. This is the same number required for a FD-SCTST calculation. We can, however, use the Two Hessian approximation from Chapter 7 to reduce this cost to just two Hessians. The AFD method is therefore given by a 1D-SCTST calculation with the replacement of the reaction frequency as:

$$\omega_F \rightarrow \omega_F + \frac{1}{2} \sum_{i=1}^{F-1} x^{\mathrm{approx}}_{iF}. \tag{8.7}$$

8.3 Results

The AFD method was tested on the two Criegee decay reactions studied in Chapters 5 and 7; the methylated unimolecular Criegee decay, R9, and the water catalysed process, R10, as well as the unimolecular carbene decay reaction, R11. Full and reduced dimensional rate constants for these reactions have been evaluated in previous chapters.

Table 8.1 shows how the individual values of x_{iF} contribute to the frequency adjustment, given by Eq. 8.7, for reactions R9 and R10. Equivalent data for reaction R11 is given in Table 7.2 in Chapter 7. The approximate values clearly lead to overestimation of the frequency adjustment. This is most significant for the water catalysed decay reaction, where many modes contribute significantly. Whilst quite accurate for individual, large values of x_{iF}, the errors accumulate for smaller values. The resulting effective frequencies are shown in Table 8.2.

Figs. 8.1 and 8.2 show the performance of AFD-SCTST for reactions R9, R10 and R11.

For the two Criegee reactions, AFD seems to perform well. Both lead to overestimation of the FD rate, but give errors smaller than the 1D+ method, which has the same computational expense. For reaction R11, however, it is not just the Two Hessian approximation that is inaccurate, but the harmonic and small-curvature approximations. Here, the AFD method seems to have very little effect, and the 2D method is far more preferable.

Since in each case the Two Hessian method clearly overestimates the frequency adjustment significantly, it is not clear that this method can be reliable in general.

8.4 Conclusions

In this chapter we have derived an approximate route to SCTST in which *all* degrees of freedom are included in the SCTST calculation, but only four Hessians are required in total. It relies on three approximations together.

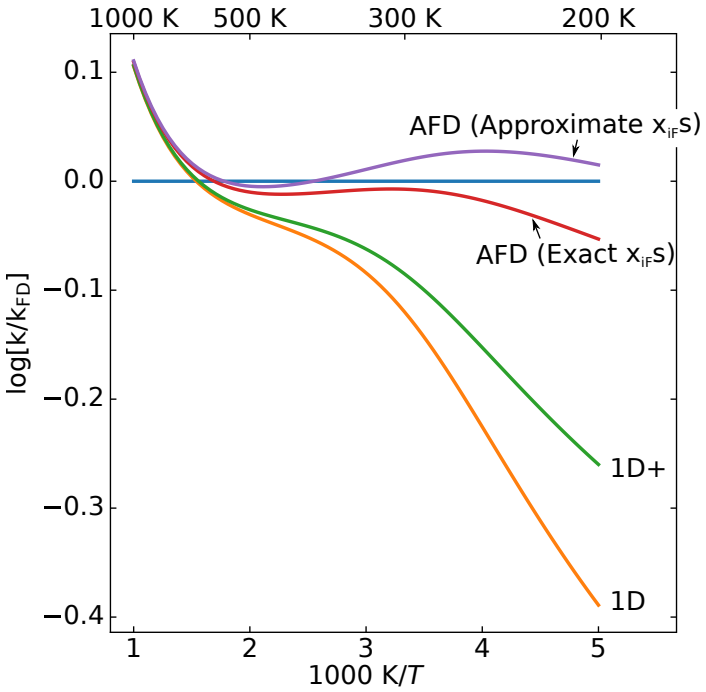
Table 8.1 How the x_{iF} terms modulate the effective imaginary frequency in AFD-SCTST, values in i cm^{-1}.

Reaction R9		
ω_i	x_{iF}	x_{iF}^{approx}
3240	-5.40	-0.45
3188	-0.10	0.24
3161	-1.29	-1.3
3119	-10.15	-3.11
3078	-0.65	-0.6
1891	98.09	93.3
1566	-0.38	-2.72
1530	1.10	0.15
1491	-0.46	0.18
1480	-0.71	-1.07
1417	0.62	0.55
1377	2.13	1.5
1352	2.49	1.83
1093	-2.52	-3.86
1057	-6.74	-7.47
1006	3.68	1.44
990	-0.66	-1.63
955	-0.69	3.52
872	11.14	5.75
758	7.10	-3.01
674	-3.80	-4.93
549	-9.78	-11.18
515	-6.79	-9.5
358	-1.86	-0.99
290	0.21	0.14
136	-0.55	-1.15
$\frac{1}{2}\sum x_{iF}$	37.0	27.8

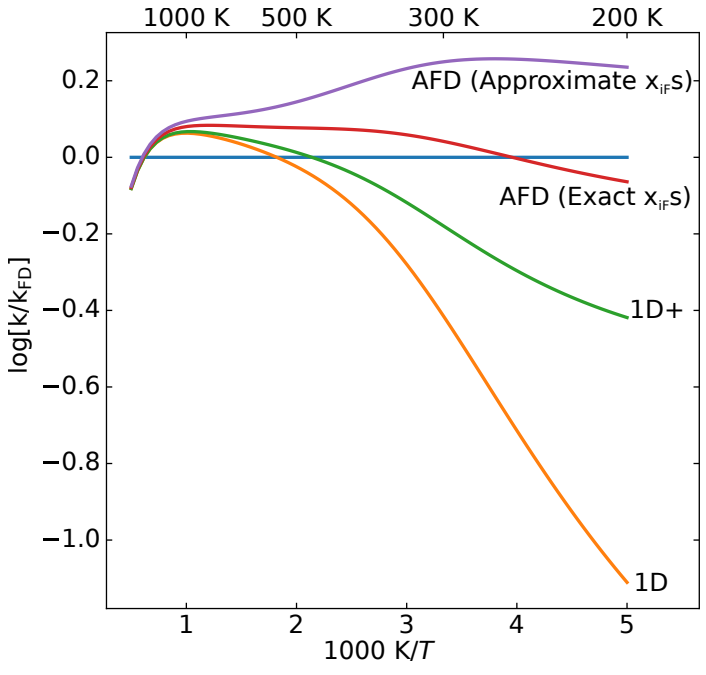
Reaction R10		
ω_i	x_{iF}	x_{iF}^{approx}
3831	10.67	-1.55
3271	-7.47	-2.07
3195	1.91	-0.61
3142	-6.91	-3.97
1745	41.77	74.83
1650	42.55	49.81
1632	50.57	69.76
1573	-13.71	-11.59
1448	3.51	4.43
1368	5.59	2.85
1325	9.87	10.9
1264	36.47	61.29
1203	29.03	45.58
1037	0.37	-0.5
1022	2.59	0.53
932	1.79	1.69
886	25.59	32.51
766	-5.44	9.76
677	3.22	10.03
654	8.34	13.52
598	-2.0	7.82
508	-2.14	3.06
434	-4.57	7.04
415	-14.1	16.95
312	-4.14	4.65
192	-6.77	0.42
$\frac{1}{2}\sum x_{iF}$	103.3	203.6

	1D	AFD (Exact x_{iF}s)	AFD (Two Hessians)
R9	1501	1529	1538
R10	1587	1690	1790
R11	823	819	826

Table 8.2 Imaginary frequencies for AFD-SCTST, in $i$cm^{-1}



(a) Reaction R9.



(b) Reaction R10.

Figure 8.1 Comparison of 1D, FD and AFD-SCTST for two Criegee decay processes.

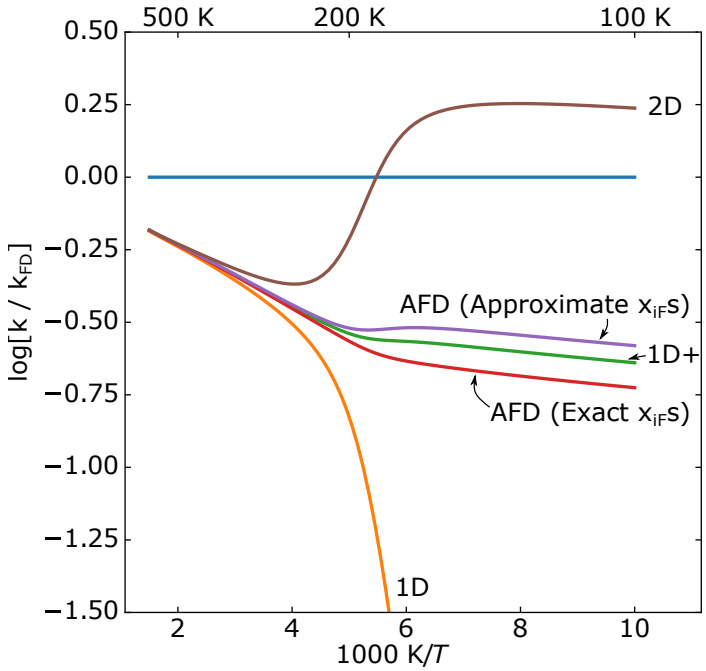


Figure 8.2 Comparison of 1D, FD, and AFD-SCTST for the cyclocarbene rearrangement, R11.

We have found the method performs well for two Criegee decay reactions, but has little effect on the 1D+ rate for the unimolecular cyclocarbene rearrangement.

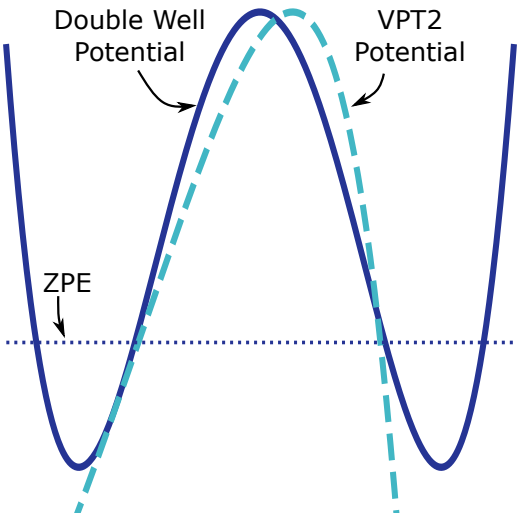
In order for this to become a useful method, more testing is required to determine the effect of each of the three approximations on rates, and the likelihood of each being accurate. The Two Hessian approximation is a pragmatic computational saving, rather than one based on a meaningful physical approximation; as such its errors are not easily understood or controlled. The Two Hessian approximation remains excellent as a signposting method (as discussed in Chapter 7), but may be insufficiently accurate to be used directly in SCTST calculations.

As such, it is clear that SCTST in reduced dimensions remains the most promising approximate approach to SCTST.

Chapter 9

Semiclassical Perturbation Theory for tunnelling splittings

In this chapter, we derive a semiclassical expression for tunnelling splittings in one-dimensional double well potentials, that improves upon the commonly used Lifshitz-Herring formula. We then show how the equations of SCTST can be recast to estimate tunnelling splittings for complex multi-dimensional systems. By testing this method on three systems - a model one-dimensional double well potential, the isomerisation of malonaldehyde, and the isomerisation of tropolone - we show the method to be efficient and reliable.



Abstract 9 The Semiclassical Perturbation Theory method can be used to estimate energy splittings in double well potentials.

9.1 Introduction

Tunnelling splittings are a spectroscopically observable property of chemical systems in which tunnelling between degenerate minima on the potential energy surface is possible. They can be thought of as a result of quantum interactions between two potential wells connected by a tunnelling path; the overlap of two localised vibrational wavefunctions (one in each potential well) leads to symmetric and anti-symmetric eigenstates, separated by an energy Δ. Tunnelling splittings are of importance in understanding the dynamics of complex molecular systems[116, 117, 304], and their calculation provides a rigorous test of potential energy surfaces and tunnelling theories.

A range of methods to determine tunnelling splittings theoretically have been developed. The most accurate (but computationally expensive) of these requires solving the nuclear Schrödinger equation on an accurate multidimensional potential energy surface (PES) using, for example, diffusion Monte Carlo (DMC)[11, 118–120], the multi-configuration time-dependent Hartree (MCTDH)[121] or other[122–126] methods. Here the lowest lying vibrational energy levels are accurately determined, which yield Δ directly. Whilst accurate, this approach requires a full-dimensional PES and expensive dynamical calculations, and so is limited to small systems, for which a PES exists, for example the water dimer[305–307].

More recently, semiclassical methods based on the path-integral formalism of quantum mechanics have been developed for the calculation of splittings[128]. Instanton methods[72, 117, 129–132] determine a 'dominant' tunnelling path by finding the trajectory of least action on the PES, from which Δ can be found directly. This still requires a full PES, or many on-the-fly calculations, which may be prohibitively expensive. Since the instanton at zero temperature is required, the instanton is spread out, and a wide region of the potential energy surface is needed.

Much cheaper methods rely on reducing the system to a one-dimensional form, for example by using the minimum energy path[308, 309] or within the sudden approximation[310, 311], and estimating the splitting using the well known

Lifshitz-Herring formula[137, 312, 313]. Some methods adjust for reaction path curvature effects[314–316], although this may be a significant expense, involving tens of thousands of *ab initio* calculations[201].

Reaction path curvature effects must be accounted for (allowing for corner-cutting trajectories), in order to achieve quantitative tunnelling splittings[316]. Accounting for these curvature effects in a systematic, computationally tractable way remains a significant problem, both in reaction kinetics[202, 226] as well as in calculating tunnelling splittings.

In this chapter we first illustrate the deficiency in the commonly used Lifshitz-Herring formula and show the one-dimensional WKB splitting can instead be determined with no approximations by using the known WKB connection formulae. We will see how this is equivalent to the Lifshitz-Herring formula to first order, and show the impact of the improved formula on a model one-dimensional potential.

We then illustrate how the equations of SCTST can be recast to calculate these splittings analytically as a function of the barrier height, vibrational frequencies and anharmonic constants. This method accounts for reaction path curvature and anharmonic effects, and does not assume the separability of the reaction mode from the other vibrational degrees of freedom. The approach is then applied, in full- and reduced-dimensions, to two multidimensional molecular systems - the isomerisation of malonaldehyde and tropolone - for which detailed experimental comparisons are possible.

9.2 Breakdown of the Lifshitz-Herring formula

In order to use the perturbation theory approach of SCTST to estimate tunnelling splittings, we first need to determine an expression for Δ as a function of $\theta(E)$. The commonly used Lifshitz-Herring formula[131, 132, 137, 201, 308–319] is given by:

$$\begin{aligned}\Delta &= \frac{\omega_R}{\pi}\exp\left[-\int_a^b p(x)dx\right] \\ &= \frac{\omega_R}{\pi}\exp\left[-\int_a^b \sqrt{2m\,(V(x)-E_0)}dx\right] \\ &\equiv \frac{\omega_R}{\pi}\exp\left[-\theta(E_0)\right]\end{aligned} \tag{9.1}$$

where ω_R is the frequency of the reaction mode in the reactant state, and E_0 is the zero-point energy of the well without tunnelling. This gives qualitatively incorrect splittings for trajectories near and above the barrier top. We can illustrate this by evaluating Eq. 9.1 on a model one-dimensional potential for which exact quantum results can be determined. Eq. 9.1 was evaluated numerically for the potential:

$$V(x) = V_0\left(\frac{x^2}{x_0^2}-1\right)^2, \tag{9.2}$$

for a range of barrier heights, V_0. x_0 was chosen such that the harmonic ZPE remains constant between them:

$$x_0 = 5\sqrt{V_0} \implies \text{Harmonic ZPE} \approx 0.283, \tag{9.3}$$

and the splittings were compared to exact quantum splittings calculated by direct diagonalisation of the Hamiltonian in a distributed Gaussian basis set. From Fig. 9.1, it is clear that the Lifshitz-Herring formula is excellent in the case of the large barriers, however it significantly overestimates the splitting when the ZPE is close to the barrier top; it differs from the exact quantum result for $V_0 = 0.25$ by nearly a factor of two.

The origin of this deficiency is clear from studying the periodic orbit derivation of Miller[313]. To reach Eq. 9.1, only periodic orbits that do not 'bounce' in the classically forbidden region are accounted for. A more accurate formula can therefore be found by including more complex trajectories in the semiclassical Green's function. This improved approach is outlined in Appendix D, and an improved periodic orbit formula is obtained for small splittings:

$$\Delta = \frac{\omega_R}{\pi}\frac{e^{-\theta}}{1+e^{-2\theta}}. \tag{9.4}$$

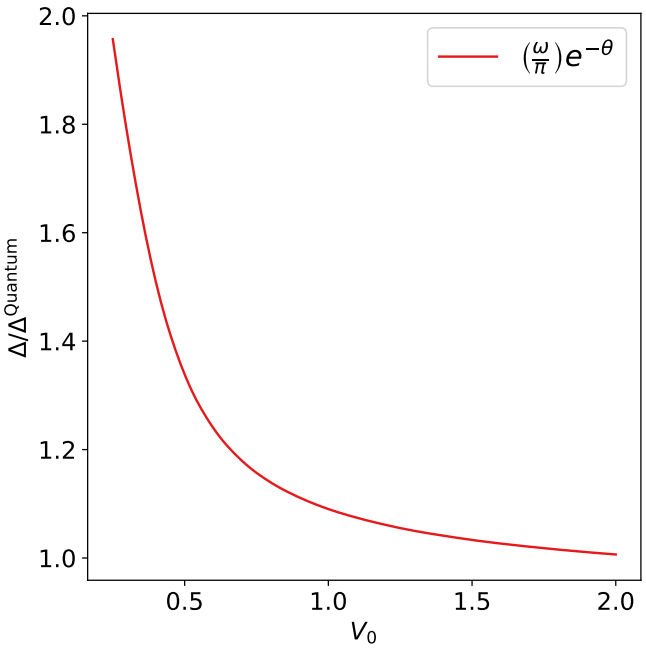


Figure 9.1 Performance of the Lifshitz-Herring formula .

The WKB splitting can, however, be found with no approximations by using the well known WKB connection formulae. In the following section we will derive this 'exact' WKB expression for tunnelling splittings in a double well potential. We will see how this is equivalent to Eq. 9.1 and 9.4 in the limit of large θ, and show the impact of the improved formula on the model one-dimensional potential.

9.3 An 'exact' WKB tunnel splitting

9.3.1 WKB quantisation in the double well

In order to find the WKB quantisation condition, we begin by studying the known WKB wavefunctions in the left and right hand wells of a symmetric double well potential at an energy, E, with classical turning points at (x_0, x_1, x_2, x_3) as shown in Fig. 9.2.

In the left hand well, $[x_0 \to x_1]$, the wavefunction is given by the known WKB result [138]:

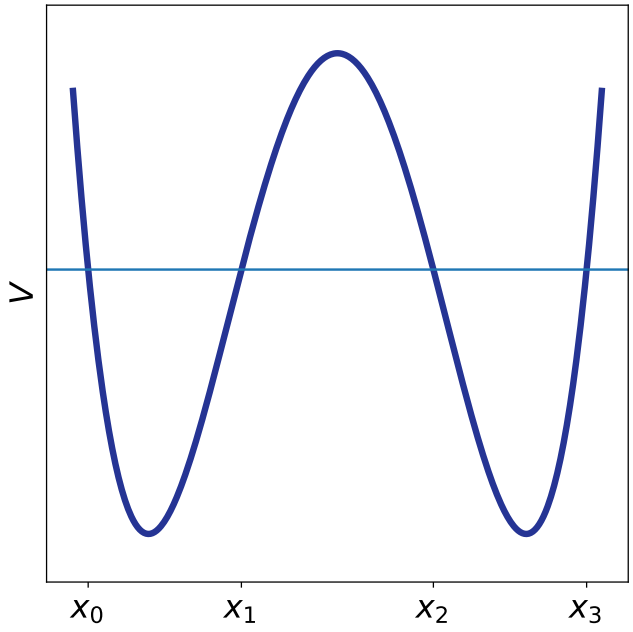


Figure 9.2 A symmetric double well potential, with the classical turning points labelled.

$$\begin{aligned}\psi_L(x) &\propto \sin\left[\frac{\pi}{4}+\int_{x_0}^{x}k(x)dx\right]\\ &= \sin\left[\frac{\pi}{4}+\phi+\int_{x_1}^{x}k(x)dx\right]\\ &= A\exp\left[\int_{x_1}^{x}k(x)dx\right]+B\exp\left[-\int_{x_1}^{x}k(x)dx\right]\end{aligned} \tag{9.5}$$

where

$$k(x)\equiv\sqrt{2(E-V(x))} \qquad \phi\equiv\int_{x_0}^{x_1}k(x)dx \tag{9.6}$$

and

$$A=\frac{e^{i\phi+i\pi/4}}{2i} \qquad B=-\frac{e^{-i\phi-i\pi/4}}{2i}. \tag{9.7}$$

Propagating ψ_L across the barrier region to the right hand well, $[x_2\to x_3]$, the wavefunction can be written:

$$\psi_R = C\exp\left[\int_{x_2}^{x}k(x)dx\right]+D\exp\left[-\int_{x_2}^{x}k(x)dx\right] \tag{9.8}$$

where C and D are given by the connection formulae for transmission through a barrier[320]:

$$\begin{pmatrix} C \\ D \end{pmatrix} = e^{\theta} \begin{pmatrix} \sqrt{1+e^{-2\theta}} & -i \\ i & \sqrt{1+e^{-2\theta}} \end{pmatrix} \begin{pmatrix} A \\ B \end{pmatrix} \tag{9.9}$$

where $\theta = \theta(E)$ is the usual barrier penetration integral. The transmitted wavefunction is therefore given by:

$$\begin{aligned} \psi_R = &\left(\sqrt{1+e^{-2\theta}}e^{2i\phi}+1\right)\frac{e^{\theta}}{2}\exp\left[-i\left(\frac{\pi}{4}+\int_x^{x_3}k(x)dx\right)\right] \\ &+\left(\sqrt{1+e^{-2\theta}}e^{-2i\phi}+1\right)\frac{e^{\theta}}{2}\exp\left[i\left(\frac{\pi}{4}+\int_x^{x_3}k(x)dx\right)\right]. \end{aligned} \tag{9.10}$$

Comparing this to the known form of the wavefunction in the right hand well:

$$\psi_R \propto \sin\left[\frac{\pi}{4}+\int_x^{x_3}k(x)dx\right], \tag{9.11}$$

requires:

$$\begin{aligned} \sqrt{1+e^{-2\theta}}e^{2i\phi}+1 &= -\sqrt{1+e^{-2\theta}}e^{-2i\phi}-1 \\ \implies \cos(2\phi) &= \frac{-1}{\sqrt{1+e^{-2\theta}}} \end{aligned} \tag{9.12}$$

Finally, defining:

$$\tan\chi = e^{-\theta} \tag{9.13}$$

the quantisation condition becomes:

$$\phi(E) = \left(N+\frac{1}{2}\right)\pi \pm \frac{\chi}{2} \tag{9.14}$$

where N is a positive integer. This is the rigorous uniform WKB quantisation condition for a symmetric double well potential. Note that in the limit of a large and wide barrier ($\theta \to \infty$) the usual Bohr-Sommerfeld quantisation for a single well is returned.

Eq. 9.14 can be solved numerically to determine the exact WKB energy levels, from which the splitting is directly calculable. Using the quartic well potential, we

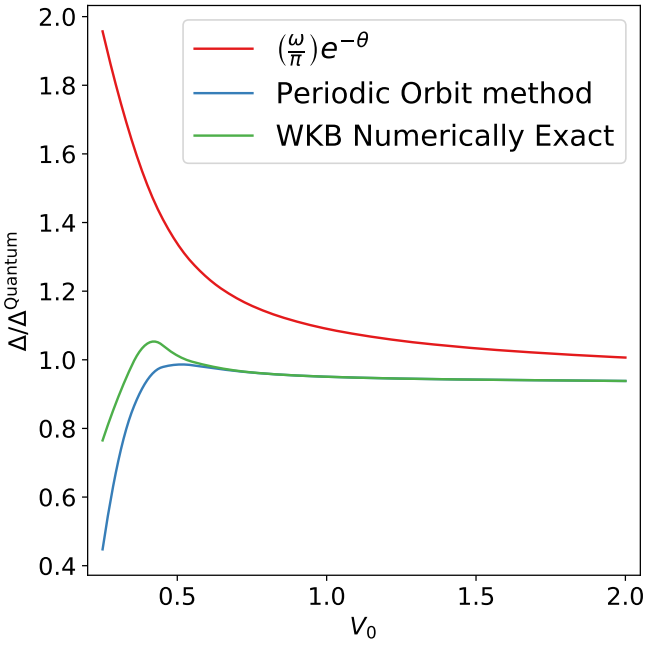


Figure 9.3 Comparing numerical results for the one-dimensional model potential, Eq. 9.2.

can compare the 'exact' WKB method with the Lifshitz-Herring formula, Eq. 9.1, and the approximate expression from the full periodic orbit analysis, Eq. 9.4. This is shown in Fig. 9.3. Clearly the improved formula performs significantly better, particularly for small barriers. The periodic orbit and exact WKB approaches agree well for barriers larger than 0.5, but the periodic orbit approach significantly underestimates the splitting for small barriers.

9.3.2 Determining the splitting

In practice, for the study of complex chemical systems, it is useful to recast the exact result to allow for an approximate, analytic treatment. Eq. 9.14 can be rewritten in terms of the energy levels of a well without tunnelling, given by the Bohr-Sommerfeld quantisation condition:

$$\phi(E) = \left(n(E) + \frac{1}{2}\right)\pi \tag{9.15}$$

where $n(E)$ is the inverse function of $E_0(n)$ for the energy levels of the unsplit well. From Eq. 9.14 and eliminating $\phi(E)$, we find:

$$n(E) = N \pm \frac{\chi}{2\pi} \tag{9.16}$$

and therefore:

$$E(N) = E_0\left(N \pm \frac{\chi}{2\pi}\right) \tag{9.17}$$

The splitting of the N^{th} vibrational state can therefore be found:

$$\Delta(N) = E_0\left(N + \frac{\chi}{2\pi}\right) - E_0\left(N - \frac{\chi}{2\pi}\right). \tag{9.18}$$

This therefore gives the tunnelling splitting for any well for which the energy levels of the well without splitting are known (or approximately known).

A harmonic well approximation

In the harmonic case, the unsplit energy levels are given by:

$$E_0(n) = \omega\left(n + \frac{1}{2}\right) \tag{9.19}$$

and therefore the ground state splitting is given by:

$$\begin{aligned}\Delta^{\text{harmonic}} &= \omega\left(N + \frac{\chi}{2\pi} + \frac{1}{2}\right) - \omega\left(N - \frac{\chi}{2\pi} + \frac{1}{2}\right) \\ &= \frac{\omega}{\pi}\arctan\left(e^{-\theta}\right)\end{aligned} \tag{9.20}$$

The connection between Eq. 9.20 and 9.1 is clear by expanding Eq. 9.20 in powers of $e^{-\theta}$:

$$\Delta^{\text{harmonic}} \approx \frac{\omega}{\pi}\left(e^{-\theta} - \frac{e^{-3\theta}}{3} + \ldots\right). \tag{9.21}$$

It is clear that Eq. 9.1 is a first order approximation to Eq. 9.20, for large θ.

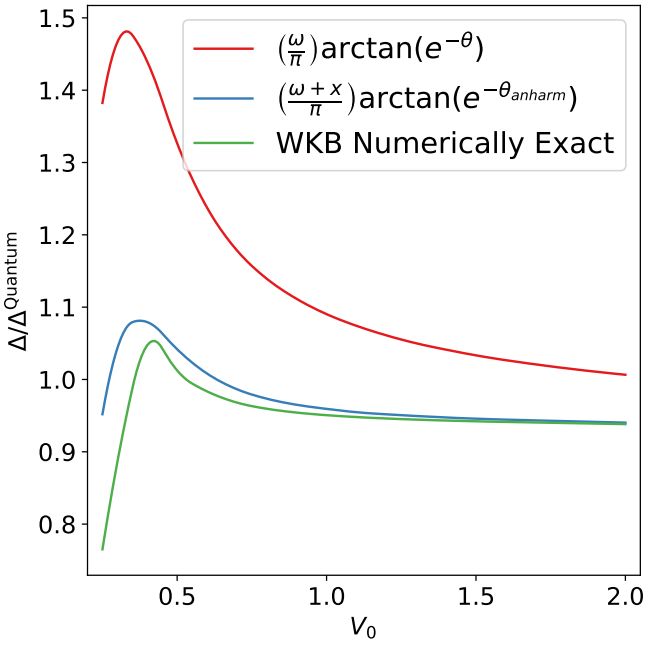


Figure 9.4 Comparing numerically exact results with differing well approximations for the potential, Eq. 9.2. θ is the penetration integral calculated at the harmonic ZPE, whilst θ_{anharm} is calculated at the anharmonic ZPE.

An anharmonic well approximation

The well model can be improved with a Morse potential for which the unsplit energy levels are given by:

$$E_0(n) = \omega\left(n+\frac{1}{2}\right) + x\left(n+\frac{1}{2}\right)^2. \tag{9.22}$$

This gives a ground state splitting:

$$\Delta^{\text{Morse}} = \frac{\omega+x}{\pi}\chi = \frac{\omega+x}{\pi}\arctan\left(e^{-\theta}\right) \tag{9.23}$$

9.3.3 Numerical results

Δ^{harmonic}, Δ^{Morse}, and the exact WKB splittings are compared for the one-dimensional model potential in Fig. 9.4. Whilst the harmonic well approximation is quite severe, the Morse well approximation is excellent.

9.4 Semiclassical Perturbation Theory of tunnelling splittings

Eqs. 9.20 and 9.23 can be used, alongside the perturbation theory approach of SCTST to determine Δ analytically, as a function of the barrier height, vibrational frequencies and anharmonic constants. This is a multidimensional generalisation of the WKB splitting. $\theta(E)$ can be calculated using Eq. 2.30, at an energy equal to the anharmonic zero point energy of the reactant. ω_R corresponds to the reaction mode frequency in the reactant state, identified as the vibrational mode of lowest-frequency that is of the same symmetry as the imaginary mode at the transition state[308, 309]. The splitting is thus determined analytically, without assuming the separability of the Hamiltonian such that anharmonicity and corner-cutting effects are accounted for[3, 79]. We will refer to this as the Semiclassical Perturbation Theory (SPT) route to tunnelling splittings.

In this work we calculate splittings through the vibrational ground state of the TS, and study systems with just two degenerate minima. It is relatively straightforward to extend this to systems with multiple degenerate minima, connected by various transition states (for example, in water clusters), for example using a Hückel-type approximation[117, 308, 309].

We can gain insight into the accuracy of SPT, by comparison to exact quantum results for the one-dimensional double well potential, Eq. 9.2. SPT parameters for this potential can be calculated analytically. Since higher order derivatives are easy to obtain for this potential, we can also determine the impact of the level of vibrational perturbation theory on the predicted splitting, as well as effect of the harmonic and anharmonic well approximations.

Fig. 9.5a compares SPT results with VPT0, VPT2 and VPT4 approximations. It is clear the VPT0 (parabolic) treatment is insufficient to give quantitative splittings. For the larger barriers, the ZPE lies well below the barrier top, and so the barrier is less well described by the derivatives of the PES at the TS. Increasing the level of perturbation theory leads to a better description of the barrier, and more accurate splittings; the VPT2 method remains within 60% of the exact quantum results over

the whole range, and the VPT4 results stay within 20%. Increasing the level of perturbation theory also has the effect of an improved anharmonic ZPE correction, which has a significant impact for barrier heights close to the ZPE.

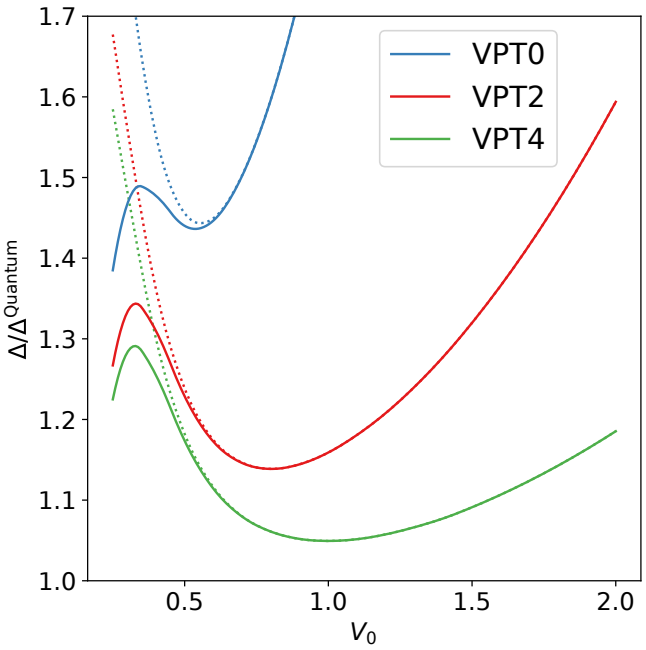
Fig. 9.5b shows how the SPT treatment is improved with a Morse well description, using Eq. 9.23. It offers a slight improvement for large barriers, and a significant improvement for small barriers.

The success of VPT2-SPT can be understood by visualising the VPT2 barriers. Since, VPT2-SPT gives the exact value of $\theta(E)$ for an inverted Morse barrier[3], this can illustrate the 'effective barrier' used in the calculation. This allows for a graphical comparison to the quartic barrier (however, note that in order to perform an SCTST calculation no barrier need be explicitly constructed - its purpose here is simply illustrative). These are shown in Fig. 9.6. The VPT2 effective barrier clearly provides a good description of the model potential in the tunnelling region, and is able to accurately predict the barrier width at the ZPE. Increasing the level of perturbation theory will give an even better fit.

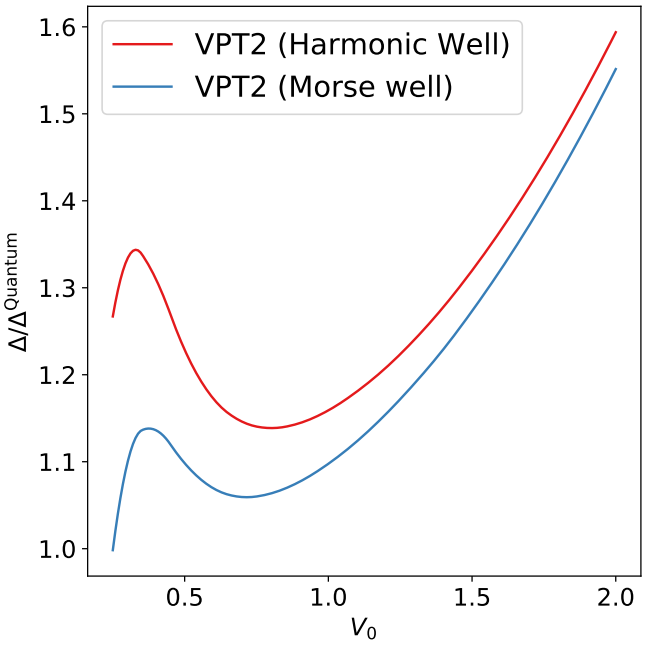
Note that the error due to the perturbation theory approximation is very sensitive to the exact form of the model potential used. It is thus not easy to precisely quantify this error for real, multidimensional reaction potentials. These tests, however, indicate VPT2 is likely to be sufficiently accurate to be useful for these purposes. It is possible that a deep tunnelling correction, analogous to that of Wagner for bimolecular reactive systems[87], may be able to further improve these results for large barriers.

9.5 Application to malonaldehyde

We can now test VPT2-SPT for a real chemical system; the isomerisation of Malonaldehyde. Here we use the harmonic well approximation as the multidimensional generalisation of the Morse well approach is less convenient. Malonaldehyde shows a tunnelling splitting through an intramolecular H-transfer, as shown in Fig. 9.7. The splitting has been investigated experimentally[112–114] and theoretically[120, 121, 303, 321–324], and is a common test case for tunnelling



(a) Comparison of level of perturbation theory, using the harmonic well approximation. Dashed lines show the corresponding Lifshitz-Herring result.



(b) Comparison of harmonic and anharmonic well approximations in VPT2-SPT.

Figure 9.5 SPT performance on the model one-dimensional potential.

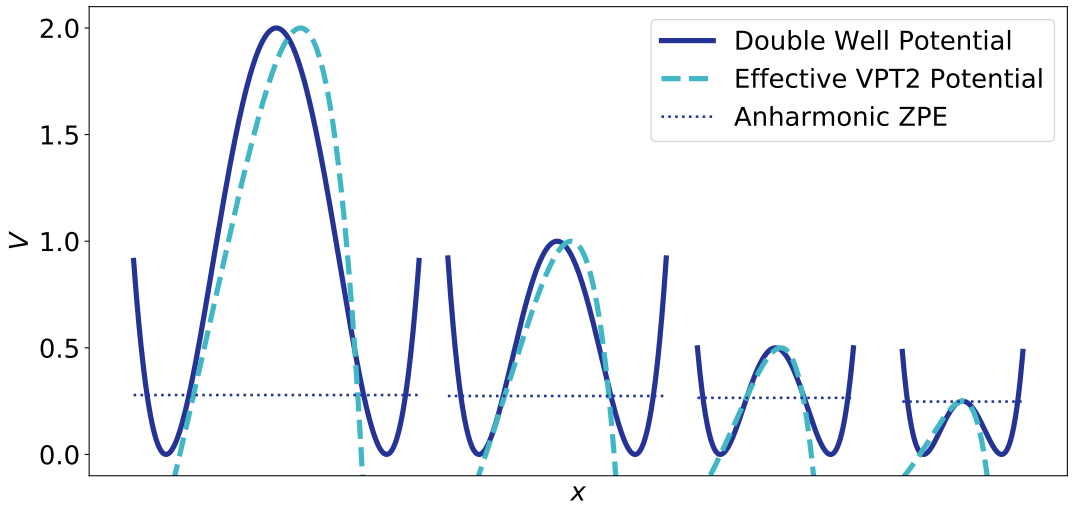


Figure 9.6 The effective VPT2-SPT well potential for the one-dimensional model potential.

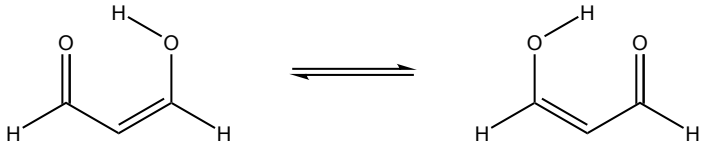


Figure 9.7 Isomerisation of malonaldehyde.

splitting theories.

9.5.1 Computational methods

Molecular structures were optimised, and frequencies calculated at the MP2 level of theory, and barrier heights were corrected using CCSD(T) calculations at the MP2 optimised geometry.

Calculations were performed using the cc-pVTZ, and the aug-cc-pVQZ basis sets[169], to determine the sensitivity of these calculations to basis set size. For the aug-cc-pVQZ calculations, anharmonic constants from the cc-pVTZ calculations were used, due to the prohibitive expense of using the larger basis set. This method of using a cheaper method to determine just the anharmonic constants has been previously tested successfully[2], as discussed in Chapter 5.

9.5.2 Results

SPT parameters found from the *ab initio* calculations are shown in Table 9.1, for both the isomerisation shown in Fig. 9.7, and for the deuterium-substituted isotopologue. Comparing one-dimensional and full-dimensional results shows the effect of corner-cutting through the potential energy surface. Including all degrees of freedom in the anharmonic calculation leads to a larger effective barrier height, and a less negative anharmonic constant (corresponding to a narrower barrier). The effective imaginary frequency, $\Omega_{\{0\}}$, itself is relatively unchanged, since the effect of the x_{iF}s largely cancel out (see Fig. 9.8).

	SPT Level	V_0 (kJ/mol)	$\Omega_{\{0\}}$ (cm^{-1})	x_{FF} (cm^{-1})	ω_R (cm^{-1})
H-transfer	1D	5.64	1185	-319	290
	FD	6.37	1187	-274	290
D-transfer	1D	9.28	887	-190	280
	FD	10.0	873	-145	280

Table 9.1 Adiabatic barrier heights, effective imaginary frequencies and anharmonic constants for aug-cc-pVQZ levels of theory for malonaldehyde.

Table 9.2 shows good agreement between SPT and experiment. It is clear by comparing cc-pVTZ and aug-cc-pVQZ results that using high quality *ab initio* calculations is essential. This is straightforward in SPT due to the relatively few calculations required compared to other methods. The MCTDH, DMC and instanton calculations were all performed in full dimensions on the same surface by Wang *et al*[11], fit to 11,147 near basis-set-limit frozen-core CCSD(T) electronic energies. SPT agrees within 15% of the experimental value for the H-transfer, and within 30% for the deuterium transfer. This is similar to the errors obtained by using different *ab initio* potentials; for example the augmented and non-augmented basis set results differ by about 30%.

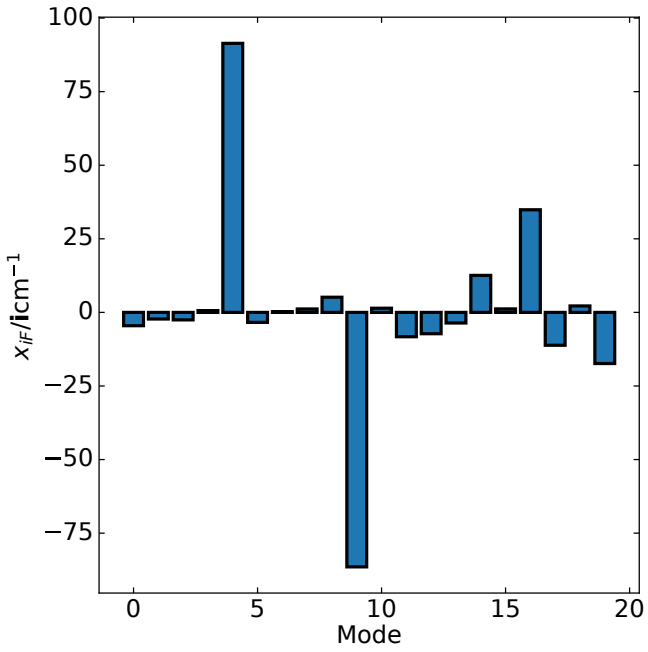


Figure 9.8 Values for x_{iF} for malonaldehyde at the cc-pVTZ level of theory. Modes labelled in order of descending frequency.

9.6 Application to tropolone

Tropolone also presents a tunnelling splitting, although much smaller than that of malonaldehyde, due to the larger barrier to isomerisation. The tropolone motif is found in many natural products, and has known biological activity[326], so has been the subject of experimental[115, 327] and theoretical[310, 311, 328, 329] interest. Its structure is shown in Fig. 9.9. For this system, with 15 atoms, a full-dimensional treatment using a large basis set is prohibitively expensive. Here we present results of using SPT in one dimension, as well as the 1D+ formalism developed for SCTST in Chapters 5 and 7. Thus vibrational couplings are partially accounted for, and a better estimate of the shape of the barrier is used. The computational cost is just two Hessian calculations more than 1D SPT , and has been shown to be a useful correction to 1D-SCTST in kinetics[2, 4].

SPT parameters are shown in Table 9.3 and the resultant splittings are shown in Table 9.4. 1D and 1D+ SPT perform very well for the H-transfer reaction, both lying within 8% of the experimental values. Again we find the agreement is less

	Method	Reference	Δ / cm^{-1}
H-Transfer	1D SPT (cc-pVTZ)		**26.48**
	1D SPT (aug-cc-pVQZ)		**22.23**
	FD SPT (cc-pVTZ)		**21.69**
	FD SPT (aug-cc-pVQZ)		**18.69**
	MCTDH (CCSD(T) based PES)	Schröder, 2011[121]	23.4
	DMC (CCSD(T) based PES)	Wang, 2008[11]	21.6 ± 2
	Instanton (CCSD(T) based PES)	Cvitaš, 2016[321]	25
	DMC (CCSD(T)(F12*) based PES)	Mizukami, 2014[325]	21.0(4)
	Experiment	Baughcum, 1981[114]	21.58
	Experiment	Firth, 1991[113]	21.6
	Experiment	Baba, 1999[112]	21.58
D-Transfer	1D SPT (cc-pVTZ)		**3.33**
	1D SPT (aug-cc-pVQZ)		**2.267**
	FD SPT (cc-pVTZ)		**2.694**
	FD SPT (aug-cc-pVQZ)		**2.065**
	Instanton (CCSD(T) based PES)	Cvitaš, 2016[321]	3.4
	DMC (CCSD(T) based PES)	Wang, 2008[11]	3.0 ± 2
	DMC (CCSD(T)(F12*) based PES)	Mizukami, 2014[325]	3.2(4)
	Experiment	Baughcum, 1984[114]	2.915

Table 9.2 Δ values for Malonaldehyde from theory and experiment. Values in **bold** are from this work.

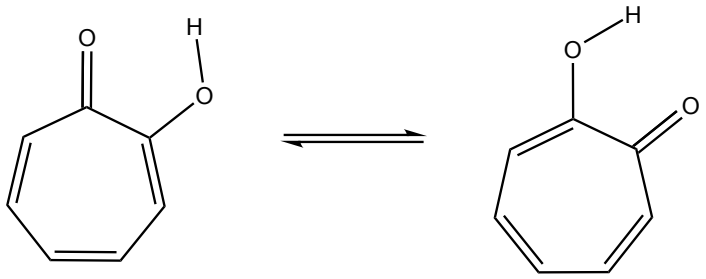


Figure 9.9 Isomerisation of tropolone.

	SPT Level	V_0 (kJ/mol)	$\Omega_{\{0\}}$ (cm^{-1})	x_{FF} (cm^{-1})	ω_R (cm^{-1})
H-transfer	1D	17.22	1231	-190	350
	1D+	17.22	1231	-183	350
D-transfer	1D	20.82	906.2	-24.1	336
	1D+	20.82	906.2	-96.2	336

Table 9.3 Adiabatic barrier heights, effective imaginary frequencies and anharmonic constants for aug-cc-pVQZ levels of theory studied in this work for the isomerisation of tropolone

	Method	Reference	Δ / cm^{-1}
H-Transfer	1D SPT (aug-cc-pVQZ)		**0.904**
	1D+ SPT (aug-cc-pVQZ)		**0.978**
	Experiment	Tanaka, 1999[115]	0.974
	Experiment	Frost, 1996 [330]	1.0 ± 0.4
	Experiment	Redington, 2008 [331]	0.974
D-Transfer	1D SPT (aug-cc-pVQZ)		**0.181**
	1D+ SPT (aug-cc-pVQZ)		**0.023**
	Experiment	Redington, 2008 [331]	0.051

Table 9.4 Δ values for tropolone from theory and experiment. Values in **bold** are from this work.

close for deuterium transfer; the 1D+ estimates a splitting about half as large as experiment, likely due to the errors in approximating the larger barrier shape with derivatives at the TS.

9.7 Conclusions

In this chapter we have shown how an improved semiclassical approach to tunnelling splittings, in combination with vibrational perturbation theory, allows for a simple, cost-effective and analytical route to tunnelling splittings in multidimensional systems, that strongly resembles the SCTST theory of reaction rates. This Semiclassical Perturbation Theory method accounts for anharmonic

and corner-cutting effects by including couplings between vibrational modes. It can also be systematically improved with higher orders of perturbation theory, although the expense is likely prohibitive for calculations going beyond second order. The SPT method for splittings can also take advantage of the various approximations that have been developed for the SCTST theory of rates, such as reduced-dimensional methods.

Testing on a model one-dimensional potential indicates that SPT is a good approximation to the exact result for a range of barrier heights. The semiclassical approximation itself is, as expected, most accurate when applied to systems with a high and wide barrier. The method's application (in full and reduced dimensions) to multidimensional systems was illustrated by application to malonaldehyde and tropolone splittings. In both cases SPT performed well, with calculated splittings lying close to experimental results and other theoretical calculations. We also illustrate that an accurate theoretical result is highly dependent on high quality *ab initio* calculations, further motivating the need for theories that require an absolute minimum of such computations. Variants of the SPT method, such as the 1D and 1D+ methods, may satisfy these needs.

Since the method does not require a PES, and only a few *ab initio* computations are needed, this method could have application in approximating tunnelling splittings in large and complex systems for which a full treatment of the dynamics may not be possible.

Chapter 10

Conclusions

In this thesis, we have studied the Semiclassical Transition State Theory method of calculating the rate constants of chemical reactions. We have investigated the method theoretically, applied it to a range of reactions, and developed the theory for more efficient use and for the study of new problems. The key conclusions, developed throughout this thesis, are described below.

SCTST is capable of estimating rate constants accurately, for a diverse set of polyatomic reactions.

We have provided detailed comparisons of SCTST rates with experimental and other theoretical rates for several complex reactions. These indicate SCTST is a reliable method for treating unimolecular rearrangements, reactions with internal rotational degrees of freedom and heavy-light-heavy reactions. We have also demonstrated how SCTST can produce accurate microcanonical rate constants.

SCTST in its one-dimensional form can also give excellent results in some cases.

Using the symmetric hydrogen transfer reaction, R1, we have found good agreement between 1D-SCTST and both experiment and quantum scattering calculations. We showed how careful treatment of internal rotational degrees of freedom in 1D-SCTST (for example, by using Truhlar's *tanh* formula) is critical for obtaining accurate results. We also showed that 1D-SCTST can be expected to give better results that alternative methods of a similar expense, owing to its improved description of barrier width, and that deep tunnelling corrections

are essential for one-dimensional calculations. We also found that higher orders of perturbation theory may be unhelpful. 1D-SCTST was also seen to give rate constants within 50% of the FD-SCTST result for the unimolecular Criegee decay reaction, reaction R9, at 298 K and reproduced accurately the relative rates of the decay of methylhydroxycarbene as determined by the more expensive semiclassical instanton method. For some reactions the one-dimensional approach is insufficient; we found a difference of a factor of three at 298 K for the water catalysed Criegee decay process, reaction R10.

SCTST in reduced dimensions can produce full-dimensional quality results for a fraction of the computational cost.

We showed how the most significant vibrational modes can be signposted cheaply and accurately, and how these can be included in a reduced dimensionality SCTST framework. Whilst some reactions only require a small number of active modes to achieve full-dimensional quality results, more complex reactions may require many modes before satisfactory results are reached. Further testing of this method is required, before these can be applied with confidence to new systems.

SCTST accounts implicitly for variational and corner-cutting effects.

By using a two-dimensional model potential we illustrated how SCTST accounts implicitly for key multidimensional effects in the limit that motion along the reaction mode is slow compared to other degrees of freedom. The method is, however, unable to treat accurately extreme corner-cutting effects, and adiabatic effects caused by coupling to low frequency modes are the most likely to be poorly treated. For the most common reactions we expect these inaccuracies to be small, but reactions with muonium atoms, or extreme heavy-light-heavy reactions may lead to large errors. We also showed the impact of corner-cutting on a reaction can be determined using a small-curvature approximation to SCTST.

SCTST can aid the interpretation of experimental results, and make predictions about complex reactions.

Using SCTST, we showed that decay of Criegee intermediates in the atmosphere is likely to have significant contribution from a water-catalysed pathway, rather than just proceeding via a unimolecular hydrogen transfer reaction. We also studied enol-formation from a charge-tagged phenyl pyruvic acid derivative, and provided evidence for an alternative reaction mechanism, consistent with recent experimental results. Despite these reactions containing up to 29 atoms atoms, these rate calculations were feasible due to the efficiency of the SCTST method.

The SCTST equations can be recast to estimate tunnelling splittings.

The Semiclassical Perturbation Method for calculating tunnelling splittings in medium sized molecules, which closely resembles the SCTST theory of reaction rates, was introduced for the first time. By applying this method to a model potential and to real systems, we showed this is a reliable and efficient way to estimate splittings.

Further comparative testing is required

In order for semiclassical rate theories to become a powerful tool in molecular science, better understanding of the theoretical and practical relationship between different methods is needed. A comprehensive review comparing SCTST, VTST and instanton rate theory would allow for potential end-users of these methods to understand the errors associated with each, the benefits and drawbacks of each approach and what the best method to use is for any given calculation. This would require a collaborative effort, directly comparing theoretical results (and computational costs) for a set of benchmark reactions with which accurate scattering calculations can be compared. The method's applicability to larger reactions could also be tested.

Semiclassical Transition State Theory has been shown to be a reliable and widely applicable method, that has been rigorously tested and is able to provide useful insight to a wide range of experimental systems. The new *pySCTST* software makes its application simple and widely accessible. We hope this becomes a widely adopted tool for studying interesting chemical systems in the years to come.

References

1. Burd, T. A. H., Shan, X. & Clary, D. C. Tunnelling and the kinetic isotope effect in $CH_3 + CH_4 \rightarrow CH_4 + CH_3$: An application of semiclassical transition state theory. *Chem. Phys. Lett.* **693,** 88–94 (2018).
2. Burd, T. A. H., Shan, X. & Clary, D. C. Catalysis and Tunnelling in the Unimolecular Decay of Criegee Intermediates. *Phys. Chem. Chem. Phys.* **20,** 25224–25234 (2018).
3. Shan, X., Burd, T. A. H. & Clary, D. C. New Developments in Semiclassical Transition-State Theory. *J. Phys. Chem. A* **123,** 4639–4657 (2019).
4. Burd, T. A. H., Shan, X. & Clary, D. C. Tunnelling in Cyclocarbenes: An Application of Semiclassical Transition State Theory in Reduced Dimensions. *Chem. Phys. Lett.* **735,** 136783 (2019).
5. Burd, T. A. H., Shan, X. & Clary, D. C. Hydrogen Tunnelling in the Rearrangements of Carbenes: The Role of Dynamical Calculations. *Phys. Chem. Chem. Phys.* **22,** 962–965 (2020).
6. Burd, T. A. H. & Clary, D. C. An Analytic Route to Tunnelling Splittings Using Semiclassical Perturbation Theory. *J. Chem. Theory Comput.* **16,** 3486–3493 (2020).
7. Arrhenius, S. Über Die Reaktionsgeschwindigkeit Bei Der Inversion von Rohrzucker Durch Säuren. *Z. Phys. Chem* **4U,** 226–248 (1889).
8. Eyring, H. The activated complex in chemical reactions. *J. Chem. Phys.* **3,** 107–115 (1935).
9. Lucas Bao, J. & Truhlar, D. G. Variational transition state theory: theoretical framework and recent developments. *Chem. Soc. Rev.* **46,** 7548–7596 (2017).
10. Fu, B., Shan, X., Zhang, D. H. & Clary, D. C. Recent Advances in Quantum Scattering Calculations on Polyatomic Bimolecular Reactions. *Chem. Soc. Rev.* **46,** 7625–7649 (2017).
11. Wang, Y., Braams, B. J., Bowman, J. M., Carter, S. & Tew, D. P. Full-Dimensional Quantum Calculations of Ground-State Tunneling Splitting of Malonaldehyde Using an Accurate Ab Initio Potential Energy Surface. *J. Chem. Phys.* **128,** 224314 (2008).
12. Maisuradze, G. G., Thompson, D. L., Wagner, A. F. & Minkoff, M. Interpolating Moving Least-Squares Methods for Fitting Potential Energy Surfaces: Detailed Analysis of One-Dimensional Applications. *J. Chem. Phys.* **119,** 10002–10014 (2003).

13. Guo, Y., Kawano, A., Thompson, D. L., Wagner, A. F. & Minkoff, M. Interpolating Moving Least-Squares Methods for Fitting Potential Energy Surfaces: Applications to Classical Dynamics Calculations. *J. Chem. Phys.* **121,** 5091–5097 (2004).

14. Lorenz, S., Groß, A. & Scheffler, M. Representing High-Dimensional Potential-Energy Surfaces for Reactions at Surfaces by Neural Networks. *Chem. Phys. Lett.* **395,** 210–215 (2004).

15. Gassner, H., Probst, M., Lauenstein, A. & Hermansson, K. Representation of Intermolecular Potential Functions by Neural Networks. *J. Phys. Chem. A* **102,** 4596–4605 (1998).

16. Prudente, F. V. & Soares Neto, J. J. The Fitting of Potential Energy Surfaces Using Neural Networks. Application to the Study of the Photodissociation Processes. *Chem. Phys. Lett.* **287,** 585–589 (1998).

17. Hu, W. & Schatz, G. C. Theories of Reactive Scattering. *J. Chem. Phys.* **125,** 132301 (2006).

18. Schatz, G. C. Scattering Theory and Dynamics: Time-Dependent and Time-Independent Methods. *J. Phys. Chem.* **100,** 12839–12847 (1996).

19. Skouteris, D. *et al.* Van Der Waals Interactions in the Cl + HD Reaction. *Science* **286,** 1713–1716 (1999).

20. Skouteris, D., Castillo, J. F. & Manolopoulos, D. E. ABC: A Quantum Reactive Scattering Program. *Comput. Phys. Commun.* **133,** 128–135 (2000).

21. Harich, S. A. *et al.* Forward Scattering Due to Slow-down of the Intermediate in the H + HD $\rightarrow$ D + H_2 Reaction. *Nature* **419,** 281 (2002).

22. Dai, D. *et al.* Interference of Quantized Transition-State Pathways in the H + D_2 $\rightarrow$ D + HD Chemical Reaction. *Science* **300,** 1730–1734 (2003).

23. Fu, B., Zhou, Y. & H. Zhang, D. Shape Resonance in the H + D_2O $\rightarrow$ D + HOD Reaction: A Full-Dimensional Quantum Dynamics Study. *Chem. Sci.* **3,** 270–274 (2012).

24. Song, H., Yang, M. & Guo, H. Communication: Equivalence between Symmetric and Antisymmetric Stretching Modes of NH_3 in Promoting H + NH_3 $\rightarrow$ H_2 + NH_2 Reaction. *J. Chem. Phys.* **145,** 131101 (2016).

25. Chen, L., Shao, K., Chen, J., Yang, M. & Zhang, D. H. Full-Dimensional Quantum Dynamics Study of the $H_2 + C_2H \rightarrow H + C_2H_2$ Reaction on an Ab Initio Potential Energy Surface. *J. Chem. Phys.* **144,** 194309 (2016).

26. Yang, M., Zhang, D. H. & Lee, S.-Y. A Seven-Dimensional Quantum Study of the $H + CH_4$ Reaction. *J. Chem. Phys.* **117,** 9539–9542 (2002).

27. Yang, M., Lee, S.-Y. & Zhang, D. H. Seven-Dimensional Quantum Dynamics Study of the $O(^3P) + CH_4$ Reaction. *J. Chem. Phys.* **126,** 064303 (2007).

28. Wang, Y. *et al.* Mode Specific Dynamics of the $H_2 + CH_3 \rightarrow H + CH_4$ Reaction Studied Using Quasi-Classical Trajectory and Eight-Dimensional Quantum Dynamics Methods. *J. Chem. Phys.* **143,** 154307 (2015).

29. Zhang, Z., Chen, J., Yang, M. & Zhang, D. H. Time-Dependent Wave Packet Study of the $H_2 + CH_3 \rightarrow H + CH_4$ Reaction. *J. Phys. Chem. A* **119,** 12480–12484 (2015).

30. Zhang, Z., Zhou, Y., Zhang, D. H., Czakó, G. & Bowman, J. M. Theoretical Study of the Validity of the Polanyi Rules for the Late-Barrier Cl + CHD_3 Reaction. *J. Phys. Chem. Lett.* **3,** 3416–3419 (2012).

31. Song, H., Lu, Y., Li, J., Yang, M. & Guo, H. Mode Specificity in the OH + CHD_3 Reaction: Reduced-Dimensional Quantum and Quasi-Classical Studies on an Ab Initio Based Full-Dimensional Potential Energy Surface. *J. Chem. Phys.* **144,** 164303 (2016).

32. Weichman, M. L. *et al.* Feshbach Resonances in the Exit Channel of the F + CH_3OH $\rightarrow$ HF + CH_3O Reaction Observed Using Transition-State Spectroscopy. *Nat. Chem.* **9,** 950–955 (2017).

33. Craig, I. R. & Manolopoulos, D. E. Quantum Statistics and Classical Mechanics: Real Time Correlation Functions from Ring Polymer Molecular Dynamics. *J. Chem. Phys.* **121,** 3368–3373 (2004).

34. Habershon, S., Manolopoulos, D. E., Markland, T. E. & Miller, T. F. Ring-Polymer Molecular Dynamics: Quantum Effects in Chemical Dynamics from Classical Trajectories in an Extended Phase Space. *Annu. Rev. Phys. Chem.* **64,** 387–413 (2013).

35. Chandler, D. & Wolynes, P. G. Exploiting the Isomorphism between Quantum Theory and Classical Statistical Mechanics of Polyatomic Fluids. *J. Chem. Phys.* **74,** 4078–4095 (1981).

36. Manolopoulos, D. E. & Lawrence, J. E. Path Integral Methods for Reaction Rates in Complex Systems. *Faraday Discuss.* **221,** 9–29 (2019).

37. Bowman, J. M. Reduced dimensionality theory of quantum reactive scattering. *J. Phys. Chem.* **95,** 4960–4968 (1991).

38. Kerkeni, B. & Clary, D. C. Ab Initio Rate Constants from Hyperspherical Quantum Scattering: Application to $H + C_2H_6$ and $H + CH_3OH$. *J. Chem. Phys.* **121,** 6809–6821 (2004).

39. von Horsten, H. F., Banks, S. T. & Clary, D. C. An Efficient Route to Thermal Rate Constants in Reduced Dimensional Quantum Scattering Simulations: Applications to the Abstraction of Hydrogen from Alkanes. *J. Chem. Phys.* **135,** 094311 (2011).

40. Shan, X. & Clary, D. C. Quantum Effects in the Abstraction Reaction by H Atoms of Primary and Secondary Hydrogens in n-C_4H_{10}: A Test of a New Potential Energy Surface Construction Method. *Phys. Chem. Chem. Phys.* **15,** 1222–1231 (2012).

41. Shan, X. & Clary, D. C. Quantum Dynamics of the Abstraction Reaction of H with Cyclopropane. *J. Phys. Chem. A* **118,** 10134–10143 (2014).

42. Banks, S. T. & Clary, D. C. Chemical Reaction Surface Vibrational Frequencies Evaluated in Curvilinear Internal Coordinates: Application to $H + CH_4 \rightleftharpoons H_2 + CH_3$. *J. Chem. Phys.* **130,** 024106 (2009).

43. Palma, J., Echave, J. & Clary, D. C. Rate Constants for the $CH_4 + H \rightarrow CH_3 + H_2$ Reaction Calculated with a Generalized Reduced-Dimensionality Method. *J. Phys. Chem. A* **106,** 8256–8260 (2002).

44. Kabeláč, M., Hobza, P. & Špirko, V. The Ab Initio Assigning of the Vibrational Probing Modes of Tryptophan : Linear Shifting of Approximate Anharmonic Frequencies vs. Multiplicative Scaling of Harmonic Frequencies. *Phys. Chem. Chem. Phys.* **11,** 3921–3926 (2009).

45. Remmert, S. M., Banks, S. T. & Clary, D. C. Reduced Dimensionality Quantum Dynamics of $CH_3 + CH_4 \rightarrow CH_4 + CH_3$: Symmetric Hydrogen Exchange on an Ab Initio Potential. *J. Phys. Chem. A* **113,** 4255–4264 (2009).

46. Banks, S. T., Tautermann, C. S., Remmert, S. M. & Clary, D. C. An Improved Treatment of Spectator Mode Vibrations in Reduced Dimensional Quantum Dynamics: Application to the Hydrogen Abstraction Reactions M+ CH_4, H+CH_4, D+CH_4, and CH_3+CH_4. *J. Chem. Phys.* **131,** 044111 (2009).

47. Truhlar, D. G., Hase, W. L. & Hynes, J. T. Current status of transition-state theory. *J. Phys. Chem.* **87,** 2664–2682 (1983).

48. Garrett, B. C., Truhlar, D. G., Wagner, A. F. & Dunning, T. H. Variational transition state theory and tunneling for a heavy–light–heavy reaction using an ab initio potential energy surface. ^{37}Cl + H(D)^{35}Cl $\rightarrow$ H(D)^{37}Cl + ^{35}Cl. *J. Chem. Phys.* **78,** 4400–4413 (1983).

49. Garrett, B. C., Truhlar, D. G. & Schatz, G. C. Test of variational transition state theory and multidimensional semiclassical transmission coefficients methods against accurate quantal rate constants for H+ H_2/HD, D + H_2, and O+ H_2/D_2/HD, including intra-and intermolecular kinetic isotope effects. *J. Am. Chem. Soc.* **108,** 2876–2881 (1986).

50. Isaacson, A. D. *et al.* POLYRATE: A general computer program for variational transition state theory and semiclassical tunneling calculations of chemical reaction rates. *Comp. Phys. Comm.* **47,** 91–102 (1987).

51. Tucker, S. C. & Truhlar, D. G. *Dynamical formulation of transition state theory: Variational transition states and semiclassical tunneling* in *New Theoretical Concepts for Understanding Organic Reactions* (Springer, 1989), 291–346.

52. Truong, T. N., Truhlar, D. G., Chelikowsky, J. R. & Chou, M. A new ab initio potential energy surface for hydrogen atom on ruthenium (0001) and its use for variational transition state theory and semiclassical tunneling calculations of the surface diffusion of hydrogen and deuterium. *J. Phys. Chem.* **94,** 1973–1981 (1990).

53. Wentzel, G. Eine Verallgemeinerung der Quantenbedingungen für die Zwecke der Wellenmechanik. *Z. Phys.* **38,** 518–529 (1926).

54. Kramers, H. A. Wellenmechanik und halbzahlige Quantisierung. *Z. Phys.* **39,** 828–840 (1926).

55. Brillouin, L. La Mécanique Ondulatoire de Schrödinger; Une Méthode Générale de Resolution Par Approximations Successives. *Compt. Rend. Hebd. Seances Acad. Sci.* **183,** 24–26 (1926).

56. Kuppermann, A. & Truhlar, D. G. Exact Tunneling Calculations. *J. Am. Chem. Soc.* **93,** 1840–1851 (1971).

57. Zhang, F. & Dibble, T. S. Impact of Tunneling on Hydrogen-Migration of the n -Propylperoxy Radical. *Phys. Chem. Chem. Phys.* **13,** 17969–17977 (2011).

58. Fernandez-Ramos, A. & Truhlar, D. G. Improved Algorithm for Corner-Cutting Tunneling Calculations. *J. Chem. Phys.* **114,** 1491–1496 (2001).

59. Meana-Pañeda, R., Truhlar, D. G. & Fernández-Ramos, A. Least-Action Tunneling Transmission Coefficient for Polyatomic Reactions. *J. Chem. Theory Comput.* **6,** 6–17 (2010).

60. Truhlar, D. G. & Kuppermann, A. Exact and Approximate Quantum Mechanical Reaction Probabilities and Rate Constants for the Collinear H + H_2 Reaction. *J. Chem. Phys.* **56,** 2232–2252 (1972).

61. Lu, D.-h. *et al.* POLYRATE 4: A New Version of a Computer Program for the Calculation of Chemical Reaction Rates for Polyatomics. *Comput. Phys. Commun.* **71,** 235–262 (1992).

62. Garrett, B. C., Joseph, T., Truong, T. N. & Truhlar, D. G. Application of the Large-Curvature Tunneling Approximation to Polyatomic Molecules: Abstraction of H or D by Methyl Radical. *Chem. Phys.* **136,** 271–293 (1989).

63. Bondi, D. K., Connor, J. N. L., Garrett, B. C. & Truhlar, D. G. Test of Variational Transition State Theory with a Large-curvature Tunneling Approximation against Accurate Quantal Reaction Probabilities and Rate Coefficients for Three Collinear Reactions with Large Reaction-path Curvature: Cl+HCl, Cl+DCl, and Cl+MuCl. *J. Chem. Phys.* **78,** 5981–5989 (1983).

64. Kreevoy, M. M., Ostovic, D., Truhlar, D. G. & Garrett, B. C. Phenomenological Manifestations of Large-Curvature Tunneling in Hydride-Transfer Reactions. *J. Phys. Chem.* **90,** 3766–3774 (1986).

65. Miller, W. H., Schwartz, S. D. & Tromp, J. W. Quantum Mechanical Rate Constants for Bimolecular Reactions. *J. Chem. Phys.* **79,** 4889–4898 (1983).

66. Feynman, R. P., Hibbs, A. R. & Styer, D. F. *Quantum mechanics and path integrals* (Courier Corporation, 2010).

67. Miller, W. H. Path Integral Representation of the Reaction Rate Constant in Quantum Mechanical Transition State Theory. *J. Chem. Phys.* **63,** 1166–1172 (1975).

68. Richardson, J. O. Derivation of Instanton Rate Theory from First Principles. *J. Chem. Phys.* **144,** 114106 (2016).

69. Richardson, J. O. Microcanonical and Thermal Instanton Rate Theory for Chemical Reactions at All Temperatures. *Faraday Discus.* **195,** 49–67 (2017).

70. Richardson, J. O. Ring-polymer instanton theory. *Int. Rev. Phys. Chem.* **37,** 171–216 (2018).

71. Richardson, J. O. Perspective: Ring-Polymer Instanton Theory. *J. Chem. Phys.* **148,** 200901 (2018).

72. Richardson, J. O. Full- and Reduced-Dimensionality Instanton Calculations of the Tunnelling Splitting in the Formic Acid Dimer. *Phys. Chem. Chem. Phys.* **19,** 966–970 (2017).

73. Fang, W. *et al.* Origins of fast diffusion of water dimers on surfaces. *Nat. Commun* **11,** 1–9 (2020).

74. Cvitaš, M. T. & Richardson, J. O. Quantum Tunnelling Pathways of the Water Pentamer. *Phys. Chem. Chem. Phys.* (2019).

75. Laude, G., Calderini, D., Tew, D. P. & Richardson, J. O. Ab Initio Instanton Rate Theory Made Efficient Using Gaussian Process Regression. *Faraday Discus.* **212,** 237–258 (2018).

76. Andersson, S., Nyman, G., Arnaldsson, A., Manthe, U. & Jónsson, H. Comparison of Quantum Dynamics and Quantum Transition State Theory Estimates of the H + CH_4 Reaction Rate. *J. Phys. Chem. A* **113,** 4468–4478 (2009).

77. Winter, P. & Richardson, J. O. Divide-and-Conquer Method for Instanton Rate Theory. *J. Chem. Theory Comput.* **15,** 2816–2825 (2019).

78. Miller, W. H. Semiclassical limit of quantum mechanical transition state theory for nonseparable systems. *J. Chem. Phys.* **62,** 1899–1906 (1975).

79. Miller, W. H. Semi-classical theory for non-separable systems:. Construction of "good" action-angle variables for reaction rate constants. *Faraday Discus.* **62,** 40–46 (1977).

80. Miller, W. H., Hernandez, R., Handy, N. C., Jayatilaka, D. & Willetts, A. Ab initio calculation of anharmonic constants for a transition state, with application to semiclassical transition state tunneling probabilities. *Chem. Phys. Lett.* **172,** 62–68 (1990).

81. Chapman, S., Garrett, B. C. & Miller, W. H. Semiclassical Eigenvalues for Nonseparable Systems: Nonperturbative Solution of the Hamilton–Jacobi Equation in Action-angle Variables. *J. Chem. Phys.* **64,** 502–509 (1976).

82. Wang, F. & Landau, D. P. Efficient, Multiple-Range Random Walk Algorithm to Calculate the Density of States. *Phys. Rev. Lett.* **86,** 2050–2053 (2001).

83. Wang, F. & Landau, D. P. Determining the Density of States for Classical Statistical Models: A Random Walk Algorithm to Produce a Flat Histogram. *Phys. Rev. E* **64,** 056101 (2001).

84. Basire, M., Parneix, P. & Calvo, F. Quantum Anharmonic Densities of States Using the Wang–Landau Method. *J. Chem. Phys.* **129,** 081101 (2008).

85. Nguyen, T. L. & Barker, J. R. Sums and Densities of Fully Coupled Anharmonic Vibrational States: A Comparison of Three Practical Methods. *J. Phys. Chem. A* **114,** 3718–3730 (2010).

86. Aieta, C., Gabas, F. & Ceotto, M. An Efficient Computational Approach for the Calculation of the Vibrational Density of States. *J. Phys. Chem. A* **120,** 4853–4862 (2016).

87. Wagner, A. F. Improved Multidimensional Semiclassical Tunneling Theory. *J. Phys. Chem. A* **117,** 13089–13100 (2013).

88. Stanton, J. F. Semiclassical Transition-State Theory Based on Fourth-Order Vibrational Perturbation Theory: The Symmetrical Eckart Barrier. *J. Phys. Chem. Lett.* **7,** 2708–2713 (2016).

89. Goel, P. & Stanton, J. F. Semiclassical Transition State Theory Based on Fourth Order Vibrational Perturbation Theory: Model System Studies beyond Symmetric Eckart Barrier. *J. Chem. Phys.* **149,** 134109 (2018).

90. Nguyen, T. L., Stanton, J. F. & Barker, J. R. Ab Initio Reaction Rate Constants Computed Using Semiclassical Transition-State Theory: HO + $H_2 \rightarrow H_2O + H$ and Isotopologues. *J. Phys. Chem. A* **115,** 5118–5126 (2011).

91. Nguyen, T. L. & Stanton, J. F. High-level theoretical study of the reaction between hydroxyl and ammonia: Accurate rate constants from 200 to 2500 K. *J. Chem. Phys.* **147,** 152704 (2017).

92. Greene, S. M., Shan, X. & Clary, D. C. Rate constants of chemical reactions from semiclassical transition state theory in full and one dimension. *J. Chem. Phys.* **144,** 244116 (2016).

93. Shiekh, B. A., Kaur, D., Seth, B. & Mahajan, S. The Theoretical-Cum-Statistical Approach for the Investigation of Reaction NO_2 + $O(^3P) \rightarrow$ NO + O_2 Using SCTST and a Full Anharmonic VPT2 Model. *Chem. Phys. Lett.* **662,** 244–249 (2016).

94. Greene, S. M., Shan, X. & Clary, D. C. An investigation of one- versus two-dimensional semiclassical transition state theory for H atom abstraction and exchange reactions. *J. Chem. Phys.* **144,** 084113 (2016).

95. Weston, R. E., Nguyen, T. L., Stanton, J. F. & Barker, J. R. HO + CO Reaction Rates and H/D Kinetic Isotope Effects: Master Equation Models with ab Initio SCTST Rate Constants. *J. Phys. Chem. A* **117,** 821–835 (2013).

96. Lam Nguyen, T., Ravishankara, A. R. & Stanton, J. F. Analysis of the Potential Atmospheric Impact of the Reaction of NO_2 with OH. *Chem. Phys. Lett.* **708,** 100–105 (2018).

97. Barker, J. R., Nguyen, T. L. & Stanton, J. F. Kinetic Isotope Effects for $Cl + CH_4 \rightleftharpoons HCl + CH_3$ Calculated Using Ab Initio Semiclassical Transition State Theory. *J. Phys. Chem. A* **116,** 6408–6419 (2012).

98. Drozd, G. T., Kurtén, T., Donahue, N. M. & Lester, M. I. Unimolecular Decay of the Dimethyl-Substituted Criegee Intermediate in Alkene Ozonolysis: Decay Time Scales and the Importance of Tunneling. *J. Phys. Chem. A* **121,** 6036–6045 (2017).

99. Amiri, A., Noorbala, M. R. & Saheb, V. Kinetics and Mechanisms of the Hydrogen Abstraction Reactions of $CF_3CF_2CH_2CH_2F$ and $CF_3CH_2CH_2CF_3$ with Hydroxyl Radicals: Theoretical Studies. *J. Fluorine Chem.* **218,** 116–121 (2019).

100. Lara-Cruz, G. A. & Moyano, G. E. OCS Isomerization and Dissociation Kinetics from Statistical Models. *Theor. Chem. Acc.* **137,** 79 (2018).

101. Saheb, V. & Maleki, S. Ab Initio Theoretical Studies on the Kinetics of Hydrogen Abstraction Type Reactions of Hydroxyl Radicals with CH_3CCl_2F and CH_3CClF_2. *Russ. J. Phys. Chem. A* **92,** 442–448 (2018).

102. Saheb, V., Hashemi, S. R. & Hosseini, S. M. A. Theoretical Studies on the Kinetics of Multi-Channel Gas-Phase Unimolecular Decomposition of Acetaldehyde. *J. Phys. Chem. A* **121,** 6887–6895 (2017).

103. Shiekh, B. A. & Kaur, D. The role of torsional motion on the properties of propiolic acid and its H/D isotopic analogs: A density functional study using SCTST and a full anharmonic VPT2 model. *Chem. Phys. Lett.* **646,** 168–173 (2016).

104. Nguyen, T. L., Xue, B. C., Weston, R. E., Barker, J. R. & Stanton, J. F. Reaction of HO with CO: Tunneling Is Indeed Important. *J. Phys. Chem. Lett.* **3,** 1549–1553 (2012).

105. Shan, X. & Clary, D. C. Application of one-dimensional semiclassical transition state theory to the $CH_3OH + H \rightleftharpoons CH_2OH/CH_3O + H_2$ reactions. *Phil. Trans. R. Soc. A* **376,** 20170147 (2018).

106. Shan, X., Sambrook, M. R. & Clary, D. C. Theoretical Study of Gas-Phase Unimolecular Decomposition of Simulants of the Nerve Agent VX. *J. Phys. Chem. A* **123,** 59–72 (2019).

107. Shan, X. *et al.* A Combined Theoretical and Experimental Study of Sarin (GB) Decomposition at High Temperatures. *J. Phys. Chem. A* **121,** 6200–6210 (2017).

108. Greene, S. M., Shan, X. & Clary, D. C. Reduced-Dimensionality Semiclassical Transition State Theory: Application to Hydrogen Atom Abstraction and Exchange Reactions of Hydrocarbons. *J. Phys. Chem. A* **119,** 12015–12027 (2015).

109. Goroya, K. G., Zhu, Y., Sun, P. & Duan, C. High Resolution Jet-Cooled Infrared Absorption Spectra of the Formic Acid Dimer: A Reinvestigation of the C–O Stretch Region. *J. Chem. Phys.* **140,** 164311 (2014).

110. Ortlieb, M. & Havenith, M. Proton Transfer in $(HCOOH)_2$: An IR High-Resolution Spectroscopic Study of the Antisymmetric C-O Stretch. *J. Phys. Chem. A* **111,** 7355–7363 (2007).

111. Baughcum, S. L., Duerst, R. W., Rowe, W. F., Smith, Z. & Wilson, E. B. Microwave Spectroscopic Study of Malonaldehyde (3-Hydroxy-2-Propenal). 2. Structure, Dipole Moment, and Tunneling. *J. Am. Chem. Soc.* **103,** 6296–6303 (1981).

112. Baba, T., Tanaka, T., Morino, I., Yamada, K. M. T. & Tanaka, K. Detection of the Tunneling-Rotation Transitions of Malonaldehyde in the Submillimeter-Wave Region. *J. Chem. Phys.* **110,** 4131–4133 (1999).

113. Firth, D. W. *et al.* Tunable Far-infrared Spectroscopy of Malonaldehyde. *J. Chem. Phys.* **94,** 1812–1819 (1991).

114. Baughcum, S. L., Smith, Z., Wilson, E. B. & Duerst, R. W. Microwave Spectroscopic Study of Malonaldehyde. 3. Vibration-Rotation Interaction and One-Dimensional Model for Proton Tunneling. *J. Am. Chem. Soc.* **106,** 2260–2265 (1984).

115. Tanaka, K. *et al.* Determination of the Proton Tunneling Splitting of Tropolone in the Ground State by Microwave Spectroscopy. *J. Chem. Phys.* **110,** 1969–1978 (1999).

116. Richardson, J. O. *et al.* Investigation of Terahertz Vibration–Rotation Tunneling Spectra for the Water Octamer. *J. Phys. Chem. A* **117,** 6960–6966 (2013).

117. Richardson, J. O., Althorpe, S. C. & Wales, D. J. Instanton Calculations of Tunneling Splittings for Water Dimer and Trimer. *J. Chem. Phys.* **135,** 124109 (2011).

118. Gregory, J. K. & Clary, D. C. Calculations of the Tunneling Splittings in Water Dimer and Trimer Using Diffusion Monte Carlo. *J. Chem. Phys.* **102,** 7817–7829 (1995).

119. Sorenson, J. M., Gregory, J. K. & Clary, D. C. Diffusion Monte Carlo Studies of Isotope-Substituted Water Trimers. *Chem. Phys. Lett.* **263,** 680–686 (1996).

120. Viel, A., Coutinho-Neto, M. D. & Manthe, U. The Ground State Tunneling Splitting and the Zero Point Energy of Malonaldehyde: A Quantum Monte Carlo Determination. *J. Chem. Phys.* **126,** 024308 (2007).

121. Schröder, M., Gatti, F. & Meyer, H.-D. Theoretical Studies of the Tunneling Splitting of Malonaldehyde Using the Multiconfiguration Time-Dependent Hartree Approach. *J. Chem. Phys.* **134,** 234307 (2011).

122. Althorpe, S. C. & Clary, D. C. Calculation of the Intermolecular Bound States for Water Dimer. *J. Chem. Phys.* **101,** 3603–3609 (1994).

123. Shida, N., Barbara, P. F. & Almlöf, J. A Reaction Surface Hamiltonian Treatment of the Double Proton Transfer of Formic Acid Dimer. *J. Chem. Phys.* **94,** 3633–3643 (1991).

124. Althorpe, S. C. & Clary, D. C. A New Method for Calculating the Rovibrational States of Polyatomics with Application to Water Dimer. *J. Chem. Phys.* **102,** 4390–4399 (1995).

125. Shida, N., Barbara, P. F. & Almlöf, J. E. A Theoretical Study of Multidimensional Nuclear Tunneling in Malonaldehyde. *J. Chem. Phys.* **91,** 4061–4072 (1989).

126. Althorpe, S. C., Clary, D. C. & Bunker, P. R. Calculation of the Far-Infrared Spectra for $(HF)_2, (HCl)_2$ and $(HBr)_2$. *Chem. Phys. Lett.* **187,** 345–353 (1991).

127. Kamarchik, E., Wang, Y. & Bowman, J. Reduced-Dimensional Quantum Approach to Tunneling Splittings Using Saddle-Point Normal Coordinates. *J. Phys. Chem. A* **113,** 7556–7562 (2009).

128. Mátyus, E., Wales, D. J. & Althorpe, S. C. Quantum Tunneling Splittings from Path-Integral Molecular Dynamics. *J. Chem. Phys.* **144,** 114108 (2016).

129. Richardson, J. O. & Althorpe, S. C. Ring-Polymer Instanton Method for Calculating Tunneling Splittings. *J. Chem. Phys.* **134,** 054109 (2011).

130. Smedarchina, Z., Siebrand, W. & Zgierski, M. Z. An Instanton Approach to Intramolecular Hydrogen Exchange: Tunneling Splittings in Malonaldehyde and the Hydrogenoxalate Anion. *J. Chem. Phys.* **103,** 5326–5334 (1995).

131. Smedarchina, Z., Fernandez-Ramos, A. & Siebrand, W. Calculation of the Tunneling Splitting in the Zero-Point Level and CO-Stretch Fundamental of the Formic Acid Dimer. *Chem. Phys. Lett.* **395,** 339–345 (2004).

132. Yagi, K., Mil'nikov, G. V., Taketsugu, T., Hirao, K. & Nakamura, H. Effect of Out-of-Plane Vibration on the Hydrogen Atom Transfer Reaction in Malonaldehyde. *Chem. Phys. Lett.* **397,** 435–440 (2004).

133. Watanabe, N. & Kouchi, A. Ice surface reactions: A key to chemical evolution in space. *Progr. Surf. Sci.* **83,** 439–489 (2008).

134. Oba, Y. *et al.* Water formation through a quantum tunneling surface reaction, OH+ H_2, at 10 K. *Astrophys. J.* **749,** 67 (2012).

135. Minissale, M. *et al.* Quantum Tunneling of Oxygen Atoms on Very Cold Surfaces. *Phys. Rev. Lett.* **111,** 053201 (2013).

136. Berry, M. V. & Mount, K. E. Semiclassical Approximations in Wave Mechanics. *Rep. Prog. Phys.* **35,** 315–397 (1972).

137. Razavy, M. *Quantum theory of tunneling* (World Scientific, 2003).

138. Griffiths, D. J. & Schroeter, D. F. *Introduction to quantum mechanics* (Cambridge University Press, 2018).

139. Kemble, E. C. A contribution to the theory of the BWK method. *Phys. Rev.* **48,** 549 (1935).

140. Greene, S. M. *Semiclassical transition state theory for chemical reactions* PhD thesis (University of Oxford, 2016).

141. Barone, V. Anharmonic vibrational properties by a fully automated second-order perturbative approach. *J. Chem. Phys.* **122,** 014108 (2004).

142. Truhlar, D. G., Garrett, B. C. & Klippenstein, S. J. Current Status of Transition-State Theory. *J. Phys. Chem.* **100,** 12771–12800 (1996).

143. Nguyen, T. L., Stanton, J. F. & Barker, J. R. A practical implementation of semi-classical transition state theory for polyatomics. *Chem. Phys. Lett.* **499,** 9–15 (2010).

144. Aieta, C., Gabas, F. & Ceotto, M. Parallel Implementation of Semiclassical Transition State Theory. *J. Chem. Theory Comput.* **15,** 2142–2153 (2019).

145. Beyer, T. & Swinehart, D. Algorithm 448: number of multiply-restricted partitions. *Commun. ACM* **16,** 379 (1973).

146. Stein, S. E. & Rabinovitch, B. Accurate evaluation of internal energy level sums and densities including anharmonic oscillators and hindered rotors. *J. Chem. Phys.* **58,** 2438–2445 (1973).

147. Frisch, M. J. *et al. Gaussian16 Revision B.01* Gaussian Inc. Wallingford CT. 2016.

148. Richardson, L. F. & Gaunt, J. A. VIII. The Deferred Approach to the Limit. *Philos. Trans. R. Soc. A* **226,** 299–361 (1927).

149. Kungwan, N. & Truong, T. Kinetics of the hydrogen abstraction CH_3 plus alkane $\rightarrow$ CH_4 plus alkyl reaction class: An application of the reaction class transition state theory. *J. Phys. Chem. A* **109,** 7742–7750 (2005).

150. Dainton, F., Ivin, K. & Wilkinson, F. The kinetics of the exchange reaction CH_3 + $CH_4 \rightarrow CH_4$ + CH_3 using ^{14}C as tracer. *J. Chem. Soc. Faraday Trans.* **55,** 929–936 (1959).

151. Kerr, J. A. & Parsonage, M. J. *Evaluated kinetic data on gas phase hydrogen transfer reactions of methyl radicals* (Butterworths London, 1976).

152. Rice, F. O. & Varnerin, R. E. Activation Energies of Reactions of Methyl Radicals with Organic Molecules1. *J. Am. Chem. Soc.* **77,** 221–224 (1955).

153. Ramazani, S. Direct-dynamics VTST study of hydrogen or deuterium abstraction and C–C bond formation or dissociation in the reactions of CH_3 + CH_4, CH_3 + CD_4, CHD_3 + CD_3, CH_3CH_3 + H, and CH_3CD_3 + D. *J. Chem. Phys.* **138,** 194305 (2013).

154. Huynh, L. K., Ratkiewicz, A. & Truong, T. N. Kinetics of the Hydrogen Abstraction OH + Alkane $\rightarrow$ H_2O + Alkyl Reaction Class: An Application of the Reaction Class Transition State Theory. *J. Phys. Chem. A* **110,** 473–484 (2006).

155. Temelso, B., Sherrill, C. D., Merkle, R. C. & Freitas, R. A. High-Level Ab Initio Studies of Hydrogen Abstraction from Prototype Hydrocarbon Systems. *J. Phys. Chem. A* **110,** 11160–11173 (2006).

156. Dybala-Defratyka, A., Paneth, P., Pu, J. & Truhlar, D. G. Benchmark Results for Hydrogen Atom Transfer between Carbon Centers and Validation of Electronic Structure Methods for Bond Energies and Barrier Heights. *J. Phys. Chem. A* **108,** 2475–2486 (2004).

157. Saeys, M., Reyniers, M. F., Marin, G. B., Van Speybroeck, V. & Waroquier, M. Ab Initio Calculations for Hydrocarbons: Enthalpy of Formation, Transition State Geometry, and Activation Energy for Radical Reactions. *J. Phys. Chem. A* **107,** 9147–9159 (2003).

158. Coote, M. L., Collins, M. A. & Radom, L. Calculation of Accurate Imaginary Frequencies and Tunnelling Coefficients for Hydrogen Abstraction Reactions Using IRCmax. *Mol. Phys.* **101,** 1329–1338 (2003).

159. Ellingson, B. A., Lynch, V. A., Mielke, S. L. & Truhlar, D. G. Statistical Thermodynamics of Bond Torsional Modes: Tests of Separable, Almost-Separable, and Improved Pitzer–Gwinn Approximations. *J. Chem. Phys.* **125,** 084305 (2006).

160. Zheng, J. & Truhlar, D. G. Multi-path variational transition state theory for chemical reaction rates of complex polyatomic species: ethanol + OH reactions. *Faraday Discus.* **157,** 59–88 (2012).

161. Lin, C. Y., Izgorodina, E. I. & Coote, M. L. How Accurate Are Approximate Methods for Evaluating Partition Functions for Hindered Internal Rotations? *J. Phys. Chem. A* **112,** 1956–1964 (2008).

162. Yu, T., Zheng, J. & Truhlar, D. G. Multi-structural variational transition state theory. Kinetics of the 1,4-hydrogen shift isomerization of the pentyl radical with torsional anharmonicity. *Chem. Sci.* **2,** 2199–2213 (2011).

163. Chuang, Y.-Y. & Truhlar, D. G. Statistical Thermodynamics of Bond Torsional Modes. *J. Chem. Phys.* **112,** 1221–1228 (2000).

164. Turovtsev, V., Belotserkovskii, A. & Orlov, Y. D. Solution of a one-dimensional torsion Schrödinger equation with a general periodic potential. *Optics and Spectroscopy* **117,** 710–712 (2014).

165. Pitzer, K. S. Internal Rotation in Molecules with Two or More Methyl Groups. *J. Chem. Phys.* **10,** 605–606 (1942).

166. Miller, Y., Chaban, G. M. & Gerber, R. B. Theoretical study of anharmonic vibrational spectra of HNO_3, $HNO_3 - H_2O$, HNO_4: Fundamental, overtone and combination excitations. *Chem. Phys.* **313,** 213–224 (2005).

167. Jung, J. O. & Gerber, R. B. Vibrational wave functions and spectroscopy of $(H_2O)_n$, n=2,3,4,5: Vibrational self-consistent field with correlation corrections. *J. Chem. Phys.* **105,** 10332–10348 (1996).

168. Burd, T. A. H. *pySCTST* `https://bitbucket.com/timothyburd/pysctst`. 2019.

169. Dunning, T. H. Gaussian basis sets for use in correlated molecular calculations. I. The atoms boron through neon and hydrogen. *J. Chem. Phys.* **90,** 1007–1023 (1989).

170. Truhlar, D. G. Basis-Set Extrapolation. *Chem. Phys. Lett.* **294,** 45–48 (1998).

171. Cavalli, S., Aquilanti, V., Mundim, K. C. & De Fazio, D. Theoretical Reaction Kinetics Astride the Transition between Moderate and Deep Tunneling Regimes: The F + HD Case. *J. Phys. Chem. A* **118,** 6632–6641 (2014).

172. Williams, I. H. Quantum Catalysis? A Comment on Tunnelling Contributions for Catalysed and Uncatalysed Reactions. *J. Phys. Org. Chem.* **23,** 685–689 (2010).

173. Wang, Q.-D., Wang, X.-J., Liu, Z.-W. & Kang, G.-J. Theoretical and Kinetic Study of the Hydrogen Atom Abstraction Reactions of Ethyl Esters with Hydrogen Radicals. *Chem. Phys. Lett.* **616-617,** 109–114 (2014).

174. Heard, D. E. Rapid Acceleration of Hydrogen Atom Abstraction Reactions of OH at Very Low Temperatures through Weakly Bound Complexes and Tunneling. *Acc. Chem. Res.* **51,** 2620–2627 (2018).

175. Chhantyal-Pun, R. *et al.* Experimental and Computational Studies of Criegee Intermediate Reactions with NH_3 and CH_3NH_2. *Phys. Chem. Chem. Phys.* **21,** 14042–14052 (2019).

176. Umesaki, K. & Odai, K. A Kinetic Approach to Double Proton-Transfer in Watson-Crick DNA Base Pairs. *J. Phys. Chem. B* **124,** 1715–1722 (2020).

177. Fermann, J. T., Blanco, C. & Auerbach, S. Modeling proton mobility in acidic zeolite clusters. I. Convergence of transition state parameters from quantum chemistry. *J. Chem. Phys.* **112,** 6779–6786 (2000).

178. Hwang, T., Goldsmith, B. R., Peters, B. & Scott, S. L. Water-Catalyzed Activation of H_2O_2 by Methyltrioxorhenium: A Combined Computational–Experimental Study. *Inorg. Chem.* **52,** 13904–13917 (2013).

179. Heinola, K. & Ahlgren, T. Diffusion of Hydrogen in bcc Tungsten Studied with First Principle Calculations. *J. App. Phys.* **107,** 113531 (2010).

180. Enescu, M. & Cardey, B. Mechanism of Cysteine Oxidation by a Hydroxyl Radical: A Theoretical Study. *ChemPhysChem* **7,** 912–919 (2006).

181. Valleau, S. & Martínez, T. J. Reaction Dynamics of Cyanohydrins with Hydrosulfide in Water. *J. Phys. Chem. A* **123,** 7210–7217 (2019).

182. Abdel-Rahman, M. A., Al-Hashimi, N., Shibl, M. F., Yoshizawa, K. & El-Nahas, A. M. Thermochemistry and Kinetics of the Thermal Degradation of 2-Methoxyethanol as Possible Biofuel Additives. *Sci. Rep.* **9,** 4535 (2019).

183. Tu, Y., Wang, J.-B. & Li, X.-Y. Theoretical Study of Hydrogen Abstraction by Small Radicals from Cyclohexane-Carbonyl-Hydroperoxide. *Theor. Chem. Acc.* **138,** 39 (2019).

184. Van Geem, K. M., Pyl, S. P., Marin, G. B., Harper, M. R. & Green, W. H. Accurate High-Temperature Reaction Networks for Alternative Fuels: Butanol Isomers. *Ind. Eng. Chem. Res.* **49,** 10399–10420 (2010).

185. Sirjean, B. *et al.* Shock Tube and Chemical Kinetic Modeling Study of the Oxidation of 2,5-Dimethylfuran. *J. Phys. Chem. A* **117,** 1371–1392 (2013).

186. Goldsmith, C. F., Green, W. H. & Klippenstein, S. J. Role of O_2 + QOOH in Low-Temperature Ignition of Propane. 1. Temperature and Pressure Dependent Rate Coefficients. *J. Phys. Chem. A* **116,** 3325–3346 (2012).

187. Jasper, A. W., Klippenstein, S. J., Harding, L. B. & Ruscic, B. Kinetics of the Reaction of Methyl Radical with Hydroxyl Radical and Methanol Decomposition. *J. Phys. Chem. A* **111,** 3932–3950 (2007).

188. Harper, M. R., Van Geem, K. M., Pyl, S. P., Marin, G. B. & Green, W. H. Comprehensive Reaction Mechanism for N-Butanol Pyrolysis and Combustion. *Combust. Flame* **158,** 16–41 (2011).

189. Paul, S., Gour, N. K. & Deka, R. C. Mechanistic Investigation of the Atmospheric Oxidation of Bis(2-Chloroethyl) Ether ($ClCH_2CH_2OCH_2CH_2Cl$) by OH and NO_3 Radicals and Cl Atoms: A DFT Approach. *J. Mol. Model.* **25,** 43 (2019).

190. Cheng, J. *et al.* Kinetics Study of H-Atom Abstraction from 3-Pentanone by H and CH_3 Radicals and the Subsequent Isomerization Reactions. *Fuel* **236,** 1018–1025 (2019).

191. Gour, N. K., Rajkumari, N. P., Deka, R. C., Paul, S. & Deka, A. Atmospheric Degradation Pathways and Kinetics of 2,2-Difluoroethanol (CHF_2CH_2OH) with Cl Atom: A Theoretical Investigation. *Chem. Phys. Lett.* **716,** 35–41 (2019).

192. Wang, L. & Wang, L. Atmospheric Oxidation Mechanism of Sabinene Initiated by the Hydroxyl Radicals. *J. Phys. Chem. A* **122,** 8783–8793 (2018).

193. Gao, Z. *et al.* Ab Initio Calculation for Isomerization Reaction Kinetics of Nitrobenzene Isomers. *Chem. Phys. Lett.* **715,** 244–251 (2019).

194. Zhang, Y. & Sun, Y. Theoretical Investigation on Atmospheric Reaction of $O(^3P)$ with CH_2CN. *J. Phys. Org. Chem.* **32,** e3913 (2019).

195. Liu, Y. *et al.* Kinetics of the Reaction of the Simplest Criegee Intermediate with Ammonia: A Combination of Experiment and Theory. *Phys. Chem. Chem. Phys.* **20,** 29669–29676 (2018).

196. Johnston, H. S. & Heicklen, J. Tunneling Corrections for Unsymmetrical Eckart Potential Energy Barriers. *J. Phys. Chem.* **66,** 532–533 (1962).

197. Saheb, V. Ab Initio Theoretical Studies on the Kinetics of the Hydrogen Abstraction Reaction of Hydroxyl Radical with $CH_3CH_2OCF_2CHF_2$ (HFE-374pc2). *Phys. Chem. Res.* **4,** 417–425 (2016).

198. Hernandez, R. & Miller, W. H. Semiclassical transition state theory. A new perspective. *Chem. Phys. Lett.* **214,** 129–136 (1993).

199. Zheng, J. *et al.* A Product Branching Ratio Controlled by Vibrational Adiabaticity and Variational Effects: Kinetics of the H + Trans-N_2H_2 Reactions. *J. Chem. Phys.* **136,** 184310 (2012).

200. Skodje, R. T., Truhlar, D. G. & Garrett, B. C. Vibrationally Adiabatic Models for Reactive Tunneling. *J. Chem. Phys.* **77,** 5955–5976 (1982).

201. Tautermann, C. S., Voegele, A. F., Loerting, T. & Liedl, K. R. The Optimal Tunneling Path for the Proton Transfer in Malonaldehyde. *J. Chem. Phys.* **117,** 1962–1966 (2002).

202. Skodje, R. T., Truhlar, D. G. & Garrett, B. C. A General Small-Curvature Approximation for Transition-State-Theory Transmission Coefficients. *J. Phys. Chem.* **85,** 3019–3023 (1981).

203. Meana-Pañeda, R., Truhlar, D. G. & Fernández-Ramos, A. Direct Dynamics Implementation of the Least-Action Tunneling Transmission Coefficient. Application to the CH_4 /CD_3H/CD_4+ CF_3 Abstraction Reactions. *J. Chem. Theory Comput.* **6,** 3015–3025 (2010).

204. Marcus, R. A. & Coltrin, M. E. A new tunneling path for reactions such as H+H_2 → H_2 +H. *J. Chem. Phys.* **67,** 2609–2613 (1977).

205. Fernandez-Ramos, A. & Zgierski, M. Theoretical Study of the Rate Constants and Kinetic Isotope Effects of the 1,2-Hydrogen-Atom Shift of Methoxyl and Benzyloxyl Radicals Assisted by Water. *J. Phys. Chem. A* **106,** 10578–10583 (2002).

206. Fernández-Ramos, A. & Truhlar, D. G. A New Algorithm for Efficient Direct Dynamics Calculations of Large-Curvature Tunneling and Its Application to Radical Reactions with 9-15 Atoms. *J. Chem. Theory Comput.* **1,** 1063–1078 (2005).

207. Liu, Y. P. *et al.* Molecular Modeling of the Kinetic Isotope Effect for the [1,5]-Sigmatropic Rearrangement of Cis-1,3-Pentadiene. *J. Am. Chem. Soc.* **115,** 2408–2415 (1993).

208. Lu, D. & Truhlar, D. G. Bond-distance and bond-angle constraints in reaction-path dynamics calculations. *J. Chem. Phys.* **99,** 2723–2738 (1993).

209. Garrett, B. C., Abusalbi, N., Kouri, D. J. & Truhlar, D. G. Test of Variational Transition State Theory and the Least-action Approximation for Multidimensional Tunneling Probabilities against Accurate Quantal Rate Constants for a Collinear Reaction Involving Tunneling into an Excited State. *J. Chem. Phys.* **83,** 2252–2258 (1985).

210. Garrett, B. C. & Truhlar, D. G. A Least-action Variational Method for Calculating Multidimensional Tunneling Probabilities for Chemical Reactions. *J. Chem. Phys.* **79,** 4931–4938 (1983).

211. Smith, I. W. Vibrational adiabaticity in chemical reactions. *Acc. Chem. Res.* **23,** 101–107 (1990).

212. Bowman, J. M. Overview of Reduced Dimensionality Quantum Approaches to Reactive Scattering. *Theor. Chem. Acc.* **108,** 125–133 (2002).

213. Qi, J. & Bowman, J. M. A Test of J-Shifting for H + CO Recombination. *Chem. Phys. Lett.* **276,** 371–374 (1997).

214. Zhang, D. H. & Zhang, J. Z. H. Uniform J-Shifting Approach for Calculating Reaction Rate Constant. *J. Chem. Phys.* **110,** 7622–7626 (1999).

215. Bittererová, M., Bowman, J. M. & Peterson, K. Quantum Scattering Calculations of the O(^{1}D)+HCl Reaction Using a New Ab Initio Potential and Extensions of J-Shifting. *J. Chem. Phys.* **113,** 6186–6196 (2000).

216. Lu, D. H., Maurice, D. & Truhlar, D. G. What is the effect of variational optimization of the transition state on α-deuterium secondary kinetic isotope effects? A prototype: CD_3H + H ⇌ CD_3+ H_2. *J. Am. Chem. Soc.* **112,** 6206–6214 (1990).

217. Suleimanov, Y. V. & Espinosa-Garcia, J. Recrossing and Tunneling in the Kinetics Study of the OH + CH_4 → H_2O + CH_3 Reaction. *J. Phys. Chem. B* **120,** 1418–1428 (2016).

218. Meana-Pañeda, R., Xu, X., Ma, H. & Truhlar, D. G. Computational Kinetics by Variational Transition-State Theory with Semiclassical Multidimensional Tunneling: Direct Dynamics Rate Constants for the Abstraction of H from CH_3OH by Triplet Oxygen Atoms. *J. Phys. Chem. A* **121,** 1693–1707 (2017).

219. Espinosa-Garcia, J. & Corchado, J. Potential Energy Surface for a Seven-Atom Reaction. Thermal Rate Constants and Kinetic Isotope Effects for CH_4+OH. *J. Chem. Phys.* **112,** 5731–5739 (2000).

220. Espinosa-Garcia, J. & Garcia-Bernaldez, J. Analytical Potential Energy Surface for the $CH_4 + O(^3P) \rightarrow CH_3 + OH$ Reaction. Thermal Rate Constants and Kinetic Isotope Effects. *Phys. Chem. Chem. Phys.* **2,** 2345–2351 (2000).

221. *Potential Energy Surfaces and Dynamics Calculations: For Chemical Reactions and Molecular Energy Transfer* (ed Truhlar, D. G.) (Springer US, 1981).

222. Joseph, T., Steckler, R. & Truhlar, D. G. A New Potential Energy Surface for the $CH_3 + H_2 \leftrightarrow CH_4 + H$ Reaction: Calibration and Calculations of Rate Constants and Kinetic Isotope Effects by Variational Transition State Theory and Semiclassical Tunneling Calculations. *J. Chem. Phys.* **87,** 7036–7049 (1987).

223. Natanson, G. A., Garrett, B. C., Truong, T. N., Joseph, T. & Truhlar, D. G. The Definition of Reaction Coordinates for Reaction-path Dynamics. *J. Chem. Phys.* **94,** 7875–7892 (1991).

224. Espinosa-Garcia, J. Analytical Potential Energy Surface for the GeH_4+H $\rightarrow$ GeH_3+H_2 Reaction: Thermal and Vibrational-State Selected Rate Constants and Kinetic Isotope Effects. *J. Chem. Phys.* **111,** 9330–9336 (1999).

225. Nguyen, K. A., Jackels, C. F. & Truhlar, D. G. Reaction-Path Dynamics in Curvilinear Internal Coordinates Including Torsions. *J. Chem. Phys.* **104,** 6491–6496 (1996).

226. Pérez de Tudela, R. *et al.* Stress Test for Quantum Dynamics Approximations: Deep Tunneling in the Muonium Exchange Reaction D + HMu $\rightarrow$ DMu + H. *J. Phys. Chem. Lett.* **5,** 4219–4224 (2014).

227. Boothroyd, A. I., Keogh, W. J., Martin, P. G. & Peterson, M. R. A Refined H3 Potential Energy Surface. *J. Chem. Phys.* **104,** 7139–7152 (1996).

228. Johnson, D. & Marston, G. The gas-phase ozonolysis of unsaturated volatile organic compounds in the troposphere. *Chem. Soc. Rev.* **37,** 699–716 (2008).

229. Kroll, J. H., Sahay, S. R., Anderson, J. G., Demerjian, K. L. & Donahue, N. M. Mechanism of HO_x Formation in the Gas-Phase Ozone-Alkene Reaction. 2. Prompt versus Thermal Dissociation of Carbonyl Oxides to Form OH. *J. Phys. Chem. A* **105,** 4446–4457 (2001).

230. Harrison, R. M. *et al.* Measurement and modelling of air pollution and atmospheric chemistry in the U.K. West Midlands conurbation: Overview of the PUMA Consortium project. *Science of The Total Environment. Urban Environmental Research in the UK: The Urban Regeneration and the Environment (NERC URGENT) Programme and associated studies.* **360,** 5–25 (2006).

231. Chhantyal-Pun, R. *et al.* Criegee Intermediate Reactions with Carboxylic Acids: A Potential Source of Secondary Organic Aerosol in the Atmosphere. *ACS Earth Space Chem.* **2,** 833–842 (2018).

232. Yin, C. & Takahashi, K. How Does Substitution Affect the Unimolecular Reaction Rates of Criegee Intermediates? *Phys. Chem. Chem. Phys.* **19,** 12075–12084 (2017).

233. Kuwata, K. T. *et al.* Quantum Chemical and Statistical Rate Theory Studies of the Vinyl Hydroperoxides Formed in Trans-2-Butene and 2,3-Dimethyl-2-Butene Ozonolysis. *J. Phys. Chem. A* **122,** 2485–2502 (2018).

234. Huang, H.-L., Chao, W. & Lin, J. J.-M. Kinetics of a Criegee intermediate that would survive high humidity and may oxidize atmospheric SO_2. *Proc. Natl. Acad. Sci. U.S.A.* **112,** 10857–10862 (2015).

235. Kumar, M., Busch, D. H., Subramaniam, B. & Thompson, W. H. Barrierless Tautomerization of Criegee Intermediates via Acid Catalysis. *Phys. Chem. Chem. Phys.* **16,** 22968–22973 (2014).

236. Berndt, T. *et al.* Competing atmospheric reactions of CH_2OO with SO_2 and water vapour. *Phys. Chem. Chem. Phys.* **16,** 19130–19136 (2014).

237. Chao, W., Hsieh, J.-T., Chang, C.-H. & Lin, J. J.-M. Direct kinetic measurement of the reaction of the simplest Criegee intermediate with water vapor. *Science* **347,** 751–754 (2015).

238. Welz, O. *et al.* Direct kinetic measurements of Criegee intermediate (CH_2OO) formed by reaction of CH_2I with O_2. *Science* **335,** 204–207 (2012).

239. Vereecken, L., Novelli, A. & Taraborrelli, D. Unimolecular decay strongly limits the atmospheric impact of Criegee intermediates. *Phys. Chem. Chem. Phys.* **19,** 31599–31612 (2017).

240. Lee, Y.-P. Perspective: Spectroscopy and kinetics of small gaseous Criegee intermediates. *J. Chem. Phys.* **143,** 020901 (2015).

241. Lewis, T. R., Blitz, M. A., Heard, D. E. & Seakins, P. W. Direct evidence for a substantive reaction between the Criegee intermediate, CH_2OO, and the water vapour dimer. *Phys. Chem. Chem. Phys.* **17,** 4859–4863 (2015).

242. Smith, M. C. *et al.* Strong Negative Temperature Dependence of the Simplest Criegee Intermediate CH_2OO Reaction with Water Dimer. *J. Phys. Chem. Lett.* **6,** 2708–2713 (2015).

243. Taatjes, C. A. *et al.* Direct Measurements of Conformer-Dependent Reactivity of the Criegee Intermediate CH_3CHOO. *Science* **340,** 177–180 (2013).

244. Chhantyal-Pun, R., Davey, A., Shallcross, D. E., Percival, C. J. & Orr-Ewing, A. J. A kinetic study of the CH_2OO Criegee intermediate self-reaction, reaction with SO_2 and unimolecular reaction using cavity ring-down spectroscopy. *Phys. Chem. Chem. Phys.* **17,** 3617–3626 (2015).

245. Buras, Z. J., Elsamra, R. M. I. & Green, W. H. Direct Determination of the Simplest Criegee Intermediate (CH_2OO) Self Reaction Rate. *J. Phys. Chem. Lett.* **5,** 2224–2228 (2014).

246. Su, Y.-T. *et al.* Extremely rapid self-reaction of the simplest Criegee intermediate CH_2OO and its implications in atmospheric chemistry. *Nat. Chem.* **6,** 477–483 (2014).

247. Aaltonen, E. T. & Francisco, J. S. $HOSO_2 - H_2O$ Radical Complex and Its Possible Effects on the Production of Sulfuric Acid in the Atmosphere. *J. Phys. Chem. A* **107,** 1216–1221 (2003).

248. Hansen, J. C. & Francisco, J. S. Radical - Molecule Complexes: Changing Our Perspective on the Molecular Mechanisms of Radical - Molecule Reactions and their Impact on Atmospheric Chemistry. *ChemPhysChem* **3,** 833–840 (2002).

249. Buszek, R. J., Torrent-Sucarrat, M., Anglada, J. M. & Francisco, J. S. Effects of a Single Water Molecule on the OH + H_2O_2 Reaction. *J. Phys. Chem. A* **116,** 5821–5829 (2012).

250. Vöhringer-Martinez, E. *et al.* Water Catalysis of a Radical-Molecule Gas-Phase Reaction. *Science* **315,** 497–501 (2007).

251. Long, B. *et al.* Theoretical Studies on Reactions of the Stabilized H_2COO with HO_2 and the $HO_2 - H_2O$ Complex. *J. Phys. Chem. A* **115,** 6559–6567 (2011).

252. Chen, L. *et al.* Water-catalyzed decomposition of the simplest Criegee intermediate CH_2OO. *Theor. Chem. Acc.* **135,** 131 (2016).

253. Ryzhkov, A. B. & Ariya, P. A. A theoretical study of the reactions of parent and substituted Criegee intermediates with water and the water dimer. *Phys. Chem. Chem. Phys.* **6,** 5042–5050 (2004).

254. Lin, L.-C., Chao, W., Chang, C.-H., Takahashi, K. & Lin, J. J.-M. Temperature dependence of the reaction of anti- CH_3CHOO with water vapor. *Phys. Chem. Chem. Phys.* **18,** 28189–28197 (2016).

255. Anglada, J. M. & Solé, A. Impact of the water dimer on the atmospheric reactivity of carbonyl oxides. *Phys. Chem. Chem. Phys.* **18,** 17698–17712 (2016).

256. Chen, L. *et al.* Role of water clusters in the reaction of the simplest Criegee intermediate CH_2OO with water vapour. *Theor. Chem. Acc.* **135,** 252 (2016).

257. Lin, L.-C. *et al.* Competition between H_2O and $(H_2O)_2$ reactions with CH_2OO/CH_3CHOO. *Phys. Chem. Chem. Phys.* **18,** 4557–4568 (2016).

258. Ryzhkov, A. B. & Ariya, P. A. The importance of water clusters $(H_2O)_n$ (n=2,...,4) in the reaction of Criegee intermediate with water in the atmosphere. *Chem. Phys. Lett.* **419,** 479–485 (2006).

259. Womack, C. C., Martin-Drumel, M.-A., Brown, G. G., Field, R. W. & McCarthy, M. C. Observation of the simplest Criegee intermediate CH_2OO in the gas-phase ozonolysis of ethylene. *Sci. Adv.* **1,** e1400105 (2015).

260. Fang, Y., Liu, F., Klippenstein, S. J. & Lester, M. I. Direct observation of unimolecular decay of CH_3CH_2CHOO Criegee intermediates to OH radical products. *J. Chem. Phys.* **145,** 044312 (2016).

261. Long, B., Bao, J. L. & Truhlar, D. G. Unimolecular Reaction of Acetone Oxide and Its Reaction with Water in the Atmosphere. *Proc. Natl. Acad. Sci. U.S.A.* **115,** 6135–6140 (2018).

262. Stephens, P. J., Devlin, F. J., Chabalowski, C. F. & Frisch, M. J. Ab Initio Calculation of Vibrational Absorption and Circular Dichroism Spectra Using Density Functional Force Fields. *J. Phys. Chem.* **98,** 11623–11627 (1994).

263. Cremer, D., Gauss, J., Kraka, E., Stanton, J. F. & Bartlett, R. J. A CCSD (T) Investigation of Carbonyl Oxide and Dioxirane. Equilibrium Geometries, Dipole Moments, Infrared Spectra, Heats of Formation and Isomerization Energies. *Chem. Phys. Lett.* **209,** 547–556 (1993).

264. Nakajima, M. & Endo, Y. Communication: Determination of the Molecular Structure of the Simplest Criegee Intermediate CH_2OO. *J. Chem. Phys.* **139,** 101103 (2013).

265. Long, B., Bao, J. L. & Truhlar, D. G. Atmospheric Chemistry of Criegee Intermediates: Unimolecular Reactions and Reactions with Water. *J. Am. Chem. Soc.* **138,** 14409–14422 (2016).

266. Fang, Y. *et al.* Communication: Real Time Observation of Unimolecular Decay of Criegee Intermediates to OH Radical Products. *J. Chem. Phys.* **144,** 061102 (2016).

267. Nguyen, T. L., McCaslin, L., McCarthy, M. C. & Stanton, J. F. Communication: Thermal unimolecular decomposition of syn-CH_3CHOO: A kinetic study. *J. Chem. Phys.* **145,** 131102 (2016).

268. Fang, Y. *et al.* Deep tunneling in the unimolecular decay of CH_3CHOO Criegee intermediates to OH radical products. *J. Chem. Phys.* **145,** 234308 (2016).

269. Chhantyal-Pun, R. *et al.* Direct Measurements of Unimolecular and Bimolecular Reaction Kinetics of the Criegee Intermediate $(CH_3)_2COO$. *J. Phys. Chem. A* **121,** 4–15 (2017).

270. Smith, M. C., Chao, W., Takahashi, K., Boering, K. A. & Lin, J. J.-M. Unimolecular Decomposition Rate of the Criegee Intermediate $(CH_3)_2COO$ Measured Directly with UV Absorption Spectroscopy. *J. Phys. Chem. A* **120,** 4789–4798 (2016).

271. Panek, P. T. & Jacob, C. R. On the benefits of localized modes in anharmonic vibrational calculations for small molecules. *J. Chem. Phys.* **144,** 164111 (2016).

272. Panek, P. T. & Jacob, C. R. Efficient Calculation of Anharmonic Vibrational Spectra of Large Molecules with Localized Modes. *ChemPhysChem* **15,** 3365–3377 (2014).

273. Molina, A., Smereka, P. & Zimmerman, P. M. Exploring the Relationship between Vibrational Mode Locality and Coupling Using Constrained Optimization. *J. Chem. Phys.* **144,** 124111 (2016).

274. Zhang, T. *et al.* Can a single water molecule really affect the $HO_2 + NO_2$ hydrogen abstraction reaction under tropospheric conditions? *Phys. Chem. Chem. Phys.* **17,** 15046–15055 (2015).

275. Paulson, S. E. & Orlando, J. J. The Reactions of Ozone with Alkenes: An Important Source of HO_x in the Boundary Layer. *Geophys. Res. Lett.* **23,** 3727–3730 (1996).

276. Schreiner, P. R. Tunneling Control of Chemical Reactions: The Third Reactivity Paradigm. *J. Am. Chem. Soc.* **139,** 15276–15283 (2017).

277. Karmakar, S. & Datta, A. Tunneling Control: Competition between 6π-Electrocyclization and [1,5]H-Sigmatropic Shift Reactions in Tetrahydro-1H-Cyclobuta[e]Indene Derivatives. *J. Org. Chem.* **82,** 1558–1566 (2017).

278. Schreiner, P. R. *et al.* Methylhydroxycarbene: Tunneling Control of a Chemical Reaction. *Science* **332,** 1300–1303 (2011).

279. Ley, D., Gerbig, D. & Schreiner, P. R. Tunneling Control of Chemical Reactions: C–H Insertion versus H-Tunneling in Tert-Butylhydroxycarbene. *Chem. Sci.* **4,** 677–684 (2013).

280. Schäfer, M. *et al.* Hydrogen Tunneling above Room Temperature Evidenced by Infrared Ion Spectroscopy. *J. Am. Chem. Soc.* **139,** 5779–5786 (2017).

281. Eckhardt, A. K., Gerbig, D. & Schreiner, P. R. Heavy Atom Secondary Kinetic Isotope Effect on H-Tunneling. *J. Phys. Chem. A* **122,** 1488–1495 (2018).

282. Paul, M. *et al.* Hydrogen Tunneling Avoided: Enol-Formation From a Charge-Tagged Phenyl Pyruvic Acid Derivative Evidenced by Tandem-MS, IR Ion Spectroscopy and Theory. *Phys. Chem. Chem. Phys.* (2019).

283. Ley, D., Gerbig, D. & R. Schreiner, P. Tunnelling Control of Chemical Reactions – the Organic Chemist's Perspective. *Org. Biomol. Chem.* **10,** 3781–3790 (2012).

284. Kästner, J. Path Length Determines the Tunneling Decay of Substituted Carbenes. *Chem.: Eur. J.* **19,** 8207–8212 (2013).

285. Zhao, Y. & Truhlar, D. G. The M06 Suite of Density Functionals for Main Group Thermochemistry, Thermochemical Kinetics, Noncovalent Interactions, Excited States, and Transition Elements: Two New Functionals and Systematic Testing of Four M06-Class Functionals and 12 Other Functionals. *Theor. Chem. Acc.* **120,** 215–241 (2008).

286. Bowman, J. M. & Schatz, G. C. Theoretical Studies of Polyatomic Bimolecular Reaction Dynamics. *Annu. Rev. Phys. Chem.* **46,** 169–196 (1995).

287. Takayanagi, T. Reduced Dimensionality Calculations of Quantum Reactive Scattering for the $H + CH_4 \rightarrow H_2 + CH_3$ Reaction. *J. Chem. Phys.* **104,** 2237–2242 (1996).

288. Clary, D. C. Quantum Theory of Chemical Reaction Dynamics. *Science* **279,** 1879–1882 (1998).

289. Aguillon, F. & Sizun, M. Reduced Dimensionality Wave Packet Study of the $NH_3^+ + H_2, D_2$ Reaction. *J. Chem. Phys.* **112,** 10179–10191 (2000).

290. Szichman, H., Gilibert, M., González, M., Giménez, X. & Navarro, A. A. Four-Dimensional Quantum Mechanical Treatment of Penta-Atomic Systems: Case $H_2 + C_2H \rightarrow H + C_2H_2$; Total Reactive Probabilities, Cross Sections, and Rate Constants. *J. Chem. Phys.* **113,** 176–183 (2000).

291. Szichman, H., Gilibert, M., González, M., Giménez, X. & Aguilar, A. A Four-Dimensional Quantum Mechanical State-to-State Study of the $H_2 + C_2H \rightarrow H + C_2H_2$ Reaction. *J. Chem. Phys.* **114,** 9882–9894 (2001).

292. Kerkeni, B. & Clary, D. C. Quantum Reactive Scattering of H + Hydrocarbon Reactions. *Phys. Chem. Chem. Phys.* **8,** 917–925 (2006).

293. Yetra, S. R., Mondal, S., Mukherjee, S., Gonnade, R. G. & Biju, A. T. Enantioselective Synthesis of Spirocyclohexadienones by NHC-Catalyzed Formal [3+3] Annulation Reaction of Enals. *Angew. Chem. Int.* **55,** 268–272 (2016).

294. Karmakar, S. & Datta, A. Role of Quantum Mechanical Tunneling on the γ-Effect of Silicon on Carbenes in 3-Trimethylsilylcyclobutylidene. *J. Phys. Chem. B* **118,** 2553–2558 (2014).

295. Sulzbach, H. M., Platz, M. S., Schaefer, H. F. & Hadad, C. M. Hydrogen Migration vs Carbon Migration in Dialkylcarbenes. A Study of the Preferred Product in the Carbene Rearrangements of Ethylmethylcarbene, Cyclobutylidene, 2-Norbornylidene, and 2-Bicyclo[2.1.1]Hexylidene. *J. Am. Chem. Soc.* **119,** 5682–5689 (1997).

296. Kaufman, G. M., Smith, J. A., Stouw, G. G. V. & Shechter, H. Pyrolysis of Salts of P-Tosylhydrazones. Simple Methods for Preparing Diazo Compounds and Effecting Their Carbenic Decomposition. *J. Am. Chem. Soc.* **87,** 935–937 (1965).

297. Friedman, L. & Shechter, H. Rearrangement and Fragmentation Reactions in Carbenoid Decomposition of Diazo Hydrocarbons. *J. Am. Chem. Soc.* **82,** 1002–1003 (1960).

298. Pezacki, J. P. *et al.* Laser Flash and Dual Wavelength Photolysis of 3,4-Diaza-2,2-Dimethoxy-1-Oxa[4.5]Spirooct-3-Ene. Migration of Hydrogen and Carbon in Cyclobutylidene and in the Excited State of Its Precursor. *J. Am. Chem. Soc.* **119,** 3191–3192 (1997).

299. Creary, X. 3-Trimethylsilylcyclobutylidene. The γ-Effect of Silicon on Carbenes. *J. Am. Chem. Soc.* **135,** 6570–6578 (2013).

300. Clark, T., Chandrasekhar, J., Spitznagel, G. W. & Schleyer, P. V. R. Efficient Diffuse Function-Augmented Basis Sets for Anion Calculations. III. The 3-21+G Basis Set for First-Row Elements, Li–F. *J. Comp. Chem.* **4,** 294–301 (1983).

301. Limbach, H.-H., Miguel Lopez, J. & Kohen, A. Arrhenius Curves of Hydrogen Transfers: Tunnel Effects, Isotope Effects and Effects of Pre-Equilibria. *Philos. Trans. R. Soc. B* **361,** 1399–1415 (2006).

302. Kästner, J. Theory and Simulation of Atom Tunneling in Chemical Reactions. *Wiley Interdiscip. Rev. Comput. Mol. Sci.* **4,** 158–168 (2014).

303. Richardson, J. O. *Ring-Polymer Approaches to Instanton Theory* Thesis (University of Cambridge, 2012).

304. Cvitaš, M. T. & Richardson, J. O. Quantum tunnelling pathways of the water pentamer. *Phys. Chem. Chem. Phys.* (2019).

305. Smit, M. J. *et al.* Vibrations, tunneling, and transition dipole moments in the water dimer. *J. Phys. Chem. A* **105,** 6212–6225 (2001).

306. Huang, X. *et al.* New Ab Initio Potential Energy Surface and the Vibration-Rotation-Tunneling Levels of $(H_2O)_2$ and $(D_2O)_2$. *J. Chem. Phys.* **128,** 034312 (2008).

307. Leforestier, C., Szalewicz, K. & van der Avoird, A. Spectra of Water Dimer from a New Ab Initio Potential with Flexible Monomers. *J. Chem. Phys.* **137,** 014305 (2012).

308. Watanabe, Y., Taketsugu, T. & Wales, D. J. An Ab Initio Study of Tunneling Splittings in the Water Dimer. *J. Chem. Phys.* **120,** 5993–5999 (2004).

309. Takahashi, M., Watanabe, Y., Taketsugu, T. & Wales, D. J. An Ab Initio Study of Tunneling Splittings in the Water Trimer. *J. Chem. Phys.* **123,** 044302 (2005).

310. Takada, S. & Nakamura, H. Effects of Vibrational Excitation on Multidimensional Tunneling: General Study and Proton Tunneling in Tropolone. *J. Chem. Phys.* **102,** 3977–3992 (1995).

311. Guo, Y., Sewell, T. D. & Thompson, D. L. Semiclassical Calculations of Tunneling Splitting in Tropolone. *J. Phys. Chem. A* **102,** 5040–5048 (1998).

312. Garg, A. Tunnel Splittings for One-Dimensional Potential Wells Revisited. *Am. J. Phys.* **68,** 430–437 (2000).

313. Miller, W. H. Periodic orbit description of tunneling in symmetric and asymmetric double-well potentials. *J. Phys. Chem.* **83,** 960–963 (1979).

314. Tautermann, C. S., Voegele, A. F. & Liedl, K. R. The Ground-State Tunneling Splitting of Various Carboxylic Acid Dimers. *J. Chem. Phys.* **120,** 631–637 (2003).

315. Tautermann, C. S., Voegele, A. F., Loerting, T. & Liedl, K. R. An Accurate Semiclassical Method to Predict Ground-State Tunneling Splittings. *J. Chem. Phys.* **117,** 1967–1974 (2002).

316. Brown, F. B., Tucker, S. C. & Truhlar, D. G. Semiclassical Reaction-path Methods Applied to Calculate the Tunneling Splitting in Ammonia. *J. Chem. Phys.* **83,** 4451–4455 (1985).

317. Mil'nikov, G., Kühn, O. & Nakamura, H. Ground-state and vibrationally assisted tunneling in the formic acid dimer. *J. Chem. Phys.* **123,** 074308 (2005).

318. Wang, Y. & Bowman, J. M. Mode-Specific Tunneling Using the Qim Path: Theory and an Application to Full-Dimensional Malonaldehyde. *J. Chem. Phys.* **139,** 154303 (2013).

319. Tautermann, C. S., Voegele, A. F. & Liedl, K. R. The ground state tunneling splitting of the 2-pyridone· 2-hydroxypyridine dimer. *Chem. Phys.* **292,** 47–52 (2003).

320. Miller, W. H. Semiclassical Treatment of Multiple Turning-Point Problems—Phase Shifts and Eigenvalues. *J. Chem. Phys.* **48,** 1651–1658 (1968).

321. Cvitaš, M. T. & Althorpe, S. C. Locating Instantons in Calculations of Tunneling Splittings: The Test Case of Malonaldehyde. *J. Chem. Theory Comput.* **12,** 787–803 (2016).

322. Mil'nikov, G. V. & Nakamura, H. Practical Implementation of the Instanton Theory for the Ground-State Tunneling Splitting. *J. Chem. Phys.* **115,** 6881–6897 (2001).

323. Tew, D. P., Handy, N. C. & Carter, S. The vibrations and tunnelling of malonaldehyde on a Møller–Plesset surface. *Mol. Phys.* **102,** 2217–2226 (2004).

324. Tew, D. P., Handy, N. C., Carter, S., Irle, S. & Bowman, J. The internal coordinate path Hamiltonian; application to methanol and malonaldehyde. *Mol. Phys.* **101,** 3513–3525 (2003).

325. Mizukami, W., Habershon, S. & Tew, D. P. A compact and accurate semi-global potential energy surface for malonaldehyde from constrained least squares regression. *J. Chem. Phys.* **141,** 144310 (2014).

326. Kahn, V. & Andrawis, A. Inhibition of Mushroom Tyrosinase by Tropolone. *Phytochemistry* **24,** 905–908 (1985).

327. Sekiya, H., Nagashima, Y. & Nishimura, Y. Electronic Spectra of Jet-cooled Tropolone. Effect of the Vibrational Excitation on the Proton Tunneling Dynamics. *J. Chem. Phys.* **92,** 5761–5769 (1990).

328. Paz, J. J., Moreno, M. & Lluch, J. M. Bidimensional Tunneling Splitting in the $\tilde{A}^1B_2$ and $\tilde{X}^1A_1$ States of Tropolone. *J. Chem. Phys.* **103,** 353–359 (1995).

329. Smedarchina, Z., Siebrand, W. & Zgierski, M. Z. Mode-specific Hydrogen Tunneling in Tropolone: An Instanton Approach. *J. Chem. Phys.* **104,** 1203–1212 (1996).

330. Frost, R. K., Hagemeister, F. C., Arrington, C. A., Zwier, T. S. & Jordan, K. D. Fluorescence-dip infrared spectroscopy of tropolone and tropolone-OD. *J. Chem. Phys.* **105,** 2595–2604 (1996).

331. Redington, R. L., Redington, T. E. & Sams, R. L. Tunneling Splittings for "O - O Stretching" and Other Vibrations of Tropolone Isotopomers Observed in the Infrared Spectrum Below 800 cm^{-1}. *J. Phys. Chem. A* **112,** 1480–1492 (2008).

332. Gutzwiller, M. C. Periodic orbits and classical quantization conditions. *J. Math. Phys.* **12,** 343–358 (1971).

Appendices

Appendix A

The pySCTST software

pySCTST is a simple and user-friendly python package for performing Semiclassical Transition State Theory calculations, and is freely available at: `bitbucket.org/timothyburd/pysctst`. The package contains tutorials and example scripts that reproduce many of the results in this thesis. This section contains a brief description of the code, and outlines the requirements to perform SCTST calculations with it. A full *Getting Started Guide* can be found at `bitbucket.org/timothyburd/pysctst`

A.1 Requirements

There are three software requirements to use the *pySCTST* software:

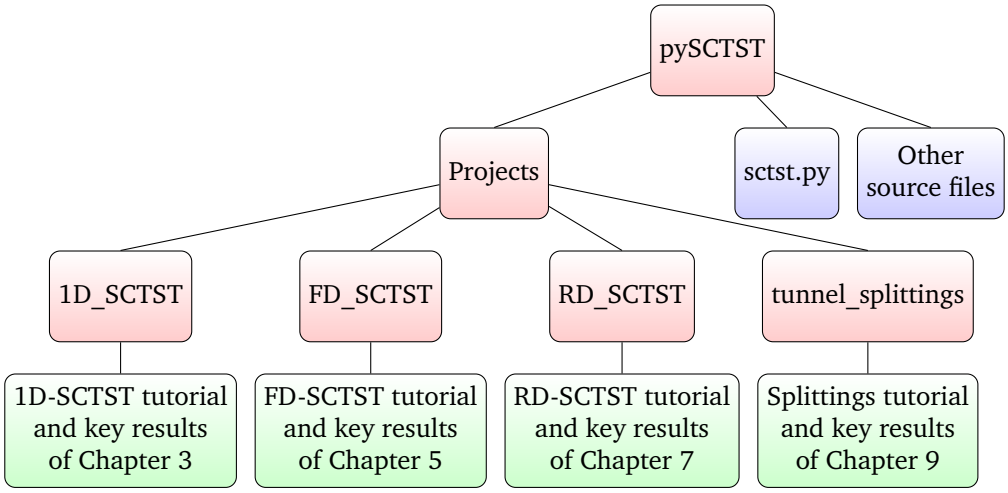
1. Python 3.5 or later
2. C complier, such as *gcc* [*Not required to run the examples in the repository*]
3. Electronic structure package [*Not required to run the examples in the repository*]
    - Currently, *pySCTST* is designed for use with Gaussian output files[147].

Within *pySCTST*, an SCTST calculation comprises of three components:

- pySCTST Source files
    - sctst.py is the main module. This contains all the important classes such as the TransitionState class, Reaction class and Series class that are used in the script file
- *ab initio* data
    - Output files form electronic structure software such as Gaussian[147] is held in `checkpoint_files` or `FD_files` (for the output of VPT2 calculations)
- Script file
    - The study-specific script that is run to produce the desired SCTST results.
    - Begins with an import of the sctst.py module
    - Creates instances of the classes from sctst.py, using data from the *ab initio* data directories
    - Generates figures and data for the reactions of interest

A.2 The repository

The repository contains four 'projects' with tutorials on 1D-SCTST, FD-SCTST, RD-SCTST and tunnelling splittings, illustrating simple calculations using *pySCTST*. Each project also contains data and scripts to reproduce many of the results of this thesis, demonstrating more complex calculations. Each project also contains a test file to ensure the code is correctly set up to reproduce the results in this thesis. The structure of the repository is shown below:



1D SCTST

This project directory contains a short tutorial on 1D-SCTST calculations, using the $CH_3 + CH_4$ reaction as an example. The main results of Section 3.2 are reproduced by the `thesis_results.py` script, to illustrate its application.

FD SCTST

This project directory contains a short tutorial on FD-SCTST calculations, using the Criegee decay reactions as an example. The main results of Chapter 5 are reproduced by the `thesis_results.py` script, to illustrate their application.

RD SCTST

This project directory contains a short tutorial on 2D-SCTST calculations, using the unimolecular carbene rearrangement reaction as an example. The main results of Chapter 5 are reproduced by the `thesis_results.py` script, to illustrate their application.

Tunnelling Splittings

This project directory contains a short tutorial on SPT calculations, using the Malonaldehyde isomerisation as an example. The main results of Chapter 9 are reproduced by the `thesis_results.py` script, to illustrate its application.

Appendix B

WKB tunnelling in a parabolic barrier

For a parabolic potential, in reduced mass coordinates,

$$V_{\text{parabola}}(x) = V_0 - \frac{1}{2}|\omega|^2 x^2 \tag{B.1}$$

where

$$\omega = i|\omega|. \tag{B.2}$$

In this case, Eq. 2.5, can be evaluated analytically:

$$\begin{aligned}
\theta_{\text{parabola}}(E) &= \sqrt{2}\int_{x_-}^{x_+} dx \sqrt{V_0 - E - \frac{1}{2}|\omega|^2 x^2} \\
&= \sqrt{2\,(V_0 - E)}\int_{x_-}^{x_+} dx \sqrt{1 - \left(\frac{x}{\alpha}\right)^2} \\
&= \frac{\sqrt{2\,(V_0 - E)}}{2}\left[x\sqrt{1 - \left(\frac{x}{\alpha}\right)^2} + \alpha \sin^{-1}\left(\frac{x}{\alpha}\right)\right]_{x_-}^{x_+}
\end{aligned} \tag{B.3}$$

where:

$$\alpha^2 = \frac{2\,(V_0 - E)}{|\omega|^2}. \tag{B.4}$$

The limits of integration are given by $x_\pm = \pm\alpha$, giving:

$$\begin{aligned}
\theta_{\text{parabola}}(E) &= \frac{\sqrt{2\,(V_0 - E)}}{2}\left[\alpha \sin^{-1}(1) - \alpha \sin^{-1}(-1)\right] \\
&= \frac{\pi\,(V_0 - E)}{|\omega|} \\
&= \frac{i\pi\,(V_0 - E)}{\omega}
\end{aligned} \tag{B.5}$$

Therefore, using Eq. 2.6:

$$P_{\text{parabola}}(E) = \exp\left[-2i\pi\frac{V_0 - E}{\omega}\right] \tag{B.6}$$

Appendix C

SCTST-θ

In Chapter 2, we discussed the most commonly used form of SCTST. This formulation, however, is not useful for more complex potential functions. If a higher order level of perturbation theory is used, for example, this can require the inversion of higher order polynomials, which is not, in general, analytic. In this section, we discuss an alternative formulation of SCTST proposed by Hernandez and Miller[198] which we shall refer to as SCTST-θ. This formulation allows for any potential $E(\theta)$ to be used.

C.1 Derivation

In Eq. 2.34, the integration is performed in the energy domain:

$$k(T) = \frac{1}{h}\frac{Q^{\dagger}_{trans}(T)Q^{\dagger}_{rot}(T)Q^{\dagger}_{elec}(T)}{Q_r(T)}\int_0^{\infty}\sum_{\{n\}'}\frac{1}{1+\exp\left[2\theta_{\{n\}'}(E)\right]}\exp(-\beta E)dE \quad \text{(C.1)}$$

Miller and co-workers [198] suggested that the same integration can also be done in the barrier penetration integral, θ, domain. The rate is then given by

$$k(T) = \frac{1}{h}\frac{Q^{\dagger}_{trans}(T)Q^{\dagger}_{rot}(T)Q^{\dagger}_{elec}(T)}{Q_r(T)}\sum_{\{n\}'}\int_{\theta_{\mathrm{T}}}^{-\infty}\frac{\exp[-\beta E_{\{n\}'}(\theta)]}{1+\exp(2\theta)}\frac{\partial E_{\{n\}'}(\theta)}{\partial\theta}\mathrm{d}\theta, \quad \text{(C.2)}$$

where $E_{\{n\}'}(\theta_{\mathrm{T}}) = 0$ for an exothermic or symmetric reaction.

Performing the integration by parts, we get

$$\begin{aligned}\int_{\theta_{\mathrm{T}}}^{-\infty}\frac{\exp[-\beta E_{\{n\}'}(\theta)]}{1+\exp(2\theta)}\frac{\partial E_{\{n\}'}(\theta)}{\partial\theta}\mathrm{d}\theta &= \frac{\exp[-\beta E_{\{n\}'}(\theta_{\mathrm{T}})]}{\beta[1+\exp(2\theta_{\mathrm{T}})]} + \frac{1}{\beta}\int_{-\infty}^{\theta_{\mathrm{T}}}\frac{\mathrm{sech}^2(\theta)}{2}\exp[-\beta E_{\{n\}'}(\theta)]\mathrm{d}\theta \\ &= \frac{1}{\beta[1+\exp(2\theta_{\mathrm{T}})]} + \frac{1}{\beta}\int_{-\infty}^{\theta_{\mathrm{T}}}\frac{\mathrm{sech}^2(\theta)}{2}\exp[-\beta E_{\{n\}'}(\theta)]\mathrm{d}\theta. \quad \text{(C.3)}\end{aligned}$$

We note that the first term of the right hand side of the equation is the Boltzmann weighted reaction probability at the reactant energy, which is negligible compared to the second part of the equation. Equation C.2 can thus be reduced to

$$k(T) = \frac{1}{h\beta}\frac{Q^{\dagger}_{trans}(T)Q^{\dagger}_{rot}(T)Q^{\dagger}_{elec}(T)}{Q_r(T)}\sum_{\{n\}'}\int_{-\infty}^{\theta_{\mathrm{T}}}\frac{\mathrm{sech}^2(\theta)}{2}\exp[-\beta E_{\{n\}'}(\theta)]\mathrm{d}\theta. \quad \text{(C.4)}$$

In order to use Eq. C.4, it is only necessary to know the potential energy as a function of θ, and no inversion is required. It is also possible, in this formulation, to show that the 1D-SCTST rate can be written as the product of a TST rate and a tunnelling correction factor[3].

C.2 Deep tunnelling in SCTST-θ

The VPT2 expression ignores tunnelling for $0 < E < E(\theta_{\mathrm{T}})$, and thus underestimates the rate constants significantly at low T. Wagner's deep tunnelling correction can be much more easily implemented and understood in the SCTST-θ framework. In this case, the energy is effectively expanded to a fourth order polynomial in θ, where the first two coefficients are as determined by VPT2, and the third and fourth order coefficients are chosen such that the forward and reverse barrier heights are correct, and that the slope of $E(\theta)$ is zero at the reactant energy. An additional parameter θ_{max}, is required, which is equal to the barrier penetration integral at $E = 0$. This is calculated numerically using Eq. C.5, and the composite potential discussed previously.

$$\theta_{\mathrm{max}} = \sqrt{2m} \int \sqrt{V(y)} \mathrm{d}y \tag{C.5}$$

$E_{\{n\}'}(\theta)$ is then given by:

$$\begin{aligned} E_{\{n\}'}(\theta) =& \Delta V_f - \hbar\Omega_{\{n\}'} \frac{\theta}{\pi} - \hbar x_{FF} \left(\frac{\theta}{\pi}\right)^2 \\ &+ \left[3\Omega_{\{n\}'} \left(\frac{\theta_{\mathrm{max}}}{\pi}\right) + 2x_{FF} \left(\frac{\theta_{\mathrm{max}}}{\pi}\right)^2 - 4\Delta V_r\right] \left(\frac{\theta}{\theta_{\mathrm{max}}}\right)^3 \\ &- \left[2\Omega_{\{n\}'} \left(\frac{\theta_{\mathrm{max}}}{\pi}\right) + \ x_{FF} \left(\frac{\theta_{\mathrm{max}}}{\pi}\right)^2 - 3\Delta V_r\right] \left(\frac{\theta}{\theta_{\mathrm{max}}}\right)^4, \end{aligned} \tag{C.6}$$

It is also interesting to note that this equation is akin to a VPT4 level expansion of energy, as it contains θ terms of the third and fourth orders. However, the coefficients of these terms in this equation are not derived from information at the TS, as one would have done in VPT4, instead they are chosen specifically to correct the energy threshold problem.

C.3 1D-SCTST-θ

In this formulation, the 1D-SCTST approximations become simpler to understand. The energy function is seperated into its dependence on θ and $\{n\}'$:

$$\begin{aligned} E^{\mathrm{1D}}_{\{n\}'}(\theta) &= \Delta V_f + G_0 + \sum_{j=1}^{F-1} \hbar\omega_j (n_j + 1/2) - \frac{\hbar\omega_F}{i} \left(\frac{\theta}{\pi}\right) - x_{FF} \left(\frac{\theta}{\pi}\right)^2. \\ &= E^0_{\{n\}'} - \frac{\hbar\omega_F}{i} \left(\frac{\theta}{\pi}\right) - x_{FF} \left(\frac{\theta}{\pi}\right)^2. \end{aligned} \tag{C.7}$$

Equation C.4 now becomes:

$$k(T) = \frac{1}{h\beta}\frac{Q^{\dagger}_{trans}(T)Q^{\dagger}_{rot}(T)Q^{\dagger}_{elec}(T)}{Q_r(T)}\sum_{\{n\}'}\int_{-\infty}^{\theta_T}\frac{\mathrm{sech}^2(\theta)}{2}\exp[-\beta E_{\{n\}'}(\theta)]\mathrm{d}\theta$$

$$= \frac{1}{h\beta}\frac{Q^{\dagger}_{trans}(T)Q^{\dagger}_{rot}(T)Q^{\dagger}_{elec}(T)}{Q_r(T)}\sum_{\{n\}'}\exp\left[-\beta\sum_{j=1}^{F-1}\hbar\omega_j(n_j+1/2)\right]\exp\left[-\beta\Delta V_f\right]$$
$$\times\int_{-\infty}^{\theta_T}\frac{\mathrm{sech}^2(\theta)}{2}\exp\left[\beta\left(\frac{\hbar\omega_F}{i}\left(\frac{\theta}{\pi}\right)+x_{FF}\left(\frac{\theta}{\pi}\right)^2-G_0\right)\right]\mathrm{d}\theta$$

$$= \frac{1}{h\beta}\frac{Q^{\dagger}_{trans}(T)Q^{\dagger}_{rot}(T)Q^{\dagger}_{elec}(T)}{Q_r(T)}Q^{\dagger}_{vib}(T)\exp\left[-\beta\Delta V_f\right]$$
$$\times\int_{-\infty}^{\theta_T}\frac{\mathrm{sech}^2(\theta)}{2}\exp\left[\beta\left(\frac{\hbar\omega_F}{i}\left(\frac{\theta}{\pi}\right)+x_{FF}\left(\frac{\theta}{\pi}\right)^2-G_0\right)\right]\mathrm{d}\theta$$

$$= k_{TST}\times\int_{-\infty}^{\theta_T}\frac{\mathrm{sech}^2(\theta)}{2}\exp\left[\beta\left(\frac{\hbar\omega_F}{i}\left(\frac{\theta}{\pi}\right)+x_{FF}\left(\frac{\theta}{\pi}\right)^2-G_0\right)\right]\mathrm{d}\theta$$

$$= \kappa_{1D}(T)\times k_{TST}(T) \tag{C.8}$$

where the tunneling correction, $\kappa_{1D}(T)$, is given by

$$\kappa(T) = \int_{-\infty}^{\theta_T}\frac{\mathrm{sech}^2(\theta)}{2}\exp\left[\beta\left(\frac{\hbar\omega_F}{i}\left(\frac{\theta}{\pi}\right)+x_{FF}\left(\frac{\theta}{\pi}\right)^2-G_0\right)\right]\mathrm{d}\theta \tag{C.9}$$

Thus the one-dimensional SCTST rate can be rewritten as a TST rate multiplied by a separable transmission factor. This is in a similar form to that used by other rate theories, such as VTST/SCT.

Appendix D

Periodic orbit splittings

The Lifshitz-Herring formula:

$$\begin{aligned}\Delta &= \frac{\omega_R}{\pi}\exp\left[-\int_a^b p(x)dx\right] \\ &\equiv \frac{\omega_R}{\pi}\exp\left[-\int_a^b \sqrt{2m\,(V(x)-E_0)}dx\right] \\ &\equiv \frac{\omega_R}{\pi}\exp\left[-\theta(E_0)\right]\end{aligned} \tag{D.1}$$

can be derived in a number of ways [137, 312, 313]. The periodic orbit analysis of Miller[313] makes it most clear where the inadequacies of this formula lie, and how it can be improved. In Miller's derivation, only a subset of the possible periodic orbits are considered. By considering the full set of trajectories we can obtain an improved formula for the splitting.

Here we will follow the derivation of Miller, but include these more general orbits. We first evaluate the quantum mechanical Green's function for a two level system. We then separately evaluate the Green's function using a semiclassical periodic orbit analysis for a symmetric double well system. By comparing the two results, we obtain an expression for the energy splitting.

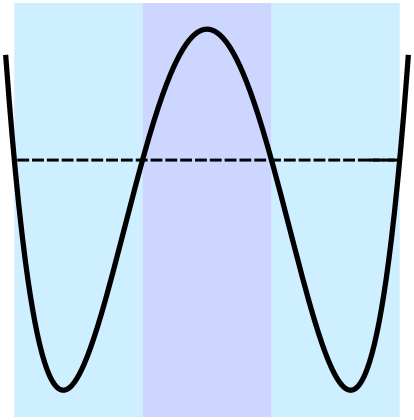


Figure D.1 A symmetric double well potential, with the classically forbidden region shaded in purple.

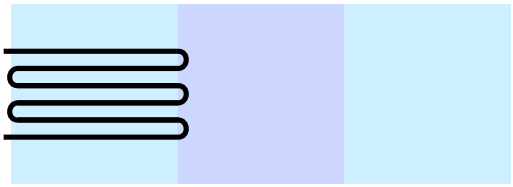


Figure D.2 Non-crossing periodic orbit, C_0

The key result is found in Eq. D.23, and we then test it on the one-dimensional quartic potential, Eq. 9.2.

D.1 Quantum mechanical Green's function

We make use of the relation that the eigenvalues, $\{E_k\}$, of a system are found at the poles of the function $g(E)$:

$$g(E) \equiv Tr[E-H]^{-1} = \sum_k (E-E_k)^{-1}. \tag{D.2}$$

For a two-level system with energies $E_0 \pm \frac{\Delta}{2}$, with $\Delta \ll E_0$,:

$$\begin{aligned} g(E) &= \frac{1}{E-E_0+\frac{\Delta}{2}} + \frac{1}{E-E_0-\frac{\Delta}{2}} \\ &\approx 2\left[\frac{1}{E-E_0} + \frac{\left(\frac{\Delta}{2}\right)^2}{(E-E_0)^3} + \frac{\left(\frac{\Delta}{2}\right)^4}{(E-E_0)^5} + \ldots\right]. \end{aligned} \tag{D.3}$$

D.2 Semiclassical Green's function

$g(E)$ can also be evaluated semiclassically. For one-dimensional systems, $g(E)$ is proportional to a sum over periodic orbits of the system[78, 332]:

$$g(E) \propto \sum_{\substack{\text{Periodic} \\ \text{orbits}}} \exp\left(i\left[\Phi - \frac{\pi l}{2}\right]\right) \tag{D.4}$$

where Φ is the total action for the orbit:

$$\Phi(E) = \oint \mathrm{d}x\; p(x,E) \tag{D.5}$$

and l is the number of turning points of the trajectory. For a symmetric double well potential, such as that shown in Fig. D.1 with classical turning points at $[x_a, x_b, x_c, x_d]$, two types of orbit need be considered; those that remain in the classically allowed region, and those that cross between the two wells, through the classically forbidden barrier region. The simplest orbit, C_0, is one that remains in the well, as shown in Fig. D.2, where the orbit can pass back-and-forth any number of times before terminating.

We can define the action of a single pass across a well:

$$\phi(E) = \int_{x_a}^{x_b} dx \sqrt{2m\left[E - V(x)\right]} \tag{D.6}$$

and so an orbit that makes k passes has action:

$$\Phi_{C_0}(E,k) = 2k\phi(E) \tag{D.7}$$



Figure D.3 The simplest crossing periodic orbit

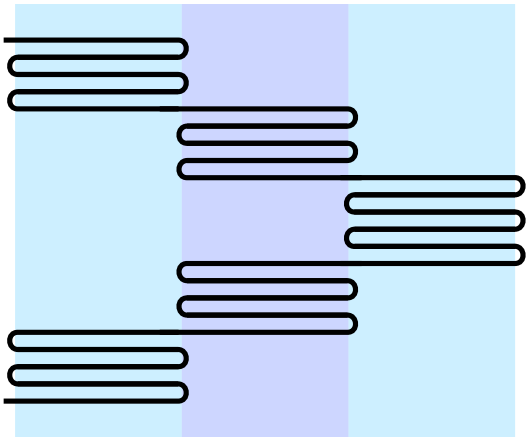


Figure D.4 Crossing periodic orbit: C_1

and the number of turning points is given by:

$$l_{C_0}(k) = 2k. \tag{D.8}$$

The contribution to the semiclassical Green's function from all orbits in a single well is therefore given by:

$$C_0 \to \sum_{k=1} e^{2ki\left[\phi-\frac{\pi}{2}\right]} = \frac{\exp\left(2i\left[\phi-\frac{\pi}{2}\right]\right)}{1-\exp\left(2i\left[\phi-\frac{\pi}{2}\right]\right)} \equiv \frac{e^{2\pi in}}{1-e^{2\pi in}} \tag{D.9}$$

where:

$$n \equiv \frac{\phi-\frac{\pi}{2}}{\pi}. \tag{D.10}$$

We now consider orbits that cross the classically forbidden barrier region. The action for one pass across the barrier region can be written:

$$\begin{aligned} \phi_B(E) &= \int_{x_b}^{x_c} dx\sqrt{2m\left[E-V(x)\right]} \\ &= i\int_{x_b}^{x_c} dx\sqrt{2m\left[V(x)-E\right]} \\ &= i\theta(E). \end{aligned} \tag{D.11}$$

The simplest tunnelling trajectory is that which goes all the way to the opposite well and comes straight back, shown in Fig. D.3, which has:

$$\Phi(E) = \phi + i\theta + 2\phi + i\theta + \phi = 4\phi + 2i\theta, \qquad l = 2 \tag{D.12}$$

However, in general, the trajectory can 'bounce' at each classical turning point, as shown in Fig. D.4, creating a general tunnelling trajectory, C_1. We consider a trajectory that makes k_1 extra passes back and forth across the first well, then tunnels and makes k_2 extra passes in the tunnelling region, then makes k_3 extra

passes in the opposite well, then makes k_4 extra passes in the barrier region on its return to the first well where it makes k_5 extra passes. It has action:

$$\begin{aligned}\Phi_{C_1}(E,\{k\}) &= (1+2k_1)\,\phi + (1+2k_2)\,i\theta + (2+2k_3)\,\phi + (1+2k_4)\,i\theta + (1+2k_5)\,\phi \\ &= 4\phi + 2i\theta + 2\phi k_1 + 2i\theta k_2 + 2\phi k_3 + 2i\theta k_4 + 2\phi k_5.\end{aligned} \tag{D.13}$$

The number of turning points is given by:

$$l_{C_1}(\{k\}) = 2 + 2k_1 + 2k_2 + 2k_3 + 2k_4 + 2k_5 \tag{D.14}$$

so each trajectory's contribution to the semiclassical Green's function is:

$$\begin{aligned}&\exp\left[i(4\phi + 2i\theta + 2\phi k_1 + 2i\theta k_2 + 2\phi k_3 + 2i\theta k_4 + 2\phi k_5) - i\frac{\pi}{2}(2 + 2k_1 + 2k_2 + 2k_3 + 2k_4 + 2k_5)\right] \\ &= -e^{4\pi i n} e^{-2\theta} e^{2\pi i n k_1} e^{-2\left(\theta+\frac{\pi i}{2}\right)k_2} e^{2\pi i n k_3} e^{-2\left(\theta+\frac{\pi i}{2}\right)k_4} e^{2\pi i n k_5}.\end{aligned} \tag{D.15}$$

Summing over all $\{k\}$ gives the tunnelling contribution to $g(E)$:

$$\begin{aligned}C_1 &\to -e^{4\pi i n} e^{-2\theta} \left(\sum_k e^{2\pi i n k}\right)^3 \left(\sum_k e^{-2\left(\theta+\frac{\pi i}{2}\right)k}\right)^2 \\ &= -e^{4\pi i n} e^{-2\theta} \left(\frac{1}{1-e^{2\pi i n}}\right)^3 \left(\frac{1}{1+e^{-2\theta}}\right)^2\end{aligned} \tag{D.16}$$

Equation D.4 thus gives:

$$g(E) \propto \left[\frac{e^{2\pi i n}}{1-e^{2i\pi n}} - e^{4\pi i n}\left(\frac{1}{1-e^{2i\pi n}}\right)^3 \left(\frac{e^{-\theta}}{1+e^{-2\theta}}\right)^2\right] \tag{D.17}$$

Following Miller, we expand n as a series about its unperturbed value. The unpeturbed eigenvalues have [1]:

$$n(E_0) = \text{integer}. \tag{D.18}$$

Requiring the perturbed levels to lie close to E_0 gives:

$$n(E) \approx n(E_0) + n'(E_0)(E - E_0). \tag{D.19}$$

and therefore:

$$\begin{aligned}e^{2\pi i n} &\approx 1 + 2\pi i n'(E_0)(E - E_0) \\ 1 - e^{2\pi i n} &\approx -2\pi i n'(E_0)(E - E_0).\end{aligned} \tag{D.20}$$

Equation D.17 then becomes:

[1] This can be shown by a periodic orbit analysis of just non-crossing trajectories, as described by Miller[313]

$$g(E) \propto \frac{1}{-2\pi i n'(E_0)} \left[\frac{1}{E-E_0} - \left(\frac{1}{E-E_0} \right)^3 \left(\frac{e^{-\theta}}{1+e^{-2\theta}} \right)^2 \left(\frac{1}{2\pi i n'(E_0)} \right)^2 \right] \quad \text{(D.21)}$$

Comparing powers of $(E-E_0)$ to the quantum mechanical expression for $g(E)$, Eq. D.3, gives:

$$\left(\frac{\Delta}{2} \right)^2 = \left(\frac{e^{-\theta}}{1+e^{-2\theta}} \right)^2 \left(\frac{1}{2\pi n'(E_0)} \right)^2 \quad \text{(D.22)}$$

so:

$$\Delta = \frac{1}{\pi n'(E_0)} \left(\frac{e^{-\theta}}{1+e^{-2\theta}} \right). \quad \text{(D.23)}$$

If you take a harmonic well approximation:

$$\begin{aligned} E &= \omega \left(n + \frac{1}{2} \right) \\ \implies n(E) &= \frac{E}{\omega} - \frac{1}{2} \\ \implies n'(E) &= \frac{1}{\omega} \end{aligned} \quad \text{(D.24)}$$

and you obtain the analogue of the most commonly used expression:

$$\Delta = \frac{\omega}{\pi} \left(\frac{e^{-\theta}}{1+e^{-2\theta}} \right). \quad \text{(D.25)}$$

This derivation also provides a clear route to systematically improve the prefactor. Using instead a Morse potential model for the well (as, for example, an SPT analysis might) gives:

$$\begin{aligned} E &= \omega \left(n + \frac{1}{2} \right) + x \left(n + \frac{1}{2} \right)^2 \\ n(E) &= \frac{-\omega \pm \sqrt{\omega^2 + 4Ex}}{2x} - \frac{1}{2} \\ n'(E) &= \left[\omega^2 + 4Ex \right]^{-0.5} \end{aligned} \quad \text{(D.26)}$$

and you obtain the analogue of the Morse well approximate approximate splitting.

More generally, the correct prefactor can be found for any given potential. $n'(E)$ can be found from differentiating the WKB quantisation formula:

$$\pi n'(E) = \frac{1}{\sqrt{2}} \int_{x_a}^{x_b} dx \frac{1}{\sqrt{E - V(x)}} \quad \text{(D.27)}$$

where (a,b) are the classical turning points of trajectories in the potential well. This can be solved (either analytically or numerically) for the potential in question.

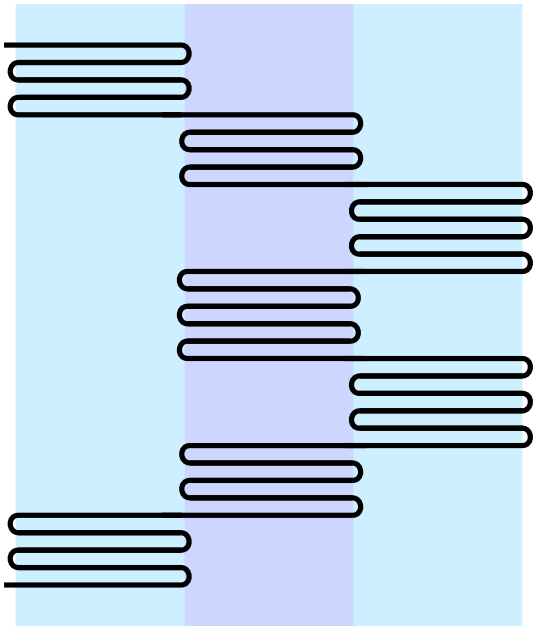


Figure D.5 Another crossing trajectory: C_2

D.2.1 More complex trajectories

In principle, more complex trajectories could be included in the semiclaissical analysis, such as shown in Fig. D.5, whereby each well is visited more than once. The are an infinite number of such trajectories. It is simple to show, however, that these do not contribute to the $\left(\frac{1}{E-E_0}\right)^3$ term in Eq. D.21 so can be ignored for this analysis.

D.3 Origin of the discrepancy with the Lifshitz-Herring formula

Miller[313] derived a similar expression also using periodic orbit analysis. The discrepancy with the analysis in this study is that the author only included crossing trajectories of the form shown in Fig. D.6. As such, it does not allow for multiple bounces in the barrier region, and will give poor performance for small barriers (or trajectories near the barrier top) where the exponential damping of these trajectories is slow. The two formulae, of course, agree in the limit of large θ.

D.4 Application to the SPT method

When used with the perturbation theory analysis of the Semiclassical Perturbation Theory method, as described in Chapter 9, the periodic orbit formula gives better results than the Lifshitz-Herring formula, as shown in Fig. D.7. It is clear that the new formula appears nearly exact when the ZPE is at the top of the barrier. The SPT results behave similarly to the analytic WKB result, except for their poor performance for large barriers - this is caused by an increasingly poor description of the whole barrier from just a Taylor expansion at the barrier top.

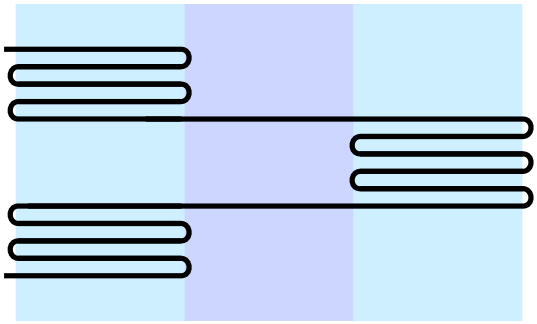


Figure D.6 The tunnelling orbits considered in ref. [313]

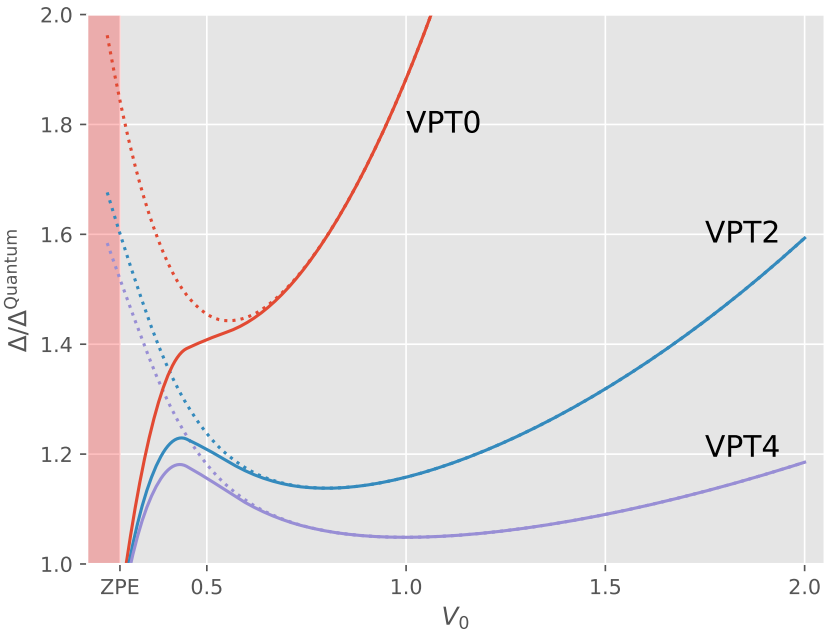


Figure D.7 Testing the periodic orbit formula, Eq. D.25 with the SPT method (Lifshtiz-Herring formula in dashed lines)